Particle Production in Deep Inelastic Muon Scattering

by

John James Ryan
Artium Baccalaurei, Princeton University, 1983

Dissertation
Submitted to the Department of Physics
in Partial Fulfillment of the Requirements
for the degree of
Doctor of Philosophy

at the

Massachusetts Institute of Technology.

February, 1991

AAB1987

Particle Production in Deep Inelastic Muon Scattering

by

John James Ryan
Artium Baccalaurei, Princeton University, 1983

Dissertation
Submitted to the Department of Physics
in Partial Fulfillment of the Requirements
for the degree of
Doctor of Philosophy

at the

Massachusetts Institute of Technology.

February, 1991

©John James Ryan, 1990. All rights reserved.

The author hereby grants to MIT permission to reproduce and to distribute copies of this thesis document in whole or in part.

Signature of Author .....
Department of Physics
December 14, 1990

Certified by .....
Wit Busza
Professor of Physics
Thesis Supervisor

Accepted by .....
George F. Koster
Chairman of Department Committee on Theses

FERMILAB
LIBRARY

Particle Production in Deep Inelastic Muon Scattering

by

John James Ryan
Artium Baccalaurei, Princeton University, 1983

Dissertation Submitted to the Department of Physics on
December 14, 1990
in Partial Fulfillment of the Requirements
for the degree of Doctor of Philosophy
at the
Massachusetts Institute of Technology.

Abstract

The E665 spectrometer at Fermilab measured Deep-Inelastic Scattering of 490 GeV/c muons off several targets: Hydrogen, Deuterium, and Xenon. Events were selected from the Xenon and Deuterium targets, with a range of energy exchange, ν, from 100 GeV to 500 GeV and for large ranges of Q^2 and X_{Bj}: $0.1(\mathrm{GeV/c})^2 < Q^2 < 100(\mathrm{GeV/c})^2$ and $0.001 < X_{Bj} < 0.1$.

The presented results include comparisons of distributions of produced hadrons, as functions of the hadron variables Z and ϕ. In both variables, the dependence of the distributions upon the *rank* of the hadrons, in terms of their momenta, has been examined. The longitudinal energy distributions (Z) show no nuclear dependence, even in the kinematic region of Shadowing. The asymmetry of the distribution of hadron azimuthal angle is demonstrated, but no nuclear dependence is observed in this asymmetry. The asymmetry exhibits strong dependence upon the *rank* of the hadron.

Thesis Supervisor: Wit Busza
Title: Professor of Physics

Acknowledgements

I should acknowledge all with whom I have worked over these past $7\frac{1}{2}$ years; to share a bit of adversity forges friendships. I want to thank Michael Schmitt for 'being a lot like me'; not only was this important in quality of work and attention to detail, but also in the conviction that some evenings were meant to be spent drinking beer. Similarly, I remember some long beer drinking discussions with Uwe Ecker; I really learned to appreciate 'making a list!' To my 'colleague, but nevertheless friend' Silhacene Aid I am grateful for help in math and hacking: "I'm sure Godot will be back any minute now". I enjoyed working with my fellow M.I.T. slave, my 'little brother' Mark Baker; we augmented each other's sense of iconoclasm in Science.

Alex Salvarani's endurance was amazing; he did hardware for a long time, then software for a long time, and then analysis for a long time. Doug Jansen did a lot of work getting our Pattern Recognition out of software. Anwar Bhatti deserves a great deal of credit; he took on some of the dirtiest, but most crucial, jobs like Alignment and Normalization, and he forged the way back to the past to work on an IBM machine. Other students whose work has been invaluable to me include Perry Anthony, Martin Erdmann, Detlev Hantke, Steve Magill, Steve O'Day, Eric Ramberg, Arnd Röser", and Stefan Soldner-Rembold. I must also thank Harry Melanson and Steve Wolbers for the roles they have played in this experiment.

I learned enormously about electronics from Richard Nickerson and about software from Suichi Kunori; I learned some analysis techniques from David Jaffe. David especially helped me by becoming a golf fanatic and motivating me to get out on the course. In the seven years on this experiment, I have developed some friendships with 'established colleagues' who have helped me understand how this field works: Helmut Braun, Volker Echart, Clive Halliwell, and Andreas Manz. I must thank Hugh Montgomery specially for being a friend and a mentor; he probably felt like he was pulling teeth, but he helped to direct my analysis.

Of course, I must thank my bosses, Wit Busza and Louis Osborne. By throwing me straight into the fire of responsibility on this experiment, they have forged me with a strong will. I will always remember Louis telling me, after I had designed and built the PTM's and the Muon Spectrometer Support Structure, "John, you have to learn how to take more responsibility." When it finally got down to real physics, Wit became really excited and interested in my analysis. His input then was absolutely essential, and I enjoyed interacting with and learning from him.

I owe a great deal of thanks to Tommy Lyons and his various crews. His style is based on the premise that nothing is impossible and "just get out of my way and let me build whatever it is you need." I have tried to adopt some portion of his style.

I even learned something from King Anti-Midas: doing something "the cheaper way" is never less expensive — it merely shuffles the cost into someone else's time. I also learned to cringe when someone talked about accomplishing a task "in a timely fashion"; this meant that the job was to be done shoddily and to await someone else to come along and redo it, properly.

I want the thank the Fox Valley Maoris Rugby Football Club for helping to keep my feet on the ground (as well as an ankle, a shoulder, ...). My teammates have been good friends, and I will miss them; but, I will always consider myself a Maori.

I also want to thank my parents, John and Ruth, for their love and support and patience. Their confidence in me was so unshakable that they have refused to believe that I did not perform the whole experiment single-handedly.

"But how can our ill-prepared nervous systems grasp the message? Certainly the average man cannot master the conceptual, mathematical bead game of the physics graduate student. Must his experimental contact with the Divine process come in watered-down symbols, sermons, hymns, robot rituals, religious calendar art, moral-behavior sanctions eventually secular in their aim? Fortunately the Great Plan has produced a happy answer and has endowed every human being with the equipment to comprehend, to know, to experience directly, incontrovertibly. It's there in that network of ten billion cells, the number of whose interconnections 'is far greater than all the atoms in the universe.'

"If you can, for the moment, throw off the grip of your learned mind, your tribal concepts, and experience the message contained in the ten-billion-tube computer which you carry behind your forehead, you would know the awe-full truth. Our research suggests that even the uneducated layman can experience directly what is slowly deduced by scientists — for example physicists, whose heavy, conceptual minds lumber along at three concepts a second, attempting to fathom the speed-of-light processes which their beautiful machines record and which their beautiful symbols portray."

— Dr. Timothy Leary [34, pp. 3-23]

(I think 3 is a bit overly-optimistic. — John Ryan)

Contents

1 Introduction **25**

1.1 From Metaphysics to Physics 25

1.2 Artillery for a Microscope 27

1.3 Thesis Overview 30

1.3.1 Labeling Conventions 32

2 Deep-Inelastic Muon Scattering **34**

2.1 Kinematics 34

2.2 Hadron Variables 38

2.3 Shadowing 40

2.4 Hadronization 46

2.4.1 Kin-1 and Kin-2 47

3 Beam and Experimental Apparatus **49**

3.1 Beam Spectrometer 50

3.2 Experimental Apparatus 51

3.2.1 Forward Spectrometer 53

3.2.2 Wide Angle Spectrometer 65

3.2.3 Muon Spectrometer 66

3.2.4 Particle Identification 68

3.3 Targets 68

3.4 Triggers 69

4 Event Reconstruction **70**

4.1 Detector Characteristics 70

4.1.1 Coordinate System 70

4.1.2 Position and Error 71

4.2 Pattern Recognition 73

4.2.1 PB Processor 79

4.2.2 PM Processor 79

4.2.3 DC Processor 79

4.2.4 PC Processor 80

4.2.5 MA Processor 82

4.2.6 PF Processor 83

4.2.7 PS Processor 84

4.2.8 MS Processor 84

4.2.9 SF Processor 84

4.2.10 SN Processor 85

4.2.11 MD Processor 86

4.2.12 PV Processor 86

4.2.13 MV Processor 87

4.2.14 DHFIT3 model 87

4.3 Track Fitting 88

4.4 Muon Matching 90

4.5 Vertex Fitting 91

5 Selection and Correction **92**

5.1 Event Selection 92

5.2 Track Rejection 94

5.3 Calorimeter Cuts 96

5.3.1 Bremsstrahlung Contamination 96

5.4 Merging SAT and LAT 103

5.4.1 Kinematic Distributions: Kin-1 and Kin-2 111

5.5 Corrections for Acceptance and Reconstruction 114

5.5.1 Fredholm Equation 114

5.5.2 The Kernel 115

5.5.3 Monte Carlo 116

6 Z Distributions **123**

6.1 Z Resolution 124

6.2 World ZZZ 129

6.2.1 Steepening with Rank 129

6.3 Xenon versus Deuterium 132

6.3.1 Rescattering of the Excited State 137

6.3.2 Rescattering in Target 141

6.4 Rescaled Z 146

6.5 Correlations 150

6.5.1 Correlation Coefficient 154

6.6 Conclusions 159

7 ϕ Distributions **160**

7.1 Definition of ϕ 160

7.2 Brief History 160

7.3 Theory 162

7.4 Data 165

7.4.1 EMC 165

7.4.2 ϕ Resolution 165

7.4.3 Deuterium 168

7.4.4 Xenon 174

7.4.5 Z-Ranking 179

7.5 Conclusions 191

8 Summary **192**

A The Fermilab E665 Collaboration **194**

B Proportional Tube Physics **196**

B.1 Introduction 196

B.2 Motions of Electrons and Ions in Gases 197

B.3 Resolving Times 199

B.4 Pulse Shapes 200

B.4.1 Parallel Plate Geometry 200

B.4.2 Cylindrical Geometry 201

B.4.3 A Proportional Tube Counter 203

B.4.4 Application 207

C Delta-Rays **210**

D PTM Proportional Tubes **214**

D.1 Construction of the Tubes 214

D.2 Construction of the Support Assembly 216

D.3 Proportional Tube Frames 219

D.4 Beam-Hole Region 222

D.4.1 Motivation 222

D.4.2 The Setup 223

D.4.3 Measurements 227

D.4.4 Analysis 230

D.4.5 Conclusions 234

D.5 Airflow Cooling of Electronics 237

D.6 PTA Chambers 241

D.7 PTM Efficiencies 242

D.7.1 Sigmas 242

D.7.2 Single Cell Efficiencies 245

D.7.3 Rate Dependence 248

D.7.4 Beam Region Efficiencies 249

E Electronics for the PTM Proportional Tubes 251

E.1 Introduction 251

E.2 Coupling Electronics 252

E.2.1 Coupler-Card 252

E.2.2 Egg-crates 252

E.3 Nanometric N-272-E Readout Card 254

E.3.1 Fast-Trigger Section 257

E.3.2 Fast-OR Section 257

E.3.3 On-Board Memory Section 258

E.3.4 Connectors 258

E.3.5 Setbit Cards 261

E.4 Motherboards 261

E.5 Memory-Address Board 262

E.5.1 Input Bit Latch 263

E.5.2 Clock 263

E.5.3 Address Bits 264

E.5.4 Write Enable Pulse 264

E.5.5 Adder and Multiplexer 265

E.5.6 Fast-Trigger-Strobe and One-Shot-Clear-Line 265

E.5.7 Output Sectors 265

E.5.8 READ State Operations 266

E.6 PTM-Fanout 268

E.7 WCS-200 Scanner 268

E.8 Megavertors 269

Curriculum Vitae **271**

List of Figures

2.1 Feynman Graph of Single-Photon Exchange 35

2.2 Shadowing Contributions 43

2.3 Shadowing in Cross Section Ratios 45

3.1 Experimental Apparatus 52

3.2 PC Chamber Efficiencies 56

3.3 PCF Chamber Efficiencies 58

3.4 DC Chamber Efficiencies 61

3.5 PCV Chamber Efficiencies 64

3.6 Trigger Acceptance 69

4.1 Resolution on an Isotropic Interval 72

4.2 Cluster-Sizes 74

4.3 Intersection of 3 Wires 76

4.4 PC Efficiency: Algorithm versus Chamber 82

4.5 DHFIT3 Model Validity versus Track Momentum 88

4.6 Distance Over Error from Vertex 91

5.1 Beam Energy, ν, Q^2, X_{Bj}, Bremsstrahlung Removal 97

5.2 $W^2, Y, \theta_\mu, \phi_\mu$, Bremsstrahlung Removal 98

5.3 Q^2 versus Y and ν, Bremsstrahlung Removal 99

5.4 Z, X_F, P_t, ϕ_h Distributions, Bremsstrahlung Removal 100

5.5 Z and Multiplicity Distributions, Bremsstrahlung Removal 101

5.6 Z and Multiplicity Distributions of D_2 LAT 102

5.7 Kinematic Distributions for Overlap Region 104

5.8 Trigger Overlap: Comparison of Z-distributions, D_2 106

5.9 Trigger Overlap: Overlay of Z-distributions, D_2 107

5.10 Trigger Overlap: Comparison of Z-distributions, Xenon 108

5.11 Trigger Overlap: Overlay of Z-distributions, Xenon 109

5.12 Trigger Overlap: Ratio of Z-distributions, D_2 110

5.13 Trigger Overlap: Ratio of Z-distributions, Xenon 110

5.14 Kinematic Distributions for Kin-1 and Kin-2, D_2 112

5.15 Kinematic Distributions for Kin-1 and Kin-2, Xenon 113

5.16 Monte Carlo Tracks eliminated by Fiducial cut 117

5.17 Acceptance (Z) 118

5.18 Acceptance (Position) 119

5.19 Acceptance (Position and Energy) 120

5.20 Acceptance (Energy) 121

5.21 Kernel of Acceptance 122

6.1 Z Resolution 125

6.2 Z Resolution, $100 < \nu < 500$ 126

6.3 Unphysical Z-values 127

6.4 Resolution on Unphysical Tracks 128

6.5 Resolution on Unphysical Tracks, (1,2,3) 128

6.6 World Z-distributions 129

6.7 Ranked Z-distributions 130

6.8 Z-Distributions, D_2: low and high kinematics 133

6.9 Z-Distributions, Xe: low and high kinematics 134

6.10 Z-Distributions, D_2: Ratio of low and high kinematics 135

6.11 Z-Distributions, Xe: Ratio of low and high kinematics 135

6.12 Z-Distributions: Ratio of Xe/D_2, low kinematics 136

6.13 Z-Distributions: Ratio of Xe/D_2, high kinematics 136

6.14 Convoluted Z-distributions 140

6.15 Target Length Effects on Z-distributions, D_2 142

6.16 Target Length Effects on Z-distributions, Xenon 143

6.17 Target Length Effects on Fiducial cuts 144

6.18 Z-Distributions: Ratio of Xe/D_2, Kin-1, Half Target 144

6.19 Z-Distributions: Ratio of Xe/D_2, Kin-2, Half Target 145

6.20 Rescaled Z-Values, low kinematics 147

6.21 Rescaled Z-Values, high kinematics 148

6.22 Ratios of Xe/D_2 Rescaled Z-Distributions, low kinematics 149

6.23 Ratios of Xe/D_2 Rescaled Z-Distributions, high kinematics 149

6.24 Track Correlations 150

6.25 Track Correlations, Acceptance Corrected 151

6.26 Track Correlations, No intermediates 152

6.27 Rescaled Track Correlations 153

6.28 Rescaled Track Correlations, No intermediates 153

6.29 Correlation Coefficient, D_2 155

6.30 Rescaled Correlation Coefficient, D_2 155

6.31 Correlation Coefficient, no missing intermediates, Kin-2 156

6.32 Rescaled Correlation Coefficient, no missing intermediates, Kin-2 . . . 157

6.33 Correlation Coefficient, no missing intermediates, Kin-1 157

6.34 Rescaled Correlation Coefficient, no missing intermediates, Kin-1 . . . 158

7.1 Azimuthal Angle ϕ 161

7.2 EMC ϕ-distribution 166

7.3 EMC $\cos\phi$ moment versus X_F 166

7.4 EMC $\cos 2\phi$ and $\sin\phi$ moments versus X_F 167

7.5 EMC $\cos\phi$ moment versus P_t cut 167

7.6 Resolution of Track Separation from Photon direction 168

7.7 $f_i(y)$ distributions, D_2 169

7.8 ϕ-distribution 170

7.9 $\cos\phi$-moments, D_2 171

7.10 $\cos 2\phi$-moments, D_2 172

7.11 $\sin\phi$-moments, D_2 173

7.12 ϕ-distribution, Xenon 175

7.13 $\cos\phi$-moments, Xenon 176

7.14 $\cos 2\phi$-moments, Xenon 177

7.15 $\sin\phi$-moments, Xenon 178

7.16 ϕ-distributions, Z-Ranked 180

7.17 ϕ-distributions, Z_1, Multiplicity> 2 181

7.18 $\cos\phi$-moments, Z-Ranked 182

7.19 $\cos\phi$-moments, Z-Ranked versus Z and P_t 183

7.20 $\cos 2\phi$-moments, Z-Ranked 184

7.21 $\sin\phi$-moments, Z-Ranked 185

7.22 $\cos\phi$-moments for the unambiguously fastest particle 187

7.23 $\cos\phi$-moments for the unambiguously fastest particle versus Z and P_t 188

7.24 $\cos 2\phi$-moments for the unambiguously fastest particle 189

7.25 $\sin\phi$-moments for the unambiguously fastest particle 190

B.1 Equivalent Circuit Diagram 204

B.2 Predicted Rate of Induced Charge 208

B.3 Predicted PTM Pulse Shape 209

B.4 Observed PTM Pulse Shape 209

C.1 Probability Distribution of Delta-Ray Emission 213

D.1 PTM Cross section 215

D.2 Muon Support Assembly 217

D.3 Muon Support Assembly Overhang 218

D.4 Aluminum Angle Precision Fastening 220

D.5 Precision Fastening 221

D.6 PTM Test Module 224

D.7 Electric Field Configurations 225

D.8 Normalization Setup 228

D.9 Measurement Grid 229

D.10 Background Setup 231

D.11 Data Setup 232

D.12 Distribution in Normalization Region 233

D.13 Efficiency Across the Deadened Region 233

D.14 Efficiency Across the Deadened Region 234

D.15 Efficiency of Module 236

D.16 Volumetric Flow versus Static Pressure 240

D.17 PTA Support Assembly 243

D.18 Stonehenge-II Support Assembly 244

D.19 PTM Sigmas 246

D.20 PTM Beam Region Efficiencies 250

E.1 PTM Read-out Card 255

E.2 Amplifier Stage of the PTM Read-out Card 256

E.3 Fast-Trigger Stage of the PTM Read-out Card 257

E.4 RAM and Shift Stage of the PTM Read-out Card 259

E.5 Connectors of the PTM Read-out Card 260

List of Tables

3.1 E665 Detectors 54

3.2 PC Efficiencies 55

3.3 PCF Efficiencies 57

3.4 DC Efficiencies 60

3.5 PSA Efficiencies 62

3.6 PCV Efficiencies 63

3.7 SMS Efficiencies 67

3.8 E665 Target Properties 68

5.1 Event Samples 93

5.2 Event Selection 93

5.3 Track Selection 95

5.4 Kinematic Overlap Samples 103

5.5 Time Dependent Acceptance 122

6.1 E665 ZZZ 130

6.2 Rescattering Limits 139

B.1 Gas Properties 198

B.2 Circuit Element Values 208

D.1 Sample Smoothing 235

E.1 Egg-crate Cross-Talk Measurements 254

Chapter 1

Introduction

1.1 From Metaphysics to Physics

Cogito ergo sum . "I am thinking, therefore I exist". Upon this famous phrase René Descartes based his philosophy. Some would say that this concept of distinguishing self from external is the basis of Western science, in which the observer is dispassionately external to the measurements he makes. Also at this time began the development of the *hypothetico-deductive* method in which many effects were examined and a relevant cause was hypothesized. This was a departure from the Aristotelian approach which was more inductive; "First Principles" were laid down, and then causes were developed from them [28, p. 298].

At the heart of Descartes' philosophy was a search for irrefutable knowledge: "What can I know for certain?" He concluded that he could only be certain about his own existence. External objects he could perceive, but he could not guarantee their existence outside his observation. Bishop George Berkeley carried this view to its fullest by stating that external objects only existed in the perception of observers. It was this concept that the German physicist, philosopher Immanuel Kant addressed in his *Prologama to Any Further Discussion of Metaphysics* and in his *Critique of Pure Reason*. He maintained that there are indeed objects which have properties in and of themselves; however, we never know anything of these 'real' properties but only those properties which we perceive, and these are the product of our perception, or interaction with the objects. This is similar to the earlier idea, which John Locke described as the distinction between primary and secondary properties of objects: those which objects really possess and those which we perceive. But Kant made the distinction more completely: we can never know anything directly about objects in

and of themselves but only about the world of our perceptions. Thus, our science is only the description of the interrelations of our perceptions. This was an important step in response to the extreme skeptic, David Hume, who claimed that we have no valid basis to expect "repeatability" to continue; for simply because B has resulted from A consistently in the past, there is no proof that it must continue to do so in the future. Kant's response is that the repeatability is built into the workings of our perception; thus, real objects may not obey repeatability, but our perceptions of these objects do.

Kant was keenly motivated to dispel the "Ideal Realism" of Berkeley — that there are only perceptions — and to construct a practical, yet rigorous, basis of our reality. The basis of Kant's philosophy can be laid down as six theses.

1 (The Temporal Thesis) *Experience essentially exhibits temporal succession.*

2 (The Thesis of Necessary Unity of Consciousness) *There must be such unity among the members of some temporally extended series of experiences as is required for the possibility of self-consciousness on the part of the subject of such experiences.*

3 (The Thesis of Objectivity) *Experience must include awareness of objects which are distinguishable from experiences of them.*

4 (The Spaciality Thesis) *These objects are essentially spatial.*

5 (The Thesis of Spatio-Temporal Unity) *There must be one unified spatio-temporal framework of empirical reality embracing all experience and its objects.*

6 (The Theses of Analogies) *Certain principles of permanence and causality must be satisfied in the physical or objective world of things in space* [60, p. 24] .

An observer must be conscious of his own existence and must be aware of the distinction of self from external. He must perceive experiences as interactions between himself and external objects; for this to occur, he must incorporate the concepts of external objects even when he is not experiencing them. This necessarily implies that the concept of an object must remain fairly stable across an interaction with that object. The World of Perceptions then adheres to a set of rules which defines the

possible experiences of the observer, regardless of the 'actual' attributes of objects in and of themselves. The boundaries of this set of rules define the limits of intuition, the domain upon which pure reason may be applied. Kant allows for the expansion of these boundaries through speculative reasoning, whereby the observer can view an experience as a different interaction with slightly different concepts of the objects in an of themselves. However, the machinery of pure reason must be defined independently of these sets of rules, and that machinery is what Kant endeavored to define in his *Critique of Pure Reason.*

This is then a basis upon which to build a picture of reality. The universe is composed of objects which we perceive to be both spacial and causal and thereby to adhere to a law-governed system. I think that it is still an act of faith to conclude that the objects themselves must adhere to a law-governed system simply because it is the simplest, based on correspondence to the fact that our world of perception does. It is, nevertheless, a practical choice, and I wish to employ it as a foundation for a more tenuous proposal as to the role of science in the description of our world of perception and its relation to the universe of objects in and of themselves. Experimental science clearly examines the interactions of objects as seen in the world of perception, but the conclusions drawn from these observations extend to a deeper level. I suggest that we are trying to develop a description of the mapping of the objects in and of themselves onto our world of perception — a transformation from the 'true reality' to the 'reality of our perceptions'. This is the realm of speculative reasoning, wherein the boundaries of intuition, the limits of possible experiences, are expanded by redefining concepts of objects to more neatly align with experiences. Based on the assumption that the true reality must adhere to a law-governed system and that there is a correspondence to the system observed in our world of perceptions, science has the role of investigating the laws of the world of perception and to project backwards causally to describe the laws of the real system, to describe the basic interactions of these objects in the universe. This is a sufficiently noble, if pretentious, ambition, that it warrants scientific integrity and justifies the rigors and the responsibilities essential to this end.

1.2 Artillery for a Microscope

The main tenet of Western science has been that the experimenter examines phenomena in a detached manner. This was valid while the observation technique, e.g. reflecting light off an object up through a microscope, did not significantly alter the object itself. However, with the development of Quantum Mechanics and the examination of the minutia of atoms and nuclei, the probes transfer enough energy to their targets to disrupt the very target makeup. This is an important issue in Quantum

Mechanics. Situations are described by wave-functions which are probability distributions for a given observable; the act of observing forces the value measured. But the Heisenberg Uncertainty Principle expresses the reality that the observing of one quantity has disrupted the values of other quantities, such that we cannot simultaneously measure several quantities to unlimited accuracy. An example of this is Compton scattering of X-rays off the electrons of an atom; measurements are made of the positions of the electrons, but momentum is transferred and they are knocked completely out of their atomic orbits by the interactions.

The use of energetic projectiles as probes is an application of de Broglie's observation that all matter exhibits wave characteristics, the frequency of which is proportional to the energy. To probe small distances one must use short wavelengths and therefore high-energy probes. Thus, a high-energy electron can be used to probe small distances, since its wavelength is correspondingly short. Other particles can be accelerated to high-energies to achieve fine spatial resolution. In 1907, Rutherford bombarded gold atoms in a thin foil with a beam of alpha particles and was astonished to witness some of them scattering at large angles. The view at the time was that atoms were a soft continuous medium, and the alpha particles should have simply torn through the foil. Rutherford's reaction was as if he had fired rounds of artillery at tissue paper and had some of the shells recochet back at him. The result was that with this new perception of the interactions of objects the description of the structure of atoms changed drastically to account for the observations.

In the beginning and middle of the 20th century many studies of the interactions of cosmic rays with emulsions and cloud chambers were performed, and a host of previously unknown particles were discovered. In the forties, fifties, and early sixties, pions and electrons were being used as projectiles to examine the results of their collisions. Many new particles were discovered, and Quantum numbers, quantities conserved in interactions, were assigned to these particles, and efforts were expended to account for all of these particles. In 1964 Murray Gell-Mann and Zweig could account for all particles as combinations of constituents, according to the prescriptions of the group theory SU(3). Gell-Mann proposed these *quarks* merely as a convenient bookkeeping aid and did not consider them to be 'real'. Before the 1960's, beams of electrons were used to study the structure of atoms. The structure of nuclei and nucleons were studied in the 1950's and 1960's. In 1968 the Nobel Prize winning Friedman, Kendall, and Taylor experiment at SLAC demonstrated the existence of point-like structure inside nucleons, and Feynman interpreted this as evidence for constituents of nucleons, and he called them *partons*. This experiment was the inelastic scattering of an electron beam from a hydrogen target. It was Bjorken's vision that this was easiest to describe as elastic scattering off point-like constituents of the nucleon; since the nucleon always disintegrated, this was termed quasi-elastic scattering of the electrons off the partons that composed the nucleons. This defined the process of Deep-Inelastic

Scattering. Gradually, the concepts of the partons and the quarks were merged, and a new picture of reality was forged: the Naïve Parton Model.

The Naïve Quark/Parton Model is part of the "standard model", which is based on group theory and is constructed of three generations of families of quarks and leptons:

$$\begin{pmatrix} u \\ d \\ e \\ \nu_e \end{pmatrix}, \begin{pmatrix} c \\ s \\ \mu \\ \nu_\mu \end{pmatrix}, \begin{pmatrix} (t) \\ b \\ \tau \\ (\nu_\tau) \end{pmatrix}.$$

A proton has valence quarks (u, u, d), and a neutron has (d, d, u). There is also vacuum polarization production of quark-antiquark pairs, and these are the sea (ocean) quarks. The gluons are the bosons which are transferred between the fermions; these gluons also carry "color" charge, which makes this theory non-abelian. All of these constituents are considered "partons".

These Deep-Inelastic Scattering experiments continued, and many important results came from them. Since quarks had never been observed individually, theories were developed which explained this *confinement* within hadrons. The model for this was a strong attractive force which was independent of distance at large distances but which was essentially zero for distances less than the size of hadrons, which is about 1 fermi. Assuming this asymptotic freedom and that the collisions of the electrons and the quarks were elastic, Bjorken predicted that the structure functions would be functions only of a scaling variable, which Feynman interpreted as the fractional momentum of the proton carried by that quark (in the infinite-momentum frame). Several integral quantities relevant to the SU(3) group should be conserved, and this suggested several sum rules. The Momentum sum rule describes the total fractional momentum of the proton carried by charged partons sampled by the interacting lepton. The maximum value of this sum is roughly 5/18, and the experiments found only 0.172 [40]; this was about half of the total proton. The missing composition of the proton was attributed to the gauge bosons of the SU(3) theory, the gluons. This, along with the scale-breaking of the structure functions with Q^2, set the relevant size of the the coupling constant of these strong interactions: $\alpha_s \sim 0.2$ [43, p. 356].

To delve deeper into this structure of the nucleons required more energetic artillery. Electrons were easy to find and to accelerate, but their propensity to radiate away energy through bremsstrahlung radiation and synchrotron radiation in a curved accelerator motivated the move to using muons as artillery. Since radiative energy loss is proportional to $1/m^2_{\text{projectile}}$, protons and muons are dramatically less affected by these losses. Protons could be accelerated in circular machines, and they produce pions copiously upon collisions with any material. Pions decay almost exclusively into muons, so there was a practical source of muons. A muon beam, of energy 150

GeV, was constructed at the National Accelerator Laboratory (now the Fermi National Accelerator Laboratory) west of Chicago, Illinois in 1972. CERN then built a bigger one, 280 GeV, and the European Muon Collaboration was born in 1978. Back at Fermilab in the late 1980's, muon scattering was performed at the highest energy: 490 GeV; this was Experiment-665, unofficially referred to as the Tevatron Muon Collaboration. The next incarnation of the EMC at CERN was the New Muon Collaboration, which collected data in 1989. However, E665 still claimed the highest energy artillery and collected more data in 1990.

1.3 Thesis Overview

The Fermilab Muon Experiment-665 was constructed in the years between 1983 and 1987. I joined the team in 1984 and was responsible for building the Muon Spectrometer proportional tubes. The first period of data taking started in 1987 and ended in 1988. The following two years were spent developing software to analyze these data. By the end of 1989, a "compromise version" of the software chain was accepted by the collaboration, and most of the data were reconstructed. The members of the collaboration as of some point after the 1987-88 data period are listed in Appendix A.

My dissertation is based on the data collected in the 1987-88 period and reconstructed in 1989. It can be divided into three rather distinct topics that closely represent the three major divisions of my tenure on the experiment. The first of these is the hardware construction. I spent the first four years on the experiment building the proportional tubes and implementing the electronics; I have included a detailed description of this work mainly as documentation for the experiment and for my future reference. Since this material is fairly irrelevant to the physics analysis of this dissertation, I have relegated it to several Appendices. In Appendix D, I discuss the construction of the proportional tubes for the Muon Spectrometer. I had seized the responsibility for the electronics for these tubes, and for documentation purposes I include the grungy details in Appendix E. On a more inquisitive impulse I examine the fundamentals of wire-chamber operation in Appendix B and compare the predicted shape of the tubes' signals with that actually observed. Appendix C includes a discussion of Delta-Ray emission and its effects on chamber operation and track reconstruction; I have included this mainly for my own reference, since I had to study several references to understand these aspects of Delta-Rays. Although I refer to some of it when discussing track reconstruction, none of the material in these Appendices is crucial to the reading of the physics of the dissertation.

The next division of my dissertation involves the labor spent on the software de-

velopment for event analysis. The performance of this software was relevant to the track reconstruction and, hence, the physics analysis; therefore, I have described the chain of the Event Reconstruction software programs in the main body of the text, in Chapter 4. This software was composed of several pieces, and many people worked on its development. The actual version of the reconstruction software employed to analyze the data had some known deficiencies, and hence I have called it a "compromise version". These deficiencies have not been well documented to date, so I have included a detailed description of specifics and the performance of some pieces of this software chain, primarily that involved with the Pattern Recognition. I have kept a keen eye on the efficiency of the algorithms for finding tracks in each event, since a large fraction of the corrections applied to the data resulted from the inefficiency of this part of the chain.

The performance of the detectors themselves impacted upon the efficiency of final track reconstruction. This was due, in part, to the effects of limited acceptance. In addition, the efficiency level of a given detector also affected which Pattern Recognition algorithms could be used to reconstruct the tracks; since the efficiencies of these algorithms differed, the net efficiency of track reconstruction depended upon the efficiency of the chambers. Hence, in Chapter 3, I describe the Experimental Apparatus in some detail, including measurements of the performance of several of the detectors which were relevant to track reconstruction.

The third major division of my dissertation involves the physics. I concentrate primarily on the final state distributions of the hadrons produced from the Deep-Inelastic Muon Scattering events. In the next chapter is a description of the basic elements of Deep-Inelastic Scattering, along with some discussion of the effect of Shadowing. This is followed by a short discourse on the hadronization process.

As E665 was a new experiment and the analysis software was in somewhat of a developmental stage, a large part of the job of analysis was to verify that the results of a given analysis were scientifically valid, i.e. not merely garbage. To this end I have included examinations of several effects; in Chapter 5, I discuss the selection criteria for events to be included in the final sample and the quality requirements imposed on the tracks of these events. The distributions of the final state hadrons have been normalized to the number of scattered muons; in the approximation of Factorization, the removal of dependence upon the scattering cross section removes the dependence upon the triggering efficiency of the data collection. The data were collected based upon two different triggers; the validity of merging these two samples depends upon the demonstration that, for similar kinematics, the two triggers do not bias the hadron distributions. This examination is presented in some detail in Chapter 5. Also in that chapter, I cover the method employed to correct the data for acceptance and reconstruction.

The fun part comes in Chapters 6 and 7, which include the data distributions as functions of the hadron variables Z and ϕ, respectively. These analyses are fairly independent, but in both I have examined the dependence of the distributions upon the *rank* of the hadrons, in terms of their momenta. Clearly, the third hadron variable, P_t, is of interest as well, but I have not studied it. I was originally studying only the longitudinal momenta, but I became fascinated with the ϕ-asymmetry, so I had to look at that variable as well. The P_t is studied in other theses, and it will be treated in a paper, of course.

In Chapter 6, I concentrate on the Z-distributions. I compare these distributions to those from EMC and CHIO. I examine the dependences of these distributions upon the event kinematics, paying particular attention to comparing the distributions from a simple target, Deuterium, to those from a nuclear target, Xenon. It is of special interest that these comparisons show no nuclear dependence, even in the kinematic region of Shadowing — hadron studies have not been performed in this kinematic region of Deep-Inelastic Scattering before E665. I examine correlations between leading particles and compare these from events scattered from different nuclei and in different kinematic regions. In addition, there appears to be some "self-similarity" in the scaling of hadrons in the fragmentation chain to the energy available to a hadron in a given position in the chain.

The asymmetry of the distribution of hadron azimuthal angle is demonstrated and compared to EMC results in Chapter 7. No nuclear dependence is observed in this asymmetry. However, in the examination of the dependence of the asymmetry upon the *rank* of the hadron, I have observed that the effect is carried almost exclusively by the very leading particle, regardless of the Z-value; this was unexpected.

Monte Carlo events, based on LUND, were used only to simulate the effects of acceptance on the distributions. They were not considered as a means of evaluating the physics of the distributions.

1.3.1 Labeling Conventions

Throughout this dissertation the presentation of the figures will adhere to certain conventions. All vertical error bars will represent only the statistical errors; horizontal error bars will indicate half the bin-width — no bin-centering will be applied. In figures where there will be more than one plot, the individual plots will be implicitly

referenced as (a,b,c,...), where the sequence runs *left to right* and then *top to bottom*:

$$\begin{bmatrix} (a) & (b) \\ (c) & (d) \\ (e) & (f) \end{bmatrix}.$$

Unless explicitly stated otherwise, all distributions will be corrected for acceptance.

Chapter 2

Deep-Inelastic Muon Scattering

2.1 Kinematics

Deep-Inelastic lepton scattering is a continuation of elastic scattering into the regime of target breakup. Both scattering processes involve the transfer of energy and momentum from the lepton to the target through an electromagnetic interaction. This interaction can be described as the transference of electromagnetic vector bosons, photons; in the Born approximation, the transference is of a single photon. Emissions of other photons are usually considered as corrections to the single-photon exchange. The linearity of the Rosenbluth plot and the equivalence of the cross sections for e^+p and e^-p indicate that the contributions from the higher order exchanges are small [43, pp. 283-4].

The Feynman graph of single-photon exchange is shown in Figure 2.1. The incoming lepton has 4-momentum k, and the outgoing lepton, scattered through a lab-angle θ, has 4-momentum k'. The initial 4-momentum of the target is defined to be P, and the 4-momentum transferred in the interaction is defined as $q = k' - k$. Since the process is virtual, the square of the 4-momentum transfer is negative: $q^2 < 0$; hence, it is customary to define the positive quantity $Q^2 \equiv -q^2$. In the laboratory system the target is initially at rest, so $P = (M; 0, 0, 0)$, where M is the nucleon mass. The energy transferred in this system is defined as $\nu \equiv E' - E$, and thus $q = (\nu; \bar{k}' - \bar{k})$. The expression for Q^2 is then

$$Q^2 = -2m_\mu^2 + 2EE' - 2|\bar{k}||\bar{k}'|\cos\theta. \tag{2.1}$$

If the momentum of the muon is great, then the muon mass can be ignored, and the

expression 2.1 reduces to

$$Q^2 = 2|\bar{k}||\bar{k}'|(1 - \cos\theta) = 4|\bar{k}||\bar{k}'|\sin^2\frac{\theta}{2}. \tag{2.2}$$

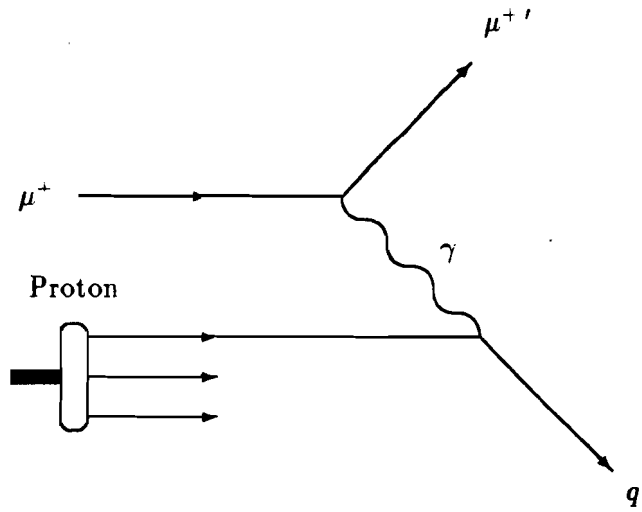

Figure 2.1: Feynman Graph of Single-Photon Exchange.

Since the interaction is inelastic, there are always two parameters needed to describe the kinematics of the scatter. In elastic scattering there is a one-to-one correspondence between the energy exchanged and the angle of the scattering:

$$2M\nu = -2m_\mu^2 + 2EE' - 2|\bar{k}||\bar{k}'|\cos\theta = Q^2. \tag{2.3}$$

In inelastic scattering, energy is contributed to the breakup of the target, and another parameter is required to describe the relative inelasticity of the interaction. The invariant mass of the final hadronic state, W, can be used for this purpose, since it includes the amount of energy absorbed into the system. The square of the 4-momentum transfer will then be described by the sum of a kinetic term and a mass term:

$$Q^2 = 2M\nu + (M^2 - W^2). \tag{2.4}$$

It is natural to define a variable which expresses the inelasticity of the interaction:

$$X \equiv \frac{Q^2}{2M\nu}, \tag{2.5}$$

which takes values in the interval (0,1), with $X = 1$ for elastic scattering. This is traditionally the variable associated with Bjorken-Scaling; however, X_{Bj} is technically defined in the infinite-momentum frame. The attractiveness of this frame is that it is easier to declare all perpendicular components of momentum to be negligible and to treat only the longitudinal components. In this frame the proton has momentum $p \rightarrow \infty$; a parton carries a fraction of this momentum, ξp. This parton is scattered elastically by absorbing 4-momentum q; as the scattering is elastic, the invariant mass squared of this parton must remain the same:

$$(\xi p + q)^2 = -m_q^2, \tag{2.6}$$

where m_q is the mass of the parton. If the mass of the parton is small and if $|\xi^2 p^2| = \xi^2 M^2 \ll q^2$, then

$$\xi \approx -\frac{q \cdot q}{2P \cdot q} = \frac{Q^2}{2P \cdot q}; \tag{2.7}$$

X_{Bj} is defined as this Lorentz-Invariant quantity:

$$X_{Bj} \equiv \frac{Q^2}{2P \cdot q}. \tag{2.8}$$

In the lab frame, $P \cdot q = M\nu$; this delivers the association to Equation 2.5.

The differential cross section for the scattering of point-like Dirac spinors is given by

$$\left(\frac{d\sigma}{d\Omega}\right)_{\text{Dirac}} = \frac{e^4}{Q^2(1 + 2(E/M)\sin^2\frac{\theta}{2})}\left(\cos^2\frac{\theta}{2} + \frac{Q^2}{2M^2}\sin^2\frac{\theta}{2}\right). \tag{2.9}$$

However, the nucleons are not point-like; they have substructure and anomalous magnetic moments. Consequently, the interaction depends upon the polarization state of the virtual photon, and to account for this, two form factors (W_1 and W_2), corresponding to the transverse and longitudinal polarization states of the photon, must be added. Then, in analogy to the Equation 2.9, the inelastic cross section can be written as

$$\left(\frac{d^2\sigma}{dQ^2 d\nu}\right)_{\text{inelastic}} = \frac{4\pi\alpha^2}{Q^4}\frac{E'}{EM}\left[W_2(Q^2,\nu)\cos^2\frac{\theta}{2} + 2W_1(Q^2,\nu)\sin^2\frac{\theta}{2}\right]. \tag{2.10}$$

These form factors depend upon the kinematics (Q^2, ν) and must be determined from experimental measurements of the cross sections. The ratio W_1/W_2 indicates the relative contributions from the magnetic and electric moments of the scattering.

From the inductive point of view, it is customary to define Structure Functions of the nucleons and to relate them to these empirical form factors:

$$F_2(Q^2,\nu) = \frac{\nu W_2(Q^2,\nu)}{M}, \quad \text{and} \tag{2.11}$$

$$F_1(Q^2,\nu) = W_1(Q^2,\nu). \tag{2.12}$$

Then, the cross section may be written in terms of these functions:

$$\frac{d^2\sigma}{dQ^2 d\nu} = \frac{4\pi\alpha^2}{Q^4}\frac{E'}{E\nu}\left[F_2(Q^2,\nu)\cos^2\frac{\theta}{2} + \frac{2\nu}{M}F_1(Q^2,\nu)\sin^2\frac{\theta}{2}\right]. \tag{2.13}$$

The coefficients of the $\cos^2\frac{\theta}{2}$ and $\sin^2\frac{\theta}{2}$ terms in Equation 2.13 can be compared to those of Equation 2.9, the cross section for scattering of Dirac spinors; dividing out the F_2 in Equation 2.13 leaves the following equivalence of the coefficients of the $\sin^2\frac{\theta}{2}$ terms:

$$\frac{Q^2}{2M_p^2} \Leftrightarrow \frac{2\nu}{M}\frac{F_1}{F_2} = \frac{Q^2}{2M^2X^2}\frac{2X\,F_1}{F_2}, \tag{2.14}$$

where M_p is the mass of the Dirac spinor parton, and the equivalence $M_p = MX$ has been postulated. Then, the interaction can be interpreted as scattering of point-like particles with Dirac magnetic moments ($\mu = ze\hbar/2M_pc$). For spin-$\frac{1}{2}$ partons, this requires the *Callan-Gross* relation to hold: $2X\,F_1 = F_2$. For spin-0 partons, the ratio would be zero: $2X\,F_1/F_2 = 0$.

The scaled-energy transfer is frequently used as an alternative kinematic variable:

$$y = \frac{\nu}{E}. \tag{2.15}$$

This quantity will occasionally be referred to as Y_{Bj} and as Y. Some combinations of kinematic variables are more succinctly expressed in terms of y:

$$\frac{E'}{E} = 1 - y, \qquad \text{and} \tag{2.16}$$

$$\frac{Q^2}{2MEX} = y. \tag{2.17}$$

With $d\nu/\nu = dx/x$ and with the approximation

$$\cos^2\frac{\theta}{2} = 1 - \frac{Q^2}{4EE'} \simeq 1,$$

Equation 2.13 can be expressed as

$$\frac{d^2\sigma}{dQ^2 dx} = \frac{4\pi\alpha^2}{Q^4 X}\left[(1-y)F_2(Q^2,\nu) + y^2 X F_1(Q^2,\nu)\right]. \tag{2.18}$$

If the scattering off the parton is point-like, then in the limit that $Q^2 \to \infty$ and $\nu \to \infty$, the structure functions remain finite, and the scattering cannot depend on Q^2 but only on the scaling variable X.

In the quark model the nucleon structure functions can be expressed as sums of the quark distributions, weighted by the squares of their charges:

$$F_2^{ep}(x) = x\left\{\frac{4}{9}[u(x)+\bar{u}(x)]+\frac{1}{9}[d(x)+\bar{d}(x)+s(x)+\bar{s}(x)]\right\} \tag{2.19}$$

$$F_2^{en}(x) = x\left\{\frac{4}{9}[d(x)+\bar{d}(x)]+\frac{1}{9}[u(x)+\bar{u}(x)+s(x)+\bar{s}(x)]\right\}. \tag{2.20}$$

Taking the average of these two yields the expression per nucleon:

$$F_2^{eN}(x) = x\left\{\frac{5}{18}[u(x)+\bar{u}(x)+d(x)+\bar{d}(x)]+\frac{1}{9}[s(x)+\bar{s}(x)]\right\} \tag{2.21}$$

$$\approx \frac{5}{18}x[u(x)+\bar{u}(x)+d(x)+\bar{d}(x)]. \tag{2.22}$$

The momentum carried by the charged constituents of the nucleons in this model is written as

$$\mathrm{MO}_{\mathbf{charged}} = \int x[u(x)+\bar{u}(x)+d(x)+\bar{d}(x)]dx. \tag{2.23}$$

Thus, if the quarks were to carry all the momentum of the nucleon, this integral should yield a value of roughly $5/18 = 0.28$.

2.2 Hadron Variables

The trajectories of the hadrons produced in a Deep-Inelastic Scattering event can be described by three variables. Typically, the three variables chosen are, relative to the direction of the virtual photon, the longitudinal momentum, the transverse momentum, and the azimuthal angle about the virtual photon axis. The azimuthal angle, ϕ, is treated in detail in Chapter 7. The transverse momentum, P_t, is a useful variable, as it is unaltered by Lorentz boosts along the axis of the virtual photon; frequently, P_t^2 is used as well.

One of the typical studies of hadronization is to examine the distribution of longitudinal momentum of the produced particles. However, the energy available for distribution among the final state particles varies from event to event, so the momenta of the hadrons will depend on the event kinematics. It is possible to scale-out this dependence on the available energy. One of the frequently chosen methods of scaling the momenta of particles is to define the Feynman scaling variable, X_F :

$$X_F \equiv \frac{p_{||}}{p_{||\mathbf{max}}} \approx \frac{p_{||}}{W/2}, \tag{2.24}$$

where $p_{||\max}$ is the maximum possible longitudinal momentum, which is well approximated by half the available energy. It is also possible to define a Lorentz Invariant quantity, Z :

$$Z \equiv \frac{P_{Target} \cdot P_{hadron}}{P_{Target} \cdot q}, \tag{2.25}$$

where P_{Target} is the 4-momentum of the target, P_{hadron} is the 4-momentum of the hadron, and q is the 4-momentum transferred in the interaction. In the Lab frame, Z reduces to the ratio of the hadron energy over the energy transfer in the event: $Z_{hadron} = E/\nu$, where E is the hadron energy. In my analysis, I have assumed a pion mass for all particles in calculating E. For the energies transferred in Experiment-665, the two variables X_F and Z are equivalent for high-momentum particles — or when X_F and Z are greater than about 0.15. In the analysis of longitudinal momentum, I will only discuss the variable Z.

In this study I have also used information regarding the *ranking* of the particles in terms of their energy. This was facilitated by ranking them according to their Z-values; the leading particle had the highest-Z and was referenced as the *fastest* particle. Similarly, the next leading particle was called the *second fastest*, and the third leading particle was called the *third fastest*. This involved only charged particles, so there was some "spill-up" of charged particles in the ranks, as their preceding neutral sisters were missed.

I defined a new variable which I have called the Rescaled-Z; this quantity is the energy of each particle scaled to the energy available to that particle, working down from the fastest. This was motivated during the studies of inter-particle Correlations, but I also compared the distributions of this variable between Xenon and Deuterium.

The Rescaled Z-values of the second and third fastest particles are defined as the following:

$$\text{scaled}(Z_2) \equiv \frac{P_{\text{nucleon}} \cdot P_2}{P_{\text{nucleon}} \cdot (q - P_1)} \xrightarrow[\text{lab}]{} \frac{E_2}{\nu - E_1}, \qquad \text{and}$$

$$\text{scaled}(Z_3) \equiv \frac{P_{\text{nucleon}} \cdot P_3}{P_{\text{nucleon}} \cdot (q - P_1 - P_2)} \xrightarrow[\text{lab}]{} \frac{E_3}{\nu - E_1 - E_2}$$

The analyses of the Z-distributions involved only reconstructed charged particles, and neutral particles were not observed. However, it was possible to put an upper limit on the maximum rank of a missed neutral by examining the sum of the Z-values for the observed charged particles:

$$Z_{sum} \equiv \sum_{ch} Z_{ch}, \tag{2.26}$$

where the summation was over the observed charged tracks. The maximum Z-value that a missing particle could have was given simply by $Z_{lost} = (1 - Z_{sum})$. Therefore, if $Z_1 > Z_{lost}$ there could not be a missing neutral which should have been ranked as the fastest particle. Similarly, if $Z_2 > Z_{lost}$ there could be no missing intermediate particle between those defined as the fastest and the second fastest, and if $Z_3 > Z_{lost}$ there could be no missing intermediate particle between those defined as the second fastest and the third fastest.

The approximation of *Factorization* is often made. This is the approximation that the scattering of the lepton can be considered independently of the breakup of the target. Then, the cross section can be written as the product of two independent cross sections:

$$\frac{d^5\sigma}{dX\,dQ^2\,dZ\,dP_t^2\,d\phi} = \frac{d^2\sigma^\mu}{dX\,dQ^2}\left[\frac{d^5\sigma^h}{(dX\,dQ^2)dZ\,dP_t^2\,d\phi}\right]. \tag{2.27}$$

The basis of this assumption is that scattering of the lepton occurs on a much shorter time scale than that of the target breakup and the formation of the final state hadrons. If the approximation holds, then the cross section can be integrated over the variables independently. This allows structure function measurements to be made without observing the final state hadrons, and it allows hadron studies to integrate over ranges of the kinematic variables and to normalize to the cross section in that range. The factor $(dX\,dQ^2)$ in the hadron cross section indicates the potential for any residual dependence upon the event kinematics. The justification for the approximation can be made empirically by examining the residual dependence of the hadron cross section on the event kinematics.

2.3 Shadowing

Deep-Inelastic Scattering off nuclear targets has been compared to that off simple protons of hydrogen. The cross section differs from simple proton scattering as a function of kinematics. There have been several effects seen as a function of the Bjorken scaling variable X; there is a rise due to Fermi motion at very high X ($0.6 < X < 1$), there is a depletion of cross section at X just below 1 ($0.3 < X < 0.6$), a pileup at $X \sim 0.3$, and another depletion at very low-X ($X < 0.01$). These are associated with the effects of Fermi motion, the "EMC effect", Anti-Shadowing, and Shadowing, respectively. Of primary interest in this analysis is the effect of Shadowing.

Shadowing is an effect which has been known in hadron-nuclear scattering; in essence, the strong nature of the interaction is such that the interaction will occur

very near the surface of the target nucleus before the incident hadron can traverse the nuclear material to reach the more downstream parts. Thus, the upstream part of the nucleus occults or "shadows" the downstream part. The cross section for the interaction depends on the target size as a function of the surface area and not the volume of material. This leads to a dependence on $A^{2/3}$ rather than on A^1, where A is the atomic weight of the nuclear target.

This effect has also been seen in real photon absorption on nuclei; the increase in cross section is approximately proportional to the area of the target nucleus and not the volume; thus, the relative cross section per target nucleon decreases as the A of the target nuclei is increased: $A^{2/3}/A \rightarrow A^{-1/3}$. This has been described traditionally as Vector Dominance. The photon can transmute itself into a virtual meson; this meson must have the same quantum numbers as the photon and hence must be spin-1: a vector meson. The lightest of these is the ρ^0 meson, which forms the basis of this description. In Generalized Vector Dominance the interaction must be summed over all possible vector mesons and the interference graphs as well, which correspond to off-diagonal elements of the scattering matrix. These off-diagonal elements of Generalized Vector Dominance cancel any strong dependence of the process on Q^2 which exists in the simple Vector Dominance picture.

Attempts have been made to describe nuclear effects based on the parton picture. The Altarelli-Parisi equations have defined the basis of a popular description of partonic distributions within the framework of the theory of *Quantum ChromoDynamics* (QCD). Employing the Renormalization Group equation and operator product expansion, based on a QCD-inspired Lagrangian, they describe the make up of a nucleon in terms of distributions of quarks (both valence and sea) and gluons. To describe the relative populations of these partons, they developed functions which involved the interactions between the partons. These were called ***splitting functions*** because they involved the emission of gluons from partons (both quarks and gluons).

In the more recent works [16, 42, 27] another set of functions have been added which describes the process of recombining partons; this creates a more thorough characterization of the interactions between the partons. Particular attention was paid to the recombination of partons from neighboring nucleons in nuclei. As the fraction of nucleonic momentum carried by a parton, X, becomes small, the localization of the parton must become less precise, so the wee-X partons of a nucleon will overlap spatially with those of neighboring nucleons in a nucleus. The valence quarks will not stray far from the valence domain of 1fm, but these wee-X partons may be located as far as 4fm (a typical nuclear radius) from the nucleon and, hence, recombine with the valence partons of neighboring nucleons. This will result in a net depletion of partons with wee-X values in the nucleons of nuclei relative to those of free nucleons of Hydrogen or Deuterium, and a corresponding enhancement of medium-X partons.

This description accounts for both Shadowing and Anti-Shadowing. The resultant behavior of this description is predicted to have very little dependence on the value of Q^2 of the interaction, in contrast to the picture of Vector Dominance, which predicts that the effect of Shadowing should depend on Q^{-2}.

Another suggestion of the cause of Shadowing involves "higher-twist" terms. "Twist-4" is the name given to the second moment in the operator-product expansion; this term depends on the scale parameter Q as Q^{-4}, so terms with this dependence are often called higher-twist terms. Again, for Shadowing, the prediction is for very strong dependence on Q^2.

In elementary particle physics it is typical to discuss the photon dissociating into a virtual quark-antiquark pair which then interacts with the nucleus as a hadron. From simple arguments based on the Uncertainty Principle, it can be suggested why this shadowing occurs at low-X and low-Q^2. The extension of the virtual photon into the nucleus is determined by the virtual energy-nonconservation $\triangle E = E_\gamma - E_{\text{lepton}}$. The lepton energy exchange is $E_{\text{lepton}} = \nu$, in the lab frame. The energy carried by the photon can be expressed:

$$E_\gamma = |\vec{q}|^2 = \nu^2 - q^2 = \nu^2 + Q^2.$$

Then,

$$\triangle E = \nu^2 \left[\sqrt{1 + \frac{Q^2}{\nu^2}} - 1\right] \tag{2.28}$$

$$= \nu^2 \left[(1 + \frac{1}{2}\frac{Q^2}{\nu^2} + \cdots) - 1\right] \tag{2.29}$$

$$\approx \frac{Q^2}{2\nu} = X_{Bj}M, \tag{2.30}$$

for $\nu^2 \gg Q^2$. Then, the longitudinal extension of the virtual photon can be written as

$$\triangle S_{\|} \leq c \triangle t \sim \frac{1}{X_{Bj}M}.$$

For the quark-antiquark pair separating in its center-of-mass frame at maximum velocity c, like a decay of mass m, the longitudinal extension of this virtual state can be written as

$$\triangle S_{\|} \sim \frac{1}{X_{Bj}M}\frac{Q^2}{Q^2 + m^2},$$

since the nonconservation of energy for this system goes as

$$\triangle E_{q\bar{q}} \sim X_{Bj}M \left(1 + \frac{m^2}{Q^2}\right) [12]. \tag{2.31}$$

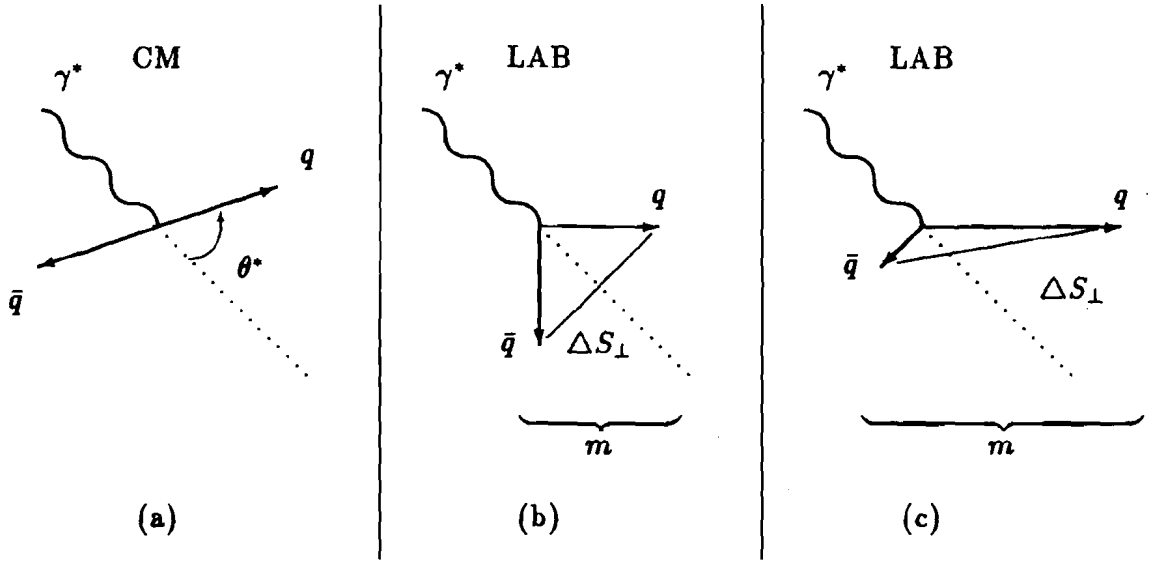

Figure 2.2: Shadowing Contributions.
In (a) is shown the dissociation of the virtual photon into a quark-antiquark pair, in the center-of-mass of the virtual pair; the angle with respect to the direction of the virtual photon is θ^*. In (b) is shown the lab frame depiction of the photon-gluon fusion contribution. In (c) is shown the lab frame depiction of the parton model contribution.

The dissociation of the virtual photon into a $q\bar{q}$-pair in the center-of-mass frame of the pair will have some angle θ^* with respect to the direction of the virtual photon, as seen in Figure 2.2(a). Isotropy predicts a uniform distribution in $\cos\theta^*$. When the q and $\bar{q}$ are boosted back to the lab frame, they will have about equal momenta if $\theta^* \sim 90°$ and vastly different momenta if $\theta^* \sim 0°$. Bjorken has treated these two regions as two distinct effects [12]: photon-gluon fusion and the Naïve Parton Model, respectively. The photon-gluon fusion case is shown in Figure 2.2(b); the mass m of the pair is approximated by $1/Q$, and the transverse separation maximizes at

$$\Delta S_\perp = 1/m = 1/\sqrt{Q^2}. \tag{2.32}$$

The Naïve Parton Model case is shown in Figure 2.2(c); the angle must be small: $\theta^* \leq \langle P_t \rangle / m$. When boosted back to the lab frame, the slower of the pair will have longitudinal fractional momentum

$$z = (1 - \cos\theta^*)/2 \leq \langle P_t^2 \rangle / m^2.$$

The perpendicular separation of this pair in the lab frame will then be given by the

expression

$$\triangle S_{\perp} = \frac{P_T}{P_L} \triangle S_{\|} = \frac{\langle P_t \rangle}{z\nu} \frac{2\nu}{Q^2 + m^2} \tag{2.33}$$

$$= \frac{2}{\langle P_t \rangle} \frac{m^2}{Q^2 + m^2}. \tag{2.34}$$

For the virtual state to act as a hadron, its transverse size must be about 1fm. For the photon-gluon fusion contribution to act as a hadron, then Q^2 must be very small: $Q^2 \leq 0.44\text{GeV}^2/c^2$. Otherwise, this process should depend upon the nuclear size as A^1, not $A^{2/3}$, and the final state hadrons should be grouped into two balanced high-P_t jets. For the Naïve Parton case, the transverse separation depends primarily upon $\langle P_t \rangle^{-1} \sim$ 1fm; so, the process will depend upon $A^{2/3}$, and the final state will be predominantly low-P_t, like the simple parton model [12]. Thus, the contributions should introduce different characteristics into the hadronic final state.

The net result is that the cross section on a nuclear target exhibits a depletion at low-X relative to a simple proton-neutron isoscalar target. The primary contribution will come from the highly asymmetrically separated $q\bar{q}$-pairs and will be roughly independent of Q^2. An additional contribution to the depletion can come from the photon-gluon fusion, only at low-Q^2.

E665 had the advantage of very high incident energy, which allowed very large values of ν, and hence very small X_{Bj} values. There were data down to the μ–e scattering peak at $X_{Bj} = 5 \cdot 10^{-4}$. The practical range of use was down to about $X_{Bj} = 0.001$. In addition, acceptance down to very small angles (1 milliradian) allowed for an examination of the Shadowing effect over very large ranges of the kinematic variables.

In experimental data there has been little evidence of any Q^2-dependence of Shadowing. In Figure 2.3 are shown the data from EMC and E665 [36, pp. 145-6]; these data have been corrected for radiative processes and acceptance. Figure 2.3(b) shows the cross section ratios for Xenon to Deuterium as a function of Q^2 for the interval of $0.001 \leq X_{Bj} \leq 0.025$ for E665 data and $0.004 \leq X_{Bj} \leq 0.018$ for EMC data; this is the kinematic region of Shadowing. Figure 2.3(c) shows the cross section ratios for Xenon to Deuterium as a function of Q^2 for the interval of $0.025 \leq X_{Bj} \leq 0.20$ for E665 data and $0.018 \leq X_{Bj} \leq 0.11$ for EMC data; this is above the kinematic region of Shadowing. On neither interval is there any evidence of a Q^2 dependence in either set of data. This suggests that the Vector Dominance picture and the photon-gluon fusion process, by themselves, are inadequate descriptions of the Shadowing process.

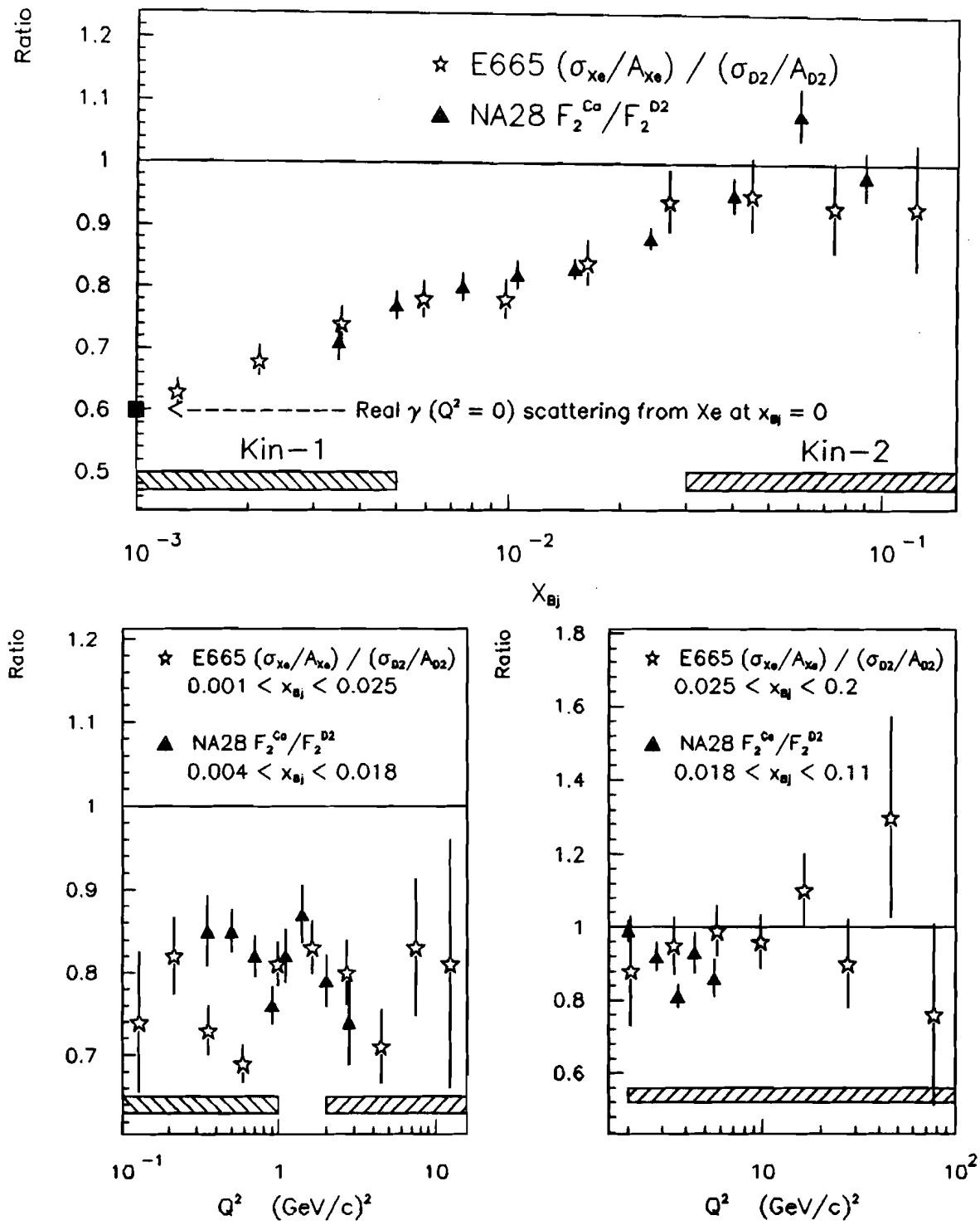

Figure 2.3: Shadowing in Cross Section Ratios.
These plots show the effect of Shadowing in the ratios of cross sections. In plot (a) the ratio is shown as a function of X_{Bj}. In plot (b) is shown the dependence of the ratio on Q^2, for a range of $0.001 < X_{Bj} < 0.025$. In plot (c) is shown the dependence of the ratio on Q^2, for a range of $0.025 < X_{Bj}$.

2.4 Hadronization

The preceding discussion of Shadowing involved only the comparisons of the total cross sections for the interactions, without knowledge of final state hadrons. E665 had the apparatus for good coverage of the final state hadrons as well. From hadron-nucleus collisions, where Shadowing of the cross section has been observed, there has been observed a correlated attenuation of final state hadrons [14, 63]. This dissertation involves a search for similar effects in Deep-Inelastic Scattering in the Shadowing region.

The process of hadronization has no basic theory but is usually described by phenomenological models. These models are all based on intuitive pictures of the evolution of the interaction into final state hadrons. The distributions of final state hadrons can be influenced by the effects of several processes. The relative times of commencement and durations of these processes will influence the final state of the system. Typically, the generation of hadrons in Deep-Inelastic Scattering can be described in two stages. The first process is the creation of the intermediate "excited" state in the nucleon by the absorption of the virtual photon. The second process is the evolution of the excited state into final state particles — the process of fragmentation and hadronization. These processes can be investigated using the two distributions of Feynman and Field [25]: the constituent functions $G_{h\to q}(x)$ and the hadronization functions $D_q^h(Z)$.

The $G_{h\to q}(x)$ represent the distributions of constituents of the struck nucleon, carrying momentum fraction x; these are based on the SU(3) description of quarks, $q(x)$, and are constructed from measurements of Deep-Inelastic structure functions. The $D_q^h(Z)$ represent the probability distributions of a constituent q disintegrating into hadrons h carrying momentum fraction z of that of the constituent. Feynman and Field exhaustively examined hadron distributions as functions of hadron variables X_F and P_t and attempted to explain charge and type dependence on the relative flavor dependence of interactions associated with the SU(3) description of quark content of the hadrons. The actual shapes of the fragmentation functions were taken from experiments; they were parameterized as functions of the hadronic kinematic variables, typically the longitudinal and transverse components. The fragmentation functions were simplified to a "reduced set" using isospin and charge-conjugation invariance.

The creation of the excited state will depend upon the constituent distributions G and the event kinematics. The excited state will propagate for some time before the formation of hadrons; this time is called the *constituent length.* The interactions of the excited state with the rest of the nucleon and with the other nucleons in a nucleus occur during this time. In a picture of Deep-Inelastic Scattering, a quark is

struck by the virtual photon, and this quark blasts out of its nucleon and subsequently fragments into hadrons. A measurement of when fragmentation commences has yet to be defined. However, during fragmentation it is imagined that partons combine to form hadrons. The *formation length* is the time required for several partons to become a hadron; this length is subject to Lorentz dilation and is given roughly by $\tau \sim E_h/m_h^2$. The formation time is taken as an extension of the Landau-Pomeranchuk phenomenon: the hadron will not interact strongly until after this time [20]. For a pion of a few GeV, this formation will complete outside of several fermi and, hence, outside of a nucleus. Thus, the interaction of the final state hadrons with the struck nucleus is expected to be a small effect.

Thus, any observed effects of nuclear targets on the distributions of final state hadrons will be due primarily to interactions of the excited state traversing the rest of the nucleons of the nucleus. Then, the distributions of the final state hadrons from a nuclear target could be expressed as the sum of contributions from excited states which interacted and from those that fragmented unaltered [11]:

$$D_A(Z) = (1 - \sigma_{qN})D_N(Z) + \sigma_{qN} \int_z h(x)D_N(x)dx. \tag{2.35}$$

Here, $D_N(Z)$ is the distribution of hadrons from a nucleon target, σ_{qN} is the total probability of rescattering of the excited state, and the function $h(x)$ is the distribution of rescattered excited states.

Another effect will be rescattering of the final state hadrons while traversing the rest of the target material and the detector elements. This effect is not of primary interest but is a source of background in the search for effects due to the evolution of the excited state.

This dissertation will examine the final state hadron distributions empirically as functions of the hadron kinematics, primarily the longitudinal momentum. In the regime of Shadowing, the picture of the virtual photon interacting as a hadron suggests that the final state hadrons should display characteristics of hadron-hadron collisions, which should then depend upon the atomic number of the target nucleus. Such differences would indicate that the propagation of the excited state is hadron-like.

2.4.1 Kin-1 and Kin-2

The objective of the study is to determine the influence of nuclear matter on the final states of the produced hadrons. The effect of *Shadowing* has been observed as a

depletion of the scattering cross section in a "low" range of kinematics. I will define this "low kinematic range" (Kin-1) as the Shadowing region:

$$X_{Bj} < 0.005 \qquad \text{and} \qquad Q^2 < 1\ \text{GeV}^2/c^2.$$

I will also define a "high kinematic range" (Kin-2) as the Non-Shadowing region:

$$X_{Bj} > 0.03 \qquad \text{and} \qquad Q^2 > 2\ \text{GeV}^2/c^2.$$

The distributions of the hadron variable Z from Xenon and Deuterium will be compared separately in these two kinematic regions.

Chapter 3

Beam and Experimental Apparatus

Fermilab Experiment-665 was a lepton scattering experiment whose spectrometer was the destination of a long 1.5km muon beam-line. A description of the equipment can be divided into two major sections: the beam and the Beam Spectrometer, and the Experimental Apparatus. The beamline generated and focused the muons through the Beam Spectrometer, where the trajectories and momenta of the muons were measured and the timing was set for triggering. The mouns impinged on a target and proceeded through the experimental apparatus, leaving their "foot prints" in the Muon Spectrometer before cruising into the earth toward West Chicago. A muon occassionally scattered from a nucleon in the target, and its trajectory was deflected. Comparing trajectories measured in the Beam Spectrometer and in the Muon Spectrometer provided the basis of "triggering" an event for Data Acquisition. In Deep-Inelastic Scattering the nucleon disintegrates into a collection of particles, and the experimental apparatus was designed to observe almost all of these resultant particles.

The global coordinate system was a right-handed Cartesian system with the X-axis defined along the nominal beam-line; this was almost due-North in Earth coordinates. The Y-axis was defined along the horizontal axis of the equipment, with the positive direction pointing West. The Z-axis was then constrained to correspond to the height vector, with the positive direction pointing 'up'. The local coordinate system of each detector was defined by a vector Θ which ran perpendicular to the direction of the wires in a wire chamber and which consequently was along the direction which that detector measured. For a plane whose *normal vector* was parallel to the X-axis, this coordinate could be expressed as a rotation in the Y, Z plane:

$\Theta = Y \sin\alpha - Z \cos\alpha$. The angle α was defined such that for a chamber with vertical wires $\alpha = \pi/2$; thus, such a chamber measured the Y-direction and was called a Y chamber. A chamber with wires running along the horizontal direction measured 'height' and was called a Z chamber; it had an angle $\alpha = \pi$. Chambers which had wire orientations positively rotated from vertical had angles defined as $\pi/2 < \alpha < \pi$ and were called U chambers. Chambers which had wire orientations negatively rotated from vertical had angles defined as $0 < \alpha < \pi/2$ and were called V chambers. The angles used in the following chamber descriptions, however, will be given in degrees from vertical.

3.1 Beam Spectrometer

The muon beam was a tertiary beam at Fermilab. Protons from the Tevatron, running at 800 GeV/c, were extracted into a channel, where they were focused onto a beryllium target 48.5 cm long. These collisions resulted in the production of pions and kaons, carrying most of the 800 GeV/c momentum. These mesons then traveled down a 1.116km evacuated tube where 20% decayed into a muon and a neutrino each, as this length is 0.25 decay lengths for pions. At the 73m mark, the remaining protons were separated from the mesons and absorbed. At the end of the meson decay tube was another assembly of beryllium 11m thick, which is 2.7 interaction lengths, and this absorbed the remainder of the undecayed mesons. The muons passed through, and those in a certain momentum range were guided into the muon FODO: FOcusing and DefOcusing beamline 366m long. Quadrupole magnets alternately focused and defocused the beam to tighten the muons into a pencil beam. Dipole magnets bent the beam through several turns, and the tuning of these fields allowed selection of mean momentum of the muon beam.

An important feature of the muon beamline was the equipment implemented to reduce the contamination of the muon beam with "halo" muons. These were muons which had low momentum relative to that of the beam but which were traveling near the beam. The method employed to eliminate these muons was to maintain toroidal magnetic fields around the beam, and the halo muons were deflected radially away from the muon beam by traversing these fields. These fields were generated in a special thick-walled iron pipe, called *mupipe*. This pipe had an inner diameter of 11.4cm and an outer diameter of 17.8cm, for the first 9.2m; the subsequent three sections each had inner and outer diameters of 12.7cm and 19.1cm, respectively. The windings were wrapped longitudinally along the pipe, and the field generated in the iron was about 2.0T. Following the mupipe there were two sets of toroid magnets: 9.2m of 1.7m-diameter magnets and 6.2m of 3.05m-diameter. The net effect of these

systems suppressed the contamination of halo muons by a factor of 5 in the ratio of halo to beam by spreading it out away from the beam. About half of the halo was still within 20cm of the beam center. The details of this beamline are described in reference [37].

The last 55.4m of the beamline housed the Beam Spectrometer. This consisted of four stations of Multi-Wire Proportional Chambers and scintillation counters, with a dipole bending magnet (NMRE) in between stations 2 and 3. The momenta of the incoming muons were then measured by reconstructing their trajectories in the two stations before NMRE and in the two after and by then determining the amount of bend in this magnetic field. The hodoscopes (SBT) were employed to measure timing information. They were segmented in a Y-view and a Z-view in each station, except the second, which had only a Y-view. The muon beam retained the "bucket-structure" of the accelerator, which ran at 53MHz, so muons would only appear at intervals of 18.9nsec; the SBT had signal-widths of about 3 buckets. This fact was used in the design of the triggers in order to use only muons from single-muon buckets.

In order to limit the adverse effects of the halo muons on event triggering and reconstruction, there was a wall of scintillators (SVW and SVJ) placed just upstream of station-4, and an in-time response from this wall vetoed triggers.

The wire chambers (PBT) in each of the four stations were built according to a standard Fermilab design. Each plane of wires had an active area of 12.8cm×12.8cm and a wirespacing of 1mm. A set was a combination of 6 planes, with wire orientations as follows: $Z, Y, V(-30°), U(30°), Y'$, and$Z'$; the Y'andZ' planes had their wires offset by half a wire with respect to the Y and Z planes.

3.2 Experimental Apparatus

The experimental apparatus is shown in Figure 3.1. The spectrometer was anchored around two superconducting dipole magnets: the CERN Vertex Magnet (CVM) and the Chicago Cyclotron Magnet (CCM). In fact, the CCM was anchored to bedrock before there was a building, which was constructed around the magnet; it was the "monument" against which all surveying was performed. This magnet was used to measure momenta of the charged particles traversing the Forward Spectrometer; multi-wire proportional chambers were placed inside and upstream of the CCM: PCF and PC, respectively, and drift chambers (DC) were placed downstream of the CCM.

systems suppressed the contamination of halo muons by a factor of 5 in the ratio of halo to beam by spreading it out away from the beam. About half of the halo was still within 20cm of the beam center. The details of this beamline are described in reference [37].

The last 55.4m of the beamline housed the Beam Spectrometer. This consisted of four stations of Multi-Wire Proportional Chambers and scintillation counters, with a dipole bending magnet (NMRE) in between stations 2 and 3. The momenta of the incoming muons were then measured by reconstructing their trajectories in the two stations before NMRE and in the two after and by then determining the amount of bend in this magnetic field. The hodoscopes (SBT) were employed to measure timing information. They were segmented in a Y-view and a Z-view in each station, except the second, which had only a Y-view. The muon beam retained the "bucket-structure" of the accelerator, which ran at 53MHz, so muons would only appear at intervals of 18.9nsec; the SBT had signal-widths of about 3 buckets. This fact was used in the design of the triggers in order to use only muons from single-muon buckets.

In order to limit the adverse effects of the halo muons on event triggering and reconstruction, there was a wall of scintillators (SVW and SVJ) placed just upstream of station-4, and an in-time response from this wall vetoed triggers.

The wire chambers (PBT) in each of the four stations were built according to a standard Fermilab design. Each plane of wires had an active area of 12.8cm$\times$12.8cm and a wirespacing of 1mm. A set was a combination of 6 planes, with wire orientations as follows: $Z, Y, V(-30°), U(30°), Y'$, and Z'; the Y' and Z' planes had their wires offset by half a wire with respect to the Y and Z planes.

3.2 Experimental Apparatus

The experimental apparatus is shown in Figure 3.1. The spectrometer was anchored around two superconducting dipole magnets: the CERN Vertex Magnet (CVM) and the Chicago Cyclotron Magnet (CCM). In fact, the CCM was anchored to bedrock before there was a building, which was constructed around the magnet; it was the "monument" against which all surveying was performed. This magnet was used to measure momenta of the charged particles traversing the Forward Spectrometer; multi-wire proportional chambers were placed inside and upstream of the CCM: PCF and PC, respectively, and drift chambers (DC) were placed downstream of the CCM.

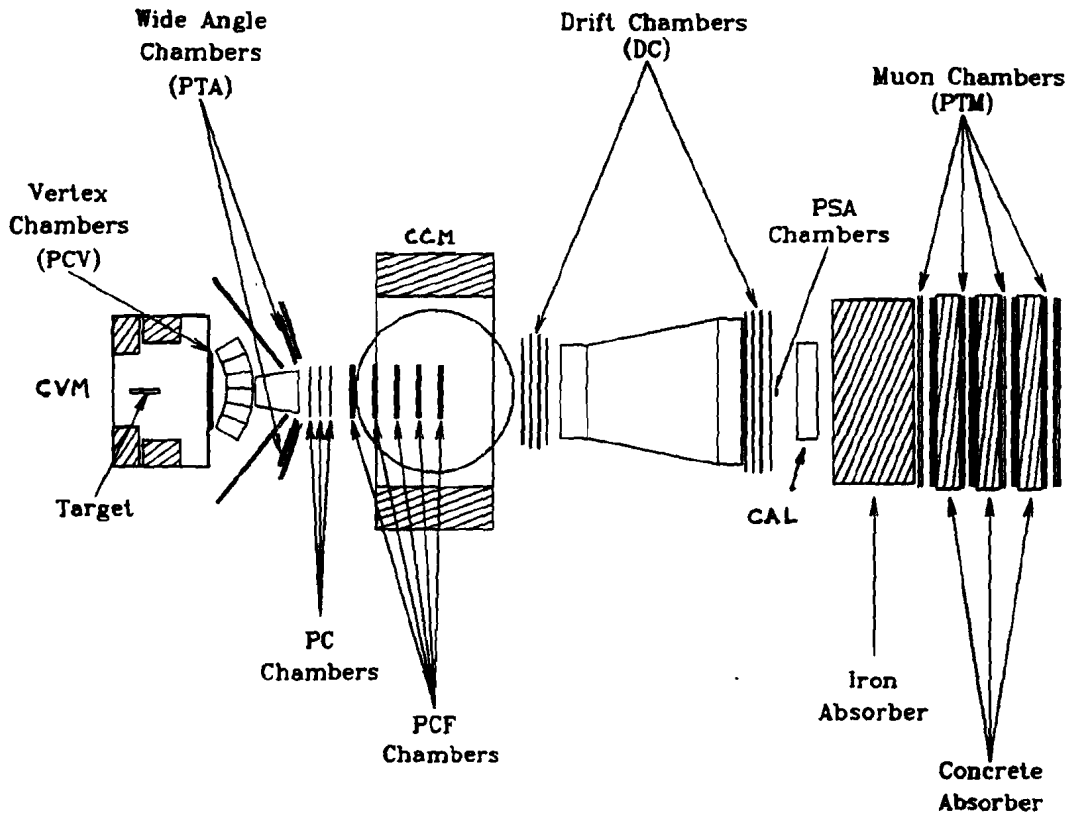

Figure 3.1: Experimental Apparatus.

The other magnet, the CVM, was used as part of a vertex system. It housed a Streamer Chamber, and thus had a hole through the top pole-face for imaging the streamers on film. In addition, since the vertices of the interactions occurred in this magnet and since the field swept the low-momentum charged particles out at wide angles, the downstream part of the yoke was built to be very "open" so as to limit the absorption of these particles.

The two magnets were energized such that their fields had opposing polarities. This was known as the *focusing condition* since it focused muons scattered at a given angle onto the same region of the Muon Spectrometer independently of the momenta of the muons. The field integral of each magnet was set to be inversely proportional to the distance of that magnet from the front of the Muon Spectrometer; thus, the CVM was run with $\int \bar{B} \cdot d\bar{l} = 4.3$Tm (Tesla-meters) and the CCM with -6.7Tm. This configuration also optimized the inclusion of charged particles in the active areas of the Forward Spectrometer chambers. A positively charged particle would be swept in the positive Y-direction (west) coming out of the CVM and then be swept in the negative Y-direction (east) coming out of the CCM. Thus, there were trajectories for which a low momentum particle could make it through both magnets, whereas at normal incidence on the CCM it would have been swept into the yoke.

The attributes of each of the detectors of the experimental apparatus are listed in Table 3.1. This table and Figure 3.1 have been reproduced from the apparatus paper, reference [1]; this reference contains many details which will not be duplicated here. The apparatus can be grouped into three spectrometers according to the reconstruction they performed. The Forward Spectrometer measured the trajectories and momenta of the high energy particles in an interaction, thus covering the "current fragmentation" region. The Wide-Angle Spectrometer detected the low momentum particles, typically from the "target-fragmentation". The Muon Spectrometer was responsible for triggering events in which a muon scattered and in reconstructing this muon. Each Spectrometer will be discussed in more detail below.

3.2.1 Forward Spectrometer

The Forward Spectrometer consisted primarily of tracking chambers anchored around the CCM. Upstream of the CCM there were multiwire proportion chambers: the PC, in three sets PC1-3. Inside the magnet there was another group of MWPC's: the PCF in 5 sets. Then, downstream of the magnet there were two sets of drift chambers: DCA and DCB; these were different sizes since DCA was at the exit of the magnet and DCB was 4m farther downstream. Each plane of the DC's was deadened in the region of the muon beam, to lessen the effects of Dead-time and radiation damage.

Wire Chambers					
Name	**Type**	**Aperture Z × Y (m)**	**Number/View of Planes**	**Wire Spacing**	**Gas**
PCV	MWPC	1.0 × 2.8	Y,U,U′,V,V′,Y	2 mm	Ar-Isobutane
PC	MWPC	2.0 × 2.0	3 × (Y,Z,V,U)	3 mm	Ar-Isobutane
PCF	MWPC	1.0 × 2.0	5 × (U,V,Z)	2 mm	Ar-CO_2
DC1-4	Drift	2.0 × 4.0	4Z,2U,2V	1 cm	Ar-Ethane
DC5-8	Drift	2.0 × 6.0	4Z,2U,2V	1 cm	Ar-Ethane
PSA	MWPC	0.13 × 0.13	Z,Y,Z′,Y′,U,V,U′,V′	1 mm	Ar-Ethane
PTM	Prop Tube	3.6 × 7.2	4 × (Y,Z)	1.27 cm	Ar-Ethane
Scintillation Counters					
Name	**Material**	**Thickness (cm)**	**Aperture Z × Y (m)**	**Number of Planes**	**Elements per Plane**
SMS	NE110	1.3	0.2 × 0.2	4 × (Y,Z)	16Y,16Z

Table 3.1: E665 Detectors.

A set of MWPC planes (PSA), similar to those used in the Beam Spectrometer was used to cover this dead region of DCB; the PSA was located downstream of DCB. Another set of MWPC's was located just downstream of the CVM: the PCV; this detector, when included on a track, helped significantly to fix the trajectory and thus reduce the error on the momentum measurement. It also narrowed the window of uncertainty of assigning tracks to vertices.

PC

The PC were three groups of four wire planes each, all located at the upstream entrance to the CCM. They had an active area of 2m×2m and a wire spacing of 3mm. In each group the planes were arranged with the wire orientations in the order $Y, U(+28°), V(-28°)$, and Z; these planes shared the same gas volume and were separated by common cathode planes. The cathode planes were mylar sheets coated with graphite; the coating was separated into three regions: a disk of 3cm radius at the center, and annulus surrounding this disk, whose outer radius was 6cm, and the rest of the plane. The three regions were insulated from each other by 3mm of sheet which was not coated with graphite; each region had high-voltage applied separately. This was installed in this manner to facilitate self-governing of space-charge build-up in this high-intensity beam region; charge deposition on the graphite surface reduced the electric field, and the resistance of the surface produced a recovery time of this region of the chamber which was decoupled from the other regions of the chamber. It was also possible to apply different levels of high-voltage to this region to reduce the

problems of space-charge and radiation damage (see reference [21]). In the 1987-88 data run the high-voltages of all three regions were set to the same value: 2.9kvolts. In addition to this structure there were "garlands" to support the horizontal wires in the Z chambers to prevent sagging and physical oscillations; these were mylar strips 5mm wide in a zig-zag configuration. There was a field wire run through this strip to smooth out the disturbances in the field. The separation between anode and cathode planes was 6mm; the distance between each of the three groups was 41.07cm, and the overall extension along the beam axis of this detector system was 86.72cm.

The operation of these chambers was such that the average efficiency per package was 94.0%, 91.1%, and 81.6%, respectively. The efficiencies per plane are shown in Table 3.2 [53]. The effects of the garlands and the ring-structure can be seen in the 2-dimensional efficiency plots in Figures 3.2(a-d).

	Target and Period					
	D_2		Xe		H_2	
Plane	0-3213	-3388	-3755	-4954	-5292	-5732
PC1Y	0.950	0.946	0.946	0.939	0.950	0.931
PC1Z	0.905	0.893	0.898	0.800	0.835	0.807
PC1V	0.962	0.959	0.962	0.957	0.964	0.948
PC1U	0.942	0.944	0.944	0.945	0.947	0.937
PC2Y	0.955	0.944	0.953	0.951	0.948	0.917
PC2Z	0.898	0.885	0.900	0.857	0.873	0.847
PC2V	0.898	0.882	0.889	0.879	0.882	0.847
PC2U	0.893	0.878	0.882	0.887	0.870	0.831
PC3Y	0.840	0.804	0.812	0.800	0.811	0.757
PC3Z	0.831	0.804	0.812	0.783	0.789	0.748
PC3V	0.776	0.722	0.744	0.718	0.735	0.659
PC3U	0.817	0.778	0.785	0.748	0.777	0.728

Table 3.2: PC Efficiencies

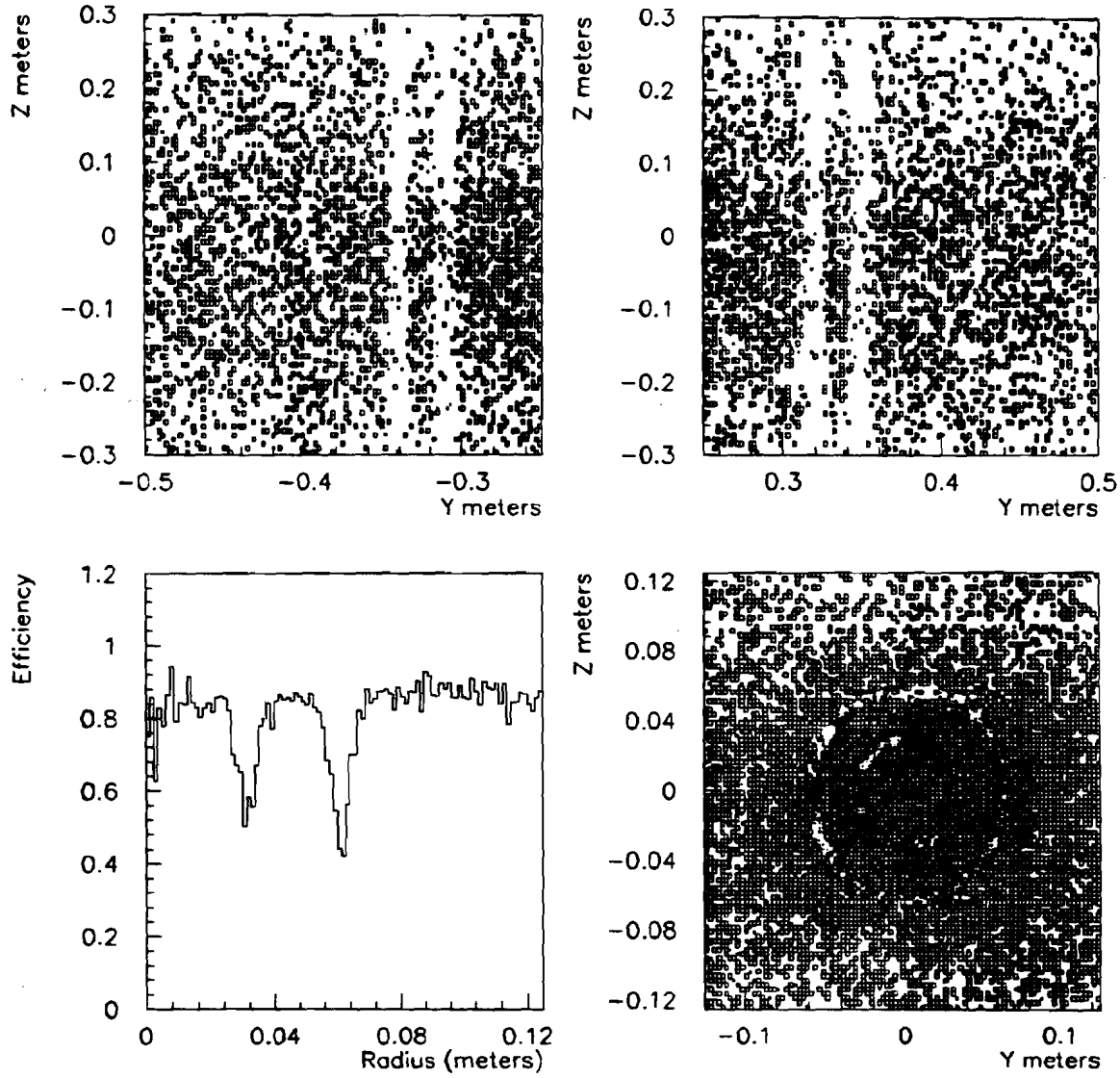

Figure 3.2: PC Chamber Efficiencies. Structure can be seen in the efficiencies of the PC chambers due to the support garlands in (a) and (b) and to the High-Voltage ring structure of the cathode planes in (c) and (d). These efficiency maps were from PC1Z; the support garlands affected only the Z-chambers, while the ring structure existed in all the planes.

PCF

The PCF chambers were MWPC's located inside the magnetic field. They consisted of 5 sets of 3 planes with wire orientations $Z, U(+15°), V(-15°)$ in each set, and a wire spacing of 2mm. The anodes shared common cathode planes, with 6.4mm separation; the cathodes were constructed of aluminized Kapton on styrofoam backing. They were run at 3.8kV, with a gas mixture of 80% argon. 19.7% CO_2, and 0.3% freon. Each plane had a support wire glued onto the anode wires, which ran across the middle of the active area at a slight angle. The effect of this support wire can be recognized in the 2-dimensional efficiency plots in Figure 3.3.

The operation of these chambers was such that the average efficiency was 90.1%. The efficiencies per plane are shown in Table 3.3 [53].

	Target and Period		
Plane	D_2 (0-3388)	Xe (3389-4954)	H_2 (4955-9999)
PCF1U	0.939	0.938	0.940
PCF1V	0.950	0.957	0.943
PCF1Z	0.922	0.929	0.917
PCF2U	0.891	0.905	0.892
PCF2V	0.900	0.903	0.898
PCF2Z	0.922	0.937	0.922
PCF3U	0.862	0.871	0.853
PCF3V	0.885	0.881	0.877
PCF3Z	0.873	0.882	0.886
PCF4U	0.912	0.930	0.926
PCF4V	0.914	0.929	0.915
PCF4Z	0.837	0.858	0.862
PCF5U	0.910	0.906	0.912
PCF5V	0.892	0.914	0.909
PCF5Z	0.916	0.949	0.932

Table 3.3: PCF Efficiencies

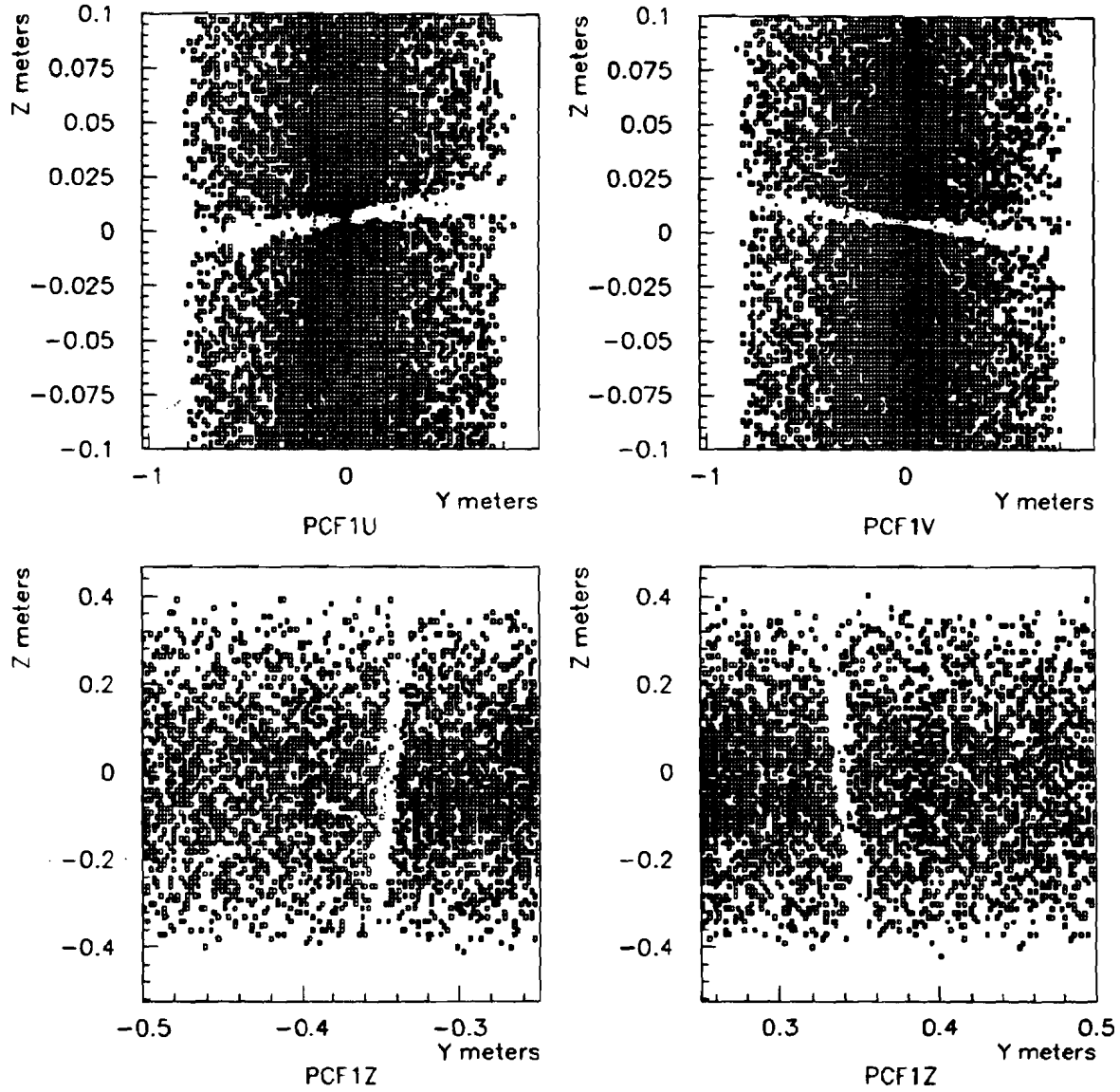

Figure 3.3: PCF Chamber Efficiencies. The support structures can be seen in the efficiencies of the PCF chambers; (a) PCF1U, (b) PCF1V, (c) PCF1Z East support wire, and (d) PCF1Z West support wire.

DC

The drift chambers were constructed in two sets, DCA and DCB, of active areas 2m×4m and 2m×6m, respectively. The 20.3μm diameter anode wires were precision placed to an accuracy of 100μm with a spacing of 50.8mm; the cathode and field-shaping wires were 102μm in diameter and placed 9.6mm from the anode. The electric fields were operated at 492V/cm which yielded a drift velocity of 4.2cm/μs and a drift time of 500nsec. The wire orientations were $Z, U(+5.758°)$, and $V(-5.758°)$; the arrangement of the planes along the X-axis was $Z, Z', U, U', V, V', Z, Z'$ in each of DCA and DCB, where the 'primed' planes were offset by half a cell with respect to the planes in front of them.

The horizontal wires of the Z-planes were separated at the center of the planes. The wires were strung across the full width, but then they were glued to a G-10 septum of width 3/4" at the center of the plane and then cut in the middle. The wires in the two halves were driven and readout separately at the two edges of the planes; this was designed to reduce ambiguities in this non-bend view. In addition, the beam regions of all planes were deadened by covering the two central anode wires with plastic sleeves, 50.8mm long; the 'primed' planes had only the central wire deadened. The electronics for the time digitization had a resolution of 2nsec and a dead time of 35nsec. However, the readout of the anode wire signals had a double-pulse resolution of 100nsec, which corresponds to 5mm of drift area, and this dominated the resolution of multiple hits. The spacial resolution of hits in the chambers was measured to be $\sim$ 400μm, for the level of alignment managed in the 1987-88 run.

The operation of these chambers was such that the average efficiency was 95%. The efficiencies per plane are shown in Table 3.4 [53]. The effects of the septum and the beam-region deadening can be seen in the 2-dimensional efficiency plots in Figure 3.4.

Plane	Target and Period		
	D_2 (0-3388)	Xe (3389-4954)	H_2 (4955-9999)
DC1Z1	0.967	0.966	0.968
DC1Z1	0.967	0.966	0.968
DC1Z2	0.950	0.956	0.953
DC1Z2	0.950	0.956	0.953
DC2U1	0.948	0.947	0.951
DC2U2	0.940	0.944	0.943
DC3V1	0.890	0.912	0.908
DC3V2	0.922	0.925	0.918
DC4Z1	0.954	0.950	0.958
DC4Z1	0.954	0.950	0.958
DC4Z2	0.951	0.950	0.950
DC4Z2	0.951	0.950	0.950
DC5Z1	0.960	0.960	0.956
DC5Z1	0.960	0.960	0.956
DC5Z2	0.962	0.962	0.961
DC5Z2	0.962	0.962	0.961
DC6U1	0.943	0.946	0.943
DC6U2	0.940	0.948	0.945
DC7V1	0.939	0.916	0.948
DC7V2	0.941	0.911	0.946
DC8Z1	0.960	0.962	0.957
DC8Z1	0.960	0.962	0.957
DC8Z2	0.960	0.960	0.956
DC8Z2	0.960	0.960	0.956

Table 3.4: DC Efficiencies

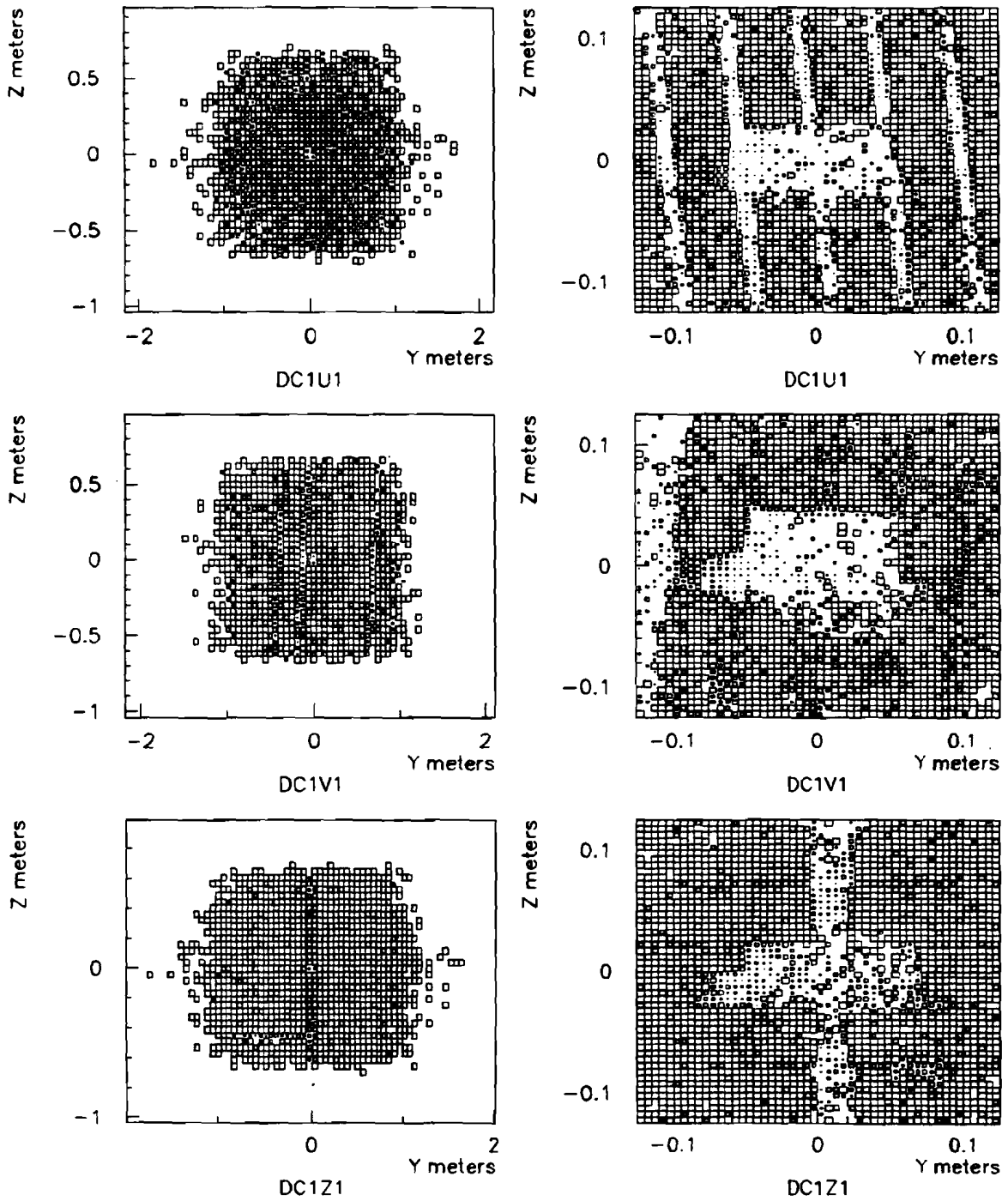

Figure 3.4: DC Chamber Efficiencies. Structure can be seen in the efficiencies of the DC chambers due to the deadened region in the U-view (a), the deadened region in the V-view (b), and the deadened region and support septum in the Z-view (c).

PSA

The PSA chambers were constructed from the same design as the chambers in the Beam Spectrometer: 12.8cm×12.8cm active area and 1mm wire spacing. The package was built in two halves; the first half had wire orientations Z, Y, Z', and Y', where the primes indicate offsetting by half a wire spacing with respect to the unprimed planes. The second half was built identically to the first but then attached rotated by 45°, which produced U, V, U', and V' orientations. These chambers used Argon-Ethane 50/50 gas and were run at 3.1kVolts.

The operation of these chambers was such that the average efficiency was 84.4%. The efficiencies per plane are shown in Table 3.5 [53].

	Target and Period							
	D_2		Xe				H_2	
Plane	0-3213	-3388	-3596	-3755	-4168	-4954	-5292	-5732
PSA1Z1	0.748	0.733	0.746	0.715	0.682	0.739	0.828	0.828
PSA1Y1	0.963	0.959	0.962	0.952	0.941	0.956	0.976	0.980
PSA1Z2	0.888	0.869	0.872	0.857	0.828	0.865	0.951	0.957
PSA1Y2	0.911	0.906	0.912	0.903	0.876	0.909	0.892	0.907
PSA1U1	0.000	0.000	0.835	0.823	0.765	0.831	0.740	0.672
PSA1V1	0.930	0.917	0.880	0.917	0.880	0.958	0.568	0.504
PSA1U2	0.901	0.896	0.978	0.967	0.953	0.954	0.979	0.979
PSA1V2	0.567	0.537	0.700	0.675	0.614	0.688	0.612	0.533

Table 3.5: PSA Efficiencies

PCV

This detector was an ensemble of six wire planes in one gas volume. The active area was 1m×2.8m, and the wire spacing was 2mm. The orientations of the wire planes was as follows: $Y, U(+45°), U'(+18.5°), V(-45°), V'(-18.5°)$, and Y. The cathodes were fabricated like those of the PC's; they were mylar sheets with graphite coatings (75μm thick). The coatings had the same structuring of the disk and annulus as the PC's.

The operation of these chambers was such that the average efficiency was 85% [47, 53]. The efficiencies per plane are shown in Table 3.6. The effects of the the ring-structure are not evident in the 2-dimensional efficiency plot in Figure 3.5; however, the disk is clearly off in PCV2V2.

Plane	Target and Period		
	D_2 (0-3388)	Xe (3389-4954)	H_2 (4955-9999)
PCV1Y	0.889	0.889	0.889
PCV1U1	0.820	0.820	0.820
PCV1U2	0.783	0.783	0.783
PCV2V1	0.785	0.785	0.785
PCV2V2	0.956	0.956	0.956
PCV2Y	0.506	0.506	0.506

Table 3.6: PCV Efficiencies

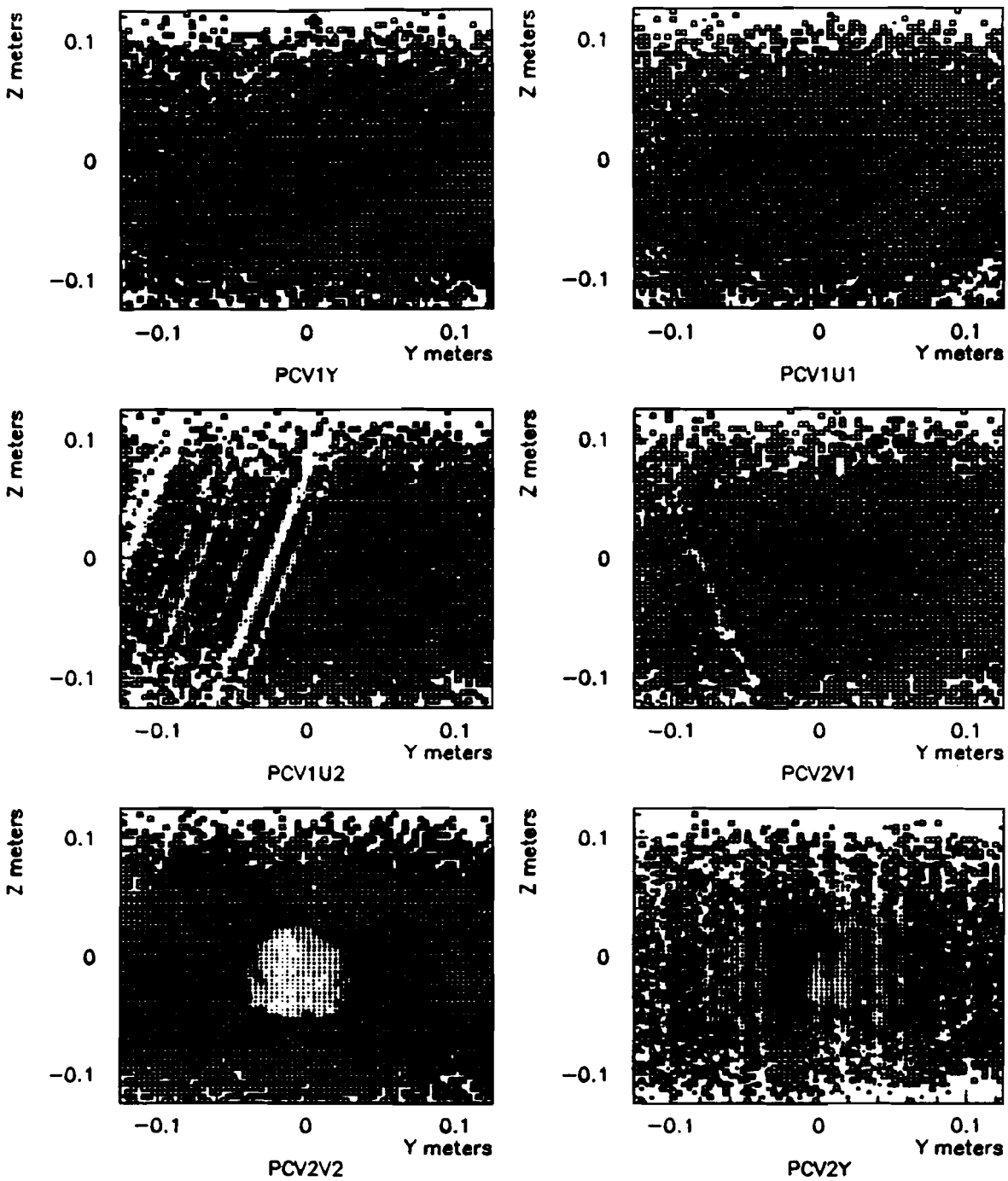

Figure 3.5: PCV Chamber Efficiencies.

Calorimeter

Another detector in the Forward Spectrometer which proved invaluable to this experiment was the Electromagnetic Calorimeter. It was located downstream of all the tracking chambers, just in front of the hadron absorber. It had an active area of 3m×3m and was composed of twenty 5mm thick planes of lead interspersed with twenty planes of proportional tubes. The proportional tubes were of the Iarocci design [29]. These tubes were molded from Poly-Vinyl-Chloride and painted with a resistive coating of graphite. This allowed for capacitive coupling of the anode wires to pads through this resistive coating which acted as the cathode.

Each tube had 8 wires with a 1cm spacing; these were ganged at the readout in groups of two tubes, which gave rise to the term "bitubes". The bitubes were arranged in horizontal and vertical orientations in alternating planes; this provided positional description of the shower extent and propagation. The pads were readout separately and summed as towers. Monte Carlo studies indicated that with the 20 radiation lengths of material, the Calorimeter samples almost 98% of the energy in showers up to 50 GeV. More detail regarding the Calorimeter may be found in references [39, 58].

3.2.2 Wide Angle Spectrometer

The Wide Angle Spectrometer was designed to detect the low momentum particles, which typically emerged from the "backward hemisphere", or the target fragmentation region, of an interaction. The four major detectors of this spectrometer were the Streamer Chamber, the PCV MWPC's, the array of proportional tubes (PTA), and the Time-Of-Flight (TOF) hodoscopes. The PCV, TOF, and PTA were all outside the magnet and could be used to reconstruct trajectories emerging from the CVM. The Streamer Chamber recorded the immediate surroundings of interactions and thus covered almost 4π steradians by itself. The tracks on the film could only yield good momentum measurements up to 20 GeV/c. The low momentum tracks could be matched to those found in the other three detectors. The TOF provided velocity information; the combination of the velocity and the momentum allowed determination of particle identity. The analysis in this dissertation has not included any information from this Wide Angle Spectrometer.

3.2.3 Muon Spectrometer

The Muon Spectrometer was designed to tag the scattered muons and provide trigger signals as well as track reconstruction. It was situated downstream of a 3m thick iron wall, which was used as a hadron absorber. This is about 18 interactions lengths of iron which should limit the level of contamination of non-interacting punch-through hadrons in the Muon Spectrometer to less than e^{-18}. The spectrometer was built in four stations with 91.4cm thick shielding block walls separating each station. This is 8.5 radiation lengths, so these concrete walls decoupled each station from delta-rays and electromagnetic showers. Thus, this spectrometer was a very clean environment for reconstructing muon tracks.

Each station was composed of a wall of (PTM) proportional tubes measuring Y, one measuring Z, and a plane of scintillator (SPM); a small hodoscope of scintillator (SMS) was used in the beam region. Both sets of hodoscopes, SPM's and SMS's, were used to trigger on scattered muons. The SMS and the PTM detectors were used for track reconstruction. These tracks could be extrapolated upstream through the absorber to indicate which track in the Forward Spectrometer belonged to the scattered muon. All this absorber material made for a clean environment, but it also was a source of multiple scattering. The multiple scattering in the concrete walls adversely affected the reconstruction of low momentum muons in the Muon Spectrometer, and the scattering in the iron absorber had to be considered in matching tracks upstream and downstream of the absorber.

SPM

The SPM hodoscopes were constructed of acrylic scintillator (ROHM GS2020), cut in 1.5m×0.5m paddles and arranged in two rows covering the top and bottom halves of a 3m×7m active area. The light was transferred to wavelength shifter bars (ROHM GS1919), which carried it to the photomultipliers. This turned out to be a very poor choice of design since the time-characteristics of this scheme, which may be fine for calorimetry, were poorly suited for use in a trigger. They had a time resolution of 300nsec, and there was a second metastable state which decayed after 600nsec, which resulted in a second pulse. For more details on these counters and their operation, see references [2, 55].

SMS

The SMS hodoscopes were constructed from fingers of NE110 scintillator, with a Y-view and a Z-view in each package. The typical width of a finger was 1.32cm, and these were arranged to cover an active area of 20cm×20cm.

These counters performed quite well (better than 99%), as indicated in a study described in reference [31]. However, the efficiency of latching the hits was lower [30], as can be seen in Table 3.7 [52]. The latched information was used in track reconstruction, so the efficiency of reconstructing tracks was less than it could have been; however, it was still quite high: 99%.

	Target and Period	
Plane	D_2 (3078-3388)	H_2 (4955-5658)
SMS1Z	0.987	0.950
SMS1Y	0.939	0.926
SMS2Z	0.904	0.914
SMS2Y	0.996	0.994
SMS3Z	0.991	0.992
SMS3Y	0.996	0.960
SMS4Z	0.993	0.982
SMS4Y	0.999	0.990

Table 3.7: SMS Efficiencies

PTM

The PTM detector was constructed of proportional tubes, which were assembled into planes of active area 3.6m×7.2m; the first plane in each station was a Y-view, and the second was a Z-view. Each tube had a square cross section of dimension 2.54cm. These tubes were arranged in "modules" which were made of custom extruded aluminum, the cross section of which is shown in Figure D.1. A module had two layers of tubes with an offset of 1/2 a cell between the two layers. This eliminated any dead regions near the walls of the cells and yielded a net wire spacing of 1.27cm. A particle passing through the module would usually fire two cells. These chambers operated at an average efficiency of 95% [51]. I describe the PTM's in much more detail in Appendix D; I spent the majority of my graduate student career designing, testing, constructing and implementing this detector.

3.2.4 Particle Identification

The experimental apparatus had the ability to discern the identity of some of the particles present in the events. As has already been discussed, the Muon Spectrometer yielded very clean indication of muon identity. The Electromagnetic Calorimeter provided information on the identity of electrons and photons. There were also some devices in the apparatus for separating hadron types; however, since they were not involved in my analysis, I will only mention their existence and design specifications. Between the PCV and PC wire chambers were located two threshold Cherenkov counters: C0 and C1. The combination of information from these two detectors should provide π, k, and p separation in the range of momentum 5 to 15 GeV/c. A Ring Imaging CHerenkov counter (RICH) was located between the two sets of drift chambers, DCA and DCB. It was designed to separate π, k, and p in the momentum range of 20 to 70 GeV/c [1].

3.3 Targets

The experiment took data scattered from several target materials: Hydrogen, Deuterium, and Xenon. The target vessels resided inside the Streamer Chamber, which required that all target material be non-metallic. The same vessel was used for both liquid targets: Hydrogen and Deuterium; this was 8.9cm in diameter and 115cm long and was constructed of 1mm thick Kapton. The Xenon was a high pressure (14atm) gaseous target, and the vessel was constructed of Kevlar^{TM} (Trade Mark of Dupont Corp.) and epoxy of thickness 1mm; this vessel had a diameter of 7.2cm and a length of 112cm. These targets, Hydrogen, Deuterium, and Xenon, had interactions thicknesses (g/cm^2) of 7.0, 16.0, and 8.5, respectively. This information is all listed in Table 3.8. Each target had less than 1/3 of a nuclear interaction length; this was important in that the reinteraction of hadrons produced in Deep-Inelastic Scatters was not an appreciable problem. However, the Xenon target was almost a full radiation length of material, and this resulted in increased incidence of muon-electron scattering and muon-bremsstrahlung events over the lighter targets.

Target	Z/A	Length (cm)	Diameter (cm)	Thickness (g/cm^2)	L/L_R	X/X_N
Xe	54/131.3	113	7.1	8.5	1.00	0.05
D_2	1/2.0	115	8.9	16.0	0.13	0.29
H_2	1/1.0	115	8.9	7.0	0.11	0.14

Table 3.8: E665 Target Properties.

3.4 Triggers

There were two physics triggers implemented in E665: the LAT (Large Angle Trigger) and the SAT (Small Angle Trigger). Their names indicate the major differences in their respective designs. The LAT had angular acceptance down to about 3 mradians, which corresponded to a minimum Q^2 of about 2.7 $(\mathrm{GeV}/c)^2$. The SAT had angular acceptance down to about 1 mradian and a minimum Q^2 of about 0.5 $(\mathrm{GeV}/c)^2$. The kinematic acceptances of these two triggers are shown in Figure 3.6.

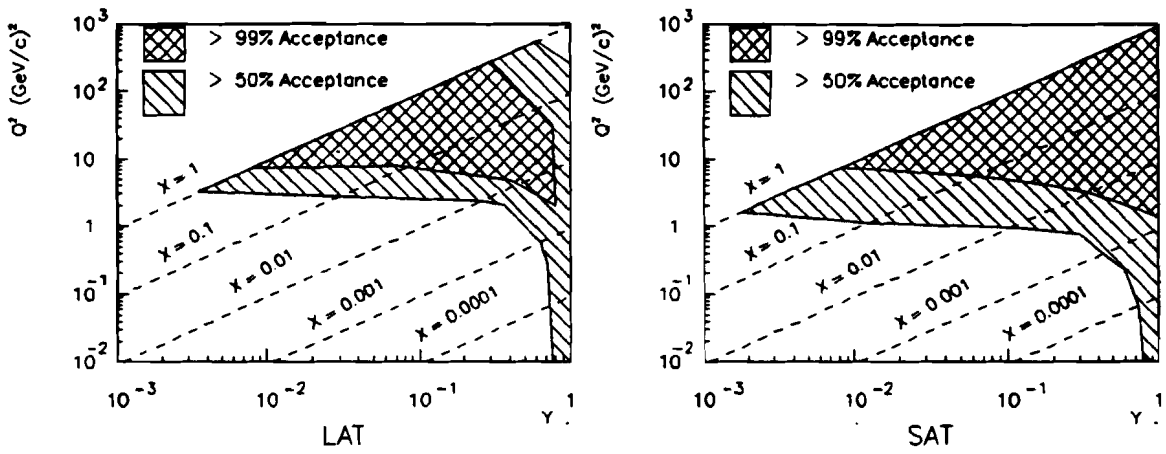

Figure 3.6: Trigger Acceptance.
Plot (a) shows the kinematic acceptance of the LAT; plot (b) shows that of the SAT.

The SAT used the hodoscopes SBT in the Beam Spectrometer to define the beam muon's trajectory; an electronic lookup table was employed to predict where this muon should impinge upon the SMS counters (in the Y-view only) in the Muon Spectrometer if it failed to scatter. If these predicted counters fired, then the event was vetoed. This trigger was prescaled to take only 12% of the beam used for the LAT.

The LAT used the SBT hodoscopes only to define intime beam muons. It required hits in the big SPM counters in the Muon Spectrometer in three out of the four stations for a valid trigger. In addition, however, the event was vetoed if there were hits in both the Y and the Z-views of the SMS counters in Stations-1 or 4. More details concerning the triggers can be found in references [1, 36, 2].

Chapter 4

Event Reconstruction

Event Reconstruction was the procedure of reconstructing tracks in the event and determining the event kinematics from the momentum and trajectory of the muon. This procedure involved the reconstruction of the tracks left in chambers by the passage of charged particles through these detectors. The reconstruction of tracks was a process composed of four major steps: Pattern Recognition, Track Fitting, Muon Matching, and Vertex Processing. Before describing the operations of these processes, I will cover some of the details of the usage of wire-chambers to record the passage of charged particles and expand upon the coordinate system used in the experiment.

4.1 Detector Characteristics

4.1.1 Coordinate System

The Global Coordinate system was described in Section 3. There was also a coordinate system basis local to the detector plane: (Y, Z), which was related to the wire and measurement directions through the rotation

$$\begin{pmatrix} \Theta \\ W \end{pmatrix} = \begin{pmatrix} \sin\alpha & -\cos\alpha \\ \cos\alpha & \sin\alpha \end{pmatrix} \begin{pmatrix} Y \\ Z \end{pmatrix}. \tag{4.1}$$

The measured values of the local coordinate Θ could be rotated back into the global coordinate system through the matrix

$$\underline{U} \equiv \begin{pmatrix} \sin\alpha & -\cos\alpha \\ \cos\alpha & \sin\alpha \end{pmatrix} \begin{pmatrix} \sin\beta & -\cos\beta \\ \cos\beta & \sin\beta \end{pmatrix} \begin{pmatrix} \sin\gamma & -\cos\gamma \\ \cos\gamma & \sin\gamma \end{pmatrix}. \tag{4.2}$$

The angle β was the angle of rotation out of the Y, Z plane, while the angle γ was the deviation from vertical. For most of the wire-chambers in the experiment these two angles, β and γ, were sufficiently close to zero that these components of the rotation matrix were ignored, and the transformation could be written simply as $Y = \Theta/\sin\alpha, Z = -\Theta/\cos\alpha$; for horizontal and vertical planes one of the coordinates mapped exactly onto the local coordinate, and the other was undefined by that plane.

4.1.2 Position and Error

The data recorded from each detector system, e.g. PCV, PC, PCF, DC, and PSA, were encoded in some specific format for each detector plane. A detector provided two quantities in the measurement of the passage of a particle: the position of the passage and the error on this position. A detector plane was defined by 1 point in space $(X_{pos}, Y_{pos}, Z_{pos})$ and its 3 angles (α, β, γ). The recorded data in each event was usually a list of wires in each plane which had registered *hits*: the close passage of a charged particle. These hits were translated into *coordinates*: distances from the origin of the local system in terms of the local coordinate, Θ. The other detector quantity which was important to reconstruction was the resolution of the detector. A wire-chamber could determine a position of particle passage only to the level "between two wires" or "near a single wire". In the drift chambers the resolution was governed by the time sampling.

This resolution could be approximated statistically by a distribution which is isotropic over an interval $\Delta\Theta$ in the measuring variable Θ (see Figure 4.1). If one integrated over this distribution, one could find a normal distribution which had identical mean and Root-Mean-Square spread. From this normal distribution, one finds that the RMS spread is simply given by the size of the interval: $\sigma_{\mathrm{RMS}} = \Delta\Theta/\sqrt{12}$. In a wire chamber, the relevant interval was the spacing between wires, and the resolution of the chamber could be well approximated by the quantity $\sigma = \mathrm{Wirespacing}/\sqrt{12}$. The accuracy of this approximation is examined in Section D.7.1.

There were several configurations of wires registering hits. The simplest was a single particle passing close to a wire ($\Theta - \Theta_{\mathrm{wire}} < 1/2\mathrm{Wirespacing}$), and firing only that wire. The next simplest was the passage of a particle between two wires (usually somewhere near the midpoint) and firing both. The other effect which was significant

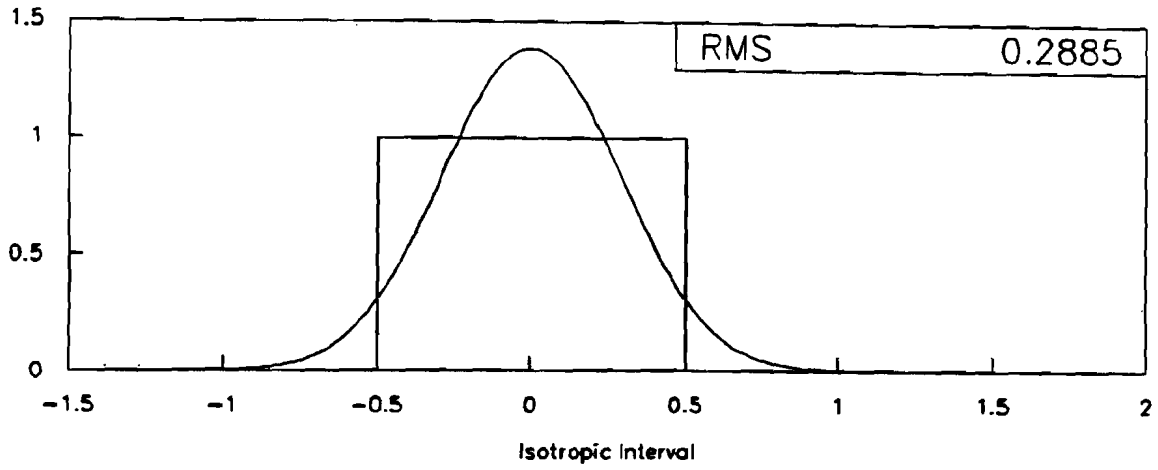

Figure 4.1: Resolution on an Isotropic Interval.
The RMS-spread of this isotropic interval is equivalent to that of a Gaussian distribution.

was the firing of wires by delta-rays emitted by the passing particle. The distribution of delta-rays follows the laws described in Appendix C.

Most of these electrons do not deviate far enough from the parent particle's track, but some do and can fire a wire other than that fired by the parent particle. This could result in the firing of a cluster of wires about 4 across or two clusters of several wires each. From the vantage of track reconstruction, it was not possible to determine to which wire the particle passed closest; therefore, the following method of handling this was chosen. The position was reported by the mean of the cluster of adjacent wires fired, and the error on this value was given as the resolution scaled up by the number of wires included in the cluster. This carried into fits of the hits in detector planes to trajectories; the position of the hit due to a large cluster, which was poorly known, was weighted less in the fit due to the scaled error.

The specifics of this clustering scheme were the following. In a detector plane, adjacent hits were grouped into clusters. If the cluster was composed of 3 or fewer wires, it was left intact. If the cluster was composed of 4, 5, or 6 wires, it was broken into two *single* hits at either edge of the cluster; this maximized the separation of the two hits, and the tight resolution of a single wire urged the choice of one hit or the other in a fit to a trajectory. This would have left the other hit available to another trajectory for those cases where two particles passed close to the same position in the detector. Finally, if a cluster was composed of more than 6 fired-wires, it was dropped altogether, as this was due most probably to an oscillation in the detector electronics. From Figure 4.2 it is apparent that there were very few real clusters lost due to this

cut and that this effect was negligibly small compared to chamber inefficiencies, which were on the order of 10^{-2}. From a Monte Carlo study it was determined that the merging of two hits from distinct tracks was at most a 2% effect [3].

4.2 Pattern Recognition

The job of Pattern Recognition was to take the lists of hits in the detectors and to sort them into groupings that corresponded to the trajectories of particles passing through the detectors. Only certain trajectories could correspond to the physical paths that charged particles could take, coming from the interactions in the events and satisfying the electrodynamics of charged particles in magnetic fields. Knowledge of these constraints must be included in Pattern Recognition in order to eliminate combinations corresponding to trajectories which were not physical or which would not belong to the event being reconstructed.

In the Pattern Recognition stage there was no information yet available about the momenta of particles, so all effects of multiple scattering were ignored, to be addressed later at the Track Fitting stage. Thus, in regions with no magnet field, the paths of all particles were along straight lines, while in magnetic fields the paths of charged particles were along helical trajectories. An additional constraint used was "target pointing"; this limited the class of possible trajectories to those which could have come from the interaction in the target. This was implemented typically as a maximum slope value and often as an interval along the X-axis for projected interception of the trajectory with the X-axis. These cuts were chosen to optimize the reconstruction of trajectories from real particles relative to that of incidental combinations of hits which passed the cuts.

In order to evaluate the validity of a grouping of hits along a trajectory, a fit was performed and the value of the *reduced* χ^2 ($\chi^2/N_{\text{degrees of freedom}}$) was checked to be below some cutoff value. The definition of χ^2 was the sum of the squares of the distances of the hits from the trajectory, normalized to the squares of the errors on each hit:

$$\chi^2 \equiv \sum_{\text{hits}} \frac{(\Theta_{\text{hit}} - \Theta_{\text{traj}})^2}{\sigma^2_{\text{hit}}}. \tag{4.3}$$

The fits were performed to minimize this quantity. The distribution of the reduced χ^2 should peak at 1 and have a long tail out to infinity; the corresponding χ^2-probability distribution should be flat between 0 and 1. A bad fit would yield a large value of reduced χ^2 (10 to infinity) and a very low value of χ^2-probability (less than 10^{-3}).

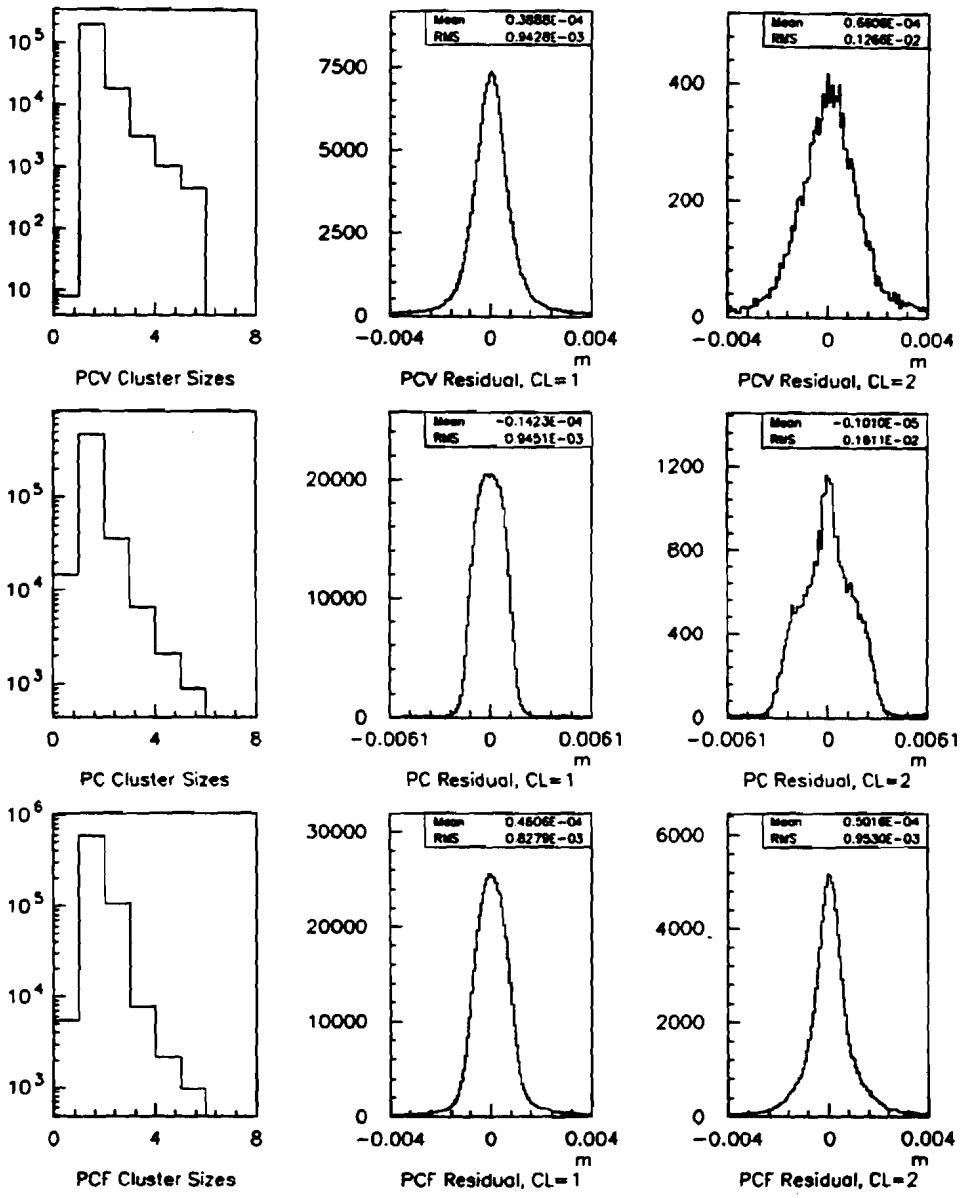

Figure 4.2: Cluster-Sizes.
Plots (a), (d), and (g) show the distribution of cluster-sizes formed in the detectors PCV, PC, and PCF, respectively. The residuals for cluster-sizes 1 and 2 are shown for each detector.

There were two basic algorithms employed for the recognition of valid combinations of hits: Projection Finding and Space-Point Finding. Projection Finding worked in 2-dimensions with the hits in the local coordinate Θ along the X-axis; this was employed in non-field regions to find straight lines in a given view. The Space-Point Finding worked at a given X-position and grouped hits in at least 3 different views which formed an intersection in this plane; it was possible to employ this algorithm inside a magnetic field. Then these points would be fit to valid trajectories.

The Projection Finding algorithm was adopted from the CERNLIB package PTRACK; it was adapted slightly to handle some idiosyncrasies of the detectors. This package accepted a list of hits in a single view; the hits had to be ordered within each detector plane and each plane had to be ordered along the X-axis. It would group these hits according to straight lines in 2-dimensions. A minimum number of hits on a line had to be specified; this was minimally 3. The algorithm would first search for lines with hits from every detector plane in the group, then one less, and so on until reaching the limit of minimum hits.

Each search involved several sub-iterations. A *seedplane* would be chosen, starting with the first in the order and moving forward at successive stages. For each seedplane a *targetplane* was chosen, beginning with the last in the order and moving backward at successive stages. Then for each pair of hits in the seedplane and in the target plane, a connecting line was projected through the other planes of the group; this line had to pass the target pointing criteria. The line had some width defined such that in each plane the algorithm would search for hits which fell inside this width. If enough hits were picked up, then a line candidate was created. This candidate was subjected to a straight-line fit, and the reduced χ^2 was checked; if it was too large, then the candidate was dropped. If the contribution to the χ^2 from any hit was too large, that hit was dropped and the line refit; this elimination could continue until the number of remaining hits fell below the minimum number, at which point the candidate would be dropped. Another option was to drop the candidate immediately if it had a hit with too large a χ^2-contribution.

These nested iterations provided coverage of all the topologies of lines in the detector with hits in various planes. The ordering of the hits was employed to reduce calculation time; once a hit in a plane had a value larger than the projected line and width, the search in that plane was aborted and the next plane was searched. The relevant parameters for the widths and the cuts were setup for each detector before the algorithm was employed for that detector.

The Space-Point Finding algorithm was developed on this experiment. It worked with chambers of different wire orientations but of close proximity in the X-direction. Some choice of valid combinations was initialized for a set of detector planes. Then the

correlations of the coordinates of the three hits were examined through the symmetric sum:

$$S = \sum_{i,j,k} \Theta_i \sin(\alpha_j - \alpha_k). \tag{4.4}$$

This sum represented the "extent" of the point formed by intersection of the three lines given by the detector plane coordinates. It was motivated by the picture in Figure 4.3. A triangle is formed by the intersections of three lines in a plane; in a

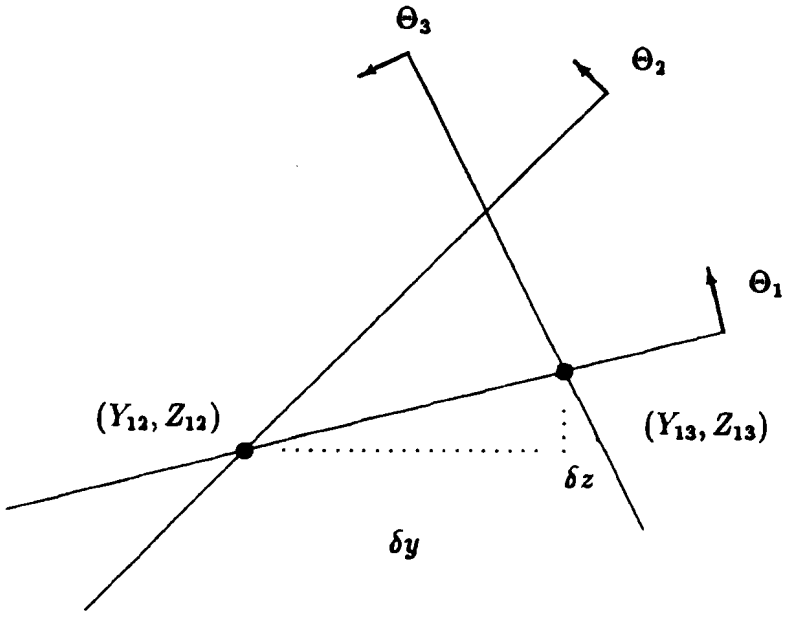

Figure 4.3: Intersection of 3 Wires.

Cartesian coordinate system each intersection point can be written as (Y_{ij}, Z_{ij}), where i and j run through the wires, 1 to 3. The wire values Θ_1 and Θ_2 are expressed in these coordinates according to the equations

$$\Theta_1 = Y_{12} \sin \alpha_1 - Z_{12} \cos \alpha_1, \tag{4.5}$$

$$\Theta_2 = Y_{12} \sin \alpha_2 - Z_{12} \cos \alpha_2. \tag{4.6}$$

Then the intersection of wires 1 and 2 yields the coordinates (Y_{12}, Z_{12}):

$$Y_{12} = \frac{\Theta_1}{\sin \alpha_1} + \cot \alpha_1 \left[\frac{\Theta_2 \sin \alpha_1 - \Theta_1 \sin \alpha_2}{\sin(\alpha_1 - \alpha_2)} \right], \quad \text{and} \tag{4.7}$$

$$Z_{12} = \frac{\Theta_1 \sin \alpha_2 - \Theta_2 \sin \alpha_1}{\sin(\alpha_1 - \alpha_2)}. \tag{4.8}$$

The coordinates (Y_{13}, Z_{13}) can be expressed in terms of (Y_{12}, Z_{12}), with the following definitions:

$$Y_{13} = Y_{12} + \delta Y \tag{4.9}$$

$$Z_{13} = Z_{12} + \delta Z. \tag{4.10}$$

Then, the coordinate Y_{12} can be expressed in several forms:

$$Y_{12} = \frac{\Theta_1 + Z_{12}\cos\alpha_1}{\sin\alpha_1} \tag{4.11}$$

$$= \frac{\Theta_2 + Z_{12}\cos\alpha_2}{\sin\alpha_2} \tag{4.12}$$

$$= \frac{\Theta_3 + (Z_{12} + \delta Z)\cos\alpha_3}{\sin\alpha_3} + \delta Y. \tag{4.13}$$

From the equivalence of expressions 4.11 and 4.12 the coordinate Z_{12} can be expressed in the form:

$$Z_{12} = \frac{\Theta_1 \sin\alpha_2 - \Theta_2 \sin\alpha_1}{\sin(\alpha_1 - \alpha_2)}. \tag{4.14}$$

From the expressions 4.11 and 4.13 the coordinate Z_{12} can be expressed in the form:

$$Z_{12} = \frac{\Theta_3 \sin\alpha_1 - \Theta_1 \sin\alpha_3}{\sin(\alpha_3 - \alpha_1)} + \frac{(\delta Y + \delta Z\cos\alpha_3)\sin\alpha_1}{\sin(\alpha_3 - \alpha_1)}. \tag{4.15}$$

Equivalencing Equations 4.14 and 4.15 and removing the common denominator yields the expression

$$\begin{aligned} 0 = {} & \Theta_3 \sin\alpha_1 \sin(\alpha_1 - \alpha_2) + \Theta_2 \sin\alpha_1 \sin(\alpha_3 - \alpha_1) \\ & -\Theta_1[\sin\alpha_1 \sin(\alpha_3 - \alpha_1) + \sin\alpha_3 \sin(\alpha_1 - \alpha_2)] \\ & +(\delta Y + \delta Z\cos\alpha_3)\sin\alpha_1 \frac{\sin(\alpha_1 - \alpha_2)}{\sin(\alpha_3 - \alpha_1)}. \end{aligned} \tag{4.16}$$

With some trigonometric identities, this reduces to the expression

$$\begin{aligned} 0 = {} & \sin\alpha_1[\Theta_3 \sin(\alpha_1 - \alpha_2) + \Theta_2 \sin(\alpha_3 - \alpha_1) + \Theta_1 \sin(\alpha_2 - \alpha_3) \\ & +(\delta Y + \delta Z\cos\alpha_3)\frac{\sin(\alpha_1 - \alpha_2)}{\sin(\alpha_3 - \alpha_1)}]. \end{aligned} \tag{4.17}$$

For Equation 4.17 to hold for an arbitrary angle α_1, the expression in square brackets must vanish. Clearly, the angles of the wires must all three be distinct, so the last term does not diverge. Therefore, the sum can be defined as

$$S \equiv (\delta Y + \delta Z\cos\alpha_3)\frac{\sin(\alpha_1 - \alpha_2)}{\sin(\alpha_3 - \alpha_1)} \tag{4.18}$$

$$= \Theta_3 \sin(\alpha_1 - \alpha_2) + \Theta_2 \sin(\alpha_3 - \alpha_1) + \Theta_1 \sin(\alpha_2 - \alpha_3). \tag{4.19}$$

Then, by minimizing this quantity S, combinations of three wires can be found which intersect at nearly a point in space; this should be the point through which the particle passed to fire the three wires.

If the extension of the intersection was too large, the combination was dropped. After all of the 3-view combinations were formed, the merging of combinations commenced. When two of the 3 hits were shared with another combination, the two combinations were merged; this merging continued and could result in a space-point with contributions from 6 views. The product of this algorithm was a set of space-points at given positions in the X-direction. These could then be used in fitting trajectories to find groupings of the space-points which belonged to valid trajectories.

The Pattern Recognition processors were setup to use one of these basic algorithms. The individual jobs of the processors were to prepare the information for the detectors to be input to one of the algorithms; this information involved the necessary tunable parameters as well as the coordinates from the hits.

The Pattern Recognition chain was performed in three basic steps. First, the reconstruction in the Beam Spectrometer was performed by the PB processor, to identify the incoming muon. If none were found, the event would be skipped. Second, the reconstruction in the Muon Spectrometer was performed by the PM processor, to identify the outgoing muon. Again, if none were found, the event would be skipped. Finally, the event was reconstructed in the Forward Spectrometer; this chain involved several steps. First, line segments were constructed in the non-field regions: in the DC's by the DC processor and in the PC's by the PC processor. The MA processor then linked these segments through the magnet, and picked up hits in the PCF's. Remaining segments in the PC's were projected into the magnet by the PF processor to pick up hits in the PCF's. Meanwhile, the PS processor was finding space-points in the PSA detector, and the MS processor then attempted to match any trajectories found by the PF processor with these space-points. Then, the SF processor found space-points from the remaining hits in the PCF's in the magnetic field, and the SN processor tried to punch these trajectories into the PC's to pickup remaining hits. Then MS was run again, and the MD processor then punched these segments into the DC's to pickup unclaimed hits. Finally, the PV processor built space-points in the PCV's, and the MV processor projected segments in the PC's into the PCV's to link these space-points with the previously found tracks.

All of the processes in the Forward Spectrometer were run in two successive phases: the Muon Phase and the Hadron Phase. The Muon Phase was the first pass, and the processors' cuts on target pointing and reduced-χ^2 were tight, in order to pick up the cleanest tracks first. It was presumed that the track of the scattered muon would be rather stiff, typically, and therefore most would be found in this stage. After the hits belonging to the tracks found in the first pass were flagged, the Hadron Phase was run, using much looser cuts on target pointing and on track quality to pickup all the remaining tracks. A Monte Carlo study indicated that the percentage of the scattered muons found in the muon pass was a function of the energy transfer, ν, and

that both phases must be run to recover as many of the events as possible[49].

The following sections will briefly discuss each processor and its performance.

4.2.1 PB Processor

The PB processor used the Space-Point Finding algorithm to construct space-points in each of the four beam stations. Each station had six views of wire orientations, so the space-points could be combinations of up to six hits. The X-position for each space-point was chosen as the mean of the X-positions of the planes used to form that space-point. Then the values of the space-points in the non-bend view, Z, were grouped to form straight lines; these lines required a contribution from a space-point in each of the four stations. If the straight line fit was sufficiently good, then the bend-view, Y, was examined. A line segment was formed by the Y-values of the space-points in stations 1 and 2 and another in stations 3 and 4; these segments were projected to the center of the bending magnet, NMRE, where they must intersect if they lay along a valid particle trajectory. If this condition was met, then the candidate was saved as a found track.

4.2.2 PM Processor

The PM processor used the Projection Finding algorithm to find projections independently in the Y-view and the Z-view. This search was performed first in the proportional tubes, PTM's, and subsequently in the small hodoscopes, SMS's. Finally, the remaining hits in both detectors were searched for tracks overlapping both detectors; this approach treated the PTM's and the SMS's as a single detector system with full area coverage. In practice, the reconstruction would have worked fine, running only this final stage "overlap processor".

4.2.3 DC Processor

The DC processor employed the Projection Finding algorithm. The drift chambers had 8 Z-views and 4 views each, U and V. In the Muon Phase of the Pattern Recognition search, the DC processor extrapolated Z-projections from the Muon Spectrometer, found by the PM processor, into the drift chamber apertures and defined local windows within which to search for hits; the constraint of target pointing was included

in the definitions of these windows. The hits in these restricted regions of the chambers were passed to the Projection Finding algorithm to find Z-projections. Next, the Y-projections from the Muon Spectrometer were extrapolated into the DC's, and a search was performed for hits in the U and V chambers which were consistent both with the Z-projections found in the DC's and with the extrapolated Y-projections from the Muon Spectrometer. From these U and V hits and the Z-projections were calculated pseudo-Y-hits in the drift chambers, and these hits were passed to the Projection Finding algorithm. In the Hadron Phase, Z-projections were found, using hits from the whole active apertures of the chambers; the pseudo-Y-hits were then generated from the found Z-projections and all the remaining hits in the U and V chambers.

Because the pseudo-Y-hits were generated based on knowledge of a given Z-projection, these 'hits' were assigned to this Z-projection. Thus, several pseudo-Y-hits generated from the same U and V hits existed, attached to the various Z-projections. The other effect of this was that there could be several Y-projections associated with each Z-projection. These degeneracies had to be eliminated. First, for each Z-projection's list of assigned pseudo-Y-hits, the resultant Y-projections were checked against each other for degeneracy, inside the Projection Finding algorithm itself; the projection with the least number of degrees of freedom was dropped, or, if that number was identical, then the projection with the worst reduced-χ^2 was dropped. Next, the Y-projections associated with distinct Z-projections were searched for degeneracy, and the same logic was followed for dropping all but one of the degenerate projections. In the end, it was still allowable that a Z-projection have more than one associated Y-projection, and thus tracks could share hits. There were minimum hit requirements as well; each Z-projection had to have at least 4 hits, and there had to be at least 2 hits in each of the stations of the drift chambers, DCA and DCB. Each Y-projection had to have at least 4 U, V hits, and there had to be at least 2 hits in each of the stations of the drift chambers, DCA and DCB.

Finally, a straight-line fit in 3-dimensions was imposed on the original hits in the Z, U, and V chambers for each of the associated (Z, Y)-projections. The survivors of a cut on reduced-χ^2 were saved as tracks. The efficiency of this processor was 90% [49].

4.2.4 PC Processor

The PC processor also employed a projection finding algorithm, but this was a local copy of the external algorithm and was modified to handle the fact that there were only three planes of each wire orientation in the PC's. Thus, for the search in each

view, the algorithm was slightly simplified; the seedplane was the first plane, and the target plane was the third plane. The combinations of the hits in these two planes which satisfied the target pointing constraints were interpolated to the middle plane to pickup hits. A straight-line fit was imposed, and the reduced-χ^2 was checked to determine survival of the combination.

The projections in the Z-view, the non-bend view, included hits from the first Z-plane of the PCF's, PCF1Z, which was outside the magnetic field. Since these combinations could have 4 hits, the external Projection Finding algorithm was used for the Z-view. The probability of finding Z-projections was then better than that for the other views, since projections could be found with hits from 3 out of the 4 Z-planes used in the search.

Then, the track projections in each view were combined to form 3-dimensional straight lines. This was carried out in three stages. The first stage involved finding tracks which were combinations of a projection in each of the 4 views. This was facilitated by taking each combination of projections from two different views and calculating the predicted values of the slopes and intercepts in the other two views and comparing these values with those of the projections in those other two views. A 3-dimensional straight-line fit was imposed, and tracks were saved if the reduced-χ^2 was sufficiently small. After all these 4-view tracks were found, the 3-view tracks were combined in the second stage. This used the same procedure, except that it was required to find at least one hit in the view without a matched projection. Similarly, in the third stage, each combination of projections from the two views predicted a path in the other two views, along which to pickup hits; there had to be at least one hit found in each view.

Tracks were allowed to share some common hits with other tracks. Specifically, a track was allowed to share one whole projection with another track and at most n hits in addition to this, or simply to share m hits with another track. Tracks which shared too many hits were considered to be degenerate, and the track with the least number of degrees of freedom was dropped, or the one with the worst reduced-χ^2 was dropped.

For this algorithm to perform efficiently, the efficiencies of the physical detector planes had to be sufficiently high. In Figure 4.4 is shown the reconstruction efficiency of this algorithm as a function of the efficiency of the detector planes. This neglects the efficiency of the software implementation itself, and is based only on the probability of finding projections and of the tracks generating enough hits to produce enough projections to be combined as tracks. The efficiency of finding a projection can be expressed as

$$\varepsilon_{\rm proj} \equiv (\varepsilon_{\rm plane})^3 \varepsilon_{\rm PR}, \tag{4.20}$$

and if the factor ϵ_{PR} is taken to be unity, this simply becomes $(\epsilon_{plane})^3$. Then, for tracks which would be found with m out of n projections the probability would be expressed as

$$P_{m/n} = \frac{n!}{(n-m)!m!}(\epsilon_{proj})^m(1-\epsilon_{proj})^{n-m}. \tag{4.21}$$

Then, for tracks which would be found with 4 out of 4 projections the probability would be expressed as

$$P_{4/4} = (\epsilon_{proj})^4 = (\epsilon_{plane})^{12}. \tag{4.22}$$

Similarly for tracks with 3 out of 4 and 2 out of 4, the expressions would be, respectively

$$P_{3/4} = 4(\epsilon_{proj})^3(1-\epsilon_{proj}) = 4(\epsilon_{plane})^9(1-\epsilon_{plane}^3), \tag{4.23}$$

$$P_{2/4} = 6(\epsilon_{proj})^2(1-\epsilon_{proj})^2 = 6(\epsilon_{plane})^6(1-\epsilon_{plane}^3)^2. \tag{4.24}$$

Therefore, it is clear that for the operation of the PC chambers, as discussed in Section 3.2.1, the efficiency for reconstructing tracks by this processor was limited to 84%. The operational efficiency of the software itself was measured to be $\epsilon_{PR} = 98\%$ [50].

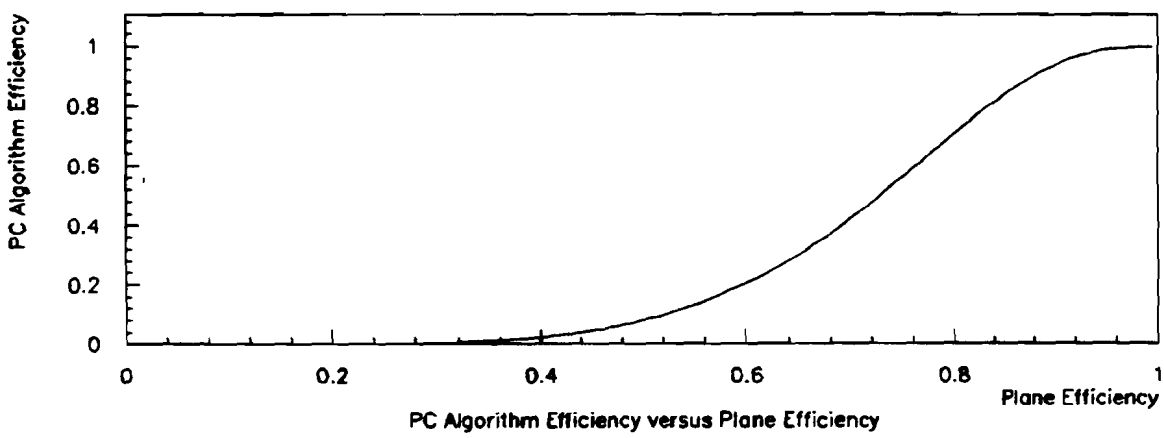

Figure 4.4: PC Efficiency: Algorithm versus Chamber. This plot shows the maximum efficiency of the PC track finding algorithm as a function of the operating efficiency of the chambers themselves.

4.2.5 MA Processor

The MA processor was used to link through the magnet tracks found in the PC's and the DC's by the PC and DC processors, respectively. This algorithm was based on

a principal components analysis of Monte Carlo tracks traversing the magnetic field. For the Y-system of four variables $(Y_{DC}, Y'_{DC}, Y_{PC}, Y'_{PC})$, a search was made for a linear combination of these variables to form a variable which displayed maximum variance, $\mathcal{Y}_1$; then, $\mathcal{Y}_2$ was constructed to be orthogonal to $\mathcal{Y}_1$ and to contain the maximum variance left in the system, and this process continued until a complete basis was constructed: $(\mathcal{Y}_1, \mathcal{Y}_2, \mathcal{Y}_3, \mathcal{Y}_4)$. Simultaneously, a rotation of basis was performed on the Z-system $(Z_{DC}, Z'_{DC}, Z_{PC}, Z'_{PC})$, to yield $(\mathcal{Z}_1, \mathcal{Z}_2, \mathcal{Z}_3, \mathcal{Z}_4)$. Then, it was possible to choose generous cuts on the outer edges of these distributions which would pass all valid tracks yet limit the number of unphysical combinations of the PC/DC-tracks. These cuts were chosen prior to the reconstruction [50].

During reconstruction the Y and Z-systems for each combination of PC/DC-tracks would be rotated into its respective principal components system, and the values checked against the cuts on the variances of these components. If the combination passed these cuts, then a radius through the magnet was calculated to define a road width in which to pickup hits in the PCF chambers. If enough PCF hits were found, then the collection of hits from the PC's, PCF's, and DC's was saved as a valid track. No final fit was imposed on these hits; track fitting, which incorporated full knowledge of the magnetic field, was better suited to determine validity of the trajectory. The efficiency of this processor for linking valid combinations of PC/DC-tracks was quite high: 97% [50].

4.2.6 PF Processor

The PF processor was used to recover tracks which entered the magnetic field but which were swept out of the magnet at large angles; these tracks therefore missed the active areas of the drift chambers and could not be found in the MA processor. This algorithm started with valid tracks found in the PC's by the PC processor and extrapolated them into the magnetic field. In the Z-view, a straight line was extrapolated to the last PCF Z-plane, and a window was searched to pickup a hit. If a hit was found, then a path was projected back through the other Z-planes of the PCF's to pickup hits. In addition, hits in the U and V views in the last PCF station were combined with the found Z-hit to form space-points at this station. From the straight line upstream of the field and a space-point within the field it was possible to calculate the complete helical path. Then, hits within some distance of this interpolated path were picked up in the other PCF planes; if enough hits were found, then the track was saved. A final fit to the DHFIT3 model was imposed on each collection of hits, and the track survived based on its value of reduced-χ^2. The efficiency of this processor was 97% [49].

4.2.7 PS Processor

The PS processor used the Space-Point Finding algorithm to construct space-points in the PSA chambers. This detector had six views of wire orientations, so the space-points could be combinations of up to six hits. The X-position for each space-point was chosen as the mean of the X-positions of the planes in the PSA used in the combination. The efficiency of this processor was measured to be 99%.

4.2.8 MS Processor

The MS processor was employed to link tracks found in the PC's and PCF's to the space-points found in the PSA's. The tracks found by either the PC and PF processors or the SF and SN processors were extrapolated using the DHFIT3 model to the position of the PSA's. This intercept and its extrapolated error defined a window at the PSA for each track, within which to search for a space-point; if a space-point lay within this window, then it was linked with the PC and PCF hits to form a redefined, longer track. The efficiency of this process was very high, 99%, since the multiplicity in the PSA was low and since tracks entering this detector had to have very large momenta.

4.2.9 SF Processor

The SF processor used the Space-Point Finding algorithm to construct space-points in each of the five stations of the PCF's. Each station had three views of wire orientations, Z, U, and V, so the space-points could be combinations of up to three hits. The X-position for each space-point was chosen as the mean of the X-positions of the planes in that station. Then the processor attempted to find groupings of these space-points which represented valid particle trajectories. It first searched for groupings with a contribution from a space-point in each of the five stations, then those with contributions from four stations, and finally those with contributions from three stations. In each search the values of the space-points in the non-bend view, Z, were grouped to form straight lines, using some generous "road widths"; this resulted in a set of track candidates composed of groupings of space-points. Then, for each track candidate, the Y-values of the space-points were examined. For a valid trajectory the Y-values should lie along a circle; it requires three points on a circle to calculate the radius. The radius of a circle was calculated from the Y-values for each group of three space-points of a given candidate. For a candidate with space-points from n-stations, there were m such combinations: $m = n!/3!$; thus, there was

only one such combination for three-station candidates, 4 for four-station candidates, and 20 for five-station candidates. Then the radii calculated for each candidate were compared and were required to be the same, within some limit, for the candidate to survive this stage. Finally, the candidates were subjected to fits to the DHFIT3 model, and the survival of each candidate was based on the value of the reduced-χ^2 being less than a tunable limit.

In order to limit the number of space-point candidates constructed from combinations of the hits in the Z, U, and V views, this processor was run only after the MA and PF processors had found tracks and claimed most of the hits. This left a manageable number of combinations to try; however, this processor was frequently aborted when the number of space-point candidates exceeded the size of a fixed-length array in the software implementation of the algorithm, and this tended to reduce the net efficiency of this processor.

In addition, some approximations were built into this algorithm which affected its efficiency. First, the success of fitting straight lines in the Z-view was a function of both the curvature and the initial Z-slope of the track; in order to find tracks, the Z-road-widths must be sufficiently generous. Second, the comparison of radii in the Y-view was affected by the fact that the first station of the chambers, PCF1, was *outside* the magnetic field; thus, the condition that the radii be similar was also a function of the curvature of the track. Finally, imposing a fit to the DHFIT3 model limited the acceptance of the algorithm to the range of tracks which can be fit well by that model; this range is discussed in Section 4.2.14.

4.2.10 SN Processor

The SN processor took trajectories from the SF processor and projected them upstream into the PC chambers. The method of projection was that of the DHFIT3 model; it used the values from the fit to intercept the trajectory with each plane of the PC's and picked up hits within a road-width. These newly picked-up hits were included with the original PCF hits in a subsequent fit, again to the DHFIT3 model; this fit was forced to go through the target by including a point at the center of the target in the fit, and corrections were applied to the position of this point, according to the magnitude of the momentum of the track. The trajectories whose reduced-χ^2 passed the cut were saved as tracks; for those which failed this cut, both the candidate with the new set of hits and the original SF-candidate were dropped.

4.2.11 MD Processor

The MD processor was used to extend tracks found in the PC and PCF chambers into the DC chambers. For tracks swept out of the magnet at large angles it was possible that the track traversed the active area of the first station of drift chambers, DCA, but missed that of the second station, DCB. Also, there was the valid topology of tracks traversing the deadened region of DCA but an active region of DCB. For both of these topologies, there would be no lines found by the DC processor, so this processor was used to recover these tracks. Tracks which were found by either the PC and PF processors or the SF and SN processors were extrapolated using the DHFIT3 model to the positions of the DC's. A set of corrections to the track parameters derived from these fits, DHFCOR, was applied to those tracks which had small radii of curvature, since the DHFIT3 model was a poor approximation for tracks with low momenta. These intercepts and their extrapolated errors defined windows for each track, within which to search for DC hits. If enough hits were found within these windows, then they were passed, with the PC and PCF hits, to another fit to the DHFIT3 model; no corrections were applied after this fit. If the value of the reduced-χ^2 was sufficiently small, then these DC hits were linked with the PC and PCF hits to form a redefined, longer track. The efficiency of this processor was 80%; it was limited primarily by the use of the DHFIT3 model for all tracks.

4.2.12 PV Processor

The PV processor used the Space-Point Finding algorithm to construct space-points in the PCV chamber. This detector had six views of wire orientations, so the space-points could be combinations of up to six hits. The X-position for each space-point was chosen as the mean of the X-positions of the planes used in the space-point. Because of the high track density in this chamber, this process was iterated in several passes, starting with narrow and straight roads in which to consider wires for making space points, and progressing to larger apertures. The efficiency of this processor was measured using a visual scan of 226 electron calibration events; there were 246 tracks input to the processor, and it found 211 space-points [45]. This is an efficiency of 86% $\pm$ 1%. A later study used Monte Carlo truth tracks to estimate the efficiency of reconstruction. This method employed a straight-line fit to a track in the PC chambers along with a point-fit in the PCV. The point-fit alone had an efficiency of 24% $\pm$ 1%. However, the combined fit had an efficiency of 73% $\pm$ 1% [46].

4.2.13 MV Processor

The MV processor was used to link hits in the PCV chamber to the tracks found in the other chambers. It was run after all the other processors and used their tracks as input. It refit the information from the PC tracks as 3-dimensional straight lines and extrapolated these lines into the PCV chambers, where it searched windows for space-points found in the PV processor. The PC hits associated with these lines and the PCV hits associated with the picked-up space-points were refit to 3-dimensional straight lines. If the value of the reduced-χ^2 was sufficiently small, then these PCV hits were linked with those from the rest of the chambers to form a redefined, longer track.

4.2.14 DHFIT3 model

The DHFIT3 model was developed as the basis of a fitting procedure for a certain class of trajectories. The trajectories of interest were those which traversed the PC, PCF, and PSA chambers. The PC's were upstream of the magnet, and the PCF's were inside. The PSA's had a very small active aperture, centered on the beamline (the X-axis) and located ~13m downstream of the center of the magnetic field. The domain of such trajectories included only those which were very stiff (had large radii of curvature) and had very small Z-slopes. These characteristics of the trajectories in this domain were utilized to simplify the fitting procedure; under these conditions a straight-line fit in the non-bend view was adequate, and the circular trajectory in the bend-view was approximated with a parabola.

For the strength of the magnet field used in this experiment, the momenta of particles whose trajectories belong to this domain were typically greater than 200 GeV/c. This model of a helical trajectory is valid down to a momentum of roughly 50 Gev/c. This can be seen in Figure 4.5, which shows the value of the reduced χ^2 returned from the fit, as a function of the momentum of the particle whose trajectory is being fitted; this was based on a study of Monte Carlo true tracks. It is clear that the model should not be employed for trajectories from particles with momenta less than 40 GeV/c. In order to measure the myths about *kinks* in the Z-view being caused by the fringe fields of the magnet, I have included a plot in Figure 4.5 based on Monte Carlo events generated with an ideal dipole magnetic field: $B_Z = B_0$ inside a cylinder of radius $R = 2.463$m, and $B_X = B_Y = 0$ everywhere. It is evident that the model is inadequate for low momentum tracks, even with a perfect dipole field. The fringe fields only augment the problem.

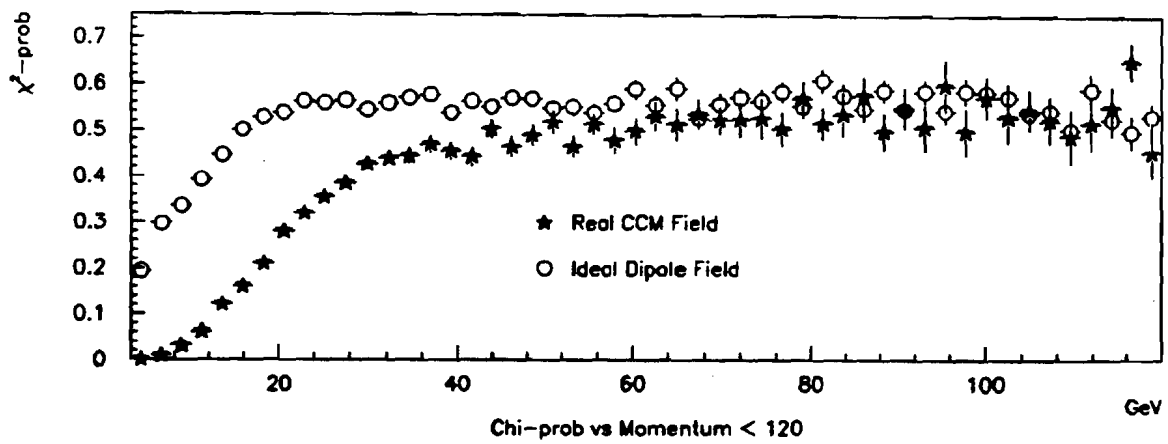

Figure 4.5: DHFIT3 Model Validity versus Track Momentum. This plot shows the mean value of the χ^2-probability, returned from a fit to the DHFIT3 model, as a function of the momentum of the particle whose trajectory was fitted. The input for each trajectory was the TRUTH hits from tracks generated by Monte Carlo; no Pattern Recognition was imposed on these hits.

4.3 Track Fitting

Track Fitting accepted as input the groups of hits produced in Pattern Recognition and imposed a quintic SPLINE fit on each of them. This SPLINE model was a piecewise continuous function in three sections: upstream of the CCM, inside the magnet, and downstream of it. This model included complete knowledge of the magnetic field and incorporated a description of the multiple scattering in the detectors. There were five parameters associated with the fit; the most important of these was the $1/p$ parameter which provided a calculation of the momentum of each charged track in the Forward Spectrometer. There were 57 detector planes in the Forward Spectrometer which could contribute simultaneously to a track, and these were grouped into 10 detectors: PCV, PC, 5 PCF's, DCA, DCB, and PSA. Each detector contributed both a Y and a Z point to the spline fit, so the maximum number of points in a fit was 20; the number of degrees of freedom in the fits therefore ranged from 1 to 15. The fit was imposed also on the tracks in the Beam Spectrometer to determine the momentum of the incoming beam muons.

Local fits, both point and line, were performed on each detector group of planes to obtain preliminary estimates of the position and slope at selected points along the X-axis. These values were then used in the quintic spline algorithm, solving the

Lorentz equation of motion for the Y and Z projections by inversion of the 5×5 system of linear equations. The error matrix was also evaluated. After this, knowledge of the momentum allowed accounting for multiple-scattering, and the fit and the error matrix were revaluated [54].

The χ^2-probability resulting from a fit was used to describe the likelihood of that track being a genuine particle trajectory, but no tracks were eliminated. Instead, these low χ^2-probability tracks were input to a postprocessing algorithm: RESCUE. The goal of this algorithm was to remove *outlier* hits from the track and then refit; in this reconstruction a hit was defined to be an outlier if it was separated from the track by more than 3 times the sigma of the hit. This procedure was iterated for up to 3 cycles; if there were still outlier hits, then the track entered *SUPERRESCUE*. This procedure started over with the track and dropped all hits in the PCV detector; a new fit was performed without the PCV hits. If there were outlier hits from this fit, they were dropped, one at a time, as in RESCUE; this procedure iterated until either there were no more outlier hits to remove or the number of hits left on the track fell below the number of parameters required in the fit. The RESCUE procedure was declared to have been successful for a track if no more outlier hits were found to be dropped and was declared to have failed if the number of degrees of freedom fell below one. After SUPERRESCUE, a hunt was performed to pickup PCV hits. The hits on the track in the PC's were fit to a straight line, and the lines from those fits with χ^2-probability$>0.1\%$ were extrapolated into the PCV to pickup hits.

The χ^2-probability threshold for submitting a track to RESCUE was chosen to be 5%; this was based on a study performed in which there was quite a shoulder at the low end of the distribution of the χ^2-probability from the fits [54]. This shoulder was due mainly to inappropriate use of sigmas in the Pattern Recognition, which was corrected before the reconstruction of the data samples; however, this threshold value was not lowered.

After Track Fitting there was a procedure run to eliminate residual degeneracy of tracks in an event. It compared combinations of tracks hit-by-hit, and if two tracks shared more than 10 hits, the track with fewer hits was dropped, or, if they had the same number of hits, the track with the lowest χ^2-probability was dropped. This procedure was written to eliminate multiply-found tracks, which existed at a 12% level at the time; after Pattern Recognition was cleaned up, multiply-found tracks existed at only a 3% level. This procedure reduced the occurrence well below this level.

4.4 Muon Matching

The Muon Matching procedure was employed to match one of the tracks in the Forward Spectrometer to a track behind the hadron absorber and therefore to identify positively the track of the scattered muon. This procedure was run after Track Fitting in order that knowledge of each track's momentum could be included in an estimation of the importance of multiple scattering in projecting the track through the steel absorber.

The matching was performed at the downstream face of the absorber. The Y and Z-projections found in the Muon Spectrometer were extrapolated to this X-position, along with the error at this position. A track in the Forward Spectrometer was projected through the steel absorber to the downstream face, along with its error. In addition, a positional error due to multiple scattering was calculated and added in quadrature to the track error. Then, in each of the views, Y and Z, the position and slope of the track and the muon-projection were compared relative to the errors. The decision of a match was based on the following quantities:

$$\chi^2_W \equiv \frac{(W_{\rm FS} - W_{\rm MS})^2}{(\sigma^2_{\rm FS} + \sigma^2_{\rm mcs} + \sigma^2_{\rm MS})}, \tag{4.25}$$

where FS stands for Forward Spectrometer, MS stands for Muon Spectrometer, and 'mcs' stands for multiple coulomb scattering, and W would run through Y, Y', Z, and Z'. The errors from the Forward Spectrometer were negligible, so the term $\sigma^2_{\rm FS}$ was not included in the calculations [5].

This comparison was made for all combinations of tracks in the Forward Spectrometer and all projections in the Muon Spectrometer. Each track in the Forward Spectrometer could be matched to at most one projection in each view of the Muon Spectrometer. However, each projection in the Muon Spectrometer could be matched to more than one track in the Forward Spectrometer, and it was left to the Vertex Processor to determine which combination was a better candidate for the scattered muon. If there were more than one set of projections in the Muon Spectrometer, then again the Vertex Processor chose which track linked best to the beam muon, and, if both linked well, then the muon with the highest energy was declared to be the scattered muon.

4.5 Vertex Fitting

The Vertex Processor was used to group tracks according to their vertices of origin. The essential job was to find the vertex of the muon scatter; this was the final definition of an interaction. From this vertex the scattering angle was defined and the kinematics were calculated. Subsequently, the processor attempted to link hadron tracks to this primary vertex and to form secondary vertices with combinations of hadrons. Hadron tracks were propagated back through the magnetic field of the CVM by the VTRACK program [10], and the distance of closest approach to each vertex, relative to the track error, was calculated for each track. This normalized quantity, Distance/Error, was used to determine whether a track was linked to a vertex. The distribution of this quantity can be seen in Figure 4.6 for all tracks relative to the primary vertex. The cutoff value of this quantity was chosen to be 4 for linking a track to a vertex. A more detailed description of this processor can be found in references [10, 2].

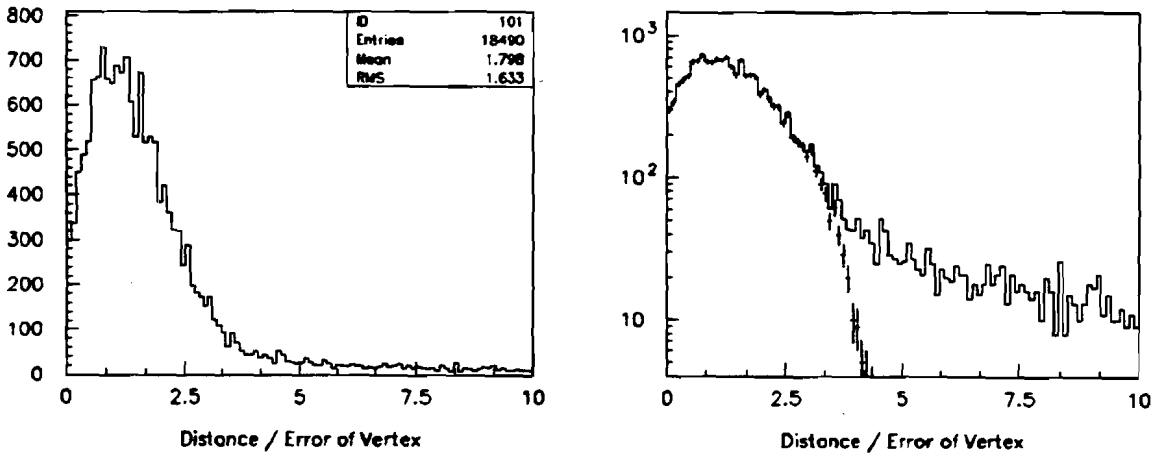

Figure 4.6: Distance Over Error from Vertex.
These plots show the distributions of the Distance Over Error calculated by the Vertex processor for all tracks with respect to the primary vertex. In Figure (b), on the log-scale the *scree* is evident at about 4; the points with errors represent the distribution of the Distance Over Error for the tracks which were declared *fitted* to the primary vertex.

Chapter 5

Selection and Correction

The events used in this analysis were taken on two targets, Deuterium and Xenon, and were based on two triggers, LAT and SAT, as described in Section 3.4. To justify merging the samples from these two triggers, I will show that no bias on the hadron distributions was introduced by the trigger requirements; since the triggers depended mainly upon the incoming and scattered muons, no strong dependence of the hadrons upon the triggers should be expected. In addition, an examination of the background will be performed and a set of "cuts" developed to limit this contamination. Two kinematic ranges will be defined: *Kin-1* and *Kin-2*. The methods used to correct the data for acceptance will be discussed; it is important to note that the acceptance correction mainly affects low-momentum tracks, and therefore Z-values below about 0.2.

5.1 Event Selection

After reconstruction of events, there was a Data-Reduction performed to skim off useful events. For the LAT trigger sample, this Data-Reduction required a reconstructed beam muon, a reconstructed scattered muon, and a reconstructed event vertex. A cut of $X_{Bj} > 0.003$ was applied to reduce the number of electromagnetic events; this was based upon a study of cross sections for electromagnetic processes and the apparent kinematic values these events would possess. In Table 5.1 is a list of the Data-Reduced tapes and numbers of events from the four data samples Deuterium (SAT), Deuterium (LAT), Xenon (SAT), and Xenon (LAT).

These samples were subjected to a set of rejection cuts; the effects of these cuts

Target	Tapes	Number of events
D2 SAT 500 GeV	XGBB50-60	72652
D2 LAT 500 GeV	XGAB50-55	31546
Xe SAT 500 GeV	XGFB50-79	216860
Xe LAT 500 GeV	XGEB50-56	32398

Table 5.1: Event Samples

Event Cuts	D2SAT	D2LAT	XeSAT	XeLAT
Initial number of events	72652	31546	216860	32398
Event Satisfies both LAT/SAT		3235		2966
EVEKIN: Error code from BETACM	1	5		4
More than One Incoming Beam	5337	1201	16951	1590
Event Cut by Kinematics	49930	10187	174280	12546
Event Cut by RHOCUT	196	136	236	136
ERROR in RHOCUT			1	1
Subsequent number of events	10062	14728	11684	12649
Event Cut by CALCUT (total)	1741	1037	3632	1478
(subtotal) Cut by CALCUT $N_{clus} < 3$	(1565	785	3296	1205)
Event Cut on low χ^2-prob vertex	43	80	58	60
Subsequent number of events	8278	13611	7994	11111

Table 5.2: Event Selection

are summarized in Table 5.2. The first operation was to remove the events from the LAT sample which satisfied both triggers SAT and LAT, to avoid double-counting them. The next line indicates that there was an error in calculating the β for the Center-of-Mass system; these few events were simply dropped. Next, the events which contained more than one incoming muon in the beam spectrometer were eliminated. The major rejection occurred due to the kinematic cuts applied:

$$Q^2 > 0.01$$

$$50 < \nu < 550$$

$$X_{Bj} > 0.0007$$

$$Y < 0.8.$$

Before declaring a final sample of Deep-Inelastic-Scattering events, I wanted to limit the level of contamination due to muon-electron scattering and muon-bremsstrahlung radiation. The maximum Y-cut and minimum X_{Bj}-cut eliminate much of this, but some should remain throughout the full kinematic range. To reduce this contamination, I applied an event rejection based on a set of Calorimeter

measurements. The energy deposited in the Calorimeter was defined to be the sum of the energies of the clusters found in the Calorimeter, which had more than 2 GeV each. If this energy was greater than 90% of the energy transferred in the event, then the event was rejected. If the event survived this cut, then a more sophisticated topology was investigated; if the event had only one or two valid clusters found in the Calorimeter which summed to more than 50% of the energy transferred, then the event was rejected. In the table this cut value is a subset of the previous line, which is the total number of events cut by the Calorimeter requirements. The final rejection applied to the event sample was that the χ^2-probability of the event vertex was greater than 0.1%. The numbers of events remaining in each sample after these cuts are listed in Table 5.2.

In order to reduce the contamination of diffractive meson production, the following criteria were employed. If an event had two and only two hadron tracks and these tracks were of opposite charge and carried greater than 90% of the energy transferred, then the invariant mass was calculated; if this mass was determined to be that of the ρ^0 (0.770 ± 0.2 GeV) or the ϕ (1.020 ± 0.2 GeV) or the photon (0.0 ± 0.2 GeV), then the event was rejected. If this mass was less than zero, then an error was returned, and the event was rejected. The numbers of events remaining after these rejections are listed in Table 5.2.

The number of events rejected by the Calorimeter cuts due to π^0's from Deep-Inelastic Scattering events should be less than about 5%. This estimate was based on the following evaluation. The probability of producing a charged hadron with fractional energy of the event greater than a half is given by the integral over the generic differential cross section for hadron production:

$$P(Z > 1/2) = C \int_{\frac{1}{2}}^{1} e^{-bZ} dZ.$$

With the generic values of $C = 2.8$ and $b = 6$, the probability is roughly 10%. It is standard to consider π^0-production to be half of that of charged pions, so this puts the probability less than 5%. Conversion of the two decay-photons into electron-positron pairs and acceptance for the members of the pairs in the Calorimeter reduces this probability even more.

5.2 Track Rejection

I imposed some quality cuts on the tracks selected. These cuts are listed in Table 5.3. The first two cuts are obvious. The tracks which failed the RESCUE procedure were

typically left with too few points in the fit and with meaningless values for the track parameters; even if these tracks were not junk before, they were after **RESCUE**. The imposition of a χ^2-probability cut of greater than 0.1% was merely a reasonable choice. Since I was studying the leading particles from hadronization and the effects of nuclear matter on their formation, I only considered particles propagating from the primary vertex. The determination of whether or not a track should be *Fitted* to the primary vertex was left to the Vertex processor. The distributions of the Distance-Over-Error parameter, which was used by the Vertex processor to evaluate the fitting of tracks to the vertex, are shown in Figure 4.6; the maximum value allowed for fitting a track to the vertex is 4, as can be seen in Figure 4.6.

Track Cuts	D2SAT	D2LAT	XeSAT	XeLAT
Number of events	8278	13611	7994	11111
Initial number of tracks	18972	36398	16801	28838
Track Cut: Failed RESCUE	837	1525	742	1290
Track Cut: χ^2-prob < 0.001	589	1180	559	1041
Track Cut: Not Primary Vertex	1688	4315	1629	3274
Track Cut: Not Fitted to Primary Vtx	3546	7235	3266	5884
Track Cut: $\Delta E/E > 0.1$	77	174	104	145
Track Cut: $E > 1.2\nu$	5	6	4	3
Final number of tracks	12230	21963	10497	17201
$100 < \nu < 500$, $Y < 0.75$, $X_{Bj} > 0.001$, ($Q^2 > 1$ .OR. $Y < 0.5$), $-11.6m < X_{\text{vertex}} < -10.6m$				
Subsequent number of events	3290	7799	2933	6327
Final number of tracks	6243	15334	5270	12256

Table 5.3: Track Selection

5.3 Calorimeter Cuts

5.3.1 Bremsstrahlung Contamination

The extent to which the Calorimeter cuts bias the resultant data samples can be examined by looking at some distributions for the events which have been cut by the Calorimeter rejection. These distributions are shown in Figures 5.1 through Figures 5.5; the distributions for the samples of Xenon SAT events which survived the Calorimeter cuts are shown on the left, and those which were rejected by the Calorimeter cuts are shown on the right. It is evident from the kinematic distributions for ν, Q^2, X_{Bj}, W^2, and Y that the rejected events are characteristically different from Deep-Inelastic Scattering. From the ϕ_μ distribution for the rejected events Figure 5.2(h), it is apparent that these events preferentially occur at $\phi_\mu \cong \pi$, which corresponds to scattering predominantly in the negative direction along the Y-axis of the E665 coordinate system. This was the bend-view in the spectrometer, so this predominance was indicative of simple energy loss in those interactions.

From the "$\log Q^2$ versus $\log Y$" plots in Figures 5.3 it is clear that the rejected events fall primarily in the region where radiative processes dominate the scattering processes. The use of a minimum cut of $X_{Bj} > 0.001$ reduces the contamination of muon-electron scattering and muon-bremsstrahlung radiation. The slanted line on the plots indicates the contour of constant X_{Bj} for a beam energy of 490 GeV; since we had beam energies between 200 and 800 GeV, the cut of $X_{Bj} > 0.001$ does not follow this line for all events. In addition to using this X_{Bj} cut, I tried to remove a bit more of the "corner" of the plot in Figures 5.3; this was facilitated by the logic of keeping the event only if:

$$X_{Bj} > 0.001 \quad \text{.AND.}$$
$$\left(Q^2 > 1\ \mathrm{GeV}^2/c^2 \quad \text{.OR.} \quad Y < 0.5\right).$$

In Figures 5.4(a) and (b), the Z-distributions indicate that the produced particle in the rejected events is fairly evenly distributed in the available energy, with some pileup near 1.0. This is suggestive of an electron from a gamma conversion. The Multiplicity distributions, Figures 5.5(c) and (d), indicate that mainly events with no produced particles are rejected, and these events have a different topology than the surviving events. The multiplicity distribution for Deuterium LAT is shown in Figure 5.6(b); this should be the sample least contaminated with electromagnetic background. This distribution looks similar to that from the events surviving the Calorimeter cuts. These cuts were imposed on the events used in the analysis of the hadronic final states.

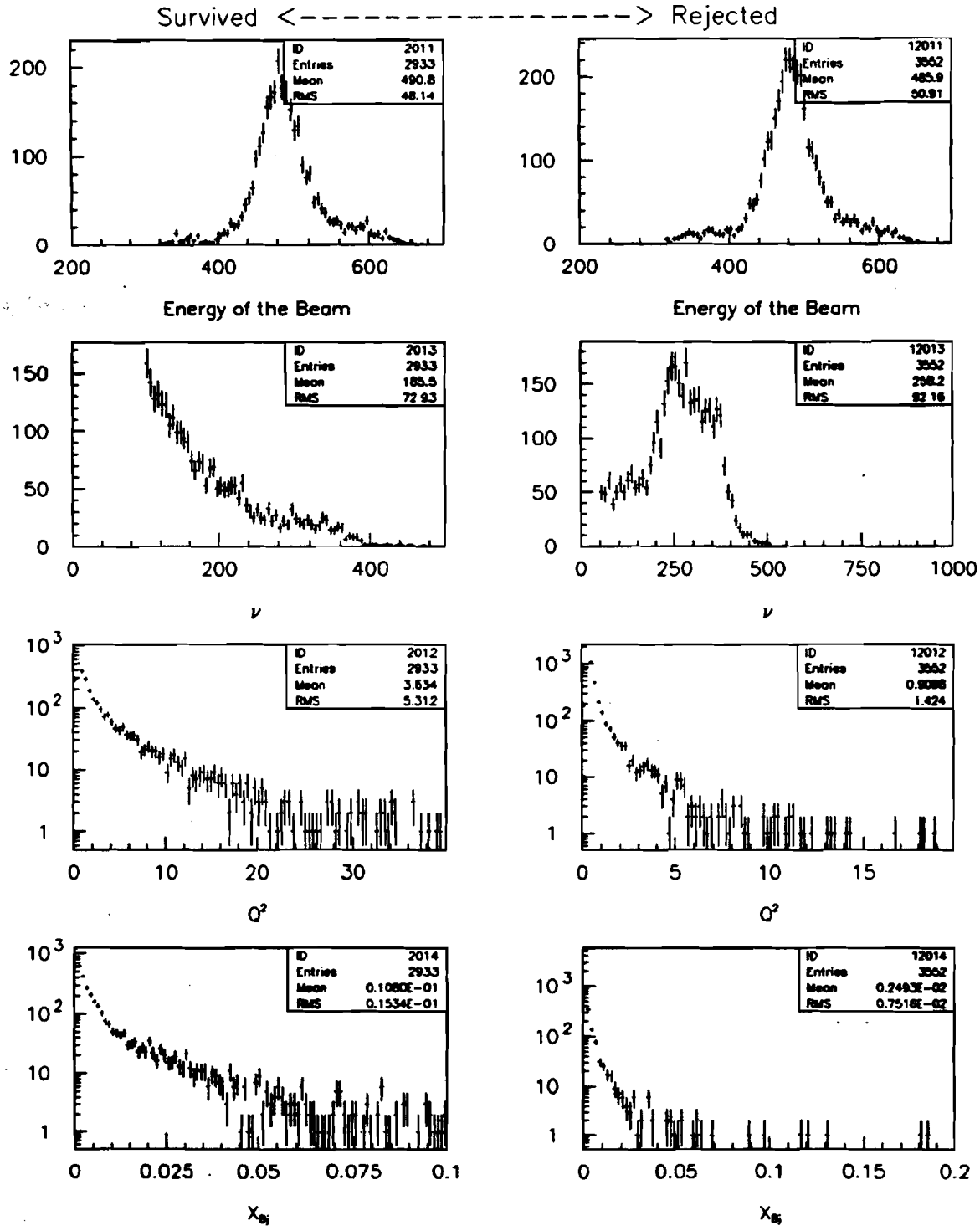

Figure 5.1: Beam Energy, ν, Q^2, X_{Bj}, Bremsstrahlung Removal.
On the left are the distributions from the events which survived the Calorimeter restrictions, and the ones on the right are from the events which were rejected by the Calorimeter. These data have not been corrected for acceptance.

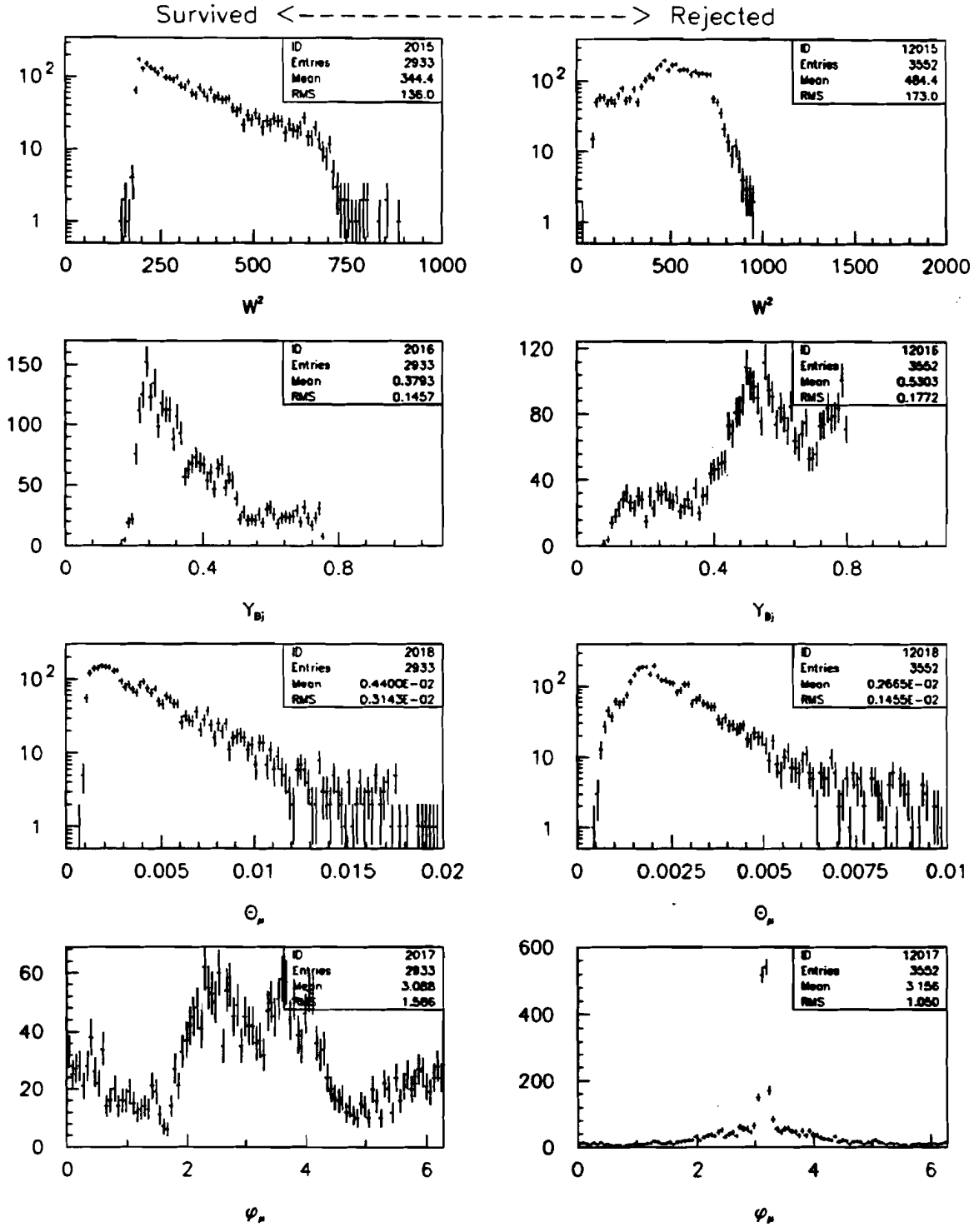

Figure 5.2: $W'^2, Y, \theta_\mu, \phi_\mu$, Bremsstrahlung Removal.
On the left are the distributions from the events which survived the Calorimeter restrictions, and the ones on the right are from the events which were rejected by the Calorimeter. These data have not been corrected for acceptance.

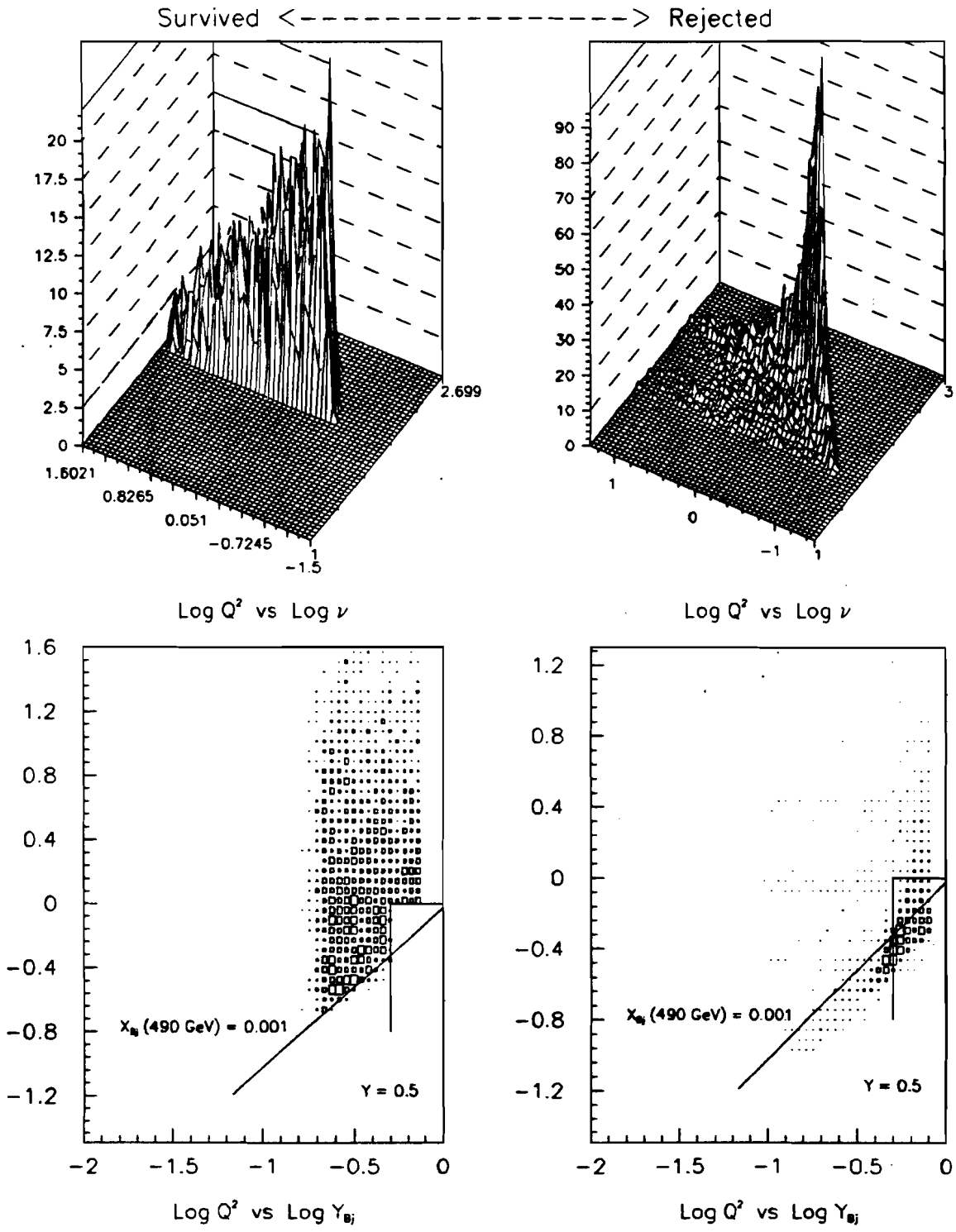

Figure 5.3: Q^2 versus Y and ν, Bremsstrahlung Removal.
On the left are the distributions from the events which survived the Calorimeter restrictions, and the ones on the right are from the events which were rejected by the Calorimeter. These data have not been corrected for acceptance.

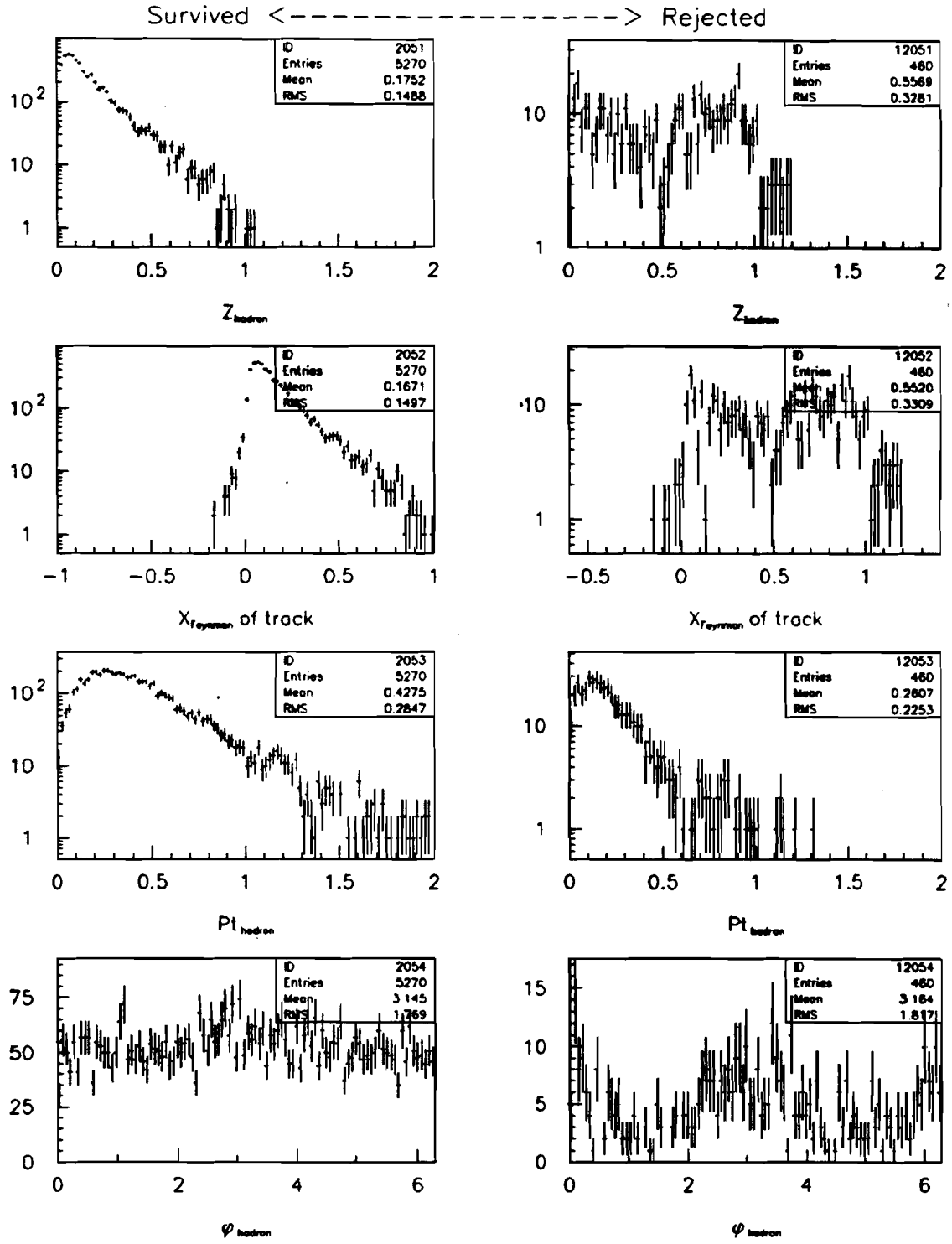

Figure 5.4: Z, X_F, P_t, ϕ_h Distributions, Bremsstrahlung Removal.
On the left are the distributions from the events which survived the Calorimeter restrictions, and the ones on the right are from the events which were rejected by the Calorimeter. These data have not been corrected for acceptance.

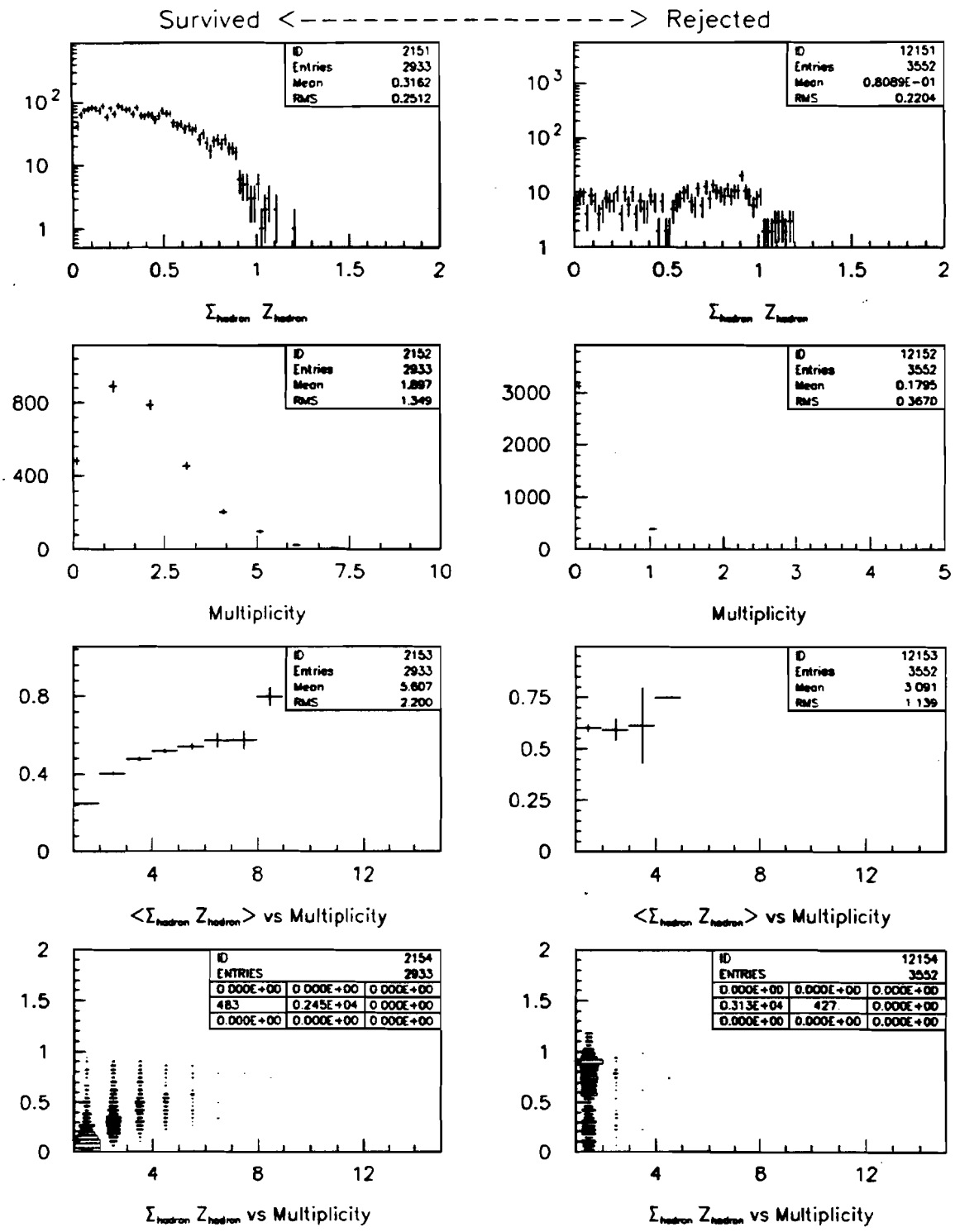

Figure 5.5: Z and Multiplicity Distributions, Bremsstrahlung Removal.
On the left are the distributions from the events which survived the Calorimeter restrictions, and the ones on the right are from the events which were rejected by the Calorimeter. Plots (a,b) show the summed-Z per event, and (c,d) show the multiplicity. Plots (g,h) show the summed-Z per event as a function of the multiplicity, whereas (e,f) show the mean-value of the summed-Z per event as a function of the multiplicity. These data have not been corrected for acceptance.

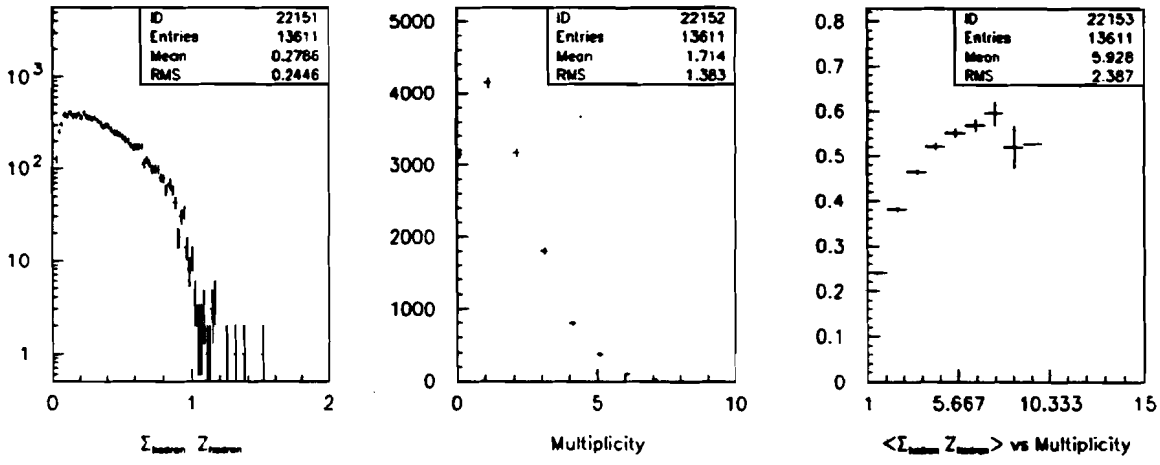

Figure 5.6: Z and Multiplicity Distributions of D_2 LAT.
Plot (a) shows the summed-Z per event, (b) shows the multiplicity distribution, and (c) shows the mean-value of the summed-Z per event as a function of the multiplicity. These data have not been corrected for acceptance.

5.4 Merging SAT and LAT

This section involves justifying the merging of the data from the SAT and LAT trigger samples. Although the acceptance of the LAT should be a subset of the SAT, the Phase Space of the Muon Beam for the SAT was only 12% of that of the LAT. The events which satisfied both the LAT and the SAT triggers were removed from the LAT samples of Deuterium and Xenon, but left in the SAT samples. Of these 3235 events in Deuterium, only 1725 passed the kinematic and RHOCUT cuts, and 1611 survived the Calorimeter cuts. There were 2966 original events in Xenon; 1258 survived the kinematic cuts, and 1089 survived the Calorimeter cuts.

In order to compare the trigger samples, I chose events with the same basic kinematic qualities by defining a *Kinematic Overlap* region:

$$0.01 < X_{Bj} < 0.3 \qquad \text{and} \qquad Q^2 > 1\ \text{GeV}^2/c^2.$$

Both trigger samples had enough events in this region to provide a valid comparison, and these numbers of events are shown in Table 5.4. The distributions of the kinematic variables Q^2, X_{Bj}, ν, and W'^2 are shown for both trigger samples in the overlap kinematic region in Figure 5.7.

Sample	Number of events
D2 SAT	853
D2 LAT	5173
Xe SAT	872
Xe LAT	4247
D2 LAT/SAT	643
Xe LAT/SAT	419

Table 5.4: Kinematic Overlap Samples.
The first four lines indicate the numbers of events of the four samples which satisfied the kinematic constraints of the Overlap region. The last two lines indicate the number of events in this Overlap region from the those which satisfied both triggers SAT and LAT; these events were also in the SAT samples.

The possible effects of the two triggers on the hadron distributions was of primary interest. The Z-distributions are plotted in Figure 5.8, with those from the SAT samples are on the left and those from the LAT sample on the right. For each sample there are four plots. In most of my analysis, I have dissected the final state hadrons and ranked them according to their values of Z; so, I frequently plot the distributions of the Z-values for the *fastest* (Z_1), *second fastest* (Z_2), and *third fastest* (Z_3) particles.

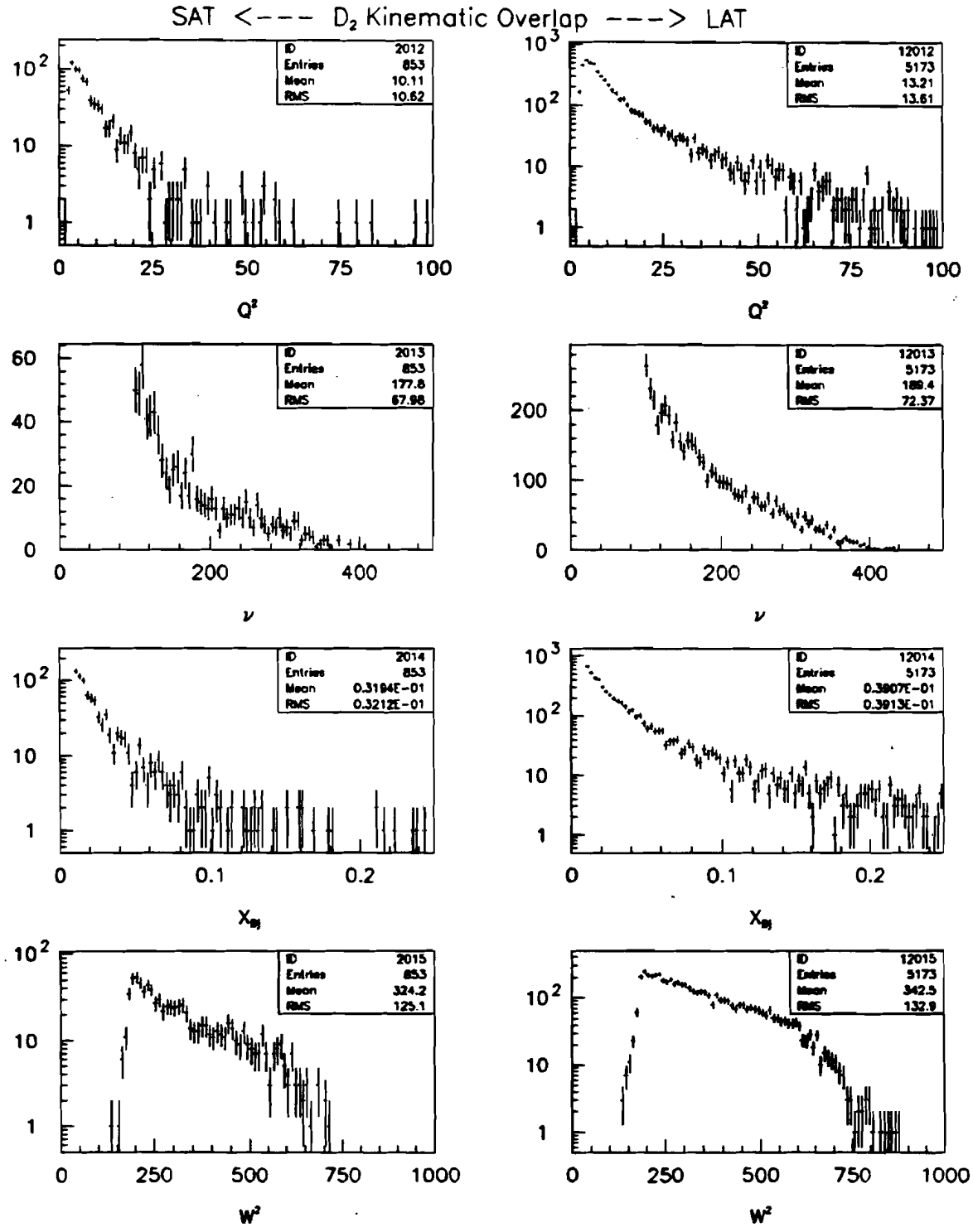

Figure 5.7: Kinematic Distributions for Overlap Region.
The plots on the left are from the SAT sample; the plots on the right are from the LAT sample. These data have not been corrected for acceptance.

Thus, the four plots for each sample are, from top to bottom, the Z-distributions for all particles, for only the fastest particles, for only the second fastest, and for only the third fastest. Each distribution has been fitted to an exponential function of the form: function = constant $\cdot$ $\exp^{\text{slope}}$. Comparing the parameters of these fits between distributions is a concise method of comparing the distributions. Since these samples are restricted to lie in a region with comparable kinematics, they should belong to the same "parent" distributions, i.e. they should look the same. Certainly, examining the parameters from the fits with their errors yields the conclusion that the distributions from the two trigger samples are consistent.

In Figure 5.9 I have overlaid the distributions from each trigger sample, along with each corresponding fit; the similarity is self-evident. Nevertheless, I have taken the ratios, and these are displayed in Figure 5.12. These plots indicate no significant deviation from a flat level at unity. The same series of plots comparing SAT and LAT for Xenon in the Kinematic Overlap region has been included in Figures 5.10, 5.11, and 5.13; again, there is no significant deviation from a flat level of unity. Emboldened with these results, I have merged the two samples from the SAT and the LAT triggers for each target, and the rest of the analysis has used these merged samples.

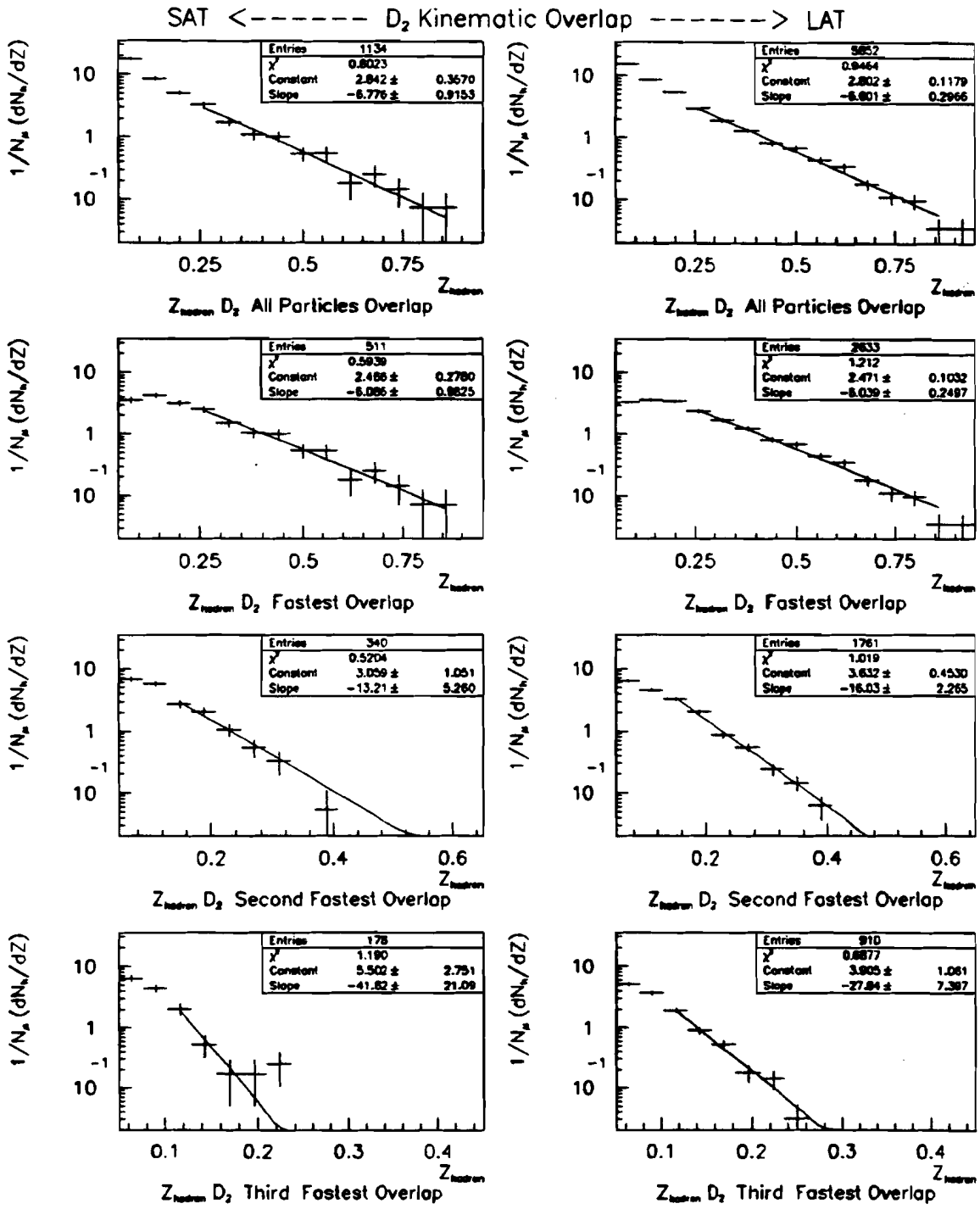

Figure 5.8: Trigger Overlap: Comparison of Z-distributions, D_2.
These plots show the the Z-distributions for all particles, the fastest, the second fastest, and the third fastest tracks; the distributions are from the Deuterium samples, with the SAT trigger on the left and the LAT trigger on the right. These data have been corrected for acceptance.

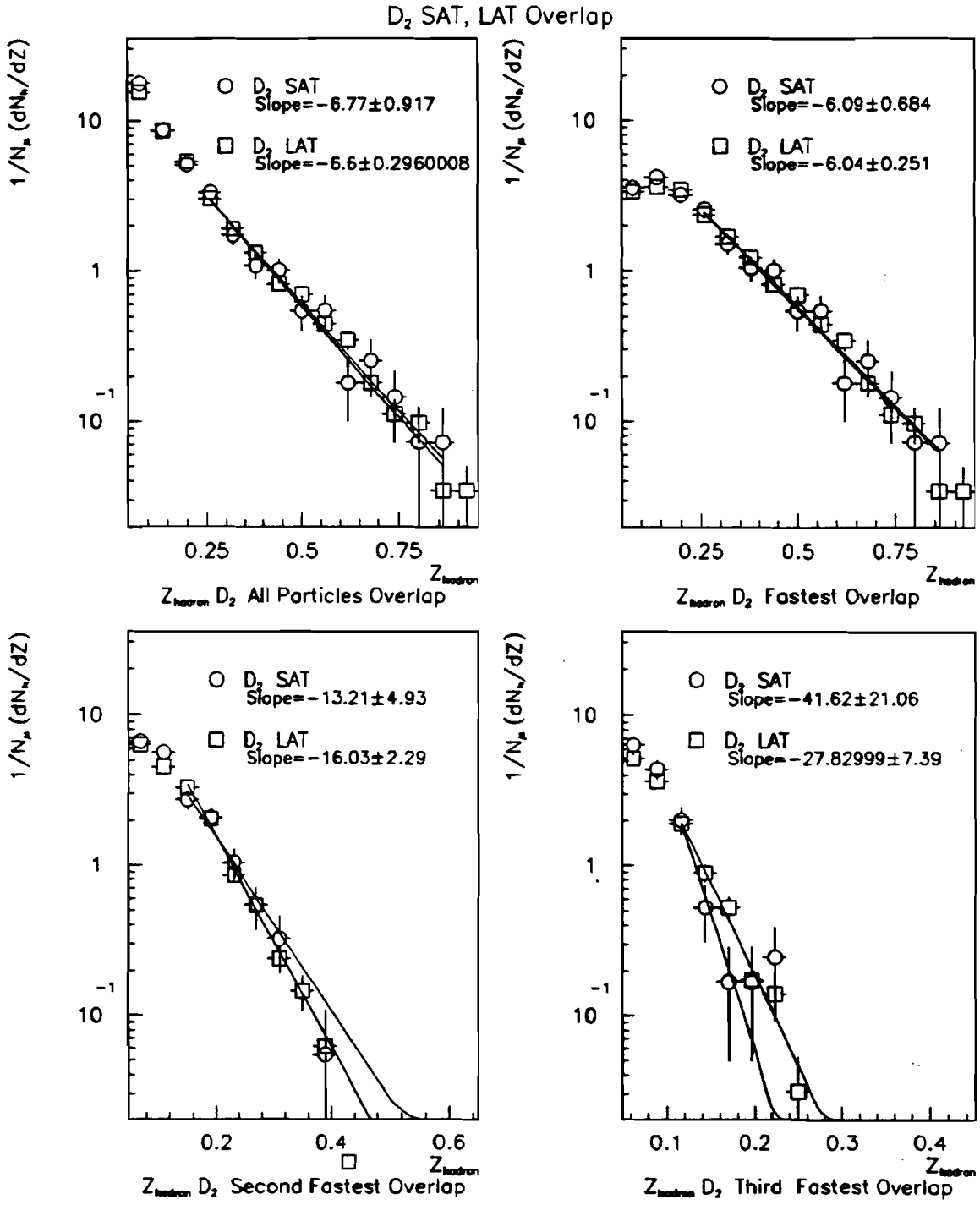

Figure 5.9: Trigger Overlap: Overlay of Z-distributions, D_2.
These plots show the overlaid distributions from the Deuterium sample, for the kinematic-overlap region of each trigger. These data have been corrected for acceptance.

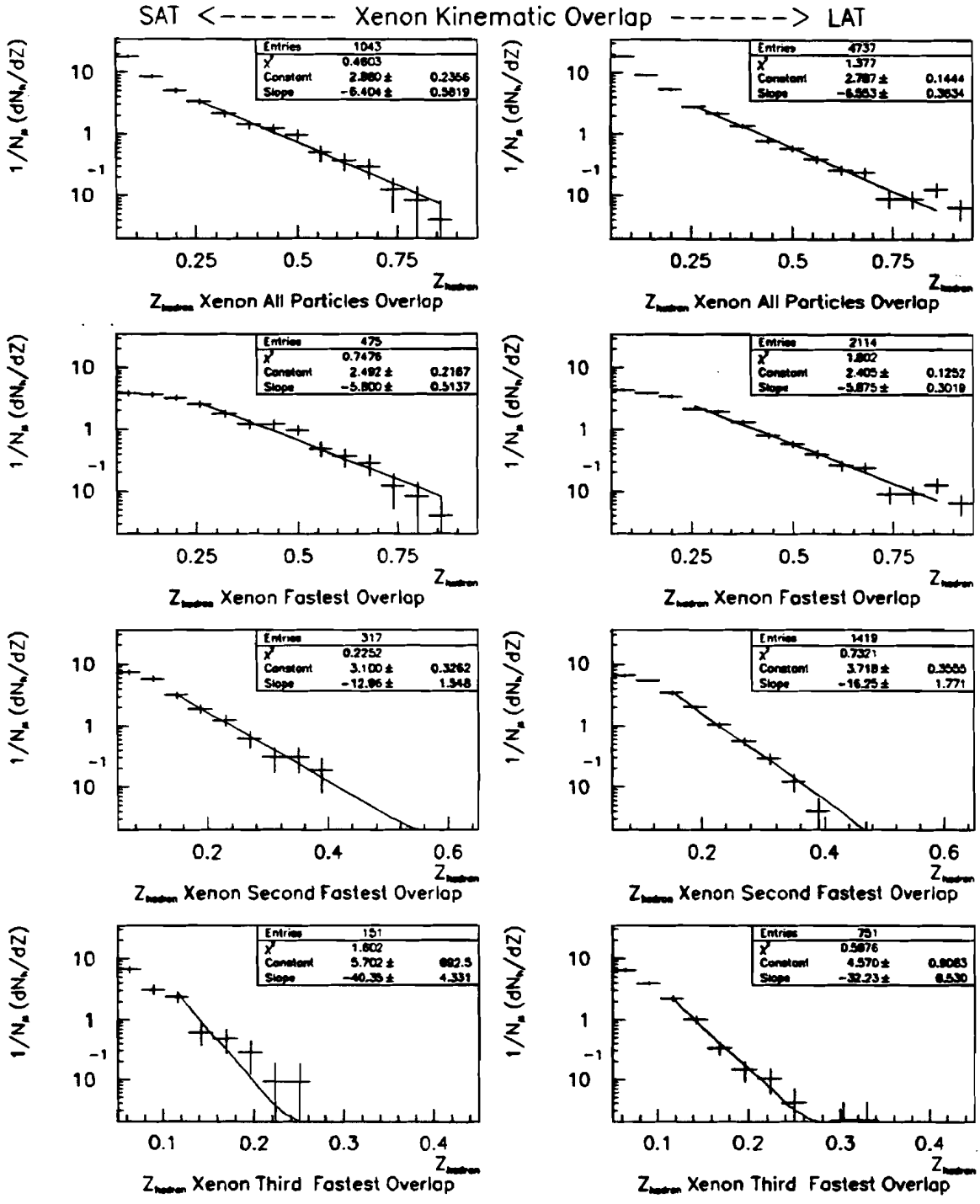

Figure 5.10: Trigger Overlap: Comparison of Z-distributions, Xenon.
These plots show the the Z-distributions for all particles, the fastest, the second fastest, and the third fastest tracks; the distributions are from the Xenon samples, with the SAT trigger on the left and the LAT trigger on the right. These data have been corrected for acceptance.

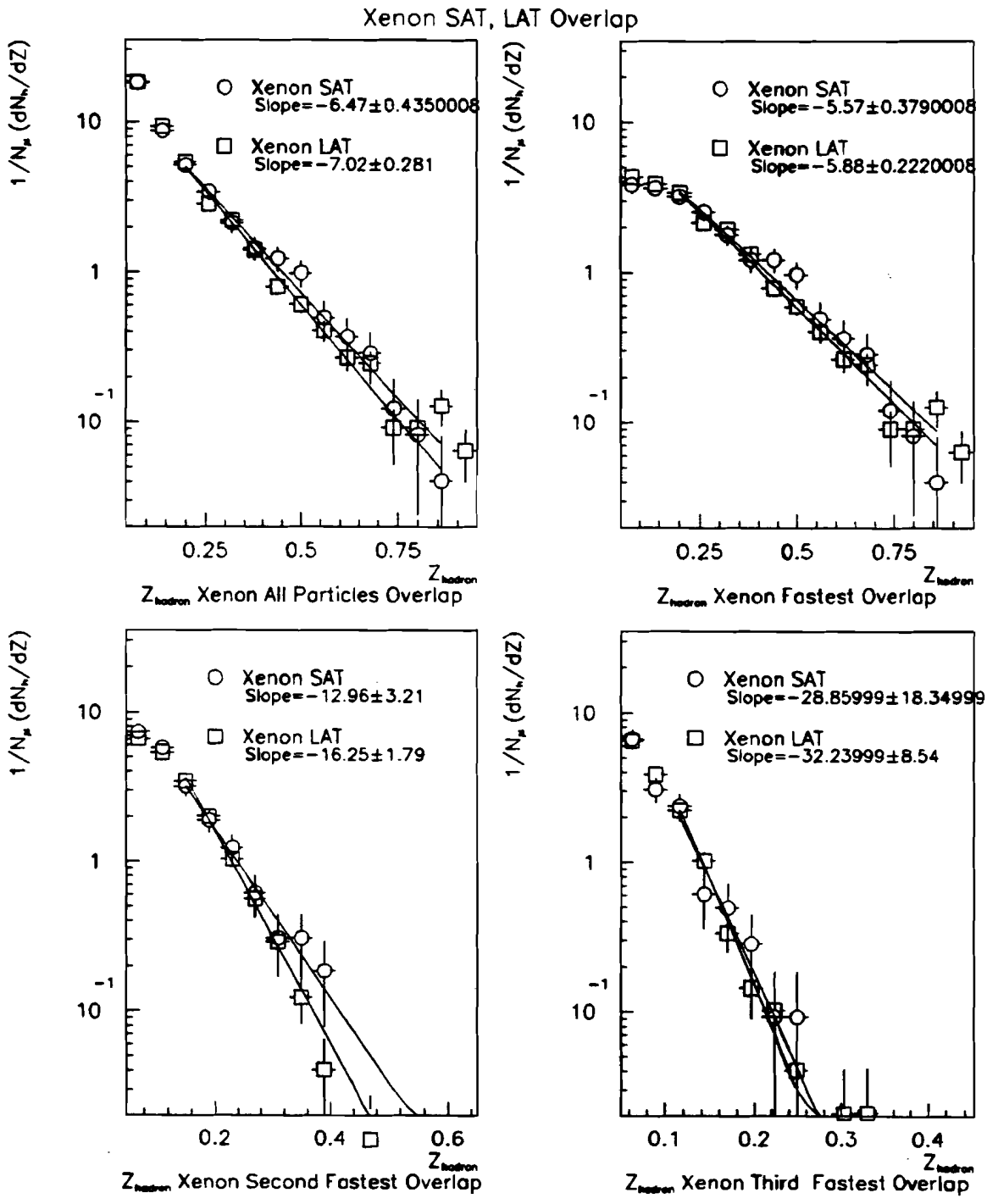

Figure 5.11: Trigger Overlap: Overlay of Z-distributions, Xenon.
These plots show the overlaid distributions from the Deuterium sample, for the kinematic-overlap region of each trigger. These data have been corrected for acceptance.

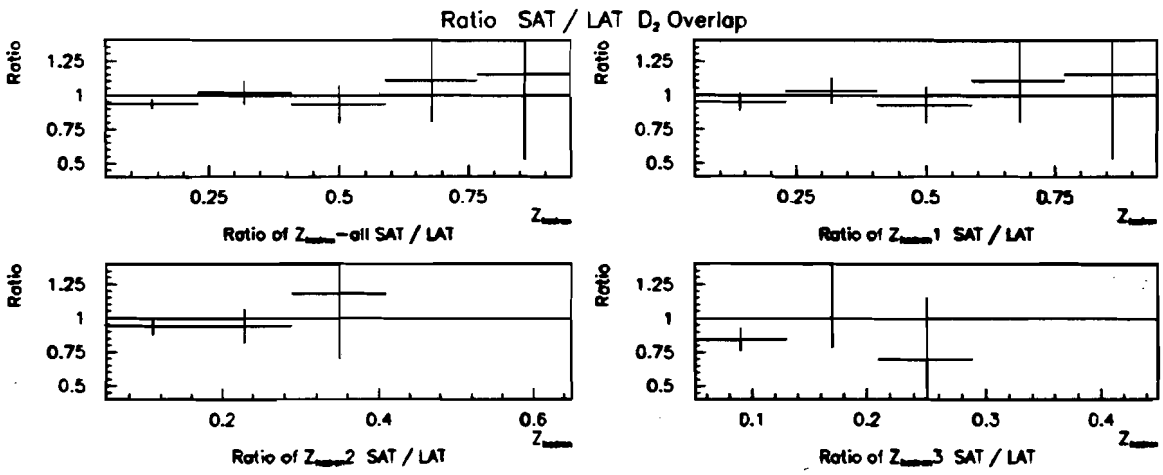

Figure 5.12: Trigger Overlap: Ratio of Z-distributions, D_2.
These plots show the ratios of the Z-distributions from the Deuterium samples: (SAT trigger) over (LAT trigger). Plots (a-d) are for all particles, the fastest, the second fastest, and the third fastest tracks, respectively. These data have been corrected for acceptance.

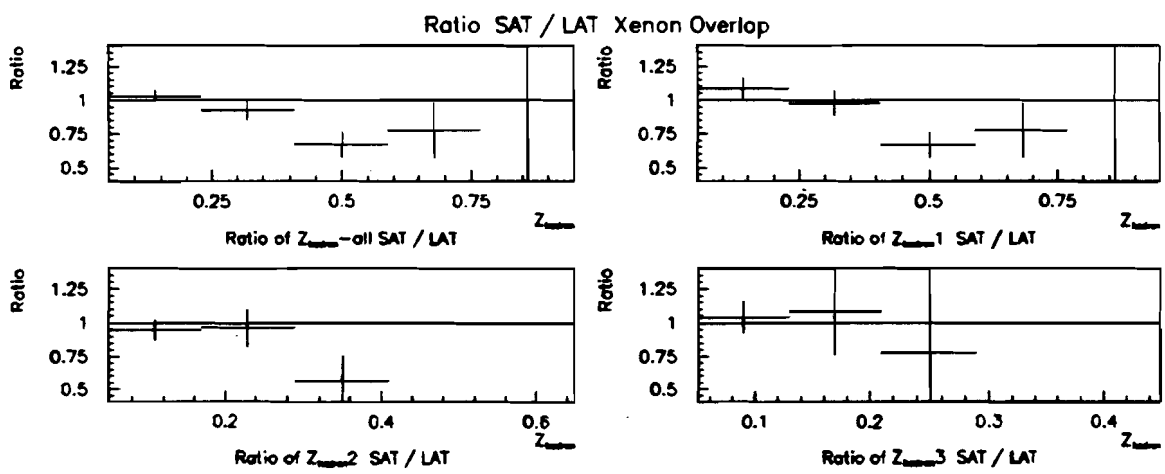

Figure 5.13: Trigger Overlap: Ratio of Z-distributions, Xenon.
These plots show the ratios of the Z-distributions from the Xenon samples: (SAT trigger) over (LAT trigger). Plots (a-d) are for all particles, the fastest, the second fastest, and the third fastest tracks, respectively. These data have been corrected for acceptance.

5.4.1 Kinematic Distributions: Kin-1 and Kin-2

The objective of the study is to determine the influence of nuclear matter on the final states of the produced hadrons. The effect of *Shadowing* has been discussed in Section 2.3, and it has been observed as a depletion of the scattering cross section in a "low" range of kinematics. The "low kinematic range" (Kin-1), the Shadowing region, was defined as:

$$X_{Bj} < 0.005 \qquad \text{and} \qquad Q^2 < 1\ \mathrm{GeV}^2/c^2.$$

Similarly, the "high kinematic range" (Kin-2), the Non-Shadowing region, was defined as:

$$X_{Bj} > 0.03 \qquad \text{and} \qquad Q^2 > 2\ \mathrm{GeV}^2/c^2.$$

The distributions of the kinematic variables Q^2, ν, X_{Bj}, and W'^2 are shown for Deuterium for these two kinematic regions in Figure 5.14. The distributions for these two regions for the Xenon samples are shown in Figure 5.15.

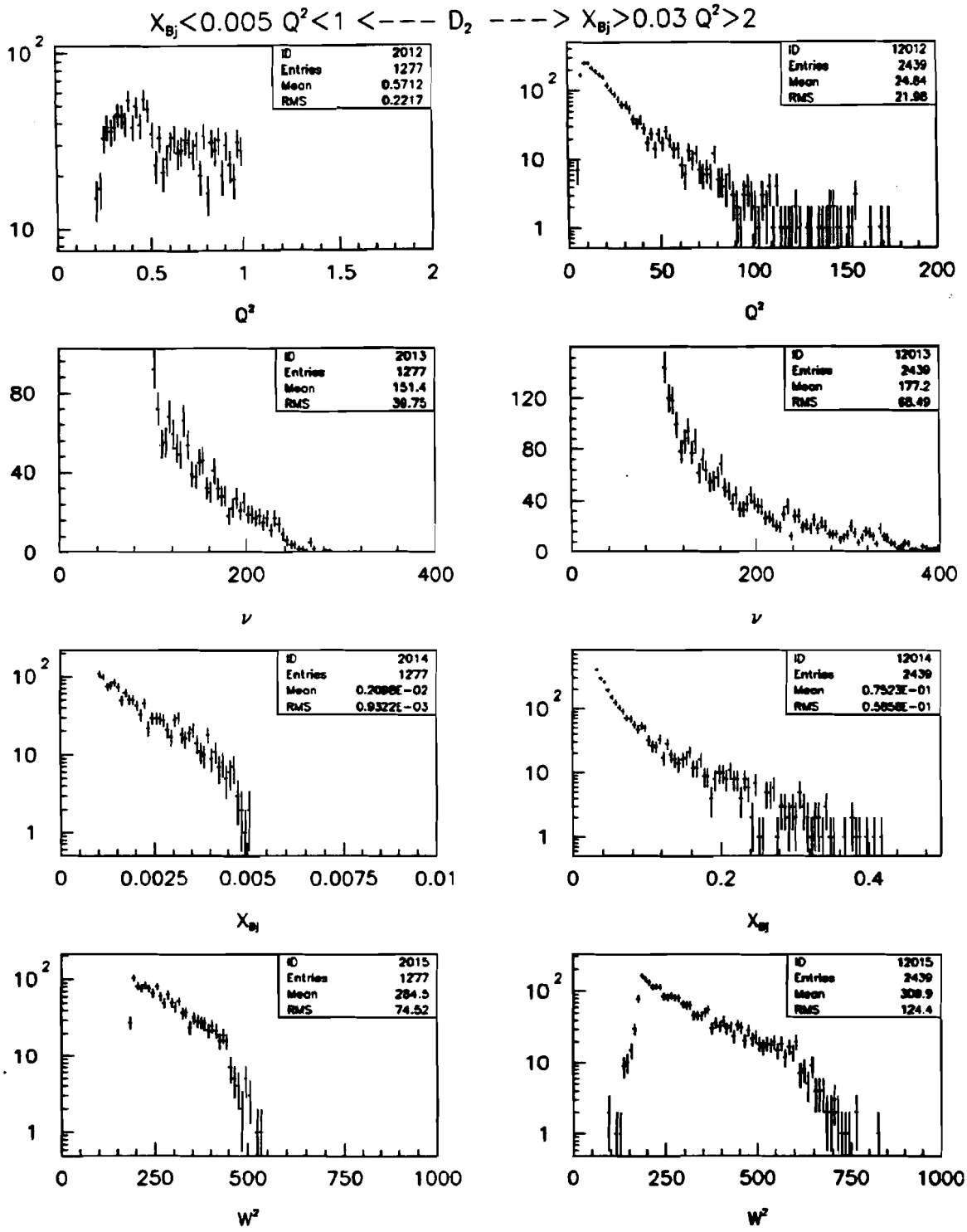

Figure 5.14: Kinematic Distributions for Kin-1 and Kin-2, D_2.
The plots on the left are from the low kinematic region, Kin-1; the plots on the right are from the high kinematic region, Kin-2. These data have not been corrected for acceptance.

typically left with too few points in the fit and with meaningless values for the track parameters; even if these tracks were not junk before, they were after **RESCUE**. The imposition of a χ^2-probability cut of greater than 0.1% was merely a reasonable choice. Since I was studying the leading particles from hadronization and the effects of nuclear matter on their formation, I only considered particles propagating from the primary vertex. The determination of whether or not a track should be *Fitted* to the primary vertex was left to the Vertex processor. The distributions of the Distance-Over-Error parameter, which was used by the Vertex processor to evaluate the fitting of tracks to the vertex, are shown in Figure 4.6; the maximum value allowed for fitting a track to the vertex is 4, as can be seen in Figure 4.6.

Track Cuts	D2SAT	D2LAT	XeSAT	XeLAT
Number of events	8278	13611	7994	11111
Initial number of tracks	18972	36398	16801	28838
Track Cut: Failed RESCUE	837	1525	742	1290
Track Cut: χ^2-prob < 0.001	589	1180	559	1041
Track Cut: Not Primary Vertex	1688	4315	1629	3274
Track Cut: Not Fitted to Primary Vtx	3546	7235	3266	5884
Track Cut: $\Delta E/E > 0.1$	77	174	104	145
Track Cut: $E > 1.2\nu$	5	6	4	3
Final number of tracks	12230	21963	10497	17201
$100 < \nu < 500$, $Y < 0.75$, $X_{Bj} > 0.001$, ($Q^2 > 1$ .OR. $Y < 0.5$), $-11.6m < X_{\text{vertex}} < -10.6m$				
Subsequent number of events	3290	7799	2933	6327
Final number of tracks	6243	15334	5270	12256

Table 5.3: Track Selection

5.3 Calorimeter Cuts

5.3.1 Bremsstrahlung Contamination

The extent to which the Calorimeter cuts bias the resultant data samples can be examined by looking at some distributions for the events which have been cut by the Calorimeter rejection. These distributions are shown in Figures 5.1 through Figures 5.5; the distributions for the samples of Xenon SAT events which survived the Calorimeter cuts are shown on the left, and those which were rejected by the Calorimeter cuts are shown on the right. It is evident from the kinematic distributions for ν, Q^2, X_{Bj}, W^2, and Y that the rejected events are characteristically different from Deep-Inelastic Scattering. From the ϕ_μ distribution for the rejected events Figure 5.2(h), it is apparent that these events preferentially occur at $\phi_\mu \cong \pi$, which corresponds to scattering predominantly in the negative direction along the Y-axis of the E665 coordinate system. This was the bend-view in the spectrometer, so this predominance was indicative of simple energy loss in those interactions.

From the "$\log Q^2$ versus $\log Y$" plots in Figures 5.3 it is clear that the rejected events fall primarily in the region where radiative processes dominate the scattering processes. The use of a minimum cut of $X_{Bj} > 0.001$ reduces the contamination of muon-electron scattering and muon-bremsstrahlung radiation. The slanted line on the plots indicates the contour of constant X_{Bj} for a beam energy of 490 GeV; since we had beam energies between 200 and 800 GeV, the cut of $X_{Bj} > 0.001$ does not follow this line for all events. In addition to using this X_{Bj} cut, I tried to remove a bit more of the "corner" of the plot in Figures 5.3; this was facilitated by the logic of keeping the event only if:

$$X_{Bj} > 0.001 \quad \text{.AND.}$$
$$\left(Q^2 > 1\ \mathrm{GeV}^2/c^2 \quad \text{.OR.} \quad Y < 0.5\right).$$

In Figures 5.4(a) and (b), the Z-distributions indicate that the produced particle in the rejected events is fairly evenly distributed in the available energy, with some pileup near 1.0. This is suggestive of an electron from a gamma conversion. The Multiplicity distributions, Figures 5.5(c) and (d), indicate that mainly events with no produced particles are rejected, and these events have a different topology than the surviving events. The multiplicity distribution for Deuterium LAT is shown in Figure 5.6(b); this should be the sample least contaminated with electromagnetic background. This distribution looks similar to that from the events surviving the Calorimeter cuts. These cuts were imposed on the events used in the analysis of the hadronic final states.

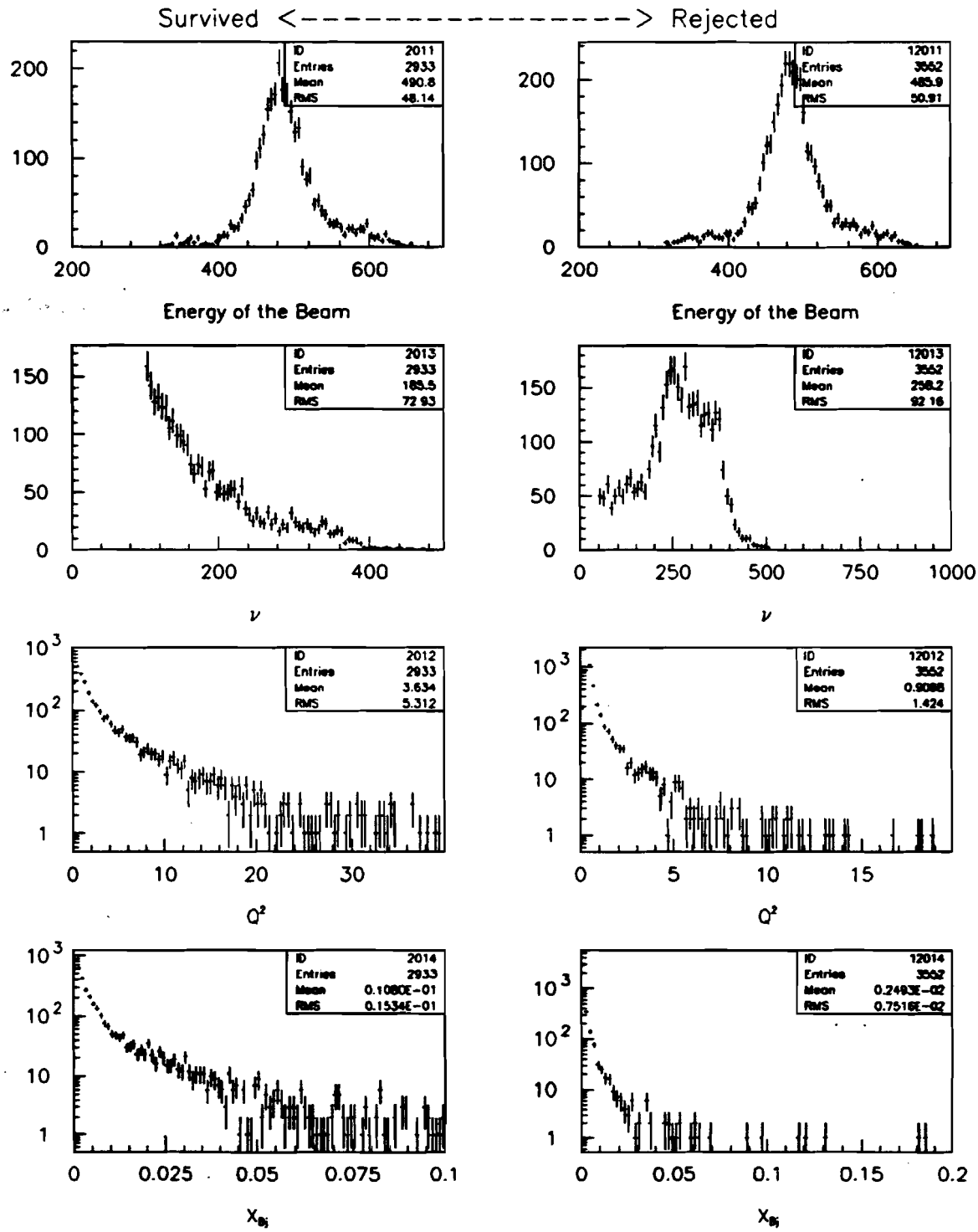

Figure 5.1: Beam Energy, ν, Q^2, X_{Bj}, Bremsstrahlung Removal.
On the left are the distributions from the events which survived the Calorimeter restrictions, and the ones on the right are from the events which were rejected by the Calorimeter. These data have not been corrected for acceptance.

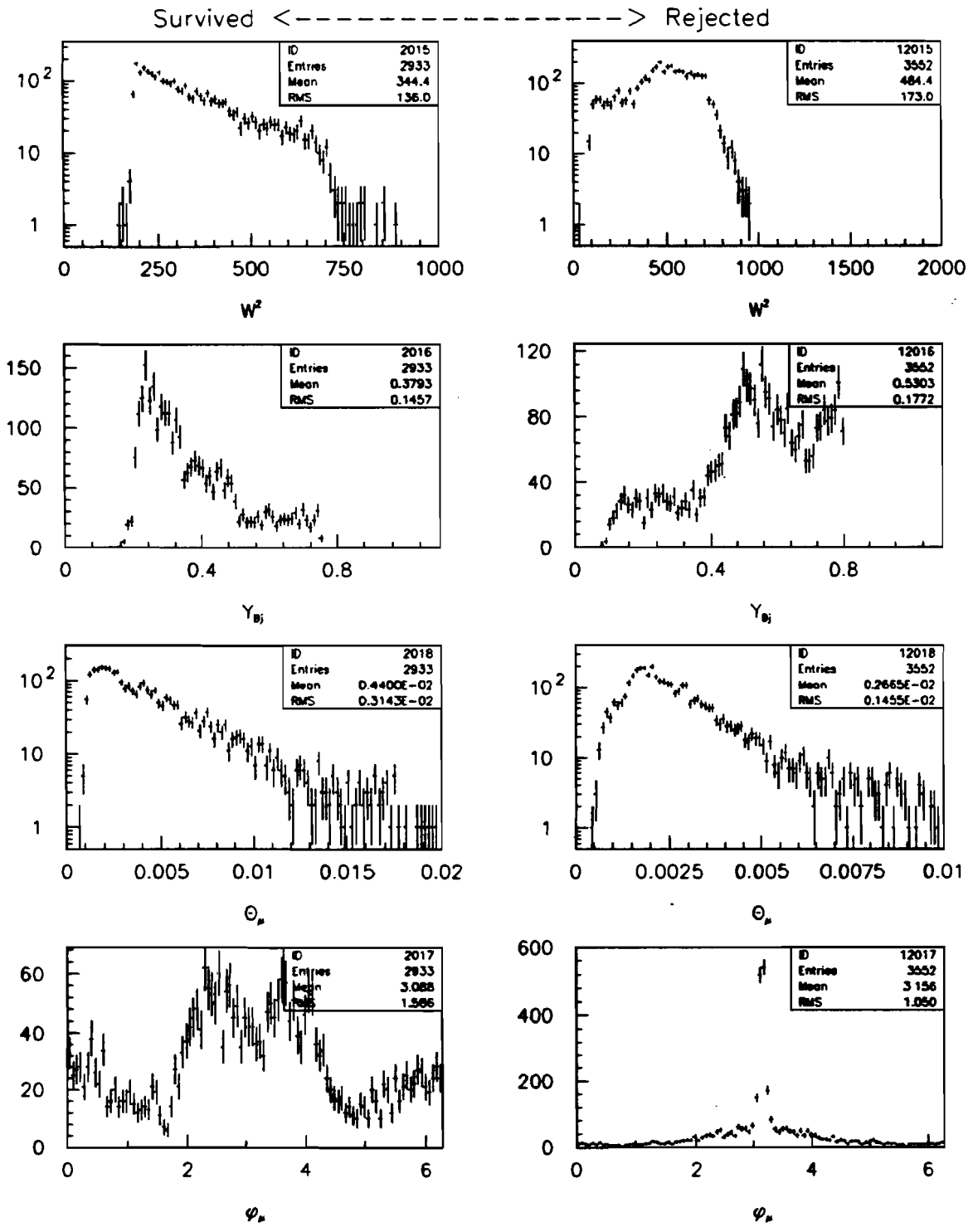

Figure 5.2: $W^2, Y, \theta_\mu, \phi_\mu$, Bremsstrahlung Removal.
On the left are the distributions from the events which survived the Calorimeter restrictions, and the ones on the right are from the events which were rejected by the Calorimeter. These data have not been corrected for acceptance.

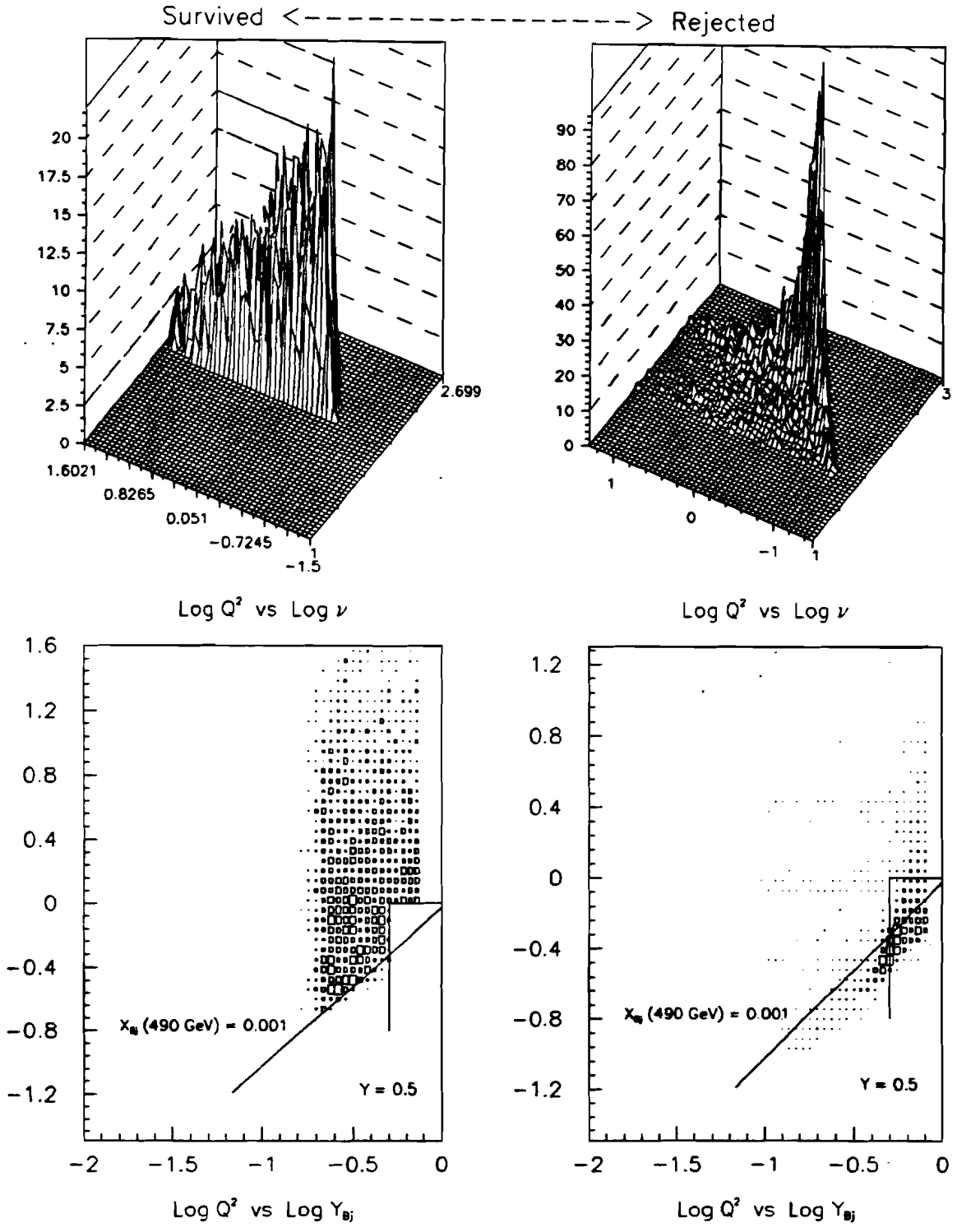

Figure 5.3: Q^2 versus Y and ν, Bremsstrahlung Removal.
On the left are the distributions from the events which survived the Calorimeter restrictions, and the ones on the right are from the events which were rejected by the Calorimeter. These data have not been corrected for acceptance.

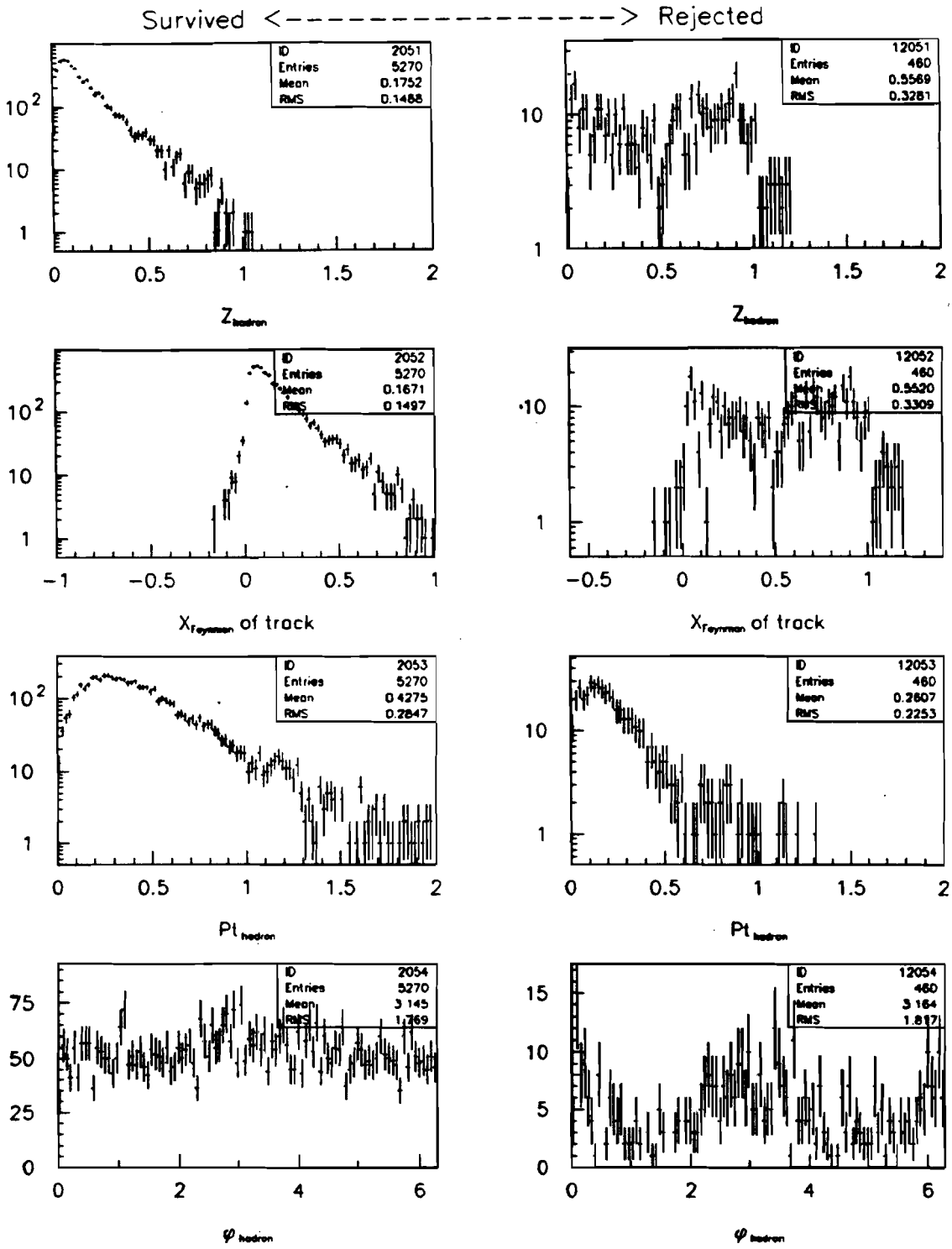

Figure 5.4: Z, X_F, P_t, ϕ_h Distributions, Bremsstrahlung Removal.
On the left are the distributions from the events which survived the Calorimeter restrictions, and the ones on the right are from the events which were rejected by the Calorimeter. These data have not been corrected for acceptance.

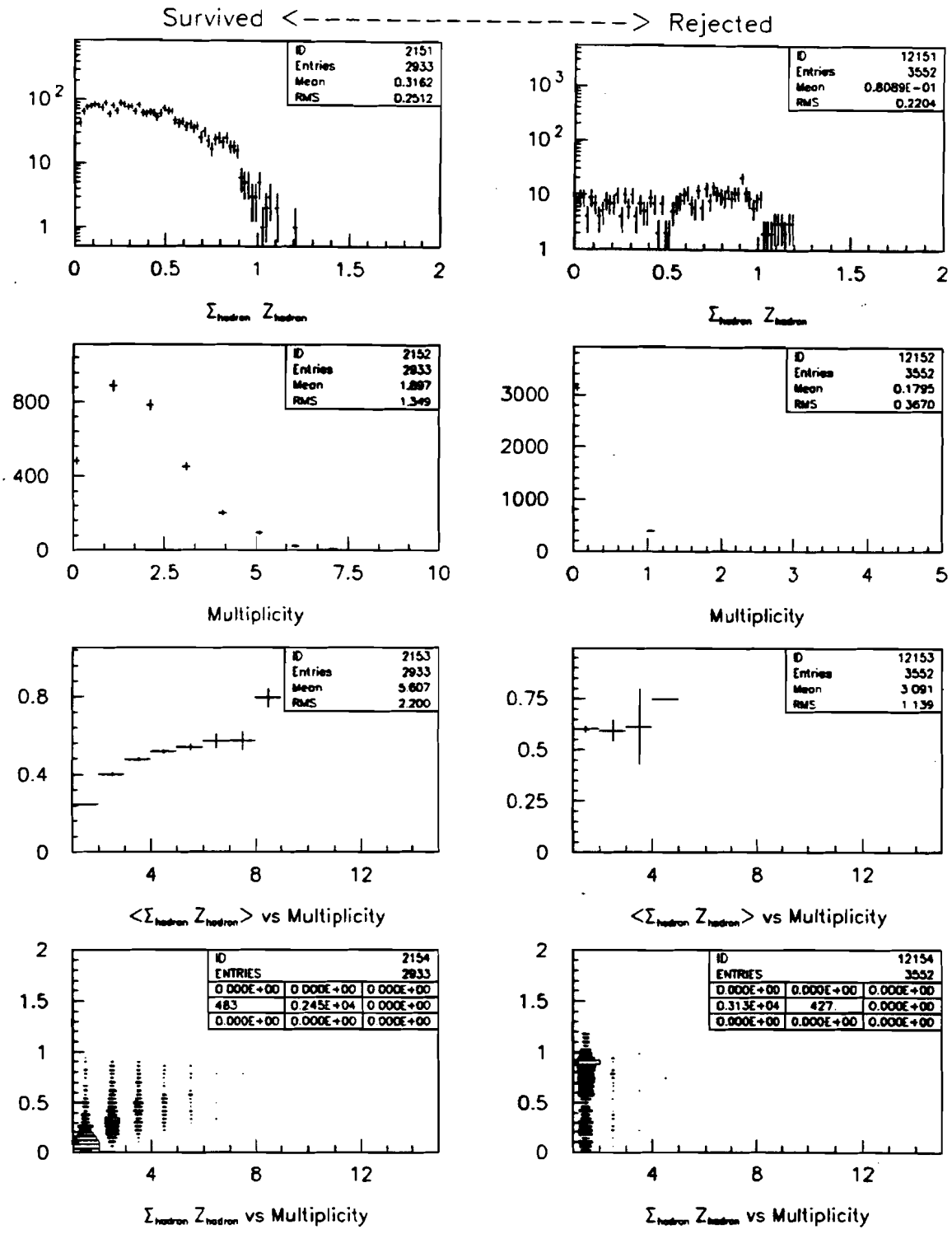

Figure 5.5: Z and Multiplicity Distributions, Bremsstrahlung Removal.
On the left are the distributions from the events which survived the Calorimeter restrictions, and the ones on the right are from the events which were rejected by the Calorimeter. Plots (a,b) show the summed-Z per event, and (c,d) show the multiplicity. Plots (g,h) show the summed-Z per event as a function of the multiplicity, whereas (e,f) show the mean-value of the summed-Z per event as a function of the multiplicity. These data have not been corrected for acceptance.

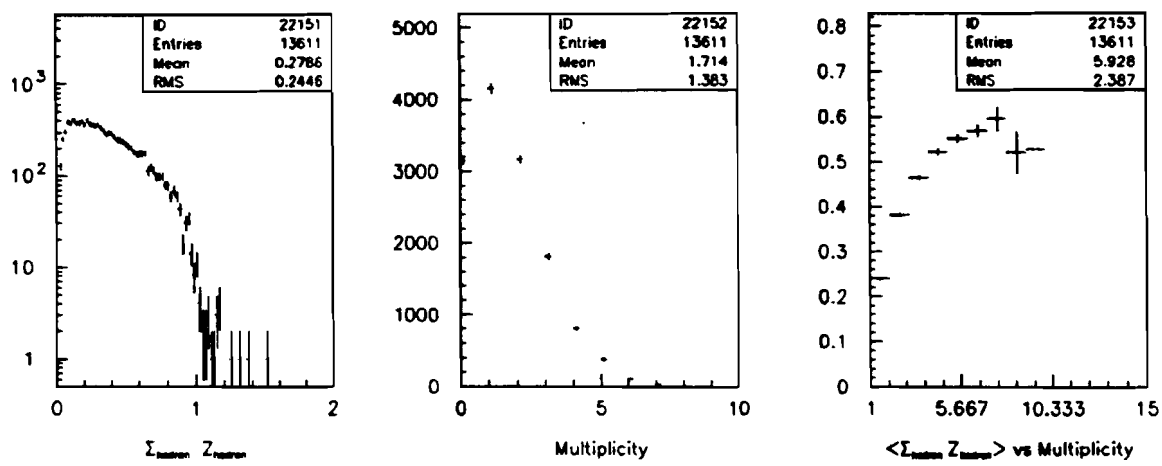

Figure 5.6: Z and Multiplicity Distributions of D_2 LAT.
Plot (a) shows the summed-Z per event, (b) shows the multiplicity distribution, and (c) shows the mean-value of the summed-Z per event as a function of the multiplicity. These data have not been corrected for acceptance.

5.4 Merging SAT and LAT

This section involves justifying the merging of the data from the SAT and LAT trigger samples. Although the acceptance of the LAT should be a subset of the SAT, the Phase Space of the Muon Beam for the SAT was only 12% of that of the LAT. The events which satisfied both the LAT and the SAT triggers were removed from the LAT samples of Deuterium and Xenon, but left in the SAT samples. Of these 3235 events in Deuterium, only 1725 passed the kinematic and RHOCUT cuts, and 1611 survived the Calorimeter cuts. There were 2966 original events in Xenon; 1258 survived the kinematic cuts, and 1089 survived the Calorimeter cuts.

In order to compare the trigger samples, I chose events with the same basic kinematic qualities by defining a *Kinematic Overlap* region:

$$0.01 < X_{Bj} < 0.3 \qquad \text{and} \qquad Q^2 > 1\ \text{GeV}^2/c^2.$$

Both trigger samples had enough events in this region to provide a valid comparison, and these numbers of events are shown in Table 5.4. The distributions of the kine-

Sample	Number of events
D2 SAT	853
D2 LAT	5173
Xe SAT	872
Xe LAT	4247
D2 LAT/SAT	643
Xe LAT/SAT	419

Table 5.4: Kinematic Overlap Samples.
The first four lines indicate the numbers of events of the four samples which satisfied the kinematic constraints of the Overlap region. The last two lines indicate the number of events in this Overlap region from the those which satisfied both triggers SAT and LAT; these events were also in the SAT samples.

matic variables Q^2, X_{Bj}, ν, and W^2 are shown for both trigger samples in the overlap kinematic region in Figure 5.7.

The possible effects of the two triggers on the hadron distributions was of primary interest. The Z-distributions are plotted in Figure 5.8, with those from the SAT samples are on the left and those from the LAT sample on the right. For each sample there are four plots. In most of my analysis, I have dissected the final state hadrons and ranked them according to their values of Z; so, I frequently plot the distributions of the Z-values for the *fastest* (Z_1), *second fastest* (Z_2), and *third fastest* (Z_3) particles.

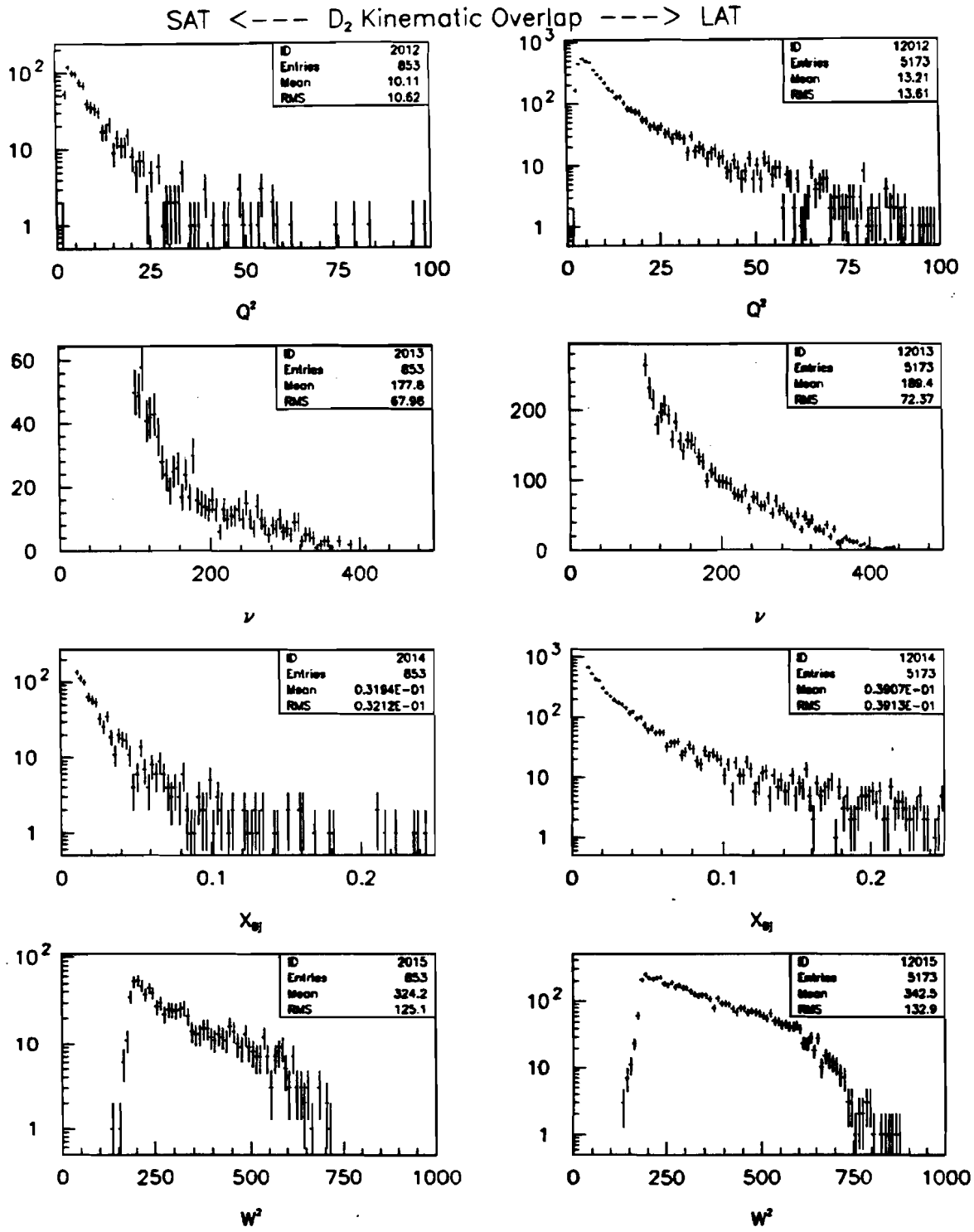

Figure 5.7: Kinematic Distributions for Overlap Region.
The plots on the left are from the SAT sample; the plots on the right are from the LAT sample. These data have not been corrected for acceptance.

Thus, the four plots for each sample are, from top to bottom, the Z-distributions for all particles, for only the fastest particles, for only the second fastest, and for only the third fastest. Each distribution has been fitted to an exponential function of the form: function = constant $\cdot$ $\exp^{\text{slope}}$. Comparing the parameters of these fits between distributions is a concise method of comparing the distributions. Since these samples are restricted to lie in a region with comparable kinematics, they should belong to the same "parent" distributions, i.e. they should look the same. Certainly, examining the parameters from the fits with their errors yields the conclusion that the distributions from the two trigger samples are consistent.

In Figure 5.9 I have overlaid the distributions from each trigger sample, along with each corresponding fit; the similarity is self-evident. Nevertheless, I have taken the ratios, and these are displayed in Figure 5.12. These plots indicate no significant deviation from a flat level at unity. The same series of plots comparing SAT and LAT for Xenon in the Kinematic Overlap region has been included in Figures 5.10, 5.11. and 5.13; again, there is no significant deviation from a flat level of unity. Emboldened with these results, I have merged the two samples from the SAT and the LAT triggers for each target, and the rest of the analysis has used these merged samples.

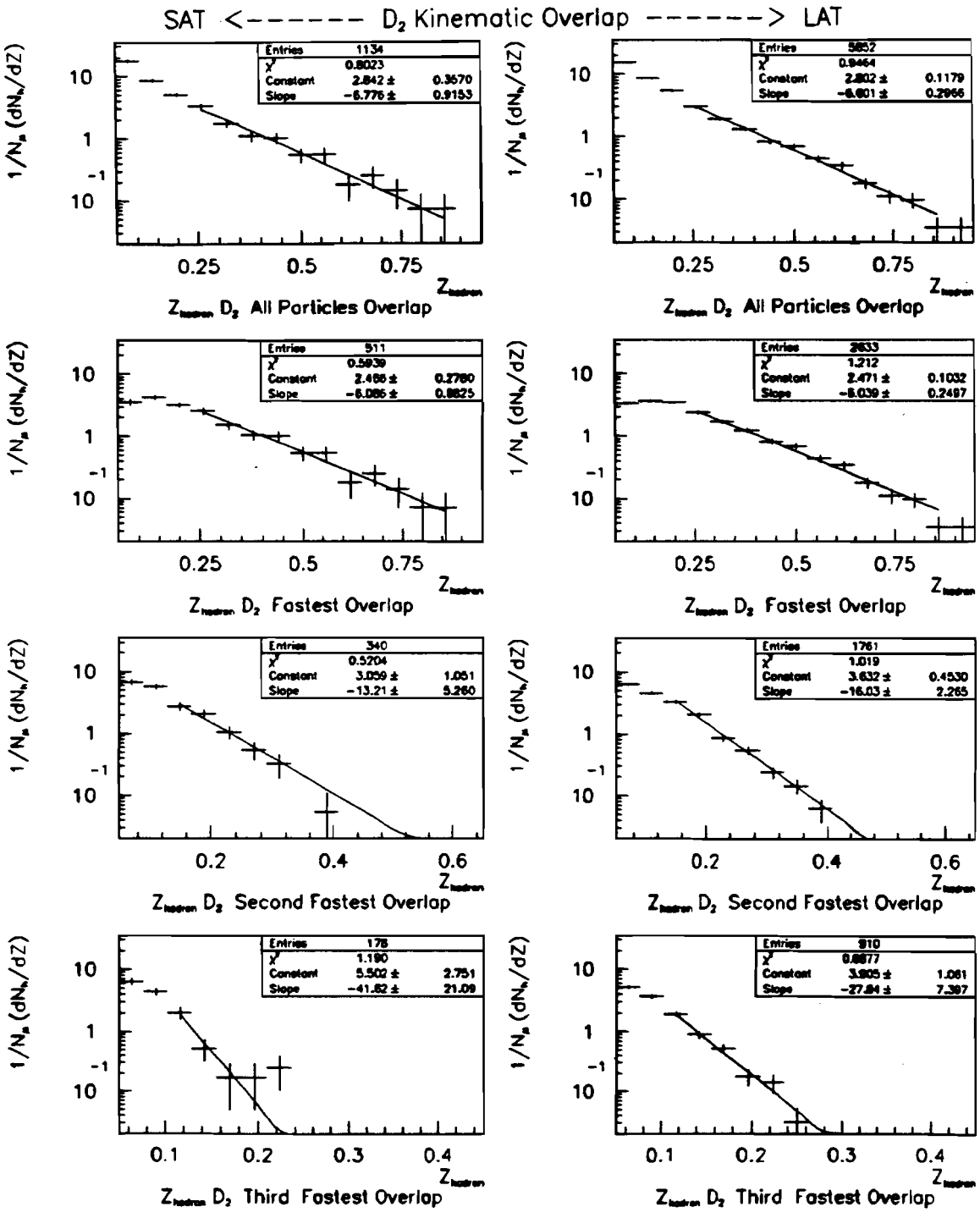

Figure 5.8: Trigger Overlap: Comparison of Z-distributions, D_2.
These plots show the the Z-distributions for all particles, the fastest, the second fastest, and the third fastest tracks; the distributions are from the Deuterium samples, with the SAT trigger on the left and the LAT trigger on the right. These data have been corrected for acceptance.

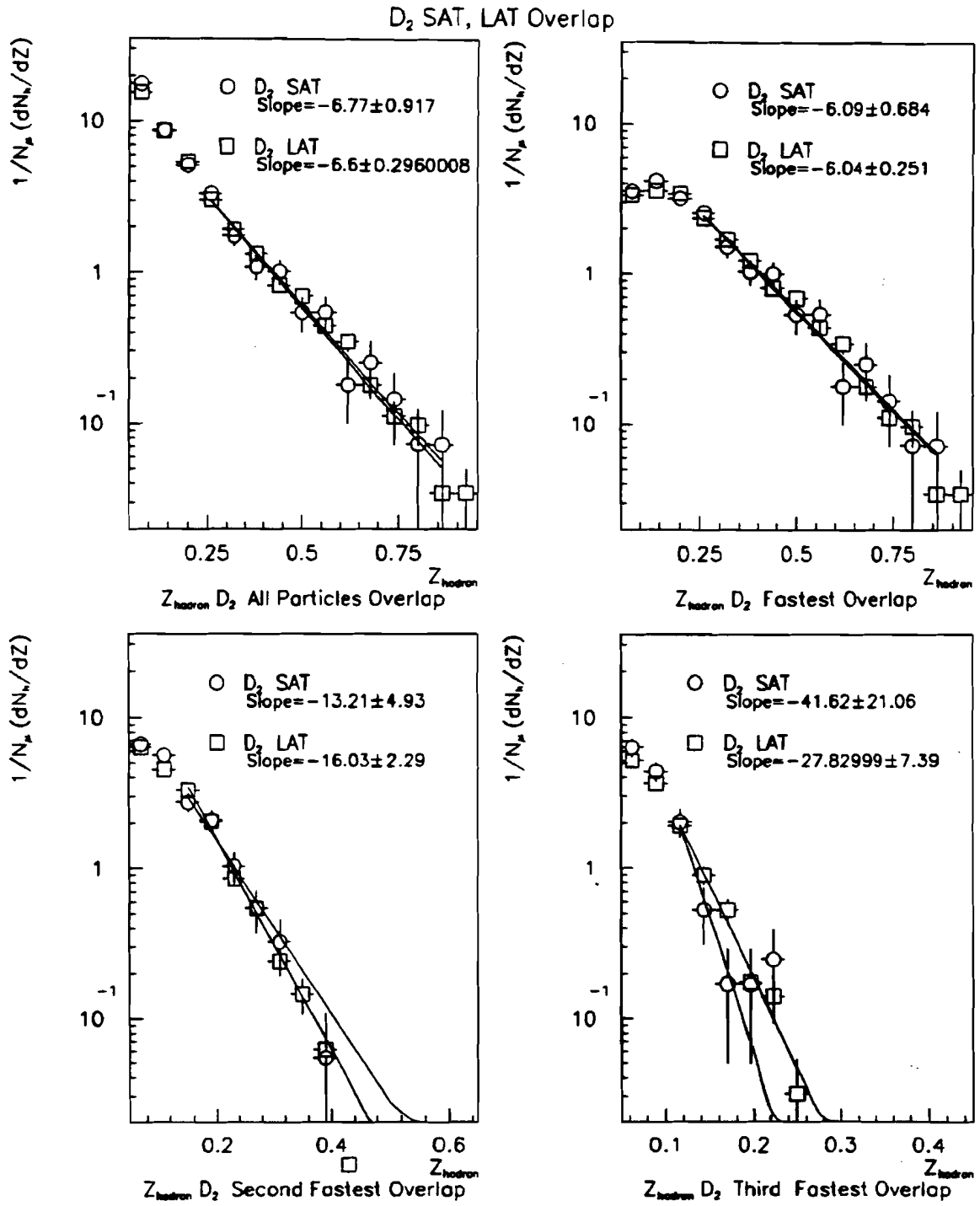

Figure 5.9: Trigger Overlap: Overlay of Z-distributions, D_2.
These plots show the overlaid distributions from the Deuterium sample, for the kinematic-overlap region of each trigger. These data have been corrected for acceptance.

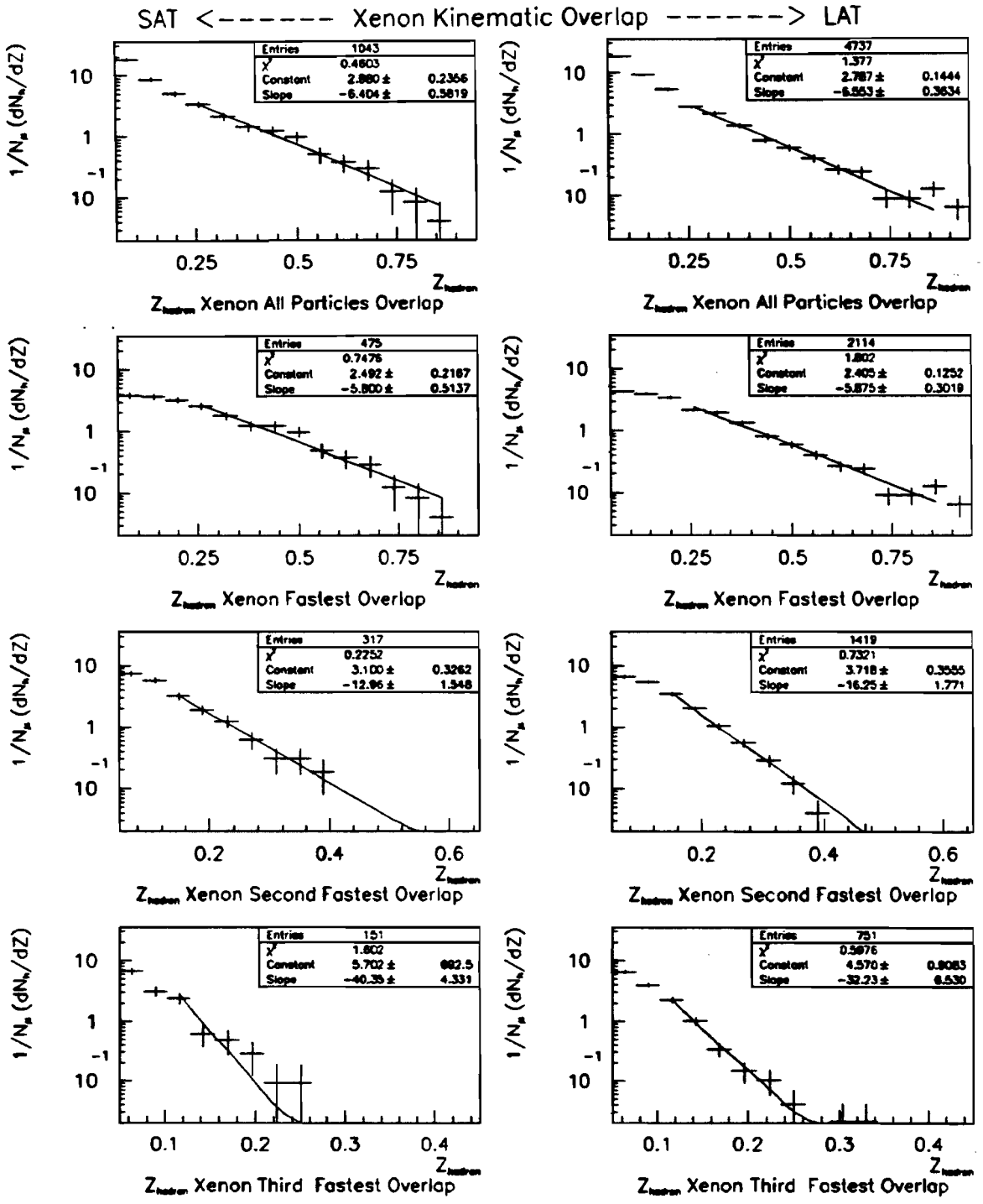

Figure 5.10: Trigger Overlap: Comparison of Z-distributions, Xenon.
These plots show the the Z-distributions for all particles, the fastest, the second fastest, and the third fastest tracks; the distributions are from the Xenon samples, with the SAT trigger on the left and the LAT trigger on the right. These data have been corrected for acceptance.

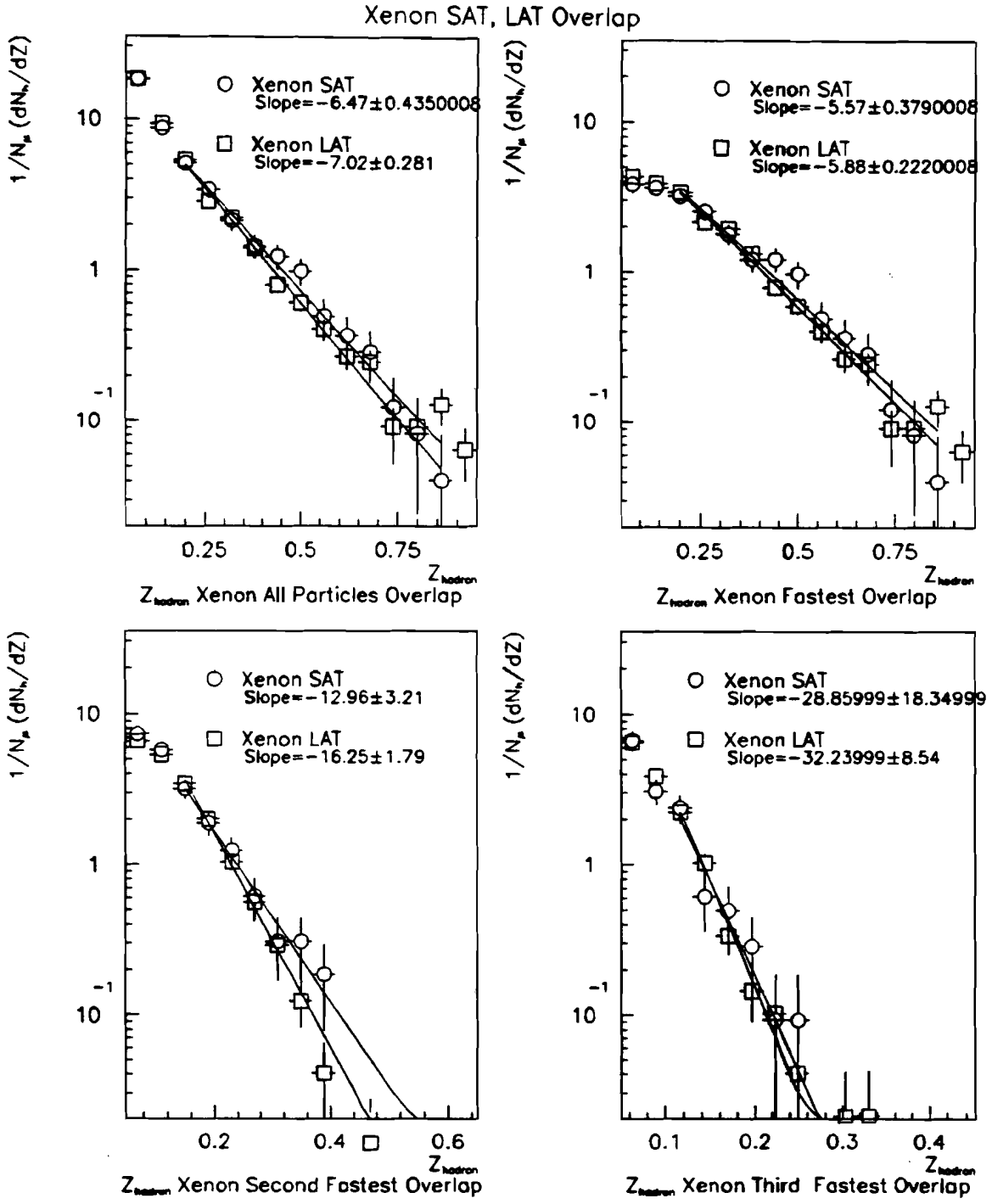

Figure 5.11: Trigger Overlap: Overlay of Z-distributions, Xenon.
These plots show the overlaid distributions from the Deuterium sample, for the kinematic-overlap region of each trigger. These data have been corrected for acceptance.

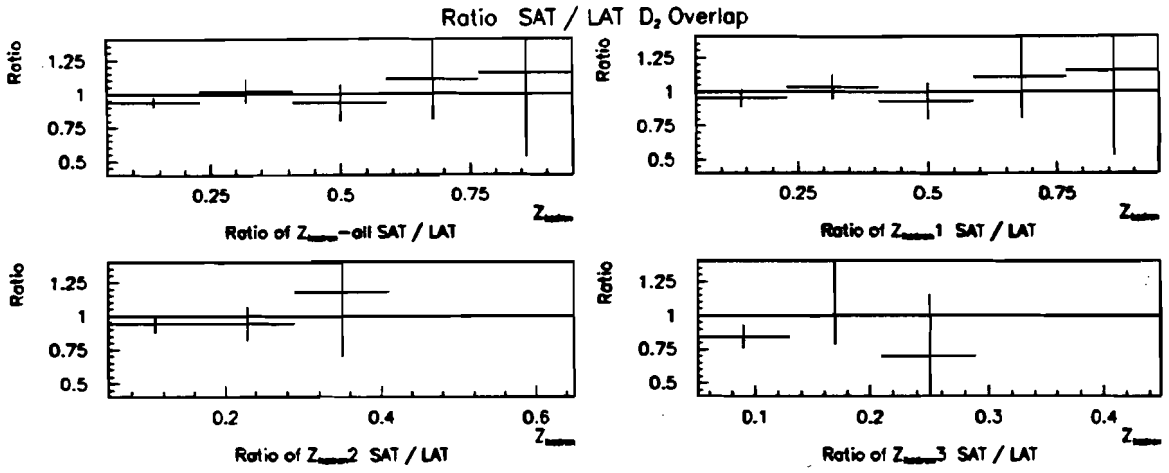

Figure 5.12: Trigger Overlap: Ratio of Z-distributions, D_2.
These plots show the ratios of the Z-distributions from the Deuterium samples: (SAT trigger) over (LAT trigger). Plots (a-d) are for all particles, the fastest, the second fastest, and the third fastest tracks, respectively. These data have been corrected for acceptance.

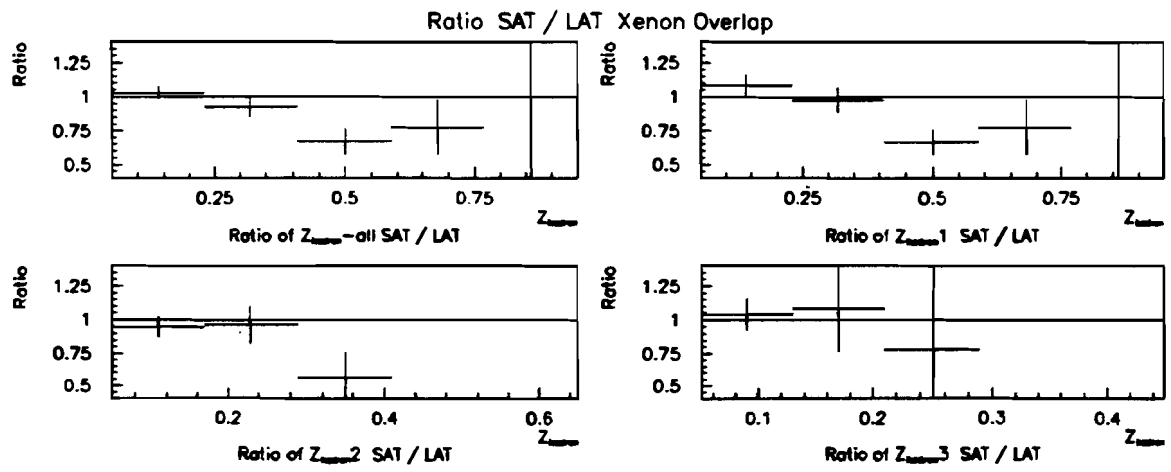

Figure 5.13: Trigger Overlap: Ratio of Z-distributions, Xenon.
These plots show the ratios of the Z-distributions from the Xenon samples: (SAT trigger) over (LAT trigger). Plots (a-d) are for all particles, the fastest, the second fastest, and the third fastest tracks, respectively. These data have been corrected for acceptance.

5.4.1 Kinematic Distributions: Kin-1 and Kin-2

The objective of the study is to determine the influence of nuclear matter on the final states of the produced hadrons. The effect of *Shadowing* has been discussed in Section 2.3, and it has been observed as a depletion of the scattering cross section in a "low" range of kinematics. The "low kinematic range" (Kin-1), the Shadowing region, was defined as:

$$X_{Bj} < 0.005 \qquad \text{and} \qquad Q^2 < 1\ \text{GeV}^2/c^2.$$

Similarly, the "high kinematic range" (Kin-2), the Non-Shadowing region, was defined as:

$$X_{Bj} > 0.03 \qquad \text{and} \qquad Q^2 > 2\ \text{GeV}^2/c^2.$$

The distributions of the kinematic variables Q^2, ν, X_{Bj}, and W'^2 are shown for Deuterium for these two kinematic regions in Figure 5.14. The distributions for these two regions for the Xenon samples are shown in Figure 5.15.

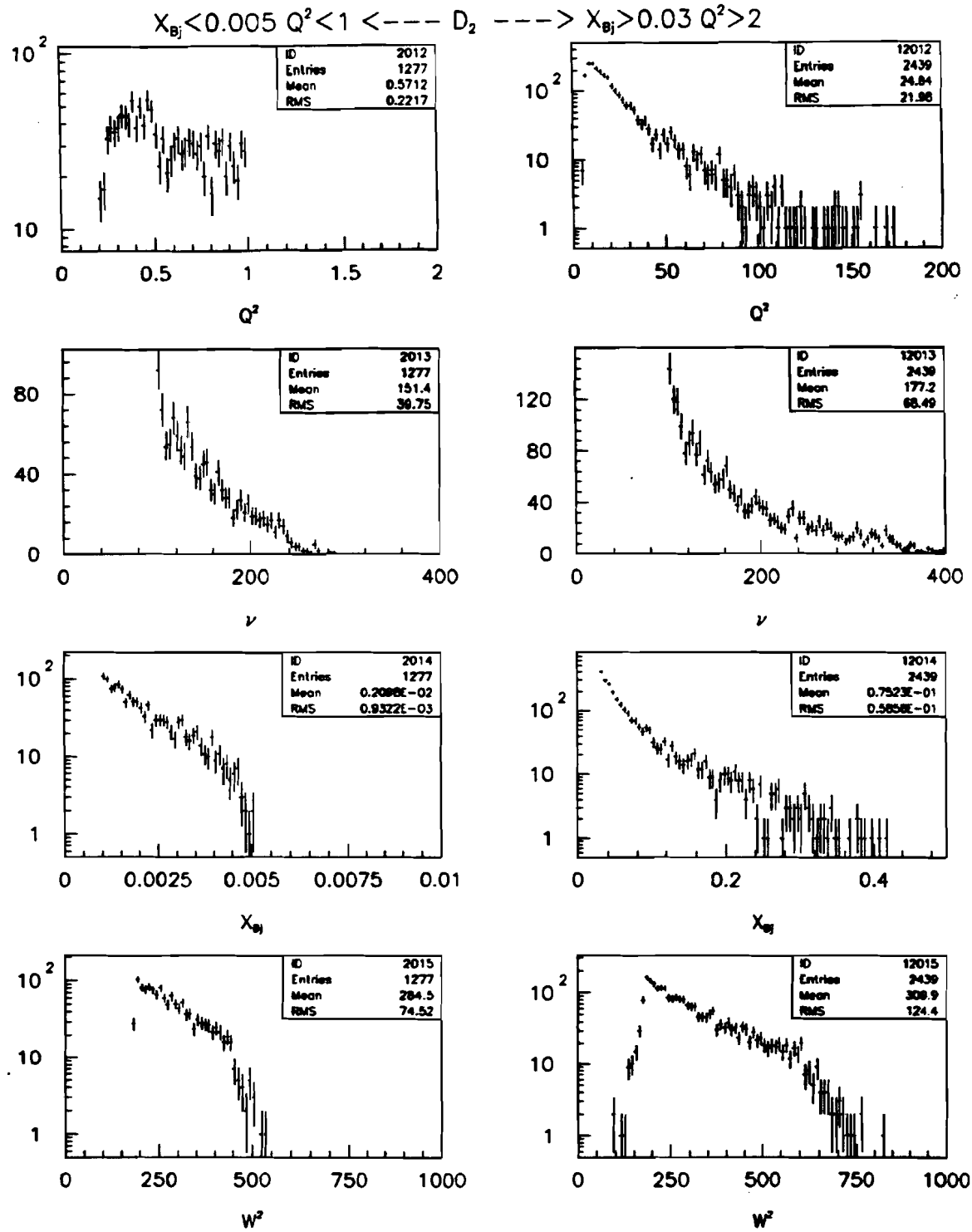

Figure 5.14: Kinematic Distributions for Kin-1 and Kin-2, D_2.
The plots on the left are from the low kinematic region, Kin-1; the plots on the right are from the high kinematic region, Kin-2. These data have not been corrected for acceptance.

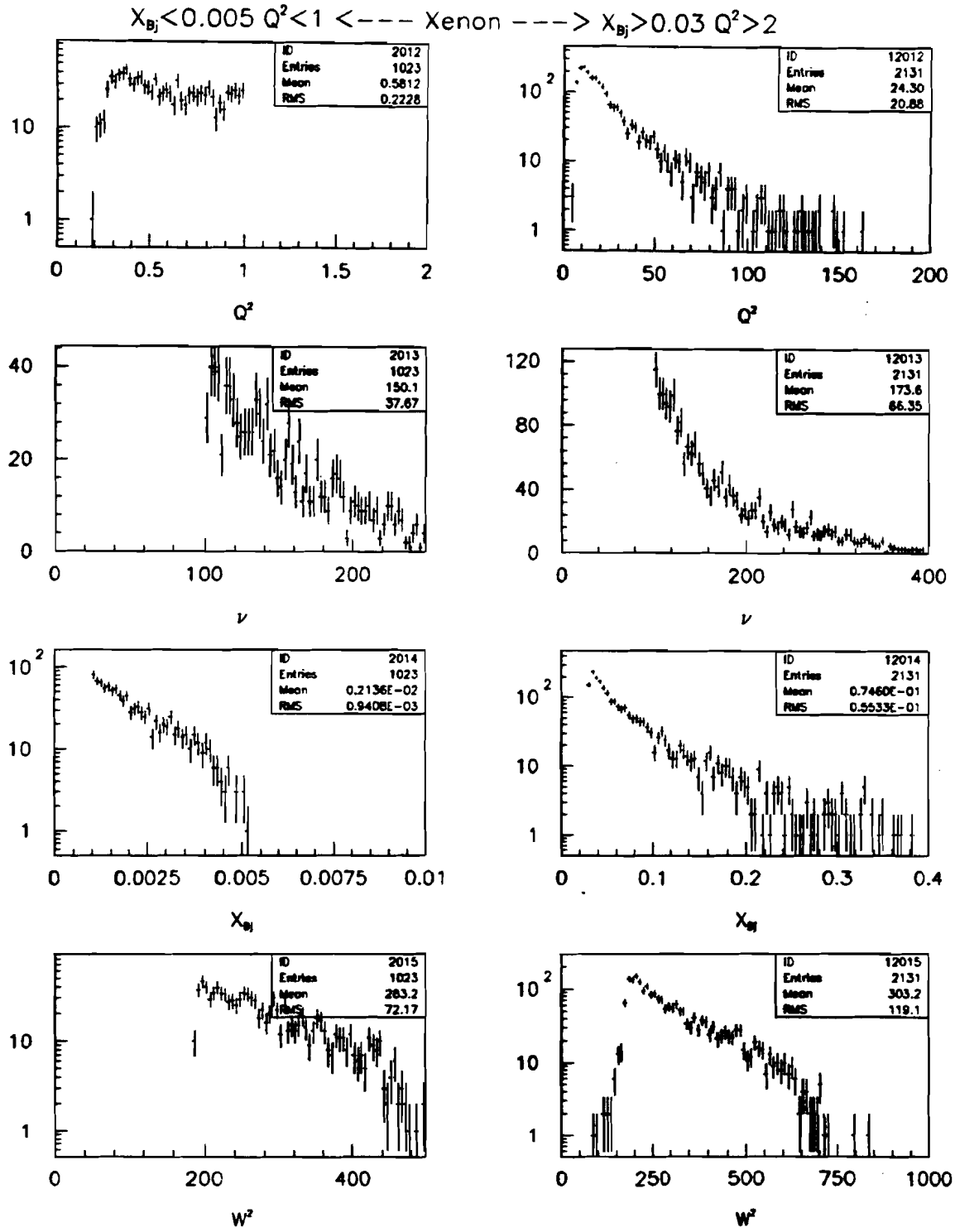

Figure 5.15: Kinematic Distributions for Kin-1 and Kin-2, Xenon.
The plots on the left are from the low kinematic region, Kin-1; the plots on the right are from the high kinematic region, Kin-2. These data have not been corrected for acceptance.

5.5 Corrections for Acceptance and Reconstruction

5.5.1 Fredholm Equation

The distributions observed in an experiment involve several processes. The one of primary interest is the physical process in question; however, the apparatus itself influences what can be observed, and the reconstruction may be limited in its performance. These latter two processes affect the final distributions seen. These effects must be removed from the distributions in order to study the physical process of interest; the distributions are said to be *corrected* for acceptance and other effects. This process can be expressed within a certain class of Integral Equations: the *Fredholm Equations.* Before attacking the problem of acceptance, I will diverge briefly to discuss the characteristics of Fredholm Equations.

A Fredholm Equation is an Integral Equation of the general form

$$\Phi(z) = \lambda \int_a^b K(z|z_0)\Phi(z_0)dz_0 + \phi(z), \tag{5.1}$$

where $\phi(z)$ is a known function; this is an *Inhomogeneous Fredholm Equation of the Second Kind.* Without the $\phi(z)$ it would be homogeneous. The essential feature of the system is that the value of a function at a given z depends on values of the function at other z's. The function $K(z|z_0)$ is called the *Kernel* and is responsible for mapping the influence of the function upon itself. A *Fredholm Equation of the First Kind* has a slightly different form:

$$\phi(z) = \int_a^b K(z|z_0)\Phi(z_0)dz_0; \tag{5.2}$$

$\phi(z)$ is a known function, and $\Phi(z_0)$ is unknown. In this system the kernel $K(z|z_0)$ maps the function $\Phi(z_0)$ onto the function $\phi(z)$. The *Volterra Equations* are special cases of Fredholm Equations in which one or both of the limits of integration are variable, as seen in the following Inhomogeneous Volterra Equation of the Second Kind:

$$\Phi(z) = \lambda \int_a^z K(z|z_0)\Phi(z_0)dz_0 + \phi(z). \tag{5.3}$$

These integral equations can be expressed in terms of operator equations in vector space. Thus, Equation 5.1 could be written as

$$\mathbf{X} = \lambda \mathbf{K} \cdot \mathbf{X} + \mathbf{g}, \tag{5.4}$$

and Equation 5.2 could be written as

$$\mathbf{x} = \mathbf{K} \cdot \mathbf{X}. \tag{5.5}$$

In the Fredholm Equation of the First Kind 5.5, the function $\mathbf{X}$ is of interest, and $\mathbf{x}$ is a known function. Clearly if the operator $\mathbf{K}$ has an inverse, then the desired function can be obtained:

$$\mathbf{X} = \mathbf{K}^{-1} \cdot \mathbf{x}. \tag{5.6}$$

The kernel has certain properties which relate to the existence of an inverse. It is *symmetric* if the operator is self-adjoint: $\mathbf{K} = \bar{\mathbf{K}}$; this corresponds to $K(z|z_0) = K(z_0|z)$. A kernel is called *definite* if for any $\mathbf{x}$:

$$(\mathbf{x}^* \cdot \mathbf{K} \cdot \mathbf{x}) > 0 \quad \text{(positive definite)}, \tag{5.7}$$

$$(\mathbf{x}^* \cdot \mathbf{K} \cdot \mathbf{x}) < 0 \quad \text{(negative definite)}. \tag{5.8}$$

In either case the corresponding integral $\int \bar{f}(z)dz \int K(z|z_0)f(z_0)dz_0$ is always real, $\mathbf{K}^{-1}$ exists and both $\mathbf{K}$ and $\mathbf{K}^{-1}$ are Hermitian.

More specifics of Fredholm Equations may be found in reference [41]. In regard to the problem of correcting for acceptance, Equation 5.5 is relevant. In this case, $\mathbf{x}$ is the distribution observed in a measurement; $\mathbf{X}$ is the distribution as generated by the physical process, and the kernel $\mathbf{K}$ modifies this distribution, forming the one observed. In order to get back to the *True* distribution $\mathbf{X}$ from the *observed* distribution $\mathbf{x}$, the kernel must be understood and its inverse found.

5.5.2 The Kernel

From the previous section it is clear that to correct the observed distributions for uninteresting effects to recover the True distributions requires an understanding of the modifying kernel $\mathbf{K}$ of the Fredholm Equation, Equation 5.5.

In principle, the kernel may be a function of several variables which are relevant to the distribution in question. Specifically, for the Z-distributions, the acceptance will be a function of the momentum of the track, the particulars of the regions of each detector through which the track passes, and perhaps the event kinematics. All of these dependences must be checked, and some basis defined for the kernel. Since inverting the kernel will be easier for fewer dependent variables, it will be worthwhile to perform a *Principal Components* analysis to determine a basis for the kernel.

5.5.3 Monte Carlo

For the purpose of understanding the effects of acceptance on a given distribution, Monte Carlo techniques can prove invaluable. What is important is that the detector system is described in sufficient detail and with sufficient accuracy, in regards to the conditions present during data taking. The characteristics of the tracks passed through these detectors must approximate reality; for example, the trajectories of charged particles traversing magnetic fields must obey Maxwell's Equations. Correspondingly, implementation of detailed descriptions of the magnetic fields is important, and describing positions of material is important to motivate multiple scattering of the tracks. In addition, noise in the chambers can effect the reconstruction, so modeling this is also important. Of course, the distributions of these particles must not be completely crazy with respect to those to be measured.

For this analysis, Monte Carlo events were generated using the LUND program, version 4.3; a description of this program can be found in references [39, 59]. As with many of these models, there are a huge number of tunable parameters to allow for close mimicry of observed data distributions. In using Monte Carlo events for the purpose of describing the effects of chamber apertures and performance on the observed distributions, these parameters are of little interest, as long as the generated distributions are reasonably similar to those observed in the data. The interested reader may find the relevant choices of parameters described in reference [4].

Specifically for this analysis, I made a fiducial cut on the Monte Carlo tracks, to use only those tracks which traversed the Forward Spectrometer. This was facilitated by requiring that the tracks reached the first plane of the PCF's; in my data analysis, I used only those tracks which made it into the CCM, the magnet in which momentum measurement was made. Thus, I have only corrected for acceptance in a region in which there were data. From the Monte Carlo, it was possible to examine the effect of the fiducial cut and, therefore, to hypothesize what tracks were not incorporated in the data analysis. In Figure 5.16 are the Monte Carlo tracks which were eliminated by the fiducial cut, plotted as a function of their energy. Of course, these are mainly low-energy tracks; the acceptance of the Forward Spectrometer was quite high above 10 GeV. The fact that the acceptance was poor below this value indicates that analyses including tracks with low energies must be taken *cum grano salis*. For the Z-distributions, since the minimum ν was set at 100 GeV, this region must lie below $Z = 0.1$. The acceptance only levels out for $Z \geq 0.2$

Using Monte Carlo is useful for determining the relevant kernel, since both the True distribution $\mathbf{X}$ and the observed distribution $\mathbf{x}$ are known. Then, for each effect

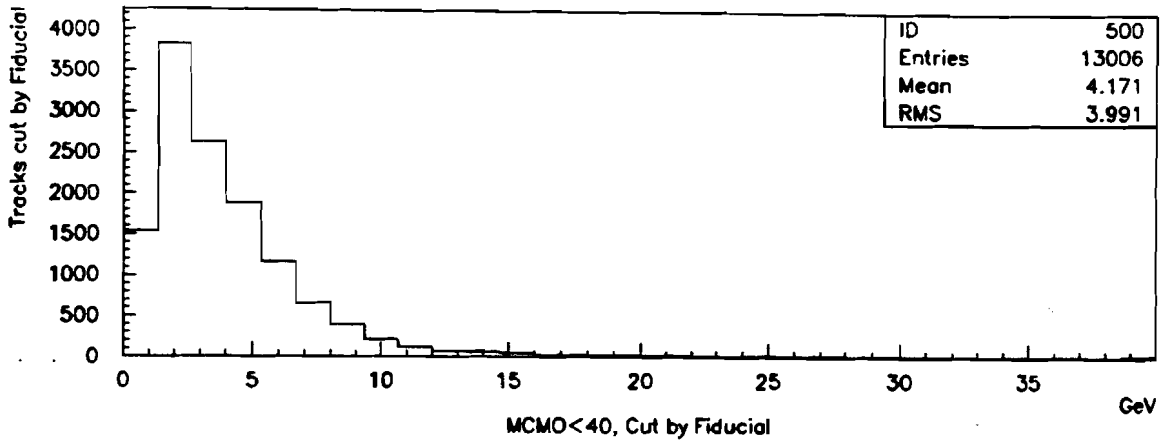

Figure 5.16: Monte Carlo Tracks eliminated by Fiducial cut.
This plot shows the Tracks eliminated by Fiducial cut, as a function of the energy of the tracks (MCMO). This was based on TRUTH Monte Carlo tracks.

a projection of the kernel onto that variable can be made:

$$K(\xi) = x(\xi)X^{-1}(\xi), \tag{5.9}$$

and the variables upon which the kernel displays major dependence can be found.

This method was applied to examine the acceptance effects on the Z-distributions. In Figure 5.17 is shown the ratio of the number of reconstructed tracks divided by the number of true tracks, as a function of the true Z-values. This was fairly flat at higher values of Z, but it displayed some loss of efficiency at low-Z. It is clear that Z was not the variable upon which the inefficiency most directly depended; low-momentum tracks were swept out of the active apertures of the chambers by the magnetic fields. At a given value of ν, a low-Z value corresponded to a low value of momentum; however, ν ranged over a quite large interval, so this smeared out the dependence of the efficiency upon Z. In Figure 5.20 is plotted the acceptance ratio as a function of the momentum of the tracks; here the dependence was much more striking and matched with intuition. In the terms of a Principal Component analysis, this variable accounted for a large part of the variance of the function, in this case acceptance. The other obvious variables upon which the acceptance might depend were the position and slope of the tracks entering the apparatus. The acceptances as functions of these variables are shown in Figure 5.18. There was little obvious dependence upon these variables, so I decided to define the basis of my kernel to involve only the one variable, the momentum of the tracks.

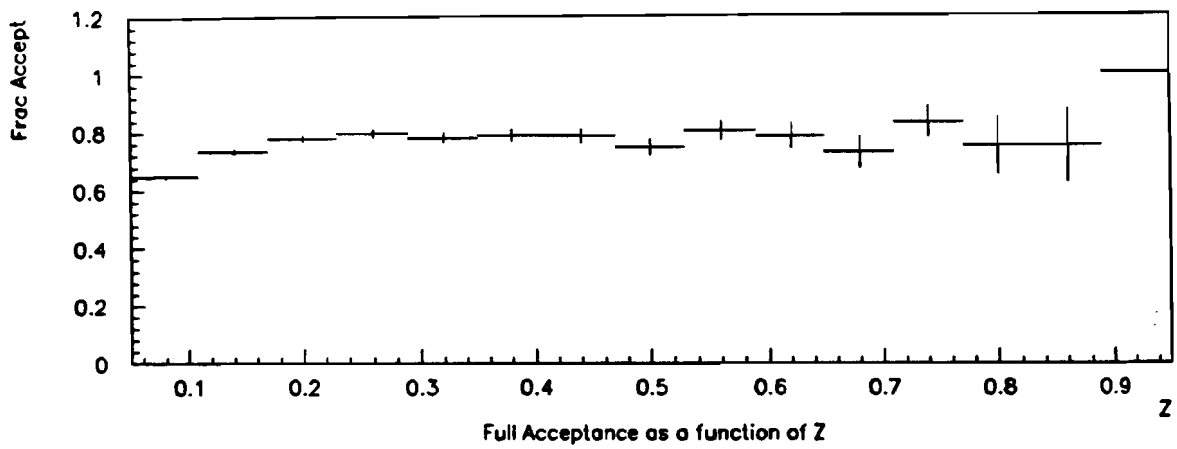

Figure 5.17: Acceptance (Z) . These plots show the ratios of the reconstructed tracks divided by the true tracks, as a function of their Z-values. This is based on Monte Carlo events, passed through reconstruction.

Then, Figure 5.20 became the definition of the kernel. One possible way to invert this function would have been simply to put the inverse of each channel contents into another histogram. However, this scheme is susceptible to statistical fluctuations from bin to bin. Smoothing a distribution for use as a kernel has been discussed in some analyses [66, 23, 6]; one technique for smoothing a distribution is to fit a parameterized curve to it. I applied that technique to the distribution in Figure 5.20; I fitted the following parameterization to this distribution, as a function of the energy of the tracks:

$$\varepsilon = P_1 - P_2 e^{-P_3 E}, \tag{5.10}$$

where E was the energy of the track and P_i were the three parameters returned from the fit. These are displayed on the plot in Figure 5.21, along with the reduced-χ^2 from the fit. The errors from the fit are much smaller at a given value of the variable than they would be from the generation itself. Choosing such a scheme alleviates the dependence on the model of the generation and reduces the number of events which must be generated to obtain sufficient statistical precision so as not to dominate the errors on the corrected distributions. For tracks with more than about 20 GeV, the correction was essentially a constant value of about 1.25 with an error of about 0.009 for a value of $Z \sim 0.5$. This was much less than the errors on the Z-distributions, so I did not propagate the error from the corrections for acceptance through to the final distributions; this source of systematic error is less than 1%.

Equation 5.10 became the definition of the kernel for the acceptance correction. Since the function was analytic, it had an inverse: $K(E|E') = 1/\varepsilon$. I applied this

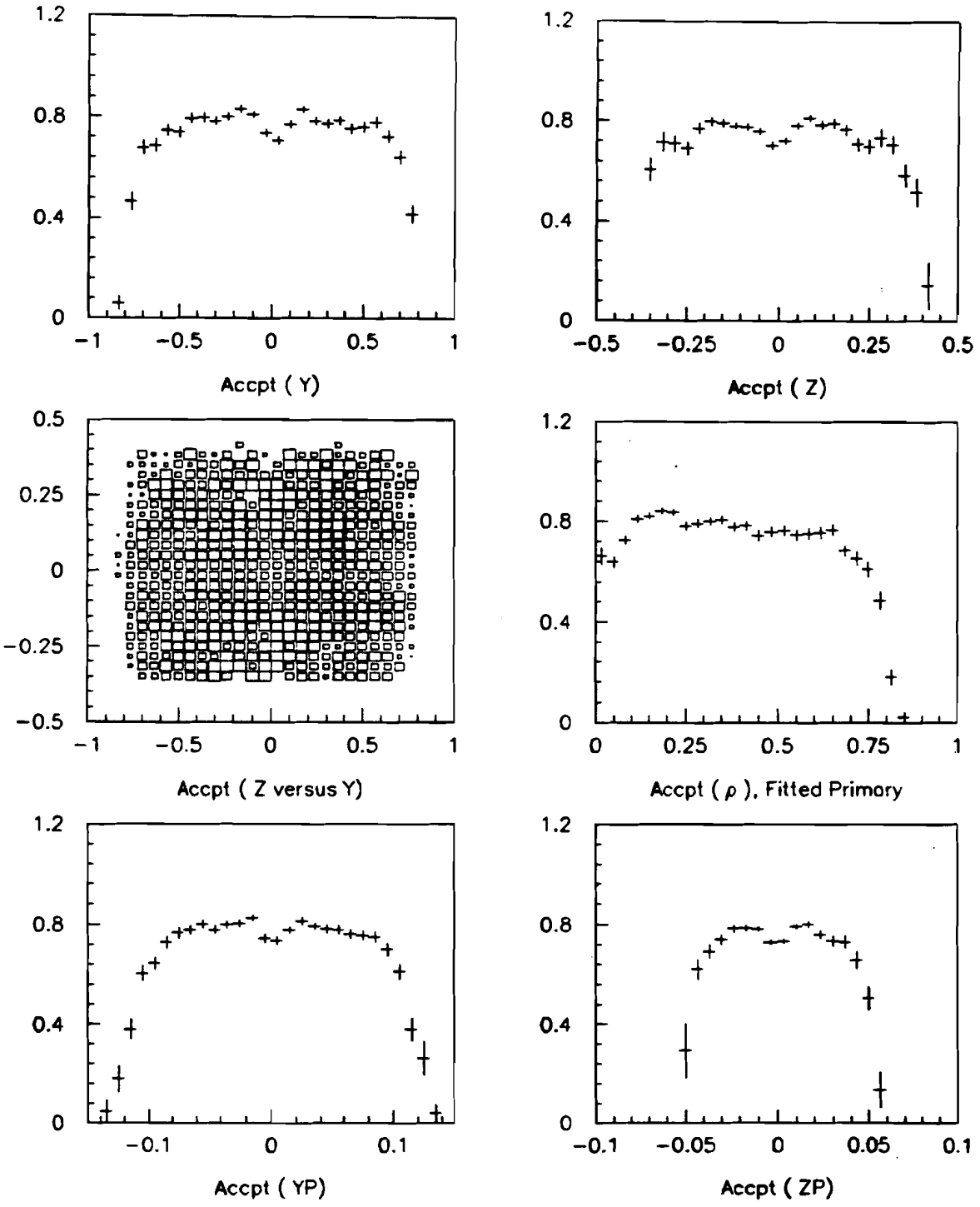

Figure 5.18: Acceptance (Position) .
These plots show the ratios of the reconstructed tracks divided by the true tracks. In (a) this efficiency is plotted as a function of the Y-position of the tracks in a plane just upstream of the magnet; in (b) as a function of Z; in (c) as a function of the (Y, Z)-position; and in (d) as a function of ρ, the radial distance from the center. In (e) and (f) are the efficiencies as functions of the Y and Z slopes of the tracks. This is based on Monte Carlo events, passed through reconstruction.

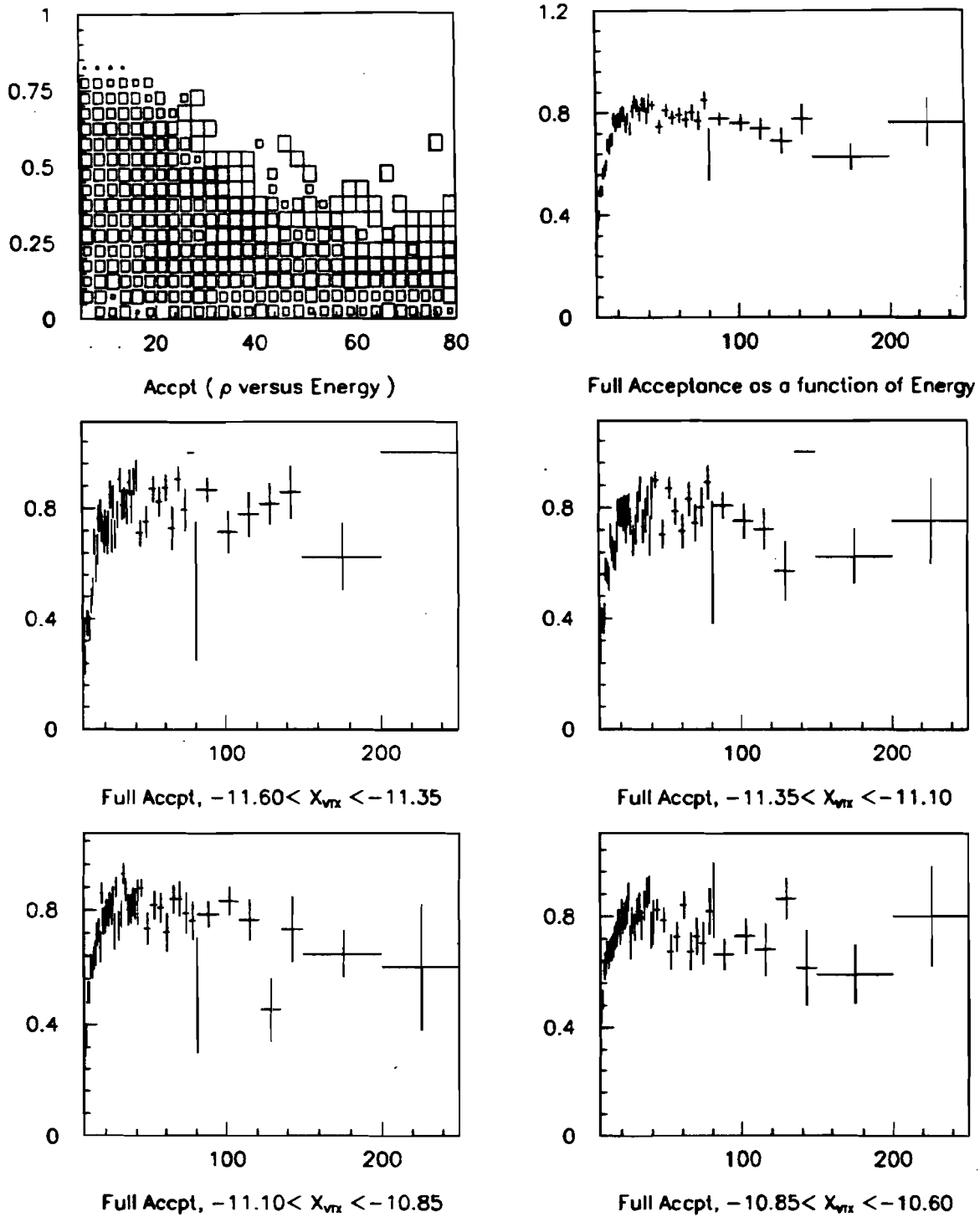

Figure 5.19: Acceptance (Position and Energy).
These plots show the ratios of the reconstructed tracks divided by the true tracks. In (a) this efficiency is plotted as a function of the radial-position of the tracks in a plane just upstream of the magnet versus the energy of the track; in (b) as a function of the Energy. In (c-f) the efficiency is plotted as a function of Energy, for four slices of the target — from most upstream to most downstream.

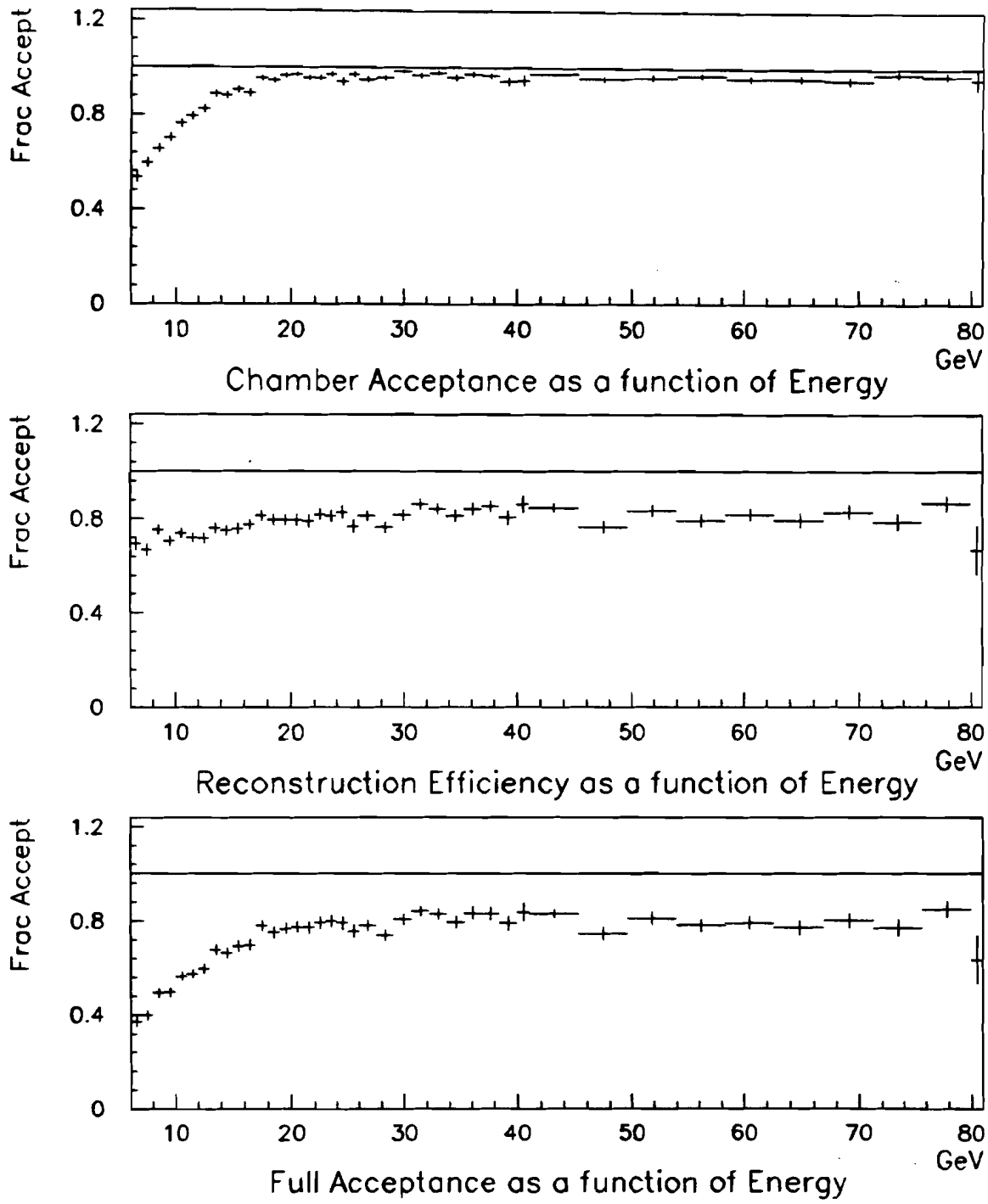

Figure 5.20: Acceptance (Energy). These plots show the ratios of the reconstructed tracks divided by the true tracks, as a function of their energy, assuming a pion mass. This is based on Monte Carlo events, passed through reconstruction.

correction on a track-by-track basis in the generation of the final Z-distributions, thus performing the integral of the Fredholm Equation 5.2. The time dependence of the chambers was taken into account in the Monte Carlo; the parameters of the kernel are shown as a function of time in Table 5.5.

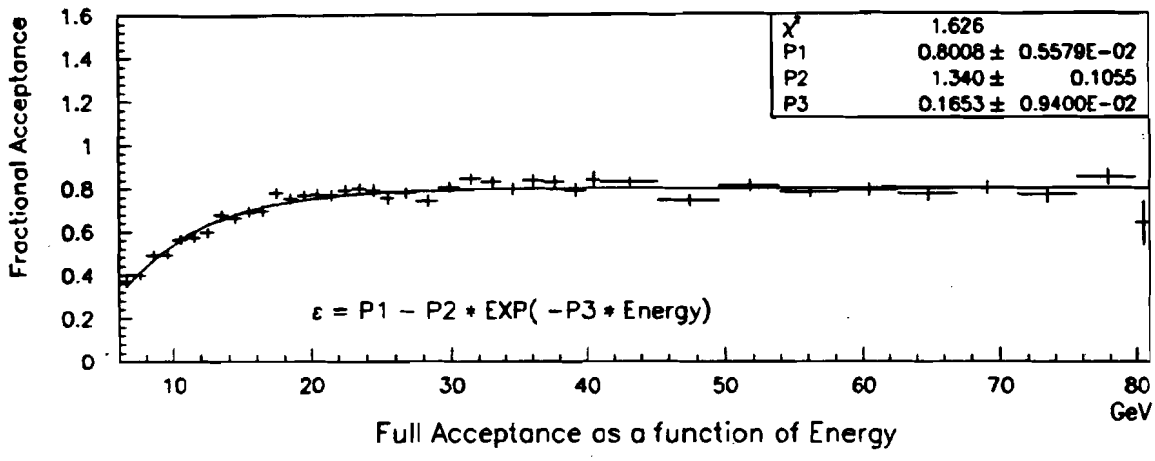

Figure 5.21: Kernel of Acceptance.
This plot shows the ratio of the reconstructed tracks divided by the true tracks, as a function of their energy; the distribution has been fitted to the functional form listed at the bottom, and the parameters from the fit are displayed, along with the reduced-χ^2.

Time Period (NRUN)	P_1	$\pm$	ΔP_1	P_2	$\pm$	ΔP_2	P_3	$\pm$	ΔP_3	χ^2_{DOF}
D_2 (0-3213)	0.8008	$\pm$	0.0055	1.339	$\pm$	0.090	0.1653	$\pm$	0.0081	1.626
D_2 (3214-3388)	0.7839	$\pm$	0.0050	1.393	$\pm$	0.100	0.1723	$\pm$	0.0086	1.623
Xe (3388-3596)	0.7489	$\pm$	0.0089	1.289	$\pm$	0.130	0.1519	$\pm$	0.0120	1.080
Xe (3597-3755)	0.7369	$\pm$	0.0087	1.339	$\pm$	0.150	0.1679	$\pm$	0.0140	1.422
Xe (3756-4168)	0.7268	$\pm$	0.0094	1.236	$\pm$	0.130	0.1499	$\pm$	0.0120	1.369
Xe (4169-4954)	0.7415	$\pm$	0.0058	1.099	$\pm$	0.067	0.1366	$\pm$	0.0073	1.096

Table 5.5: Time Dependent Acceptance

The other relevant measure of reconstruction is the fraction of fake tracks created by the software algorithms. I determined this fraction to be less than 2-4%.

Chapter 6

Z Distributions

One of the typical variables to study in hadronization is the longitudinal momentum of the produced particles. As was discussed in Section 2.2, it is convenient to scale out the dependence of the energy of the particles from the energy transferred in the event. Therefore, the Lorentz Invariant quantity, Z, is defined:

$$Z \equiv \frac{P_{Target} \cdot P_{hadron}}{P_{Target} \cdot q}, \tag{6.1}$$

where P_{Target} is the 4-momentum of the target, P_{hadron} is the 4-momentum of the hadron, and q is the 4-momentum transferred in the interaction. In the Lab frame, Z reduces to the ratio of the hadron energy over the energy transfer in the event: $Z_{hadron} = E/\nu$, where E is the hadron energy. In my analysis, I have assumed a pion mass for all particles in calculating E.

Also in this chapter much use will be made of information regarding the *ranking* of the particles in terms of their energy. This was facilitated by ranking them according to their Z-values; the leading particle had the highest-Z and was referenced as the *fastest* particle. Similarly, the next leading particle was called the ***second fastest***, and the third leading particle was called the ***third fastest***. This involved only charged particles, so there was some "spill-up" of charged particles in the ranks, as their preceding neutral sisters were missed.

The Rescaled Z-values are the energies of each particle scaled to the energy available to that particle, working down from the fastest. These are defined as the following:

$$\text{scaled}(Z_2) \equiv \frac{P_{\text{nucleon}} \cdot P_2}{P_{\text{nucleon}} \cdot (q - P_1)} \xrightarrow[\text{lab}]{} \frac{E_2}{\nu - E_1}, \qquad \text{and}$$

$$\text{scaled}(Z_3) \equiv \frac{P_{\text{nucleon}} \cdot P_3}{P_{\text{nucleon}} \cdot (q - P_1 - P_2)} \xrightarrow[\text{lab}]{} \frac{E_3}{\nu - E_1 - E_2}$$

As was mentioned in Section 2.2, the analyses of the Z-distributions involved only reconstructed charged particles, and neutral particles were not observed. By summing over the observed charged tracks, it was possible to put an upper limit on the maximum rank of a missed neutral through the quantity $Z_{lost} = (1 - Z_{sum})$, where

$$Z_{sum} \equiv \sum_{ch} Z_{ch}. \tag{6.2}$$

Therefore, if $Z_1 > Z_{lost}$ there could not be a missing neutral which should have been ranked as the fastest particle. Similarly, if $Z_2 > Z_{lost}$ there could be no missing intermediate particle between those defined as the fastest and the second fastest, and if $Z_3 > Z_{lost}$ there could be no missing intermediate particle between those defined as the second fastest and the third fastest.

6.1 Z Resolution

For examining distributions of Z it is important to understand the resolution with which the values are calculated. The fractional error on Z is determined from Equation 6.1 and can be written

$$\frac{\Delta Z}{Z} = \sqrt{\left(\frac{\Delta\nu}{\nu}\right)^2 + \left(\frac{\Delta E}{E}\right)^2}. \tag{6.3}$$

The plots in Figure 6.1(a,b,c) show this resolution as a function of Z, ν, and E, respectively, for the Deuterium sample of events. It can be seen that the resolution worsens as ν decreases; this is merely following the resolution on the measurement of ν, as can be seen in Figure 6.1d. In order to keep the resolution of the distributions of Z reasonable, I have chosen to restrict even more my sample of events with the criterion $100 < \nu < 500$. In Figure 6.2, the resolution plots of Z now have this restriction applied and are shown distinctly for three ranges of kinematics:

$$X_{Bj} < 0.005 \quad \text{and} \quad Q^2 < 1\ \text{GeV}^2/c^2 \qquad (\text{Kin} - 1),$$

$$0.01 < X_{Bj} < 0.3 \quad \text{and} \quad Q^2 > 1\ \text{GeV}^2/c^2 \qquad (\text{Overlap}),$$

$$X_{Bj} > 0.03 \quad \text{and} \quad Q^2 > 2\ \text{GeV}^2/c^2. \qquad (\text{Kin} - 2)$$

It is evident that the resolution on Z is consistent for all three ranges of kinematics.

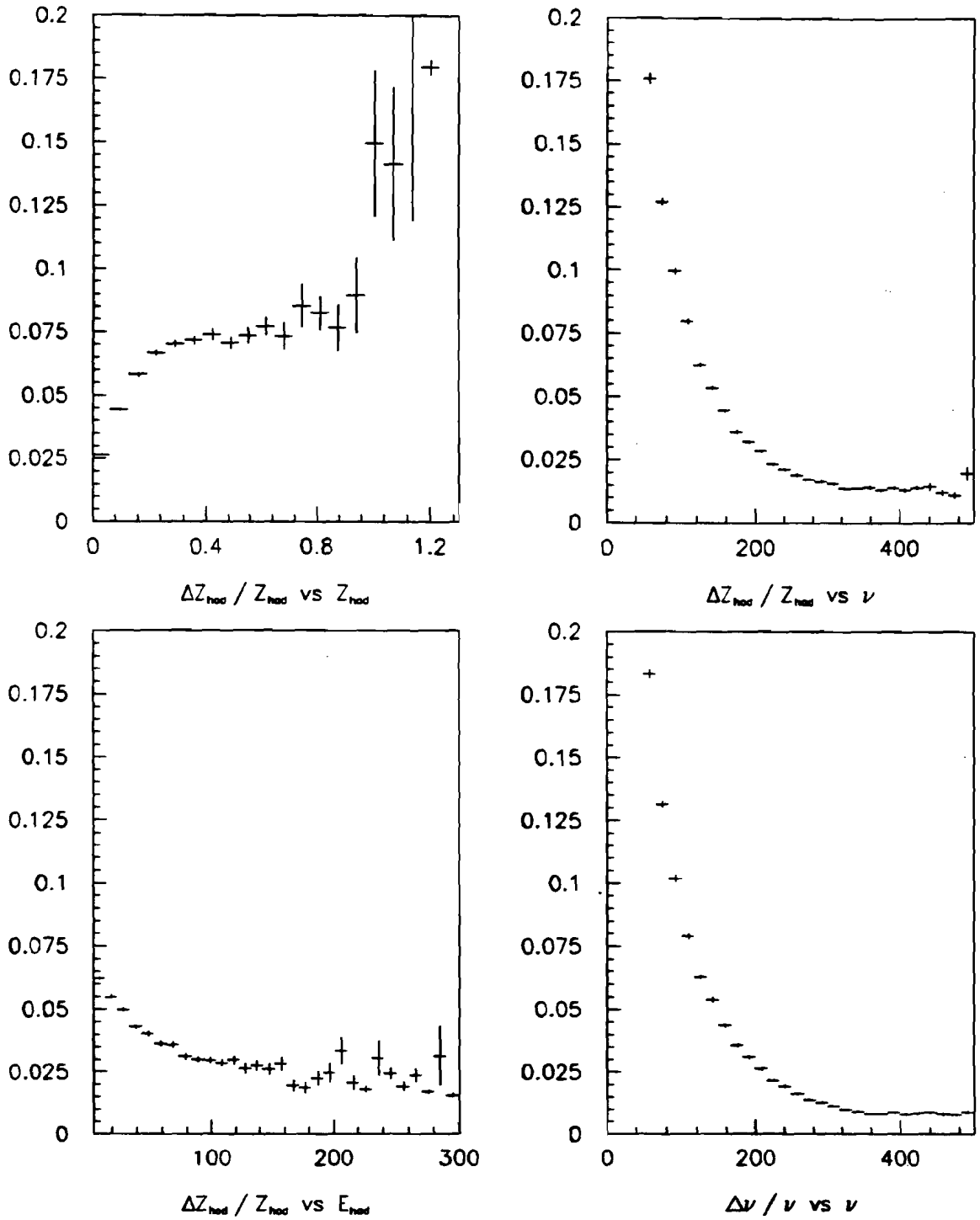

Figure 6.1: Z Resolution. These plots show the resolution on Z as a function of its dependent variables: E and ν. $\Delta Z/Z$ is plotted as a function of Z in Figure (a), of ν in (b), and of E in (c). In Figure (d) is plotted $\Delta\nu/\nu$ as a function of ν.

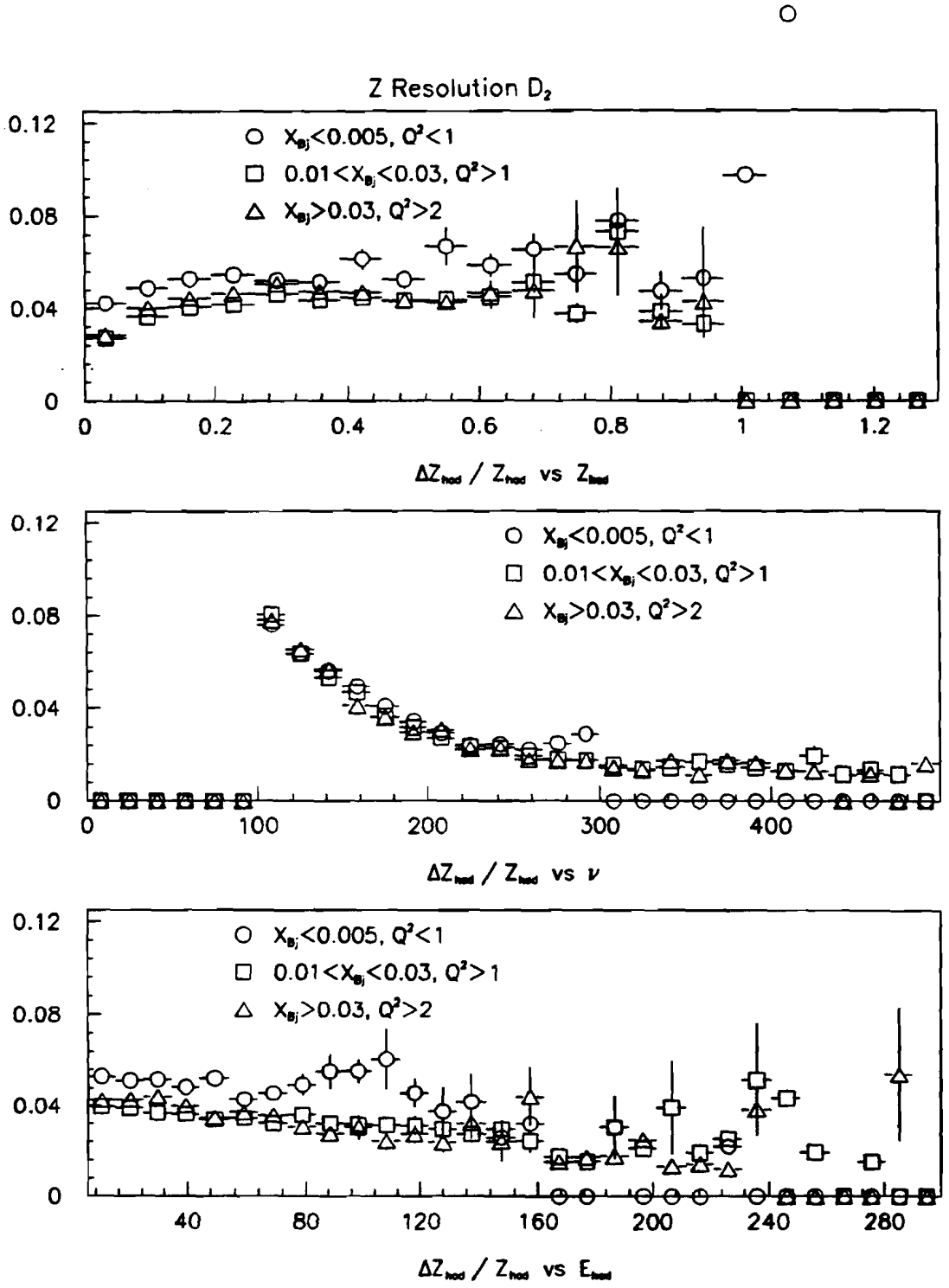

Figure 6.2: Z Resolution, $100 < \nu < 500$. These plots show the resolution on Z as a function of its dependent variables: E and ν, but with a restricted range of ν-values. $\Delta Z/Z$ is plotted as a function of Z in Figure (a), of ν in (b), and of E in (c); for each plot, three ranges of Q^2 and X_{Bj} are shown overlaid.

It is obvious from Figure 6.3 that there were tracks which were unphysical, i.e. had Z values greater than 1; there were also tracks which were second highest in energy but which had energies greater than 0.5ν. I attempted to understand the source of these tracks and to devise cuts which would reject them yet bias the remaining sample to some limited and estimable degree.

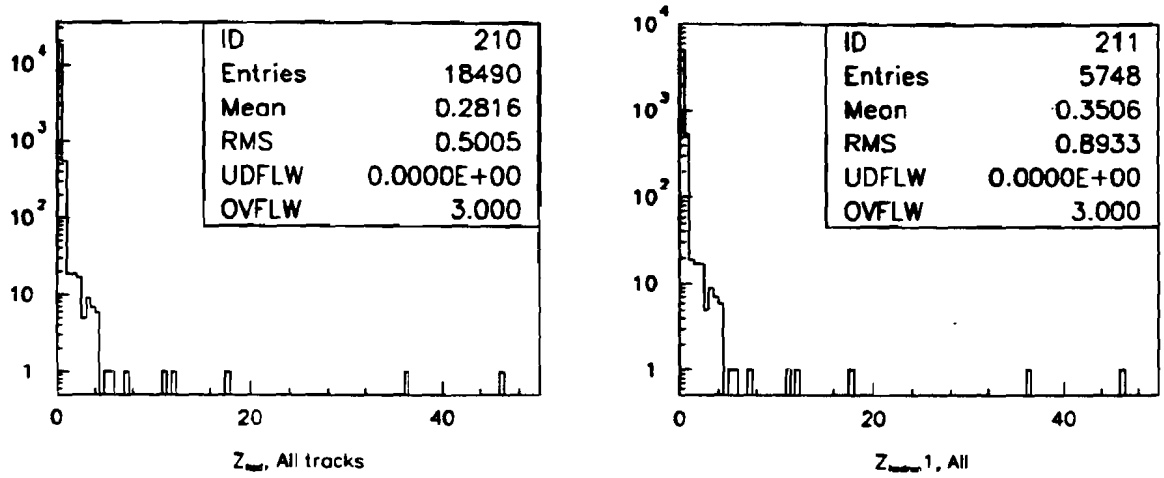

Figure 6.3: Unphysical Z-values. These plots demonstrate the existence of tracks with unphysical values of Z. Figure (a) shows the distribution of Z for all tracks, and (b) shows this for the tracks with highest Z.

With a Z-resolution of 10%, one would expect to find Z-values out to about 1.1 or so. The distributions of values of $\Delta E/E$ and $\Delta Z/Z$ for the tracks with $Z > 1$ are shown in Figures 6.4(a) and (b); it appears that the unphysical tracks may have been linked with this characteristically poor resolution. Applying a cut to tracks with poor energy resolution, $\Delta E/E > 0.1$, and restricting the energy to be physical, $E < 1.2\nu$, yields the plot in Figure 6.4(c); this shows the Z-distributions for all hadrons. In Figure 6.5 are the Z-distributions for the fastest hadron (a), the second fastest (b), and the third fastest (b); each distribution had very little leakage above its physical barrier of 1.0, 0.5, and 0.33, respectively. Examining the tracks which fail these quality cuts, I found that some of them looked like spectator muon tracks, while some of them simply had absurdly high momenta, presumably from inadequate reconstruction.

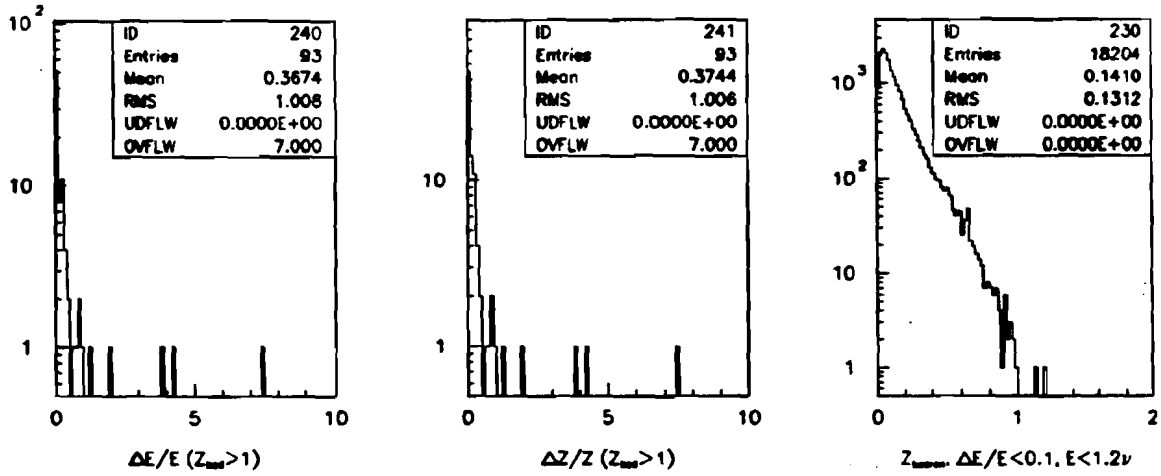

Figure 6.4: Resolution on Unphysical Tracks. These plots examines the resolution of tracks with unphysical values of Z. Figure (a) shows $\Delta E/E$ for tracks with $Z > 1$; (b) shows $\Delta Z/Z$ for tracks with $Z > 1$. Figure (c) shows the Z-distributions for all tracks restricted to have $\Delta E/E < 0.1$ and $E < 1.2\nu$.

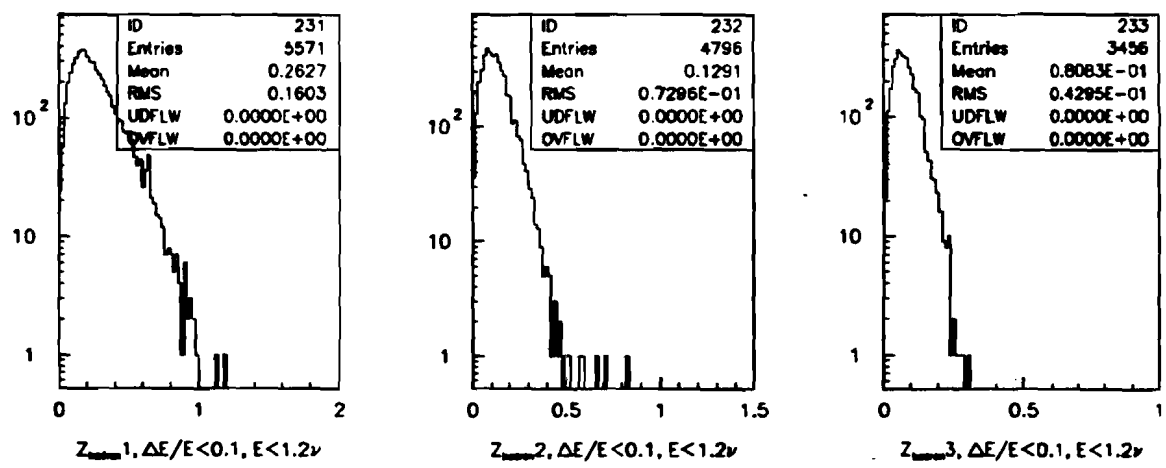

Figure 6.5: Resolution on Unphysical Tracks, (1,2,3). These plots show the Z-distributions for tracks restricted to have $\Delta E/E < 0.1$ and $E < 1.2\nu$: for the tracks with the highest Z (a), for the tracks with the second highest Z (b), and for the tracks with the third highest Z (c).

6.2 World ZZZ

In Figure 6.6 are plotted the Z-distributions from the Deuterium sample of E665, the EMC data, and the CHIO data [18] from several kinematic regions. The E665 data are tabulated in Table 6.1.

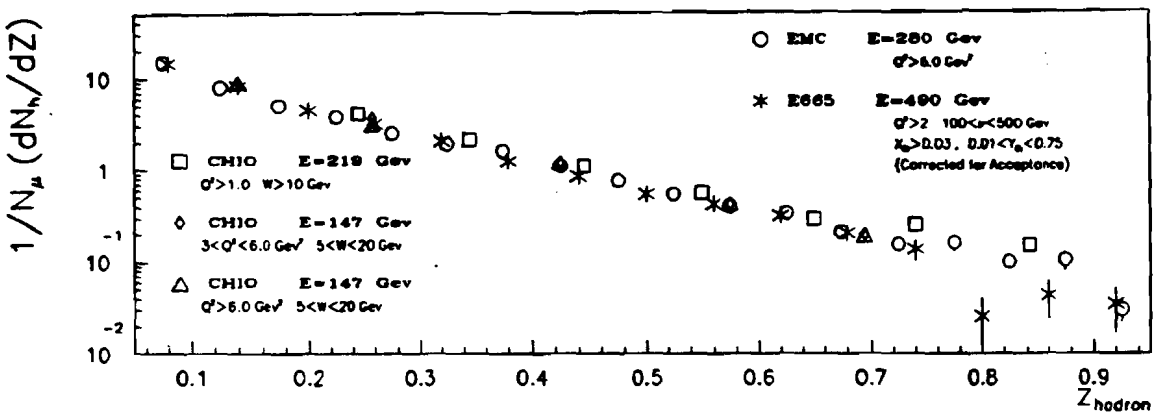

Figure 6.6: World Z-distributions.
These plots show the Z-distributions from E665 and from EMC, CHIO [18].

6.2.1 Steepening with Rank

In Figure 6.7 are plotted the Z-distributions from the Deuterium sample of E665, for the first three leading particles. It is clear that the distributions steepen with increasing rank. The indicated slope values correspond to an exponential fit; the individual plots with the fit will be found in Figures 6.8(d), (f), and (h).

The steepening of the distributions with increasing rank was to be expected, given the known distribution of multiplicity. Let the Z-distributions of the first three leading particles be represented by the functions $h_1(Z), h_2(Z)$, and $h_3(Z)$, which are defined on the intervals $(0,1),(0,1/2)$, and $(0,1/3)$, respectively. Then, the mean numbers of particles produced with these respective ranks are given by the three expressions:

$$\langle n_1 \rangle = \int_0^1 h_1(Z)dZ \tag{6.4}$$

Z	$D(Z)$	σ_D
0.08000	14.63211	0.41095
0.14000	8.38129	0.27832
0.20000	4.50018	0.19894
0.26000	3.17062	0.16597
0.32000	2.05144	0.13326
0.38000	1.24229	0.10353
0.44000	0.85509	0.08595
0.50000	0.54350	0.06848
0.56000	0.42329	0.06047
0.62000	0.31996	0.05260
0.68000	0.20719	0.04229
0.74000	0.13782	0.03446
0.80000	0.02560	0.01478
0.86000	0.04322	0.01933
0.92000	0.03450	0.01725

Table 6.1: E665 ZZZ.

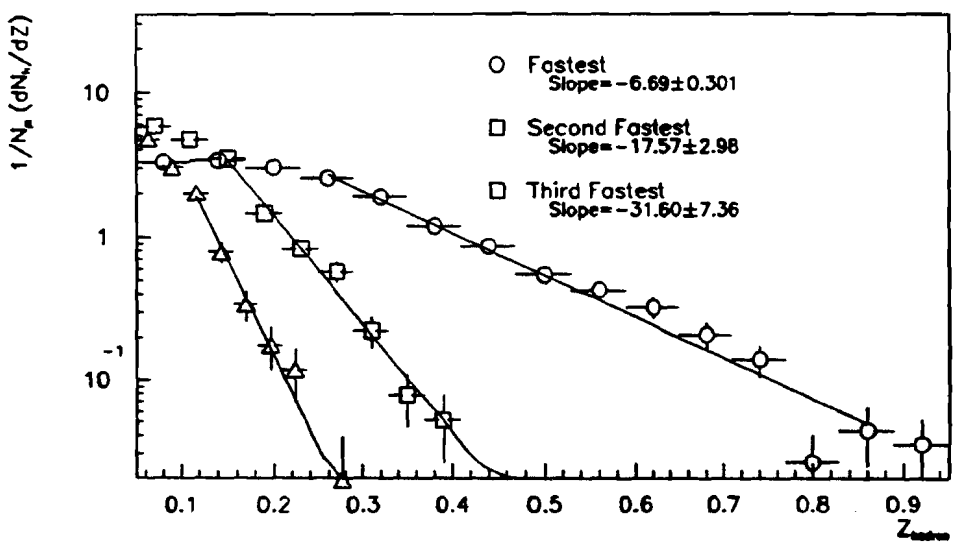

Figure 6.7: Ranked Z-distributions.
This plot shows the Z-distributions from the fastest particles, the second fastest, and the third fastest.

$$\langle n_2 \rangle = \int_0^{1/2} h_2(Z) dZ \tag{6.5}$$

$$\langle n_3 \rangle = \int_0^{1/3} h_3(Z) dZ. \tag{6.6}$$

If the distribution of the second-ranked particles were to have the same shape as that of the first-ranked particles, then the functional representations should differ only by a scale factor a_0, and the value of each of the functions at its upper limit should be equal:

$$h_2(Z) = a_0\, h_1(Z), \qquad h_2(Z \to 1/2) = h_1(Z \to 1).$$

This requires the scale factor to take the value:

$$a_0 = \frac{h_1(Z \to 1)}{h_1(Z \to 1/2)}. \tag{6.7}$$

Then, the expression for the mean production of rank-2 particles can be written in terms of that for the rank-1 particles:

$$\langle n_2 \rangle = \int_0^{1/2} h_2(Z) dZ \tag{6.8}$$

$$= a_0 \int_0^{1/2} h_1(Z) dZ \tag{6.9}$$

$$= a_0 \langle n_1 \rangle - a_0 \int_{1/2}^{1} h_1(Z) dZ \tag{6.10}$$

$$< a_0 \langle n_1 \rangle. \tag{6.11}$$

Now, for the specific case of the generic Z-distribution, the function is of the form e^{-bZ}, with $b \sim 6$. Then the scale factor between the distributions of the rank-2 and rank-1 particles should be $a_0 = e^{-b/2} \sim (1/20)$, and the production of rank-2 particles relative to rank-1 particles would be suppressed by a factor of (1/20). Similarly, rank-3 particles would be suppressed by a factor of about (1/55) with respect to the rank-1 particles. Clearly, examination of the multiplicity distributions (Figure 5.6(b)) indicates that there are many more rank-2 particles than indicated by this analysis assuming similarly shaped distributions. Therefore, since the upper limit of the distributions are fixed, the slope must steepen to increase the mean production of rank-2 particles (to increase the area under the curve).

6.3 Xenon versus Deuterium

The objective of this study was to determine the influence of nuclear matter on the final states of the produced hadrons. The effect of *Shadowing* has been discussed in Section 2.3, and it has been observed as a depletion of the scattering cross section in a "low" range of kinematics. I have defined this "low kinematic range" as the Shadowing region:

$$X_{Bj} < 0.005 \qquad \text{and} \qquad Q^2 < 1\ \mathrm{GeV}^2/c^2. \tag{6.12}$$

I have also defined a "high kinematic range" as the Non-Shadowing region:

$$X_{Bj} > 0.03 \qquad \text{and} \qquad Q^2 > 2\ \mathrm{GeV}^2/c^2. \tag{6.13}$$

The effect of Shadowing indicates a strong dependence of the scattering cross section on the number of nucleons in the target; this was illustrated in Figure 2.3. Perhaps this strong nuclear dependence will also appear in the distributions of produced hadrons from this kinematic region. This analysis will search for evidence of any difference of the Z-distributions between Xenon and Deuterium, and compare the distributions between the two kinematic regions, low and high.

The plots include the Z-distributions for the three fastest as well as all particles for these two disparate kinematic regions. In Figure 6.8 these Z-distributions for Deuterium are displayed with the "low-kinematic" region (Kin1) on the left and the "high-kinematic" region (Kin2) on the right. The slopes of the distributions for the 3 leading hadrons steepen as the rank decreases. The ratios, shown in Figure 6.10(a-d), indicate that these distributions from the two kinematic regions are consistent.

Figure 6.9 shows the four Z-distributions for Xenon, with the low kinematic region on the left and the high kinematic region on the right. From Figure 6.11, which shows the ratios of the ranked distributions, it is evident that these Z-distributions are consistent from the two kinematic regions in Xenon, as well.

I have plotted the ratios of the Z-distributions for Xenon over Deuterium. The ratios for the low-kinematic region are shown in Figure 6.12: (a) for all particles, (b) for the fastest particles, (c) for the second fastest, and (d) for the third fastest. These ratios are all consistent with unity. The ratios of the distributions for the high kinematic range are shown in Figure 6.13. These ratios also are all consistent with unity.

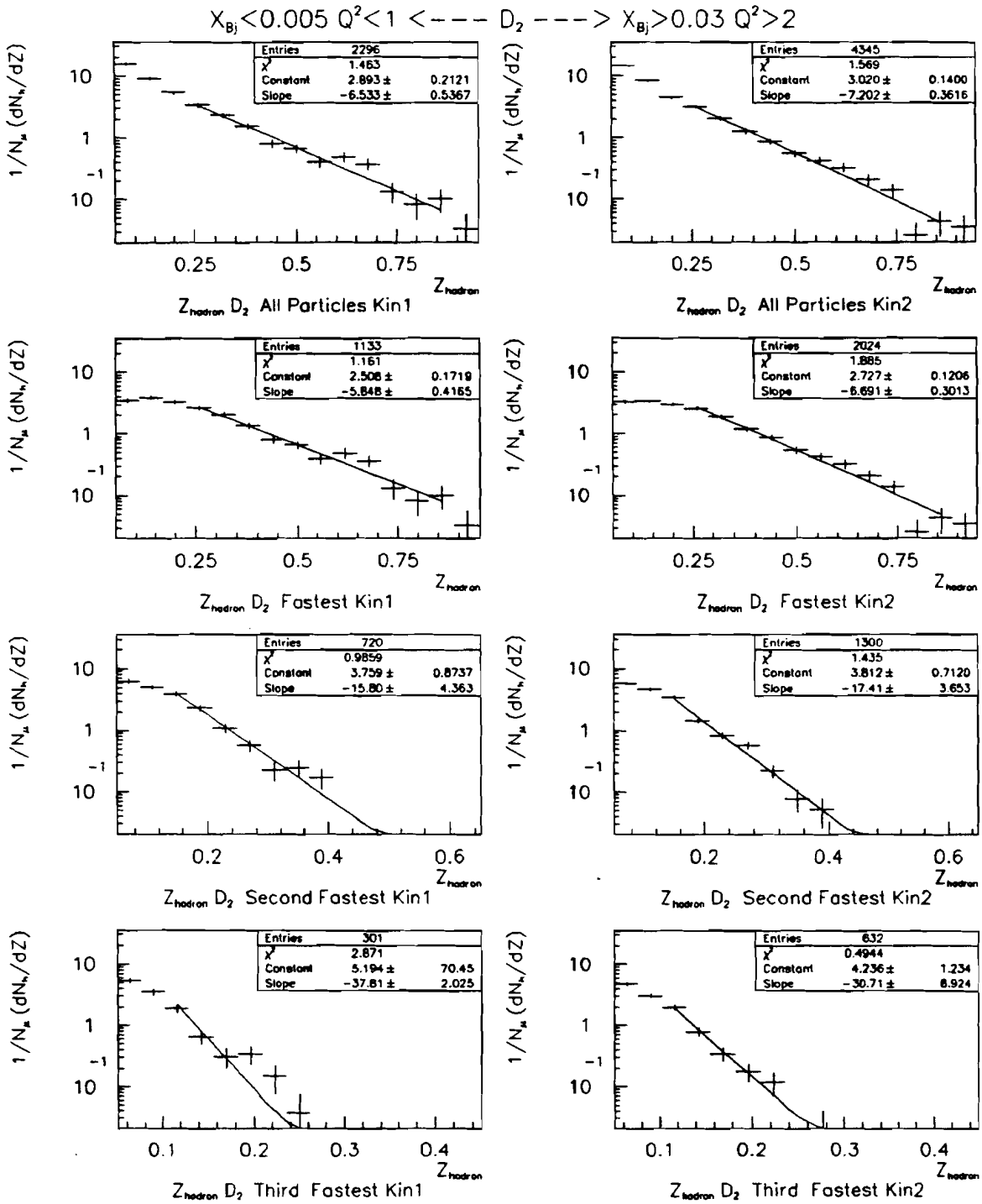

Figure 6.8: Z-Distributions, D_2: low and high kinematics.
These plots show the Z-distributions for the Deuterium sample; on the left (a,c,e,g) is shown the low kinematic region ($X_{Bj} < 0.005$, and $Q^2 < 1$), and on the right (b,d,f,h) is shown the high kinematic region ($X_{Bj} > 0.03$, and $Q^2 > 2$). The distributions include all tracks in (a) and (b), Z_1 in (c) and (d), Z_2 in (e) and (f), and Z_3 in (g) and (h).

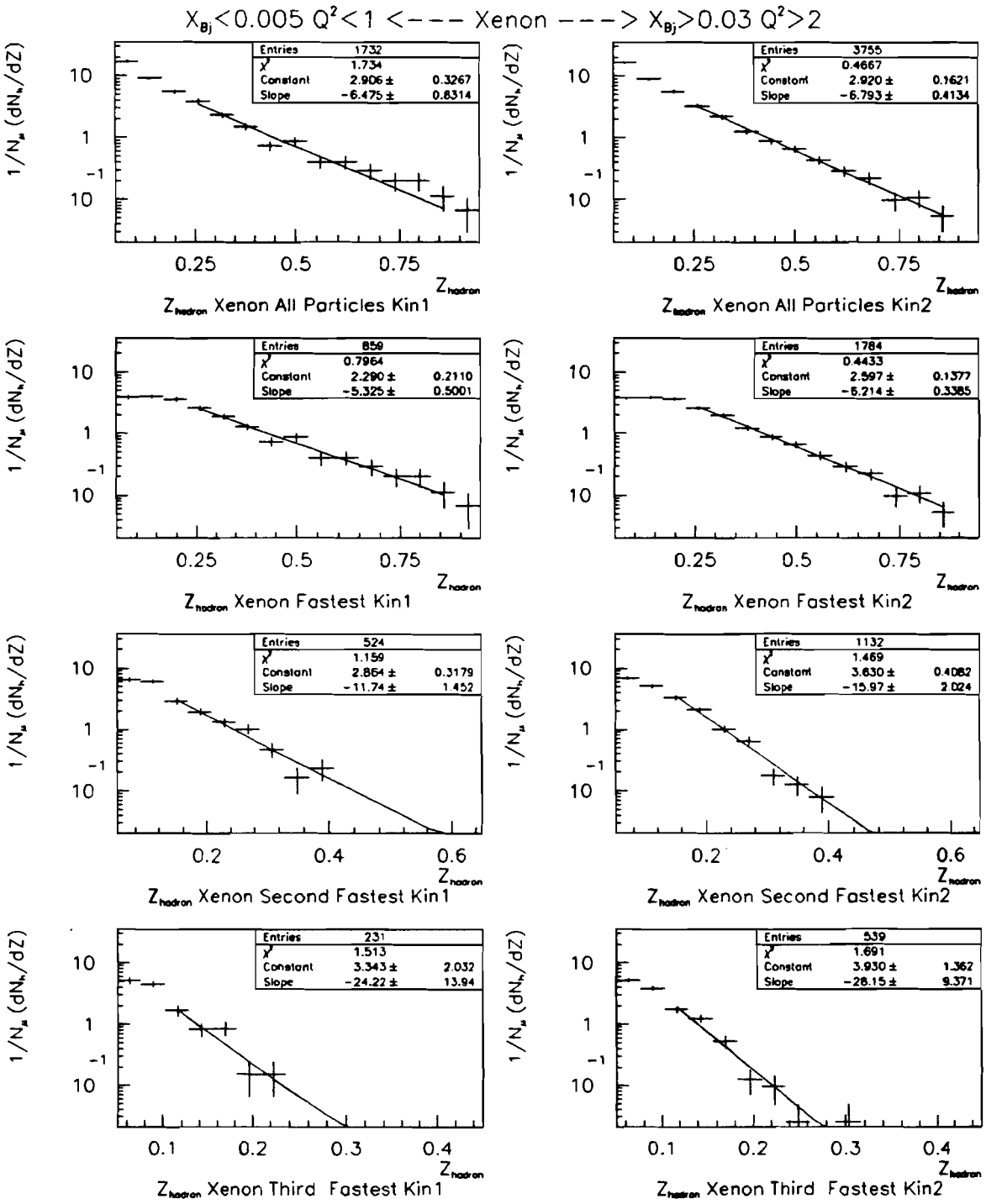

Figure 6.9: Z-Distributions, Xe: low and high kinematics.
These plots show the Z-distributions for the Xenon sample; on the left (a,c,e,g) is shown the low kinematic region ($X_{\rm Bj} < 0.005$, and $Q^2 < 1$), and on the right (b,d,f,h) is shown the high kinematic region ($X_{\rm Bj} > 0.03$, and $Q^2 > 2$). The distributions include all tracks in (a) and (b), Z_1 in (c) and (d), Z_2 in (e) and (f), and Z_3 in (g) and (h).

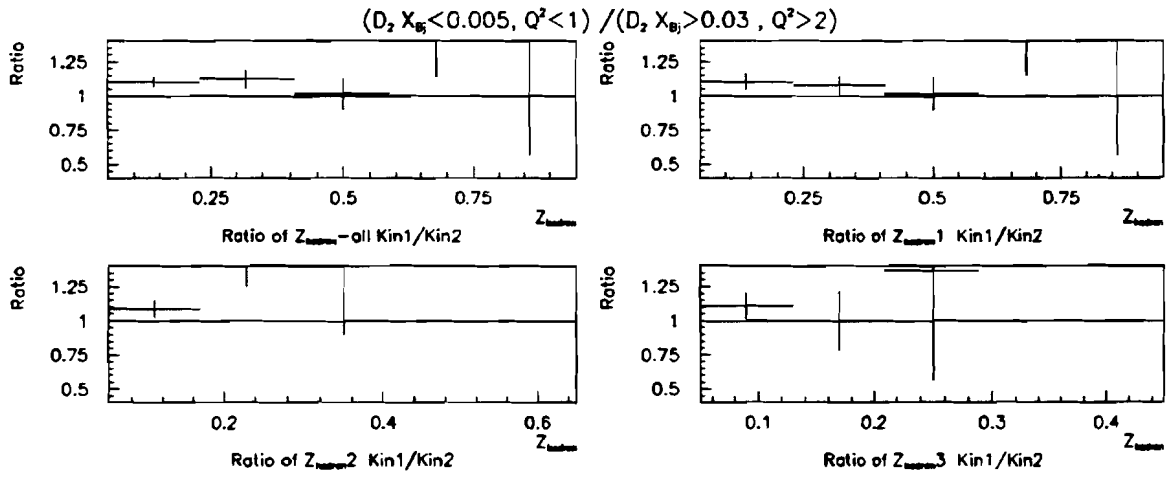

Figure 6.10: Z-Distributions, D_2: Ratio of low and high kinematics.
These plots show the ratios of the Z-distributions for the low and high kinematic regions of the Deuterium sample. $[(X_{\rm Bj} < 0.005$, and $Q^2 < 1)$ and $(X_{\rm Bj} > 0.03$, and $Q^2 > 2)]$. The ratio in (a) is of all tracks, in (b) Z_1, in (c) Z_2, and in (d) Z_3.

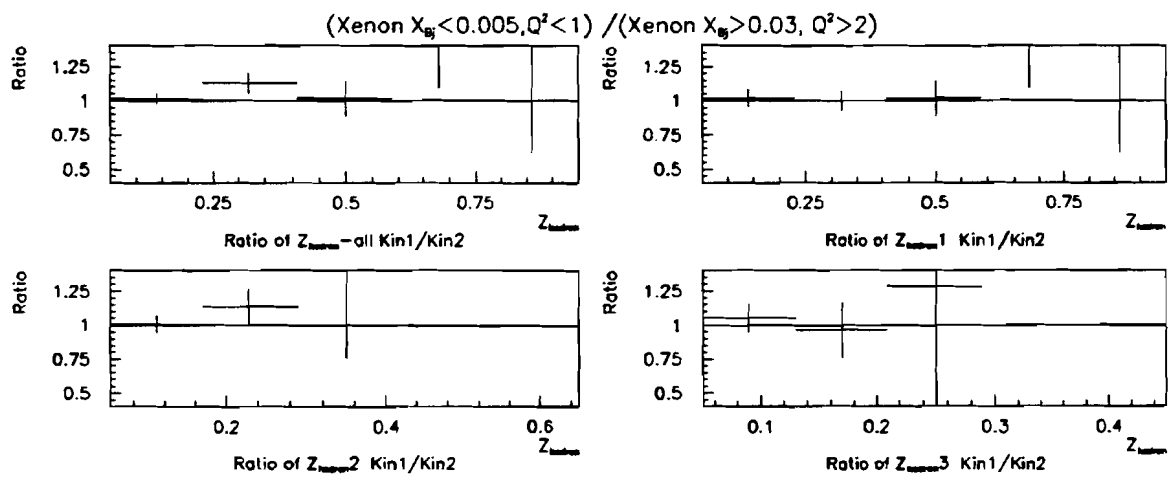

Figure 6.11: . Z-Distributions, Xe: Ratio of low and high kinematics. These plots show the ratios of the Z-distributions for the low and high kinematic regions of the Xenon sample. $[(X_{\rm Bj} < 0.005$, and $Q^2 < 1)$ and $(X_{\rm Bj} > 0.03$, and $Q^2 > 2)]$. The ratio in (a) is of all tracks, in (b) Z_1, in (c) Z_2, and in (d) Z_3.

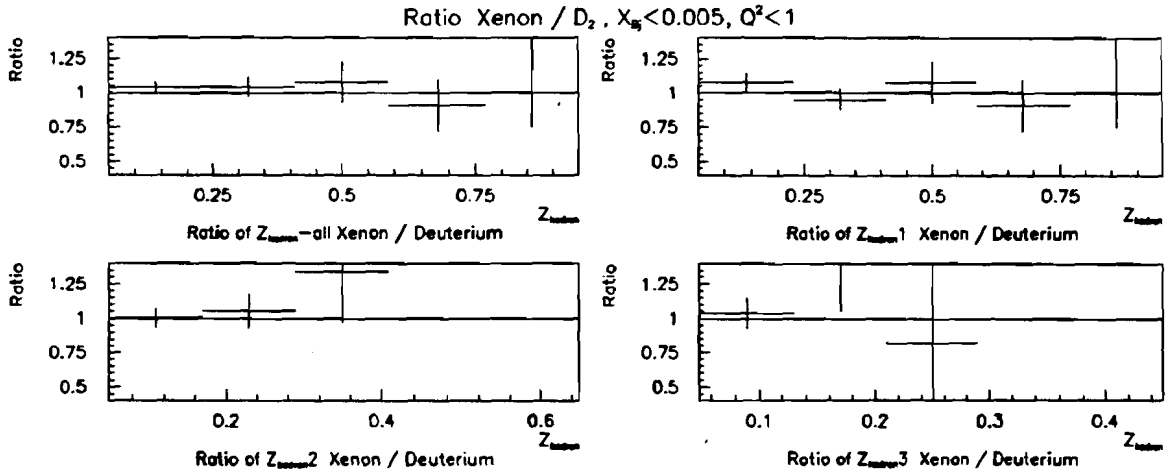

Figure 6.12: Z-Distributions: Ratio of Xe/D_2, low kinematics.
These plots show the ratios of the Z-distributions of Xenon over Deuterium for the low kinematic region: ($X_{Bj} < 0.005$, and $Q^2 < 1$). The ratio in (a) is of all tracks, in (b) Z_1, in (c) Z_2, and in (d) Z_3.

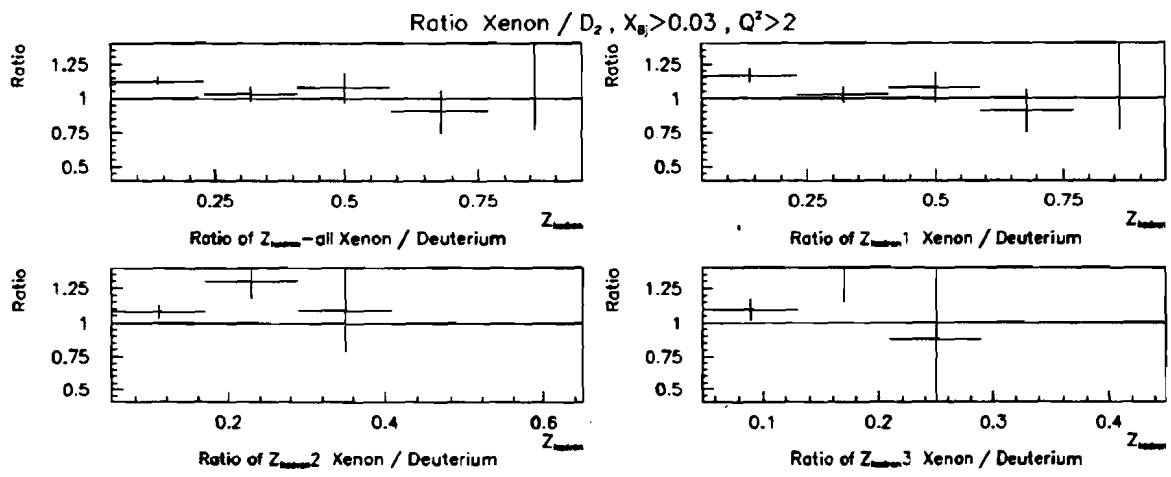

Figure 6.13: Z-Distributions: Ratio of Xe/D_2, high kinematics.
These plots show the ratios of the Z-distributions of Xenon over Deuterium for the high kinematic region: ($X_{Bj} > 0.03$, and $Q^2 > 2$). The ratio in (a) is of all tracks, in (b) Z_1, in (c) Z_2, and in (d) Z_3.

6.3.1 Rescattering of the Excited State

As discussed in Section 2.4, the rescattering of the excited state in the rest of the nucleus should modify the distribution of the final state hadrons. This should appear as a steepening of the Z-distributions in Xenon relative to Deuterium. This should occur in the Shadowing region (Kin-1), if the initial interaction were hadron-like. Since no such steepening of the Xenon distributions is apparent in either kinematic region, the level of rescattering of the excited state must be small. In order to quantify the limit of rescattering, I have examined the level at which the data can resolve a postulated effect.

Suppose that the excited state were like a hadron, similar to the picture of Vector Dominance. The initial interaction occurred at the surface of the nucleus, and this hadron-like state had to propagate through the rest of the nuclear volume. For a typical hadron (the ubiquitous pion) the inelastic cross section is $\sigma_{hN} = 20$mbarn. The collision length is given by $\lambda = [n\sigma_{hN}]^{-1}$, where n is the nuclear density. For a nucleus of radius $R = r_0 A^{1/3}$, the nuclear density is given by $n = A/(\frac{4\pi}{3}R^3)$. For Xenon, $A = 131$, and the nuclear density is $n_{Xe} = 0.1781\text{fm}^{-3}$; this gives a collision length of $\lambda_{Xe} = 2.807$fm. Then, the probability of this hadron-state interacting in the Xenon nucleus is given by $I = 1 - e^{-d/\lambda}$. I have taken half the diameter of the Xenon nucleus for the typical distance the hadron-states travel through the nuclei: $d = R_{Xe} = 5.6$fm. Then, the total probability of rescattering would be $I = 0.8639$.

The modified distribution of final states can be expressed as [11]:

$$D_A(Z) = (1 - I)D_N(Z) + I \int H(x)D_N(Z|x)dx. \tag{6.14}$$

The first term is due to the hadronization of those excited states which do not rescatter in the nucleus; the second term is due to the hadronization of those excited states which do rescatter. It is a convolution of the distribution of hadronization with that of the rescattering. The rescattering distribution $H(x)$ is defined on the interval of $x : 0 < x < 1$; it shuffles the population of excited state scaled-energies to lower values of x within this interval. For a given value of x, the distribution of final-state hadrons is given by the function $D_N(Z|x) = D_N^h(u)$, with the variable $u = Z/x$ and the function $D_N^h(u)$ taken from the hadron distribution of the unaltered excited states.

The integral yields an expression for the convoluted distribution:

$$G(Z) = \int_{-\infty}^{\infty} H(x)D(\frac{Z}{x})dx. \tag{6.15}$$

Its normalization must match that of the unaltered distribution:

$$G(Z) = \frac{N_D}{N_g}g(Z), \qquad \text{with} \tag{6.16}$$

$$g(Z) = \int_{-\infty}^{\infty} h(x) D(\frac{Z}{x}) dx. \tag{6.17}$$

For the hadronization function $D_N^h(u)$, I have used the exponential fit to the Deuterium Z-distribution: $D_N^h(u) = Cb\exp(-bu)$. The values of this fit are shown in Figure 6.8; the value listed as the "Constant" represents C, while the "Slope" represents b.

For a distribution of rescattering, I have postulated a $1/Z$-dependence; this was based on πp scattering, as discussed in reference [13]. For the πp interaction, the convolving function is given by $h(x) = 1/x$, and the integral by

$$g(Z) = Cb \int_0^1 \frac{1}{x} e^{-bZ/x} dx. \tag{6.18}$$

By a change of variable, $\zeta \equiv bZ/x$, Equation 6.18 can be rewritten as

$$g(Z) = Cb \int_{bZ}^{\infty} \frac{1}{\zeta} e^{-\zeta} d\zeta = CbE(bZ), \tag{6.19}$$

with the definition of the transcendental function

$$E(y) = \int_y^{\infty} \frac{1}{\zeta} e^{-\zeta} d\zeta. \tag{6.20}$$

The normalization of $g(Z)$ is given by

$$N_g = C\left(1 - e^{-b}\right) + CbE(b); \tag{6.21}$$

the normalization of $D_N^h(u)$ is given by

$$N_D = C\left(1 - e^{-b}\right). \tag{6.22}$$

Finally, the convoluted distribution $G(Z)$ can be written:

$$G(Z) = \frac{Cb(1 - e^{-b})E(bZ)}{(1 - e^{-b}) + bE(b)}. \tag{6.23}$$

For propagation of the errors from the fit parameters, the following four quantities are necessary:

$$\begin{aligned}
\frac{\partial G}{\partial C} &= \frac{1}{C} G(Z) \\
\frac{\partial G}{\partial b} &= G(Z) \left\{ \frac{1}{b} + \frac{e^{-b}}{1 - e^{-b}} - \frac{E(b)}{(1 - e^{-b}) + bE(b)} - \frac{e^{-bZ}}{bE(bZ)} \right\} \\
\frac{\partial D}{\partial C} &= \frac{1}{C} D_N(Z) \\
\frac{\partial D}{\partial b} &= \left(\frac{1}{b} - Z\right) D_N(Z).
\end{aligned}$$

The resultant distribution from the rescatter, defined by Equation 6.14, is overlaid on the input function for the Z-distribution from the Deuterium sample, in Figure 6.14(a). The circles represent the data distribution, taken from Figure 6.8(a); these have been laid over the dashed curve, which represents the function from the exponential fit to the distribution. The boxes are from the convoluted distribution, and these have been laid over the solid curve, which represents the function described by Equation 6.18. This convoluted distribution also has been fit to a simple exponential; the parameters of this fit are shown on the plot. The ratio of convoluted and original data distributions is shown in Figure 6.14(b). The average of the middle three points is 0.371 ± 0.057; this is 11σ below unity.

A 3σ change from the input distribution would require a value of the ratio of 0.7 ± 0.1. This level of convolution would correspond to a fraction of rescattering of 1/3. Such a distribution is shown in Figure 6.14(c), again overlaid on the input distribution; the corresponding ratio is shown in (d). From this upper limit on the fraction of rescattering, it can be estimated that these data could resolve a rescattering cross section, at the 3σ level, of 5 mbarn. These values of the means of the middle three points of the ratios are included in Table 6.2 with those from the Xenon to Deuterium ratios from Kin-1 (Figure 6.12(a)) and Kin-2 (Figure 6.13(a)).

Ratio	Value	σ_R
Xe/D_2, Kin-1	1.01	0.15
Xe/D_2, Kin-2	1.01	0.12
$D_A(Z)$/D_2, 11σ	0.371	0.057
$D_A(Z)$/D_2, 3σ	0.702	0.103

Table 6.2: Rescattering Limits.

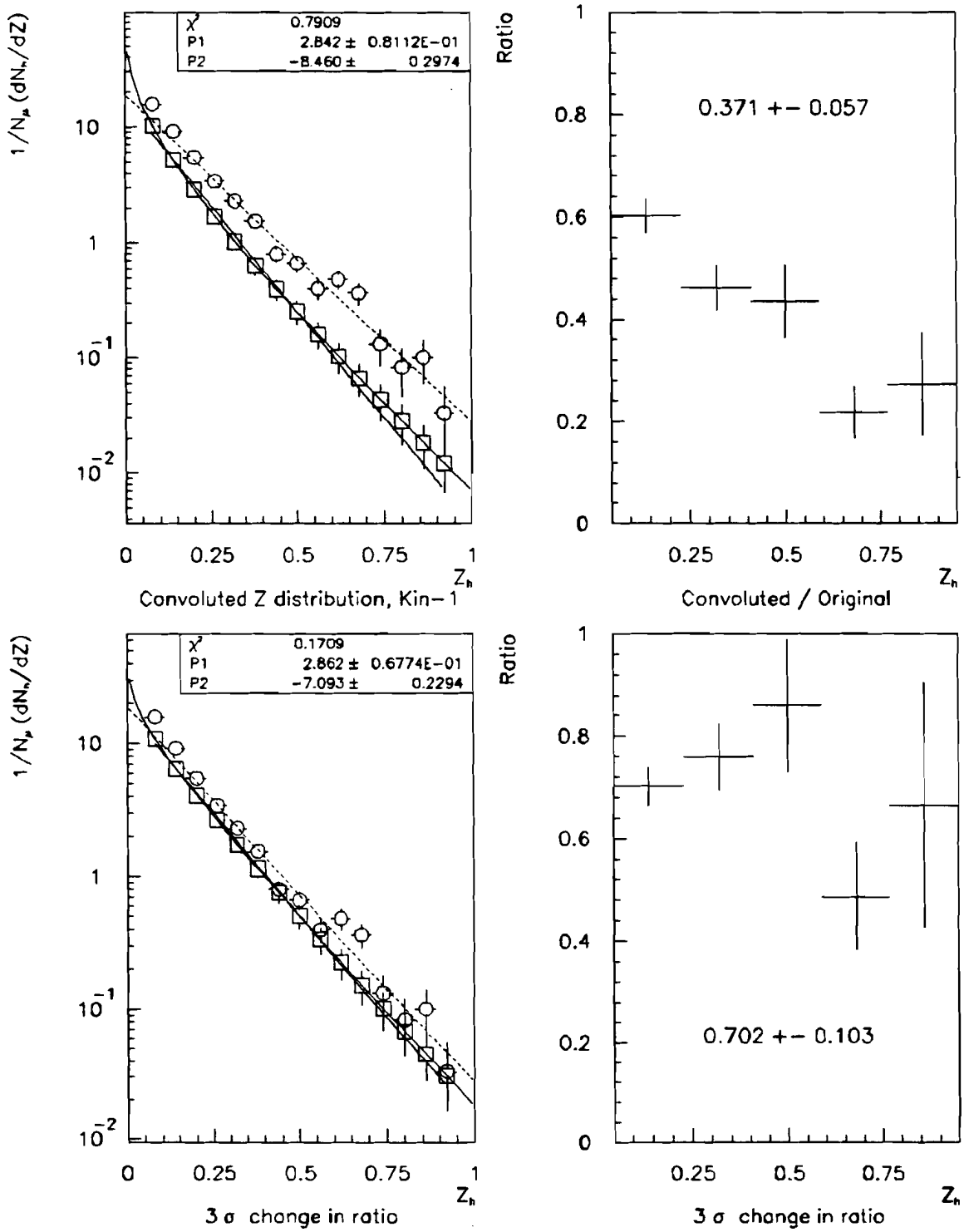

Figure 6.14: Convoluted Z-distributions.
Plot (a) shows the convoluted Z-distribution overlaid on the original distribution from the Deuterium sample; plot (b) shows the ratio of these distributions. Plot (c) shows the convoluted Z-distribution with 3σ resolution overlaid on the original distribution from the Deuterium sample; plot (d) shows the ratio of these distributions.

6.3.2 Rescattering in Target

Rescattering in the target may effect a net loss of tracks assigned to the primary vertex, which could bias the ratios of distributions of Xenon to Deuterium if the levels were different for the two targets. In Figure 6.15 are plotted the normalized distributions of $1/N_\mu dn/dZ$ versus Z for four successive regions of the Deuterium target, upstream to downstream. These distributions have been corrected for acceptance. The ratio of the most upstream region Figure 6.15(a) over the most downstream region Figure 6.15(d) is shown in Figure 6.15(e), for Deuterium. The same four segments and the ratios are shown for the Xenon target in Figure 6.16. The lowest bin in Z was the region in which acceptance corrections were quite large; the loss of tracks at low momentum was higher in the upstream end of the target than in the downstream end. This can be seen in the ratio of tracks cut due to the Fiducial cut for the upstream versus the downstream segments of the target, as displayed in Figure 6.17.

I have replotted the ratios of the Z-distributions for Xenon over Deuterium, restricting the samples to events in which the interaction occurred in the downstream *halves* of the targets. The ratios for the low-kinematic region are shown in Figure 6.18: (a) for all particles, (b) for the fastest particles, (c) for the second fastest, and (d) for the third fastest. These ratios are still all consistent with unity. The ratios of the distributions for the high kinematic range are shown in Figure 6.19. These ratios also are all consistent with unity.

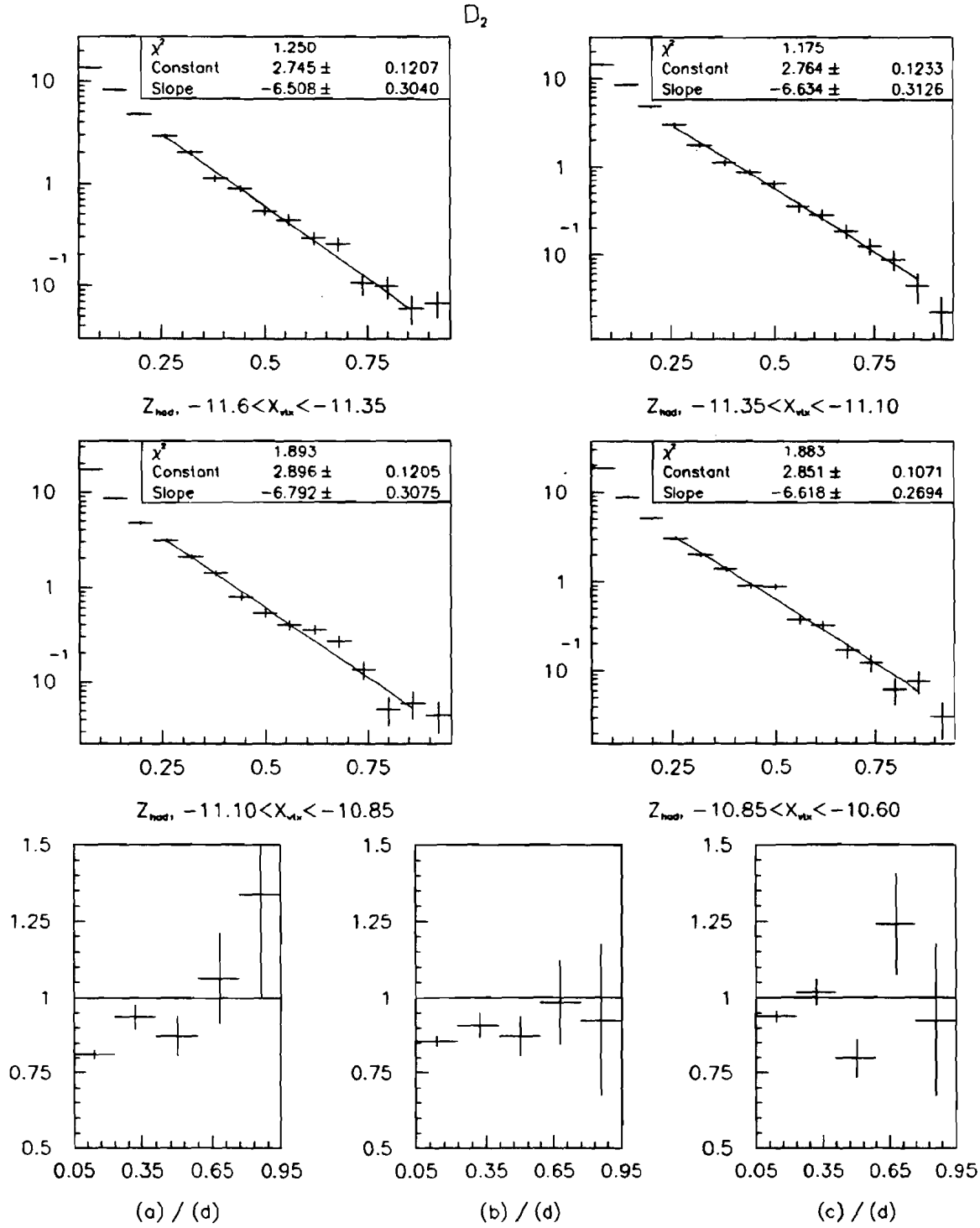

Figure 6.15: Target Length Effects on Z-distributions, D_2.
These plots show the Z-distributions from four segments of the target, from most upstream to most downstream. The ratios of the first three segments to the last are shown in plots (e), (f), and (g).

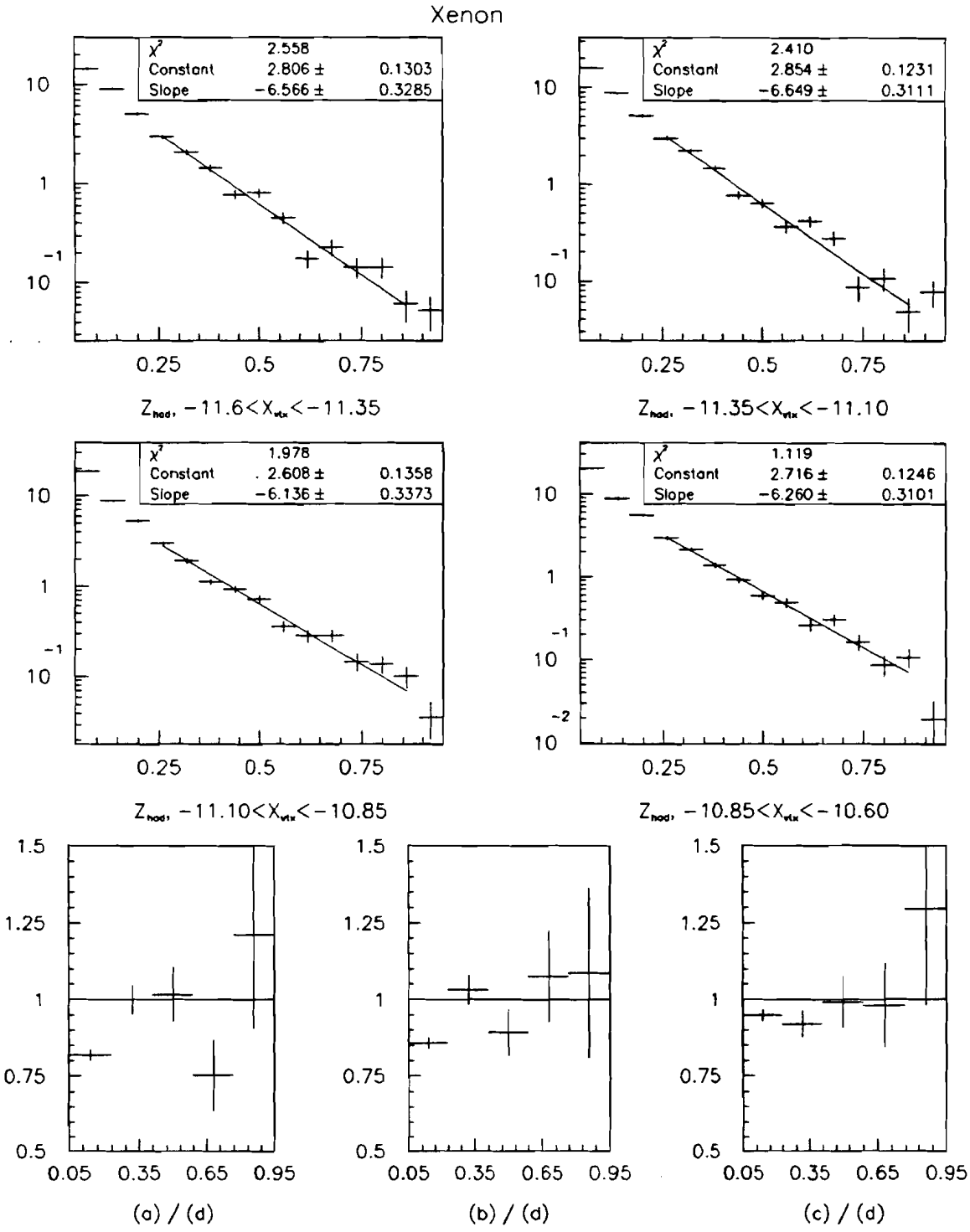

Figure 6.16: Target Length Effects on Z-distributions, Xenon.
These plots show the Z-distributions from four segments of the target, from most upstream to most downstream. The ratios of the first three segments to the last are shown in plots (e), (f), and (g).

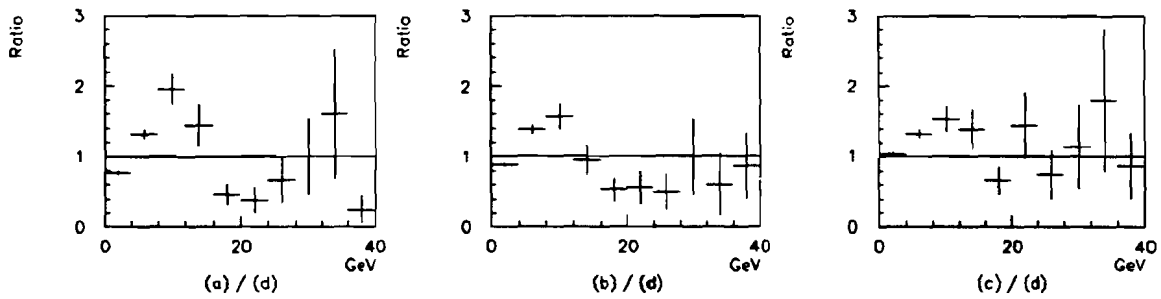

Figure 6.17: Target Length Effects on Fiducial cuts.
These plots involve the D_2 Monte Carlo tracks cut by the Fiducial cut, for the four segments of the target. The ratios of the first three segments to the last are shown in plots (a), (b), and (c).

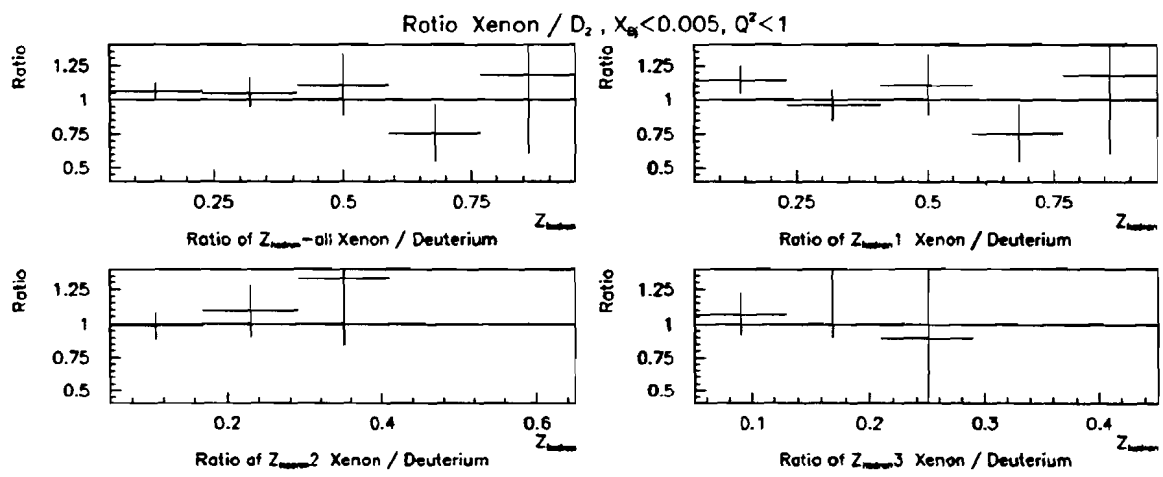

Figure 6.18: Z-Distributions: Ratio of Xe/D_2, Kin-1, Half Target.
These plots show the ratios of the Z-distributions of Xenon over Deuterium for the low kinematic region: ($X_{\rm Bj} < 0.005$, and $Q^2 < 1$). The ratio in (a) is of all tracks, in (b) Z_1, in (c) Z_2, and in (d) Z_3.

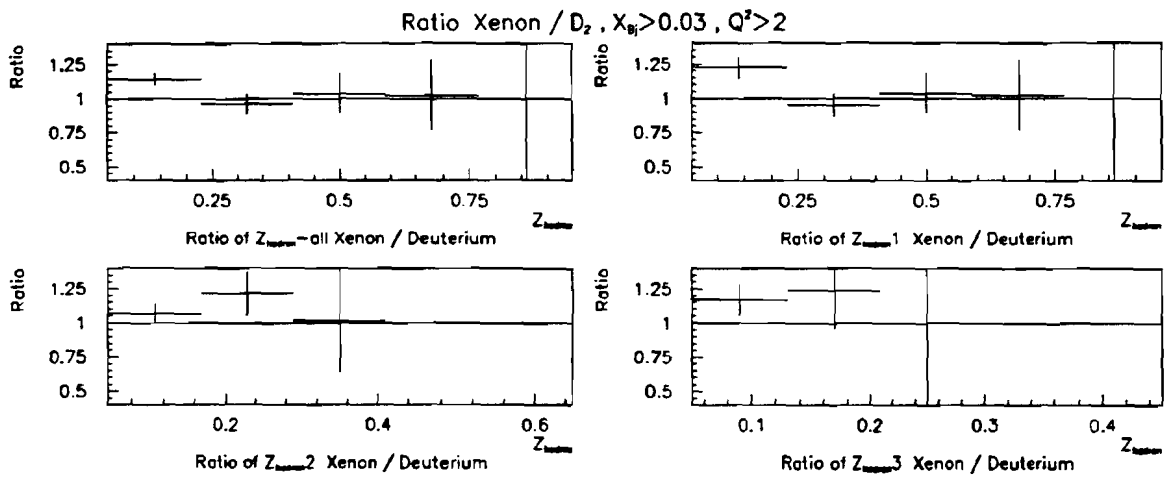

Figure 6.19: Z-Distributions: Ratio of Xe/D_2, Kin-2, Half Target.
These plots show the ratios of the Z-distributions of Xenon over Deuterium for the high kinematic region: ($X_{Bj} > 0.03$, and $Q^2 > 2$). The ratio in (a) is of all tracks, in (b) Z_1, in (c) Z_2, and in (d) Z_3.

6.4 Rescaled Z

I also compared the distributions of the Rescaled-Z variables between Xenon and Deuterium. These rescaled Z-distributions for the low kinematic range are shown in Figure 6.20, with those from Xenon on the left and Deuterium on the right. The distributions for the high kinematic range are displayed in Figure 6.21. It is apparent that the slopes of these distributions for the fastest three charged particles were all very similar. This is suggestive of some fundamental process involved in the fragmentation that results in this characteristic distribution.

The ratios of these rescaled Z-distributions of Xenon over Deuterium are shown in Figure 6.22 for the low kinematic range and in Figure 6.23 for the high; in both sets the ratios are consistent with a flat level of unity. It is also evident that the distributions for a given target are consistent across the two kinematic regions.

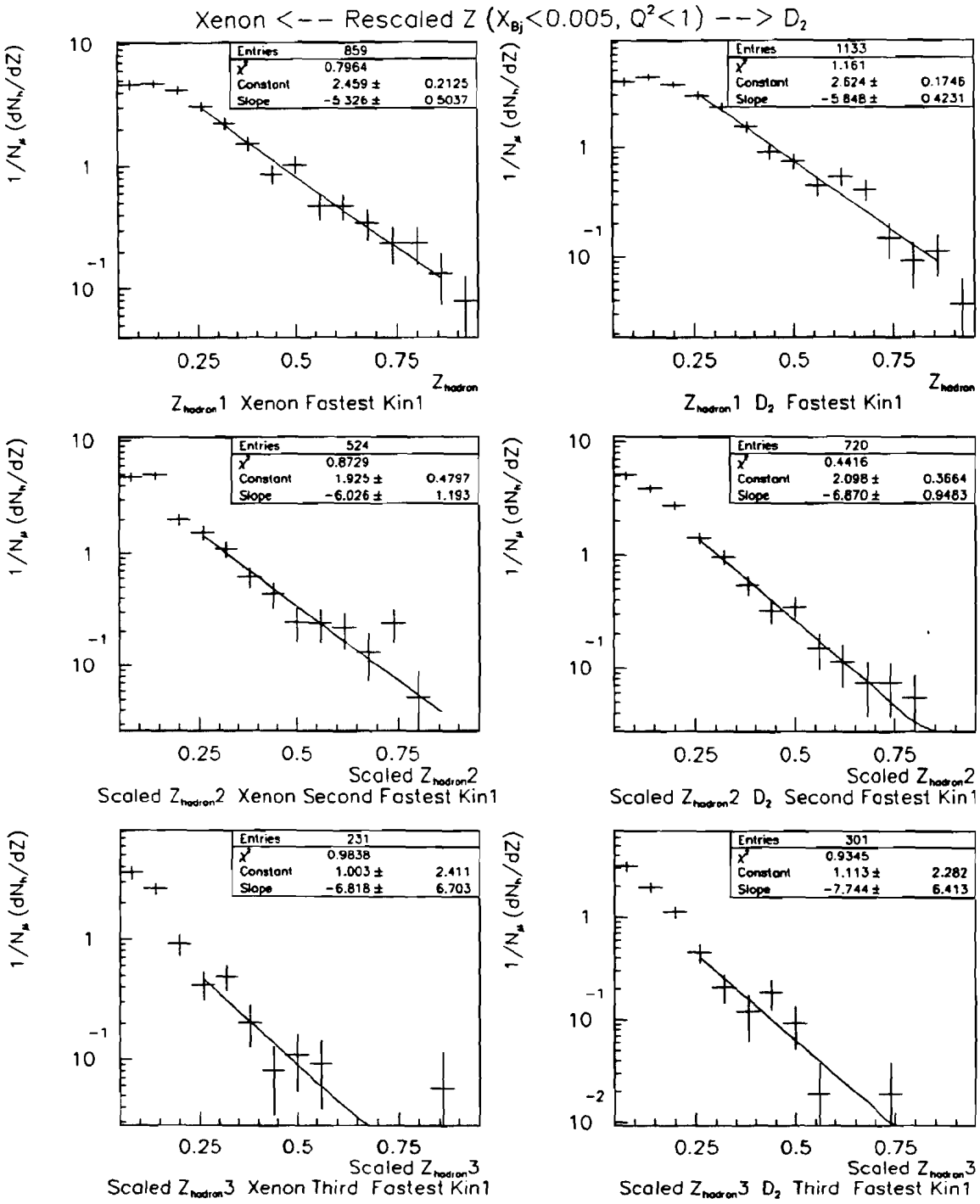

Figure 6.20: Rescaled Z-Values, low kinematics.
These plots show the distributions of the Rescaled Z-values for Xenon (a,c,e) and Deuterium (b,d,f). In (a) and (b) are the distributions for the highest Z track; the rescaling has no effect on these values. In (c) and (d) are the distributions of the rescaled Z-values for the second highest Z tracks. In (e) and (f) are the distributions of the rescaled Z-values for the third highest Z tracks. The central Z-regions were fitted with and exponential, and the slopes of these fits are the power of the exponential. The χ^2 values are the reduced-χ^2 from the fits.

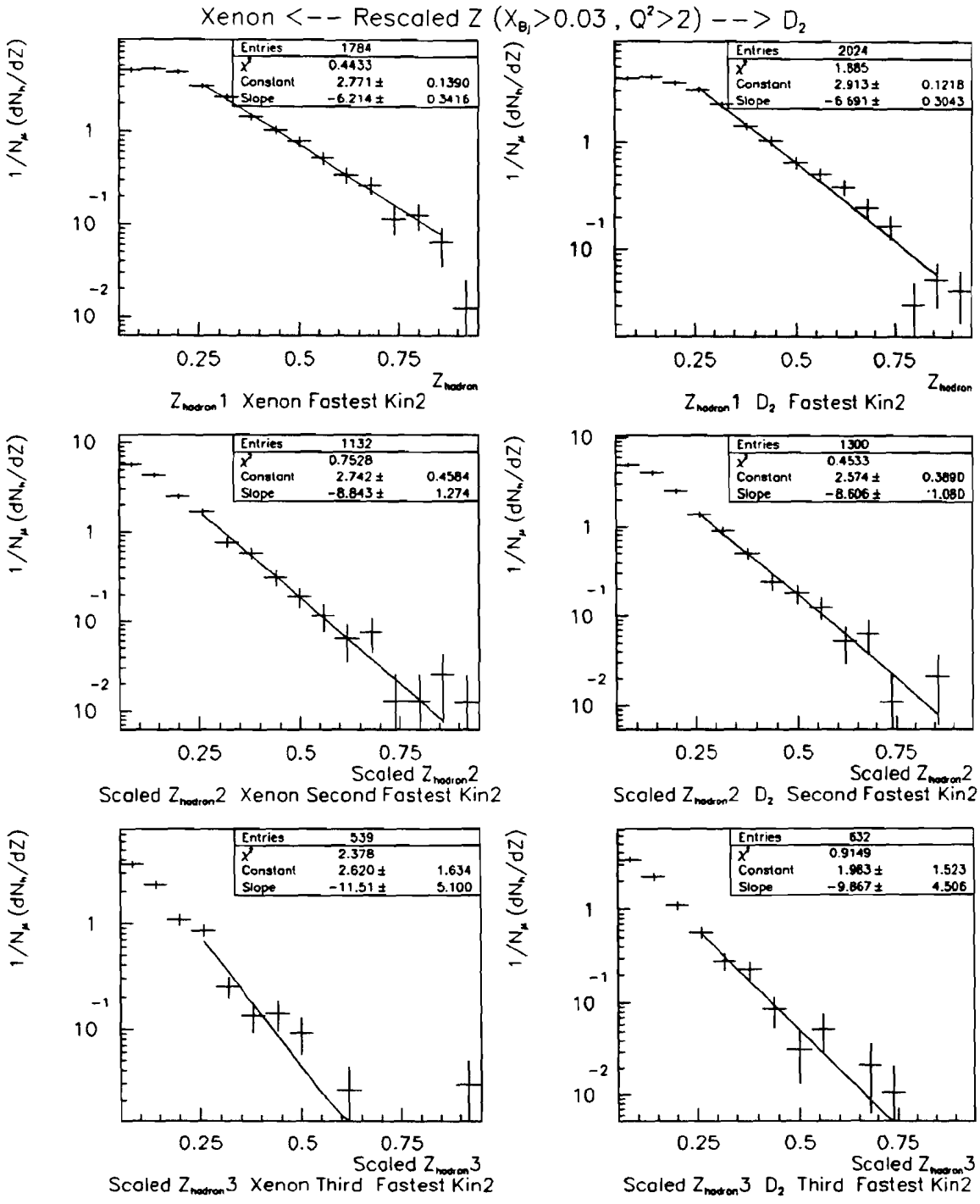

Figure 6.21: Rescaled Z-Values, high kinematics.
These plots show the distributions of the Rescaled Z-values for Xenon (a,c,e) and Deuterium (b,d,f). In (a) and (b) are the distributions for the highest Z track; the rescaling has no effect on these values. In (c) and (d) are the distributions of the rescaled Z-values for the second highest Z tracks. In (e) and (f) are the distributions of the rescaled Z-values for the third highest Z tracks. The central Z-regions were fitted with and exponential, and the slopes of these fits are the power of the exponential. The χ^2 values are the reduced-χ^2 from the fits.

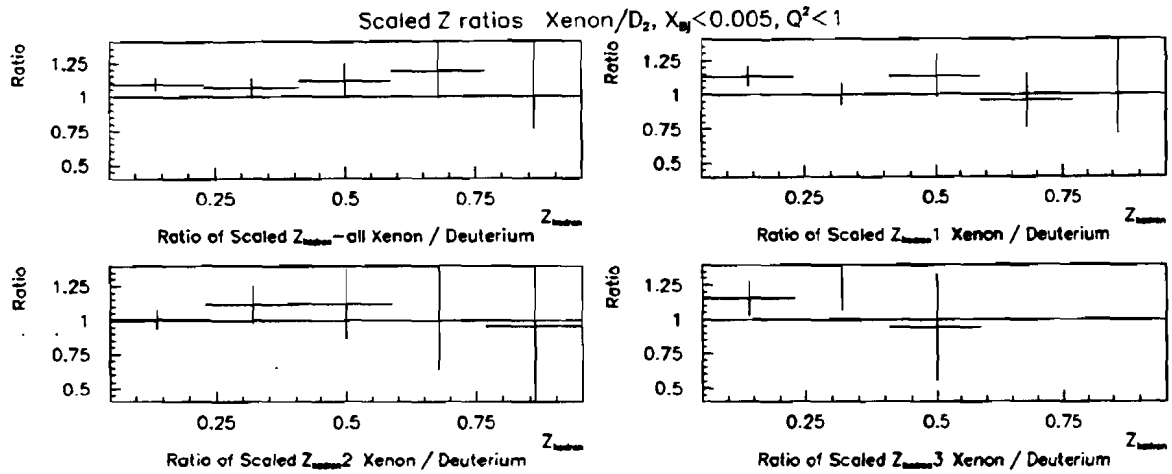

Figure 6.22: Ratios of Xe/D_2 Rescaled Z-Distributions, low kinematics.
These plots show the ratios of the rescaled Z-distributions of Xenon over Deuterium for the low kinematic region: ($X_{Bj} < 0.005$, and $Q^2 < 1$). The ratio in (a) is of all tracks, in (b) Z_1, in (c) Rescaled-Z_2, and in (d) Rescaled-Z_3.

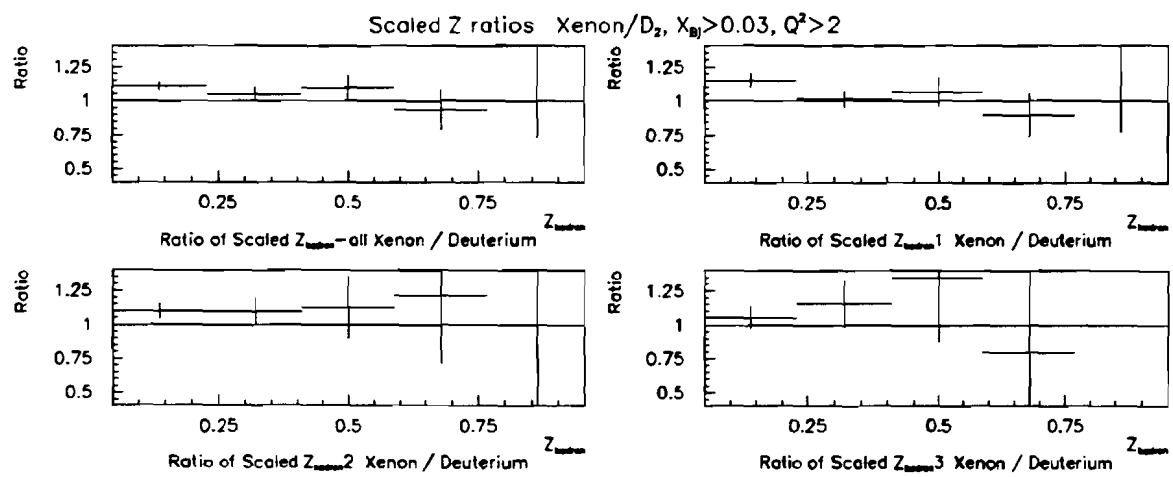

Figure 6.23: Ratios of Xe/D_2 Rescaled Z-Distributions, high kinematics.
These plots show the ratios of the rescaled Z-distributions of Xenon over Deuterium for the high kinematic region: ($X_{Bj} > 0.03$, and $Q^2 > 2$). The ratio in (a) is of all tracks, in (b) Z_1, in (c) Rescaled-Z_2, and in (d) Rescaled-Z_3.

6.5 Correlations

In the Lab-frame photon-gluon fusion description of shadowing (see Section 2.3) the virtual photon undergoes a transmutation into a quark-antiquark pair, which subsequently interacts with the nucleus; in only the low X_{Bj} and low Q^2 regions will there be significant lateral separation of the virtual quark-antiquark pair for the shadowing to occur. It is possible to imagine that this quark-antiquark pair could interact with the nucleus in such a way that each member of the pair would be associated with one of the leading hadrons. In such a mechanism these two leading particles might exhibit strong inter-correlations. Subsequent rescattering in a nuclear target could scramble this inter-correlation, so the effect should be smaller in Xenon than in Deuterium.

I have looked specifically at the Z-values of the second fastest particles as a function of those of the fastest particles; in addition, I have looked at similar correlations for the third fastest as a function of the first and the third as a function of the second. These are plotted in Figures 6.24; along the ordinates are the *mean values* of the Z's of the "correlated variable", while the values of the "function variable" are along the abscissa.

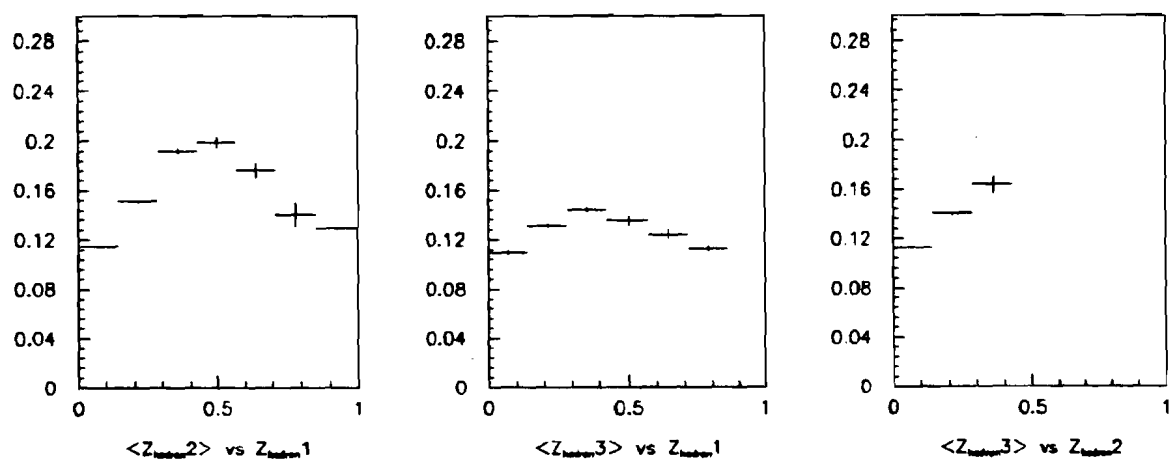

Figure 6.24: Track Correlations.
These plots show the correlations between the Z-values of tracks in the same events. In (a) the mean value of Z_2 is plotted as a function of Z_1; in (b) the mean value of Z_3 as a function of Z_1; and in (c) the mean value of Z_3 as a function of Z_2.

Since these distributions involved intra-event relations, I did not corrected them for acceptance, as the corrections per track could have been correlated. In fact, the

mean values of the exponential distributions were weighted heavily by the very low-Z values, where the acceptance was very poor. To limit this problem, I have placed a threshold cut of 0.10 on the Z-values for all ranks considered. With the minimum ν of 100 GeV, this corresponded to a momentum threshold of 10 GeV. I have attempted to correct for acceptance, neglecting any correlation of the acceptance functions. In Figure 6.25, I have corrected each "ordinate" track for acceptance, based only on its value of momentum. Since the distributions were normalized to intervals in the "abscissa" Z, I have not corrected for acceptance of these tracks. These corrections reduce the mean values of the ordinate Z by ~20%.

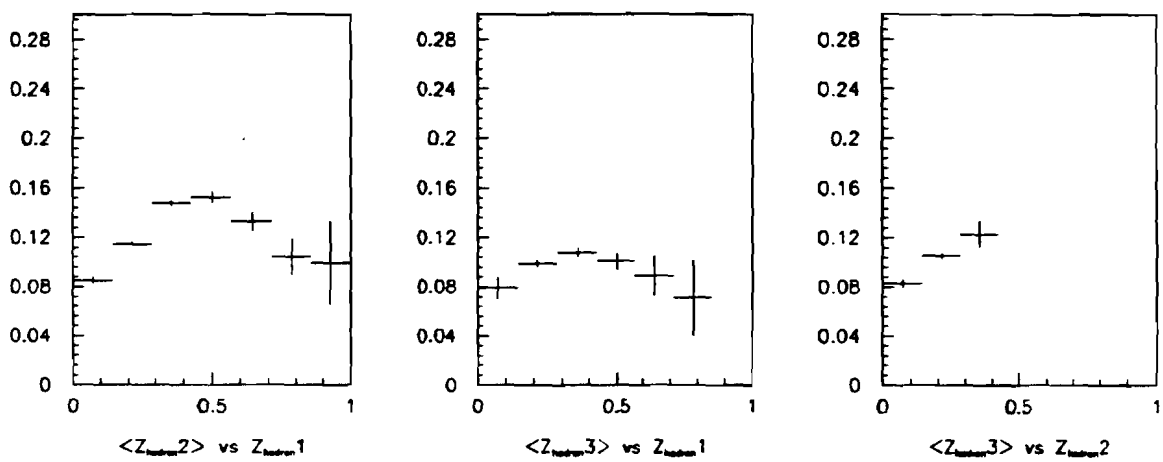

Figure 6.25: Track Correlations, Acceptance Corrected.
These plots show the correlations between the Z-values of tracks in the same events. In (a) the mean value of Z_2 is plotted as a function of Z_1; in (b) the mean value of Z_3 as a function of Z_1; and in (c) the mean value of Z_3 as a function of Z_2. Acceptance corrections have been applied for the Z-values of the ordinate.

These correlation plots have involved only reconstructed charged particles, and neutral particles were not observed. However, it was possible to use the knowledge of the sum of the Z-values for the observed charged particles to restrict the correlation measurements to tracks which could not have a missing particle between them. These constraints have been applied to the plots in Figure 6.26, restricting the correlations to include only those events in which the Z_{lost} was smaller than the lesser of the two particles in the summation. So, for the correlations between Z_1 and Z_2, the restriction $Z_2 > Z_{lost}$ was imposed; for the correlations between Z_1 and Z_2, the restriction $Z_3 > Z_{lost}$ was imposed. These correlations were corrected for acceptance and had threshold Z_i-values of 0.10.

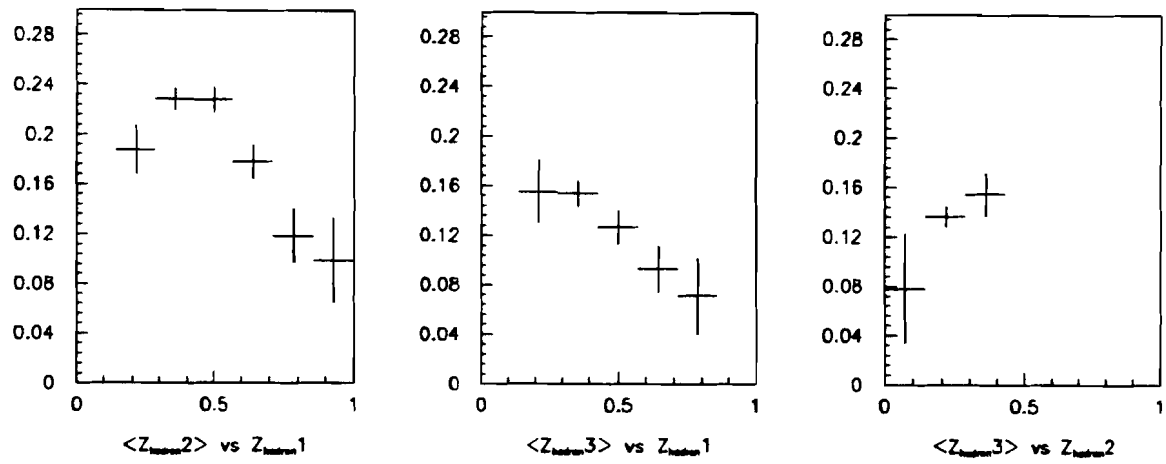

Figure 6.26: Track Correlations, No intermediates.
These correlations were corrected for acceptance and had threshold Z_i-values of 0.10.

Correlations between the Z_i would be exhibited by the mean value of the ordinate Z changing monotonically with the abscissa Z. These correlations are rather weak, and they do not suggest a simple linear dependence. However, one of the salient features of the "second fastest as a function of the fastest" (Figure 6.24(a)) is that the value decreases as the Z-value of the fastest increases above 0.5. Perhaps this can be associated trivially with the energy remaining to be distributed among the particles, given the fastest particle; since the fastest was carrying almost all of the energy in the event, there was little left to distribute to the rest of the particles in the event. Therefore, the mean value of the second fastest particle must decrease as that of the fastest goes above 0.5. In order to investigate this I used the *rescaled* Z-values for the subsequent particles, to remove this effect.

To search for leading particle correlations, I have plotted the rescaled Z-values as functions of a faster particle's value in Figures 6.27. With the rescaled values, the correlations are much flatter at higher values of the abscissa Z, but they show more slope at the lower values. Again, acceptance is an issue; the rescaling pulls more of the low-momentum tracks above the threshold. From the similarity of the rescaled distributions in Figure 6.21, one would suspect that the distributions were thrown according to some simple law, independently of those of the neighboring particles. The correlations are still small; the slope of the first four points in Figure 6.27(a) is 0.3, while above $Z_1 > 0.5$ there appears no correlation. There appears to be a little difference in the comparison of the correlation between adjacent particles (Figures 6.27(a) and (c)) with the correlation between the third and the first (Figure 6.27(b)), for low-Z values. The restriction of no intermediates has been applied to the correlations

in Figure 6.28; this obviously must raise the mean values of the distributions Z_i as it imposes a rather severe minimum value on them. However, there still appears little dependence of the mean value of the ordinate Z upon the value of the abscissa Z.

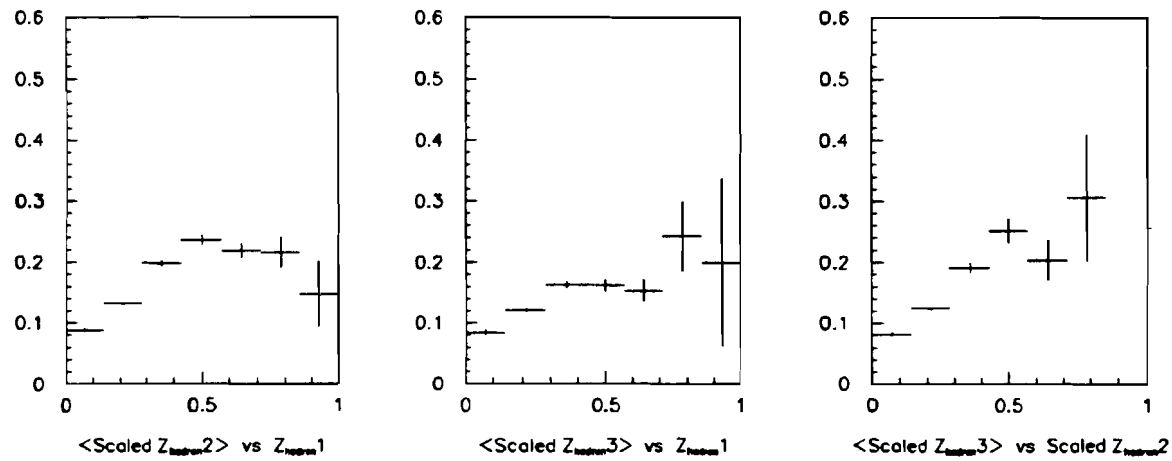

Figure 6.27: Rescaled Track Correlations.
These plots show the correlations between the Z-values of tracks in the same events, using the rescaled values of Z_2 and Z_3. In (a) the mean value of rescaled-Z_2 is plotted as a function of Z_1; in (b) the mean value of rescaled-Z_3 as a function of Z_1; and in (c) the mean value of rescaled-Z_3 as a function of rescaled-Z_2. These correlations were corrected for acceptance and had threshold Z_i-values of 0.10.

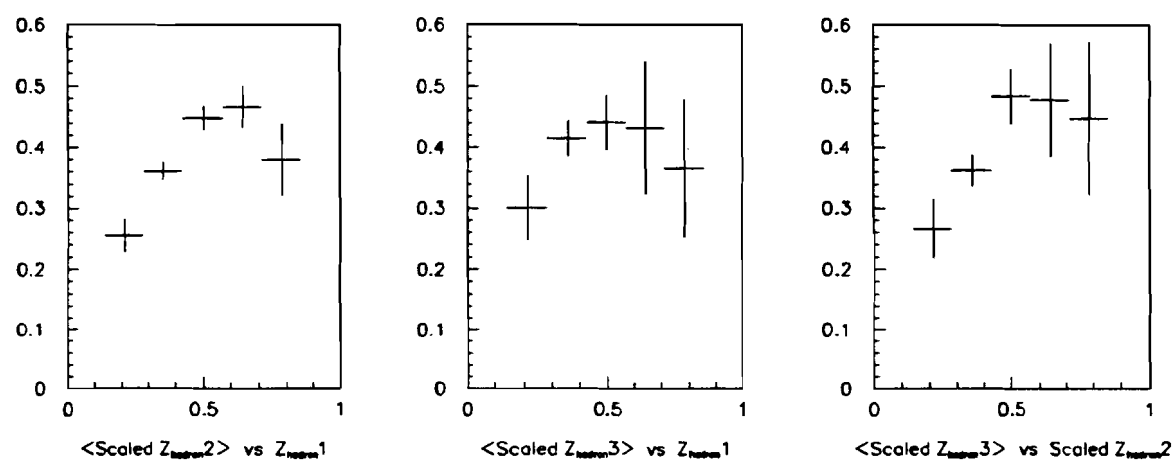

Figure 6.28: Rescaled Track Correlations, No intermediates.

6.5.1 Correlation Coefficient

A more succinct way of describing the correlations between particles in the fragmentation chain is to define the correlation coefficient as follows:

$$R_{a\neq b} \equiv \frac{1}{N-1}\sum_i \frac{(Z_{ai}-\bar{Z}_a)(Z_{bi}-\bar{Z}_b)}{\sigma_a\sigma_b}, \tag{6.24}$$

where a is either the fastest or second fastest particle, b is either the second fastest or third fastest particle, $\bar{Z}_a$ is the mean-value of the Z_a-distribution, $\bar{Z}_b$ is the mean-value of the Z_b-distribution, and σ_a and σ_b are the variances of the Z_a and Z_b distributions, respectively. The summation runs over all events which have entries for both Z_a and Z_b, and the normalization N is defined by

$$N \equiv \sum_i 1. \tag{6.25}$$

The equivalent definition of the correlation coefficient for the rescaled-Z variables Z_{R2} and Z_{R3} is

$$R_{a\neq Rb} \equiv \frac{1}{N-1}\sum_i \frac{(Z_{ai}-\bar{Z}_a)(Z_{Rbi}-\bar{Z}_{Rb})}{\sigma_a\sigma_{Rb}}. \tag{6.26}$$

The values of these correlation coefficients have been calculated including acceptance corrections which were applied independently per track. In addition, the values of the Z_a were restricted to lie in the intervals $0.10 < Z_a < 0.95$ and $0.10 < Z_{Ra} < 0.95$. These coefficients are shown in Figures 6.29 and 6.30 for the full Deuterium sample. These Coefficients have been divided into three groups, based on the relative electric charges carried by the two particles: particles with any charge relation, particles with the *Same-Sign* of charge, and those with *Opposite-Sign* of charge. For a Same-Sign example, the mean values for the second fastest particles would be examined only if the second fastest particles had the same charge as the fastest particles. The first point in each group is the value of the correlation between the fastest and second fastest particles. The second point is the value of the correlation between the fastest and third fastest particles. The third point is the value of the correlation between the second fastest and third fastest particles.

Again, these correlation plots involved only reconstructed charged particles, and neutral particles were not observed. However, it was possible to use the knowledge of the sum of the Z-values for the observed charged particles to restrict the correlation measurements to tracks which could not have a missing particle between them. These constraints have been applied in the following analysis. The values of the correlation coefficients have been calculated, restricting the summations to include only those events in which the Z_{lost} was smaller than the lesser of the two particles in the

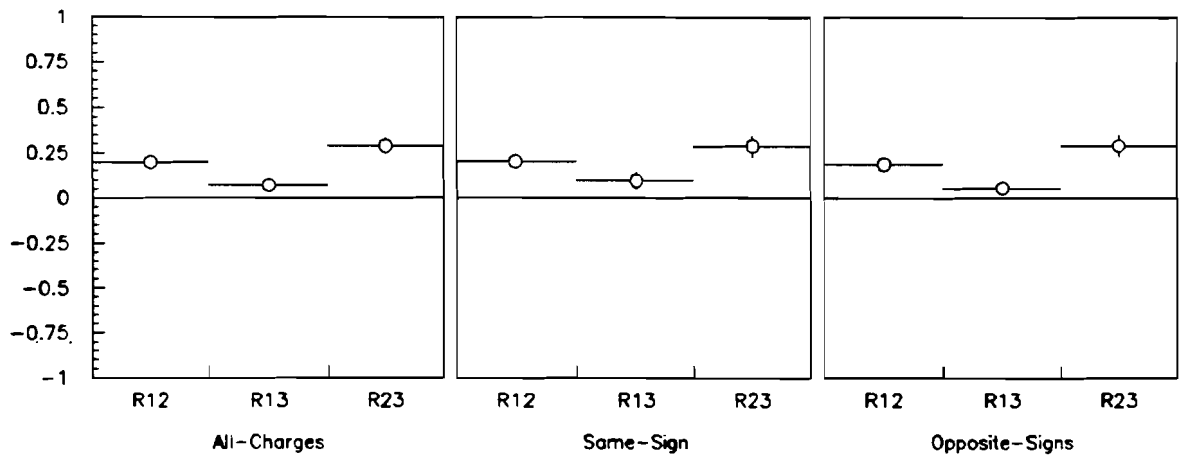

Figure 6.29: Correlation Coefficient, D_2.
These plots show the correlation coefficients defined by Equation 6.24 for the Deuterium sample. The three boxes group the Coefficients according to charge restrictions: none, Same-Sign, and Opposite-Sign. The first point in each group is the value of the correlation between the fastest and second fastest particles, the second point is that between the fastest and third fastest particles, and the third point is that between the second fastest and third fastest particles.

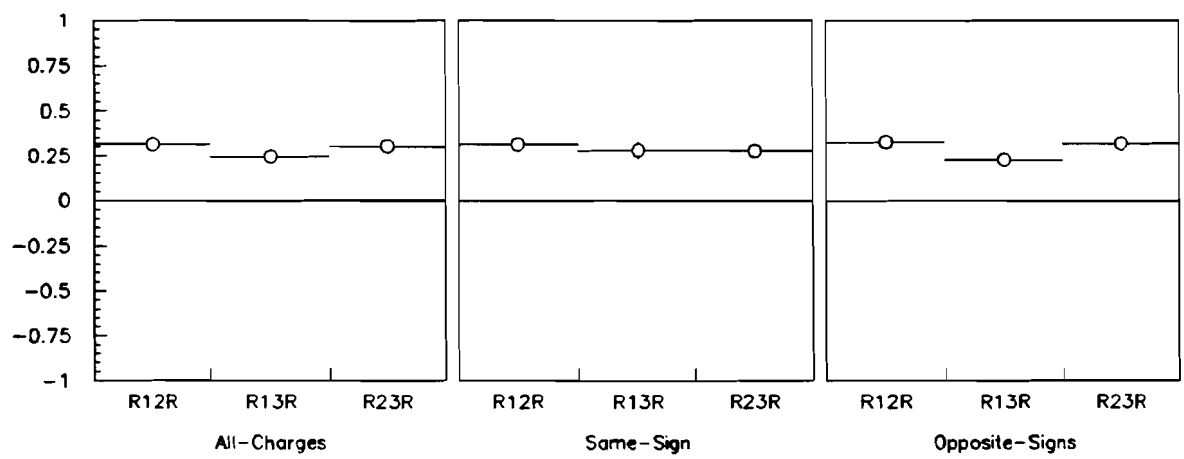

Figure 6.30: Rescaled Correlation Coefficient, D_2.
These plots show the correlation coefficients defined by Equation 6.26 for the Deuterium sample, using the rescaled-Z variables for the second and third fastest particles.

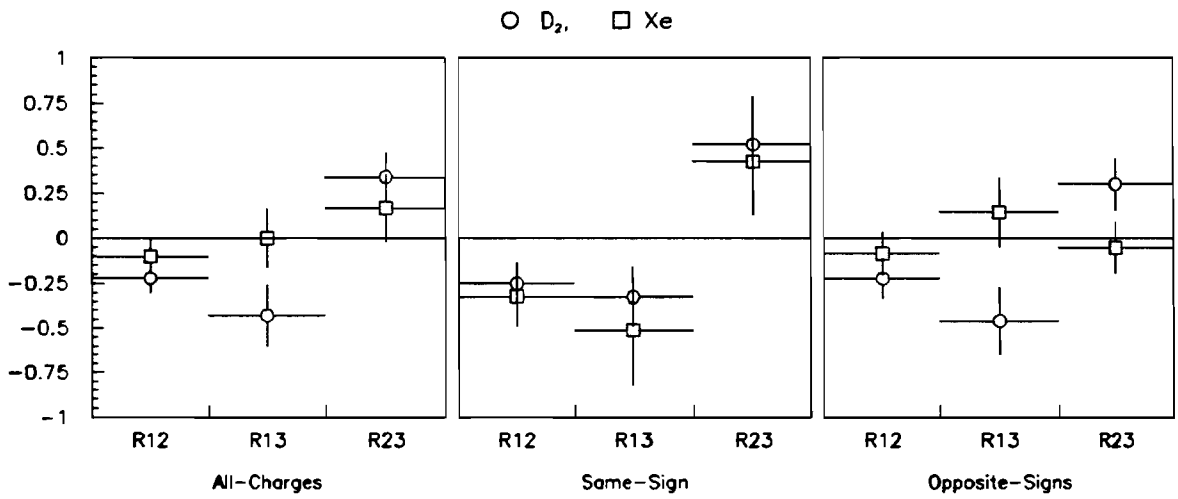

Figure 6.31: Correlation Coefficient, no missing intermediates, Kin-2.
The first point has the restriction $Z_2 > Z_{lost}$ applied to the second fastest particles, and the second and third points have the restriction $Z_3 > Z_{lost}$ applied to the third fastest particles.

summation. So, for the correlations between Z_1 and Z_2, the restriction $Z_2 > Z_{lost}$ was imposed; for the correlations between Z_1 and Z_2, the restriction $Z_3 > Z_{lost}$ was imposed.

Figure 6.31 shows the correlation coefficients for both Deuterium and Xenon, for the non-Shadowing region; the circles are the Deuterium points, and the boxes are the Xenon points. The correlation coefficients from the rescaled-Z variables are shown in Figure 6.32.

The correlations between leading hadrons have been shown to be positive, but small: less than 30%. The coefficients indicate no appreciable difference between inter-track correlations from a nuclear target and from a simple target; this is even true in the kinematic region of Shadowing. The systematic uncertainty on the correlations is rather large; corrections for acceptance may require correlated application. That the simple corrections lessen the correlations matches intuition that the correlations were strongly affected by the low-momentum particles, where the acceptance was poor. More analysis in this area is required.

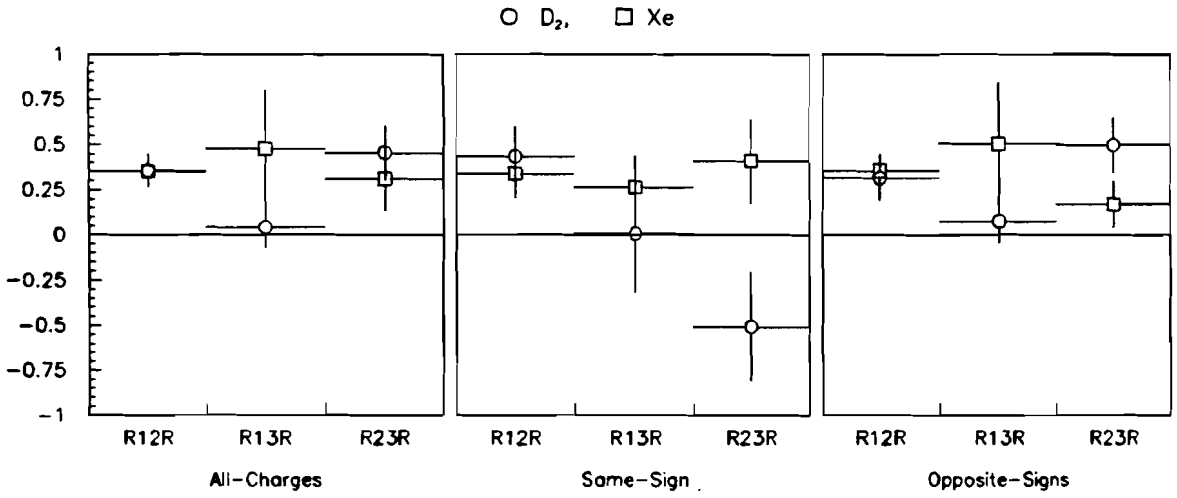

Figure 6.32: Rescaled Correlation Coefficient, no missing intermediates, Kin-2.
The first point has the restriction $Z_2 > Z_{lost}$ applied to the second fastest particles, and the second and third points have the restriction $Z_3 > Z_{lost}$ applied to the third fastest particles.

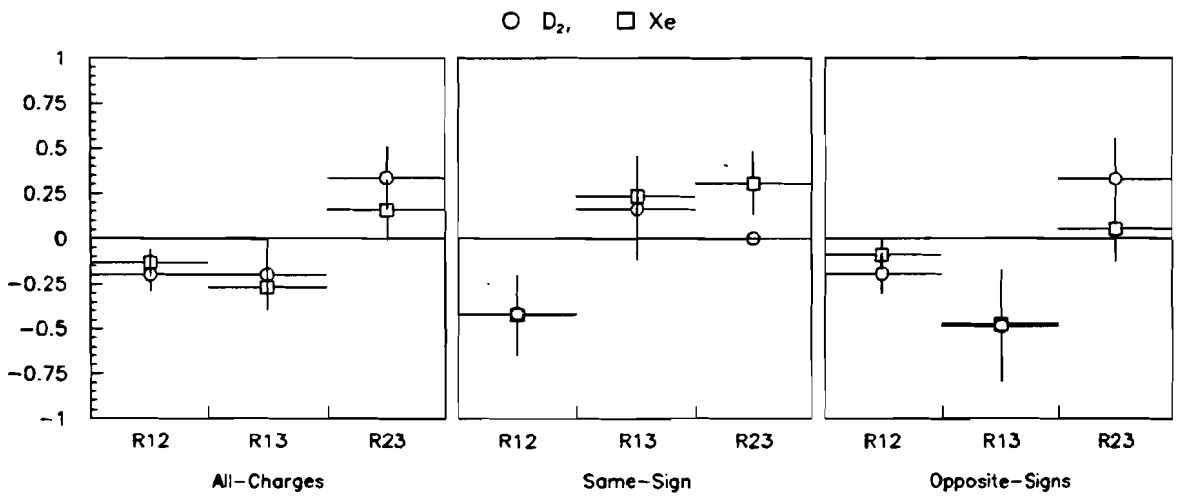

Figure 6.33: Correlation Coefficient, no missing intermediates, Kin-1.
The first point has the restriction $Z_2 > Z_{lost}$ applied to the second fastest particles, and the second and third points have the restriction $Z_3 > Z_{lost}$ applied to the third fastest particles.

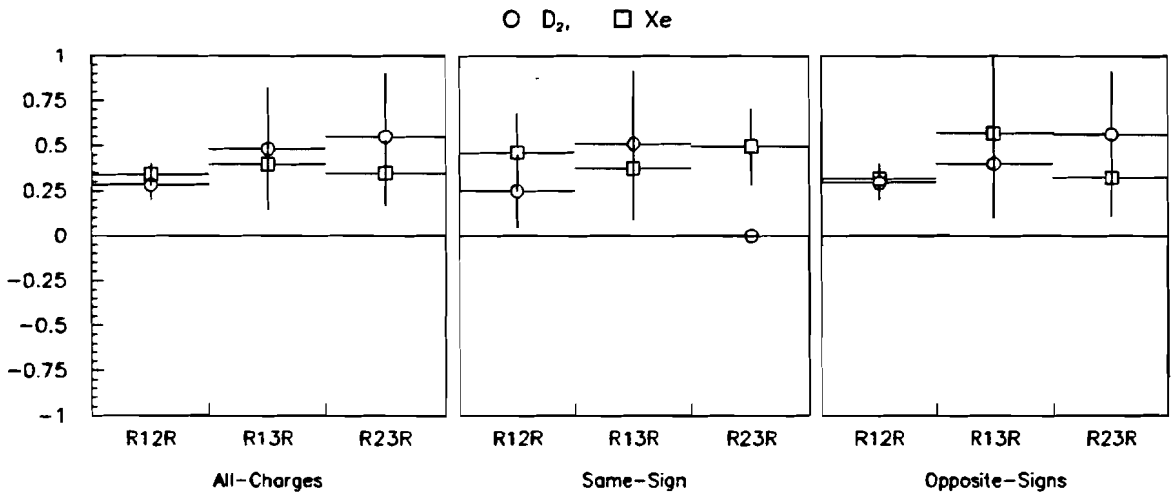

Figure 6.34: Rescaled Correlation Coefficient, no missing intermediates, Kin-1. The first point has the restriction $Z_2 > Z_{lost}$ applied to the second fastest particles, and the second and third points have the restriction $Z_3 > Z_{lost}$ applied to the third fastest particles.

6.6 Conclusions

In examining the Z-distributions for attenuation due to the struck quark traversing nuclear matter, I have found no dependence of the distributions upon the target material. The ratios of the distributions from Xenon to Deuterium are well within 1σ of unity. A postulated rescattering in the Xenon nucleus is less than 5 mbarn at the 99% confidence level. In regards to these ratios of Z-distributions, it's very flat in Illinois.

The correlations look the same within errors when comparing Xenon to Deuterium; this is even true in the low region of kinematics, where there is a strong dependence of the cross section on the nuclear target and where one might expect to see a stronger correlation between leading hadrons.

Chapter 7

ϕ Distributions

7.1 Definition of ϕ

One of the variables used to describe the trajectories of hadron tracks is the azimuthal angle about the direction of the virtual photon and relative to the lepton-plane. This is pictured in Figure 7.1. The incident and scattered lepton define the lepton-plane; the virtual photon, of course, is also in this plane. The vector of each hadron's trajectory defines its own plane with the virtual photon vector. The angle between the hadron plane and the lepton-plane is defined to be ϕ_i for the i-th hadron; the boundary condition $\phi = 0$ is defined for the hadron to be in the lepton-plane, on the same side of the virtual photon as the scattered lepton. The separation between the hadron vector and that of the virtual photon is characterized by the perpendicular momentum, P_t. For an unambiguous definition of the hadron plane (and hence ϕ), the hadron vector must be separated from the virtual photon, which requires $|P_t| > 0$.

7.2 Brief History

Georgi and Politzer [26] predicted that the distribution of ϕ of the hadrons would exhibit an asymmetry due to effects of gluon-bremsstrahlung radiation from the struck quark. They claimed that the observation of this asymmetry would be clean evidence for the occurrence of the gluon-bremsstrahlung process, an effect based on QCD. This claim was refuted in the work of Cahn [15], in which he showed that the asymmetric

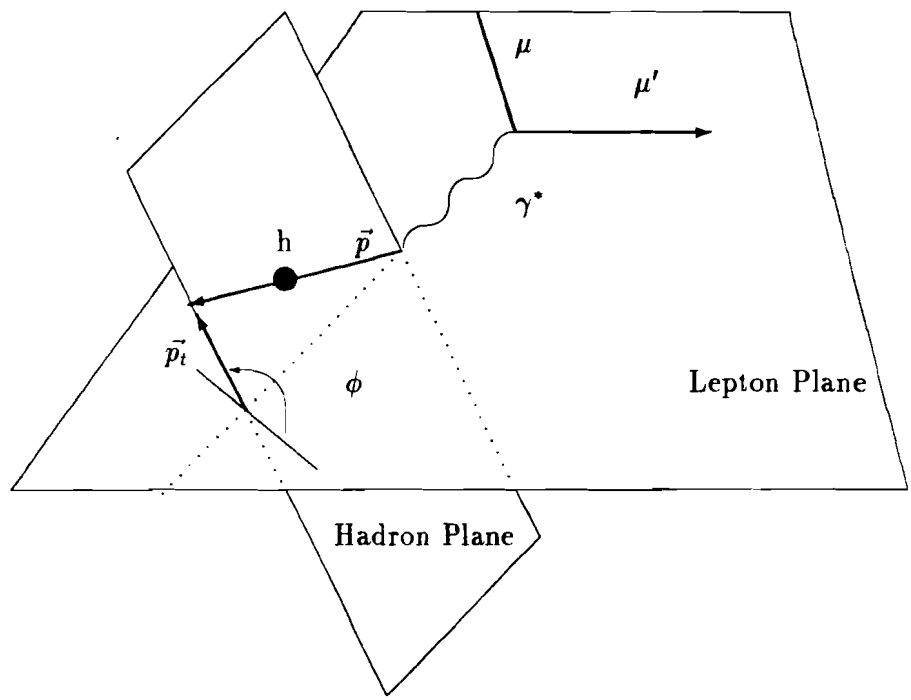

Figure 7.1: Azimuthal Angle ϕ. This figure shows the definition of the azimuthal angle ϕ.

effect could be generated by assigning some initial momentum to the struck quark that was perpendicular to the direction of the virtual photon $\bar{q}$: some primordial k_t.

These calculations were extended to predictions for neutrino scattering in references [33, 38], and the effect was, in fact, observed [22, 24]. It was also observed in a muon-proton scattering experiment [62]. The effect of the ϕ-asymmetry was measured in the EMC as well [19, 17]. König and Kroll furthered the theoretical work [32] by constructing a Monte Carlo simulation which included the effects of both primordial k_t and gluon-bremsstrahlung radiation and used fits to the EMC data; they concluded that within their model the effect could be explained mainly by the primordial k_t contributions and that the contributions from gluon-bremsstrahlung radiation were small.

7.3 Theory

The azimuthal angle was defined in section 7.1, and this can be written as the cosine of the angle:

$$\cos\phi = \frac{\bar{P}_\mu \times \bar{q}}{|\bar{P}_\mu \times \bar{q}|} \cdot \frac{\bar{p}_h \times \bar{q}}{|\bar{p}_h \times \bar{q}|}, \tag{7.1}$$

where $\bar{q}$ is the 3-momentum of the virtual photon, $\bar{P}_\mu$ is the 3-momentum of the scattered muon, and $\bar{p}_h$ is the 3-momentum of the hadron.

The cross section can be written, employing the approximation of Factorization as in Equation 2.27 as the product of the cross section for the lepton scattering and of the cross section for the final state particles:

$$\frac{d^5\sigma}{dxdydZdP_t^2d\phi} = \frac{d^2\sigma^\mu}{dxdy}\left[\frac{d^5\sigma^{h^\pm}}{(dxdy)(dZdP_t^2d\phi)}\right]. \tag{7.2}$$

The first factor can be interpreted simply as the number of scattered muons in the interval of $(dxdy)$; integration over the other two hadron variables Z and P_t, then, yields the expression

$$\frac{1}{N_\mu}\frac{dN^{h^\pm}}{d\phi} = \frac{1}{d^2\sigma^\mu/(dxdy)}\frac{d^3\sigma^{h^\pm}}{(dxdy)d\phi}, \tag{7.3}$$

where the $d^2/(dxdy)$ operator indicates the residual dependence of the hadronic production upon the kinematics of the event.

The general form of the ϕ-dependence of the hadro-production cross section has four terms:

$$\frac{1}{N_\mu}\frac{dN^{h^\pm}}{d\phi} = a + bf_1(y)\cos\phi + cf_2(y)\cos 2\phi + df_3(y)\sin\phi, \tag{7.4}$$

where the functions f_i indicate the dependence of the terms on the polarization of the virtual photon. These four terms are motivated by conservation of helicity in the exchange of the virtual photon. The term (a) represents the absorption cross section of transverse unpolarized virtual photons plus the cross section of longitudinally polarized virtual photons. The coefficient (c) represents the interference between the two transverse polarizations of the virtual photon. The other two coefficients represent the interference between the linear polarized transverse and the longitudinally polarized virtual photons: (b) is the real part and (d) is the imaginary part.

These terms are, in fact, quite general; they describe the angular momentum dependence of the interaction. This is discussed in detail in reference [8]. Thus, any process which generates angular momentum will contribute to these terms — for example, the primordial k_t and the gluon-bremsstrahlung radiation.

The dependence on y of these terms through the functions f_i is related to the helicity coefficient ϵ:

$$\epsilon = \frac{1-\cos^2\theta_\mu}{1+\cos^2\theta_\mu}. \tag{7.5}$$

Neglecting the mass for relativistic muons, this is approximately [35]

$$\epsilon = \frac{2EE'}{E^2+E'^2} = \frac{2(1-y)}{1+(1-y)^2}. \tag{7.6}$$

The corresponding function for each ϕ-term in Equation 7.4 is

$$f_1(y) = \frac{(2-y)\sqrt{1-y}}{1+(1-y)^2} \tag{7.7}$$

$$f_2(y) = \frac{(1-y)}{1+(1-y)^2} \tag{7.8}$$

$$f_3(y) = \frac{y\sqrt{1-y}}{1+(1-y)^2}. \tag{7.9}$$

With y written in terms of the helicity coefficient,

$$y = \frac{(1-\epsilon)}{2\epsilon}\left[\sqrt{1+\frac{4\epsilon}{(1-\epsilon)}}-1\right], \tag{7.10}$$

the functions can be written in terms of ϵ:

$$f_1(\epsilon) = \sqrt{\frac{2}{\epsilon}}\frac{(1+g(\epsilon)^2)g(\epsilon)}{g(\epsilon)^2} \tag{7.11}$$

$$f_2(\epsilon) = \frac{1}{2}\epsilon \tag{7.12}$$

$$f_3(\epsilon) = \sqrt{\frac{2}{\epsilon}}\frac{(1-g(\epsilon)^2)g(\epsilon)}{g(\epsilon)^2}, \tag{7.13}$$

where the function $g(\epsilon)$ is defined as

$$g(\epsilon) = \frac{1}{\sqrt{8\epsilon}}\sqrt{\epsilon^2+4\epsilon+2-2(1+\epsilon)(1-\epsilon)\sqrt{\frac{1+3\epsilon}{1-\epsilon}}}. \tag{7.14}$$

The size of the asymmetry will depend on the strengths of the contributions, and these will be described by the relative magnitudes of the four terms in Equation 7.4. It is easiest to describe these magnitudes by calculating the mean values of the three moments. Let $m(\phi)$ stand for each moment, $(\cos\phi, \cos 2\phi, \sin\phi)$, and let $S(\phi)$ stand for the cross section, as described by Equation 7.4. Then, the mean value of a given moment will be given by the integrals:

$$\langle m(\phi)\rangle = \frac{\int_0^{2\pi} S(\phi)m(\phi)d\phi}{\int_0^{2\pi} S(\phi)d\phi}. \tag{7.15}$$

The dependence of the moments upon the kinematics through the functions f_i can be removed by dividing the mean values of the moments, as calculated through Equation 7.15, by the mean value of the appropriate function, $\langle f_i(y)\rangle$.

This gives the size of the relevant contributions of the terms to the cross section. The contribution from the primordial k_t would yield the expressions [15]:

$$\langle\cos\phi\rangle/\langle f_1(y)\rangle = -\frac{2k_t}{Q} \tag{7.16}$$

$$\langle\cos 2\phi\rangle/\langle f_2(y)\rangle = \frac{2k_t^2}{Q^2}. \tag{7.17}$$

The contribution from the gluon-bremsstrahlung radiation to the $\cos\phi$ moment would yield in the limit $Z \to 1$ [26]:

$$\langle\cos\phi\rangle/\langle f_1(y)\rangle = -\kappa\frac{\alpha_s}{2}\sqrt{1-Z}, \tag{7.18}$$

where κ is a constant (which is about unity), α_s is the strong coupling constant, and Z is the normalized-energy variable of the hadron. The contributions from the

two effects should have different behavior. The contribution to $\cos\phi$ from primordial k_t from Equation 7.16 depends on Q^{-1}, while that from the QCD effect of gluon-bremsstrahlung radiation depends on α_s; the coupling constant varies only slowly with Q^2, in the form $(\log Q^2/Q_0^2)^{-1}$. These predicted curves are included in Figure 7.3.

In contrast to the contributions to the asymmetry from these effects, the effects of hadronization will tend to smear out the asymmetry. This is due to the apparently random dressing of the hadrons in fragmentation with perpendicular momentum, $P_\perp$. The work by Cahn [15] assumed a gaussian form for the $P_\perp$, which led to a dependence of the asymmetry upon $P_\perp$ of the form:

$$\frac{d\sigma}{d^3p} \propto A + B\frac{\bar{P}_\perp}{Z}\cdot\hat{x}\left(\frac{bZ^2}{a+bZ^2}\right) + C\left[2\left(\frac{\bar{P}_\perp\cdot\hat{x}}{Z}\right)^2 - \left(\frac{\bar{P}_\perp}{Z}\right)^2\right]\left[\frac{bZ^2}{a+bZ^2}\right]^2. \quad (7.19)$$

Thus, if the hadronization introduces perpendicular momentum, via a finite value for b, then the azimuthal asymmetry will be reduced by this smearing.

7.4 Data

7.4.1 EMC

The distribution of the normalized differential cross section as a function of ϕ is shown for the EMC data [17] in Figure 7.2. The plot includes charged particles with $X_F > 0.2$, and the analysis employed a minimum P_t cut on the tracks of $P_t > 0.2$ GeV. The distributions were normalized to an arbitrary scale. The plot in Figure 7.3 shows the mean value of the $\cos\phi$ moment as a function of X_F. The distributions for the $\cos 2\phi$ moment and the $\sin\phi$ moment are shown in Figures 7.4(a) and (b), respectively. The dependence of the $\cos\phi$ moment upon the minimum P_t cut is shown in Figure 7.5. The asymmetry appears mainly in the $\cos\phi$ moment, and it increases with X_F. The asymmetry also increases as the threshold P_t cut is raised.

7.4.2 ϕ Resolution

The ability to define the azimuthal angle ϕ depends upon the separation of the hadron from the virtual photon directions and, hence, upon P_t, in the form roughly of $\sin^{-1}(P_t/P)$. As can be seen in Figure 7.6, this quantity is typically much larger than the error on the value of the scattering angle, $\triangle\theta$. There were no tracks for

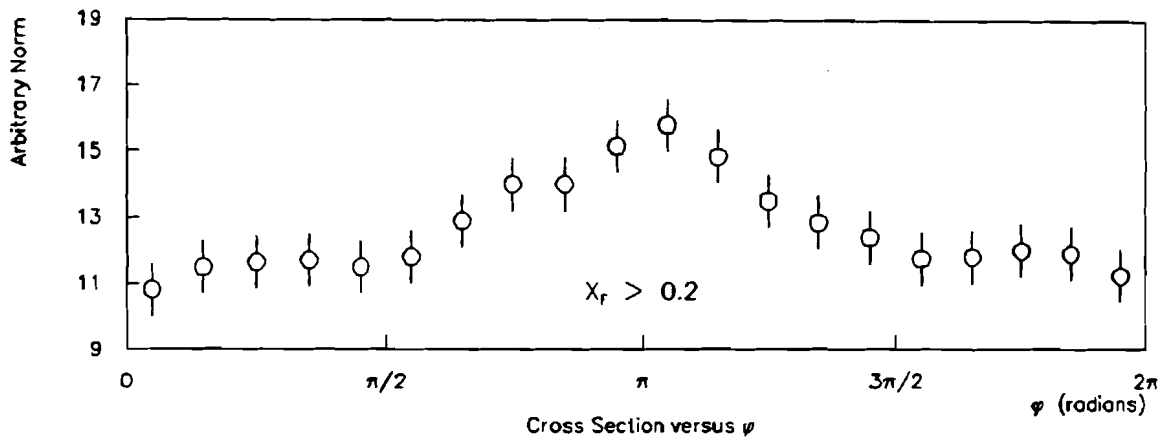

Figure 7.2: EMC ϕ-distribution.
This plot shows the ϕ-distribution from EMC [17], for charged hadrons with $P_t > 0.2$ GeV.

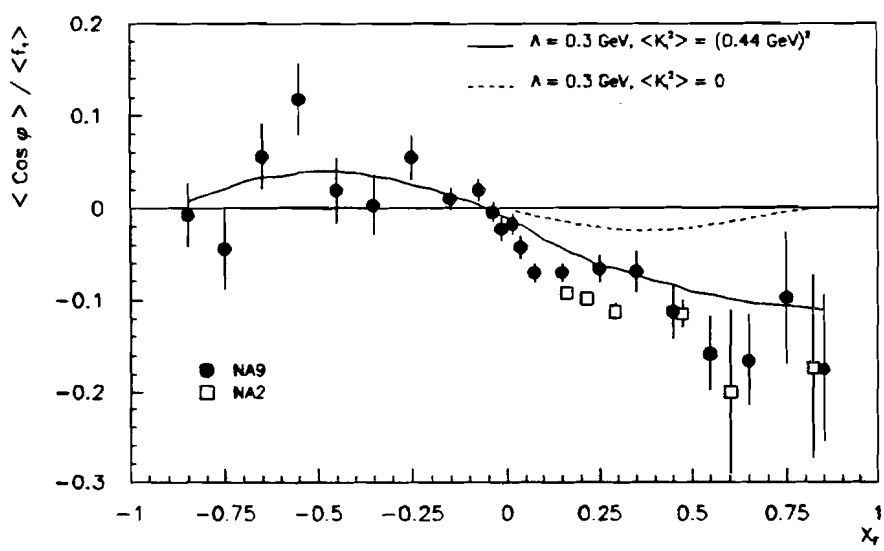

Figure 7.3: EMC $\cos\phi$ moment versus X_F.
This plot shows the $\cos\phi$ moment from EMC [19, 17], as a function of X_F, for charged hadrons with $P_t > 0.2$ GeV.

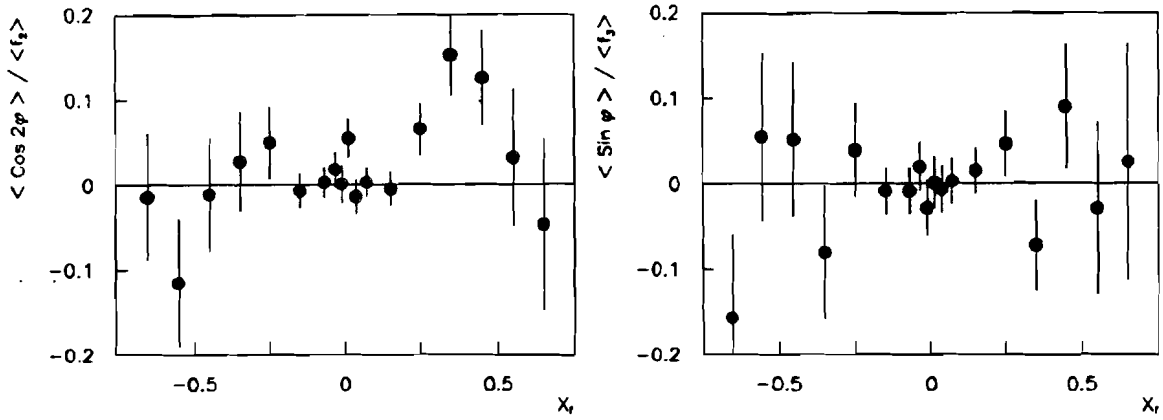

Figure 7.4: EMC $\cos 2\phi$ and $\sin \phi$ moments versus X_F .
These plots show the $\cos 2\phi$ and $\sin \phi$ moments from EMC [17], as a function of X_F, for charged hadrons with $P_t > 0.2$ GeV.

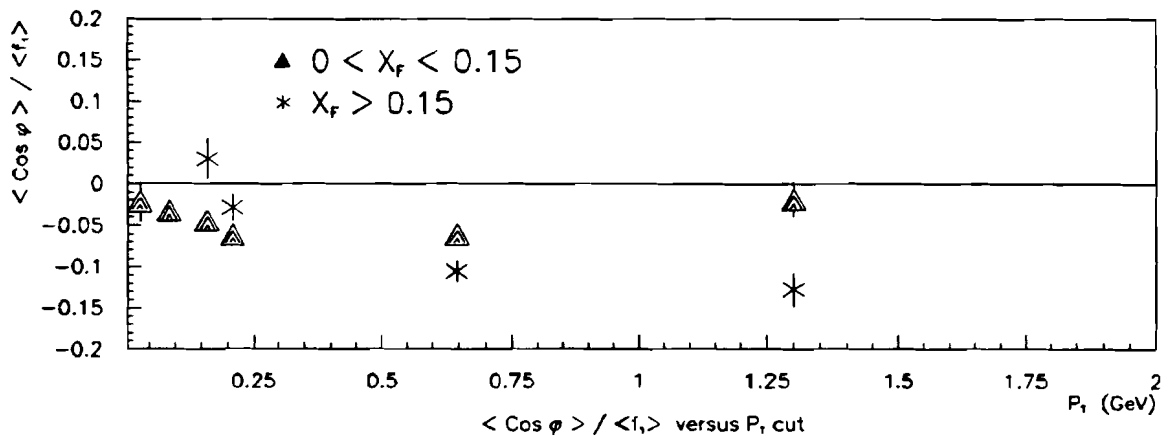

Figure 7.5: EMC $\cos \phi$ moment as a function of the minimum P_t cut imposed on the tracks [17].

which this separation was less than the resolution on the muon scattering angle ($\sin^{-1}(P_t/P) > \triangle\theta$).

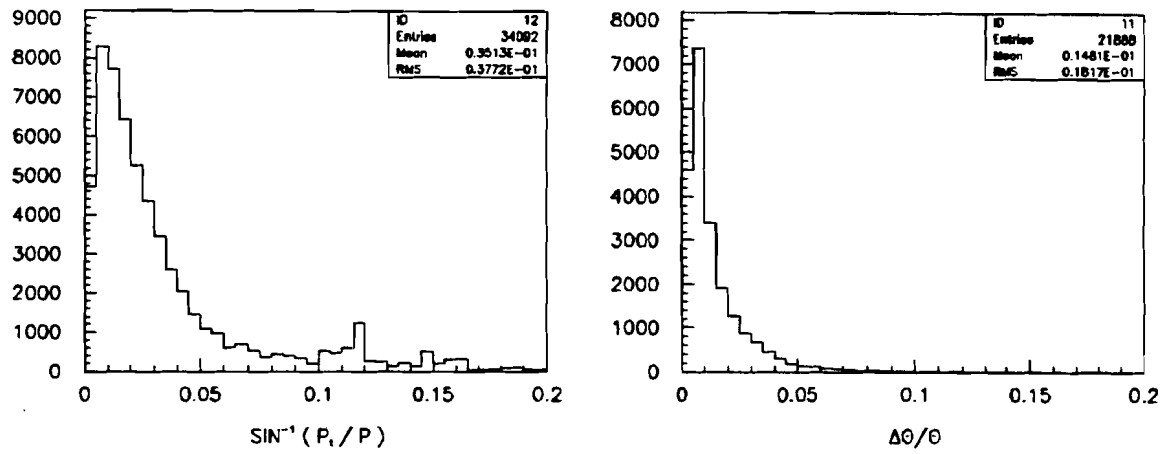

Figure 7.6: Resolution of Track Separation from Photon direction . Plot (a) shows the distribution of the quantity $\sin^{-1}(P_t/P)$, which is a measure of the separation of each track from the direction of the virtual photon. Plot (b) shows the resolution on the scattering angle, $\triangle\theta$.

In calculating the moments of the ϕ-distributions, the dependence of the moments upon the kinematic functions f_1, f_2, and f_3 was factored out by dividing the values of the moments by the mean values of these functions: $\langle f_i(y)\rangle$. The f_i distributions are shown in Figure 7.7.

7.4.3 Deuterium

The ϕ-distribution from the Deuterium data from this experiment is plotted in Figure 7.8a for all tracks. Figure 7.8b shows the effect of requiring a minimum value of $P_t > 0.2$ GeV/c and a minimum value of $Z > 0.2$ for the charged hadrons to be considered; this plot may be compared to that in Figure 7.2. Both distributions have been fit to the function described by Equation 7.4; the resultant values of the parameters are listed in the upper right-hand corner of each plot. The values of the moments, as determined by Equation 7.15, are listed in the upper left-hand corner of the plots. The distribution is clearly asymmetric, with the predominant contribution from the $\cos\phi$ moment; this moment is negative, and is significant at the 7σ level.

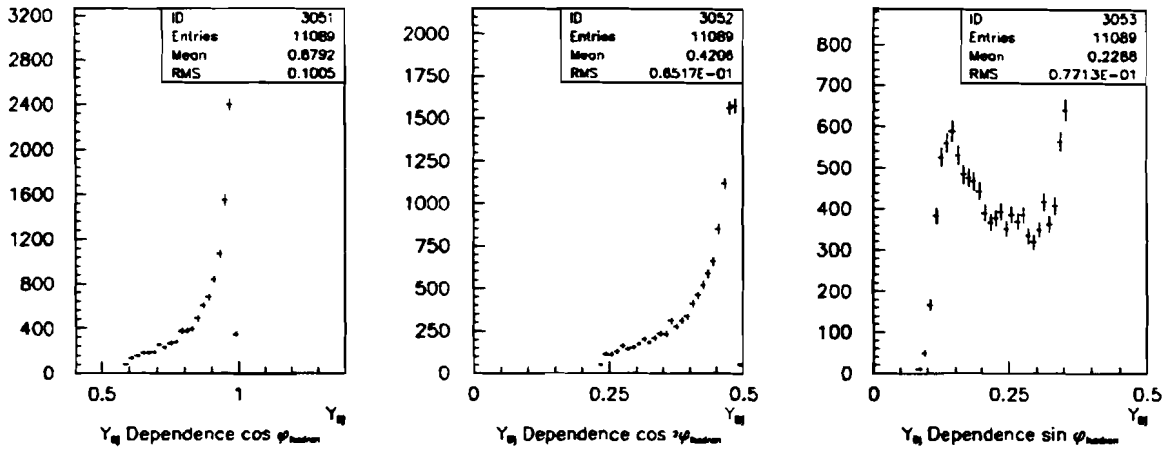

Figure 7.7: $f_i(y)$ distributions, D_2.
Plot (a) shows the distribution of $f_1(y)$, (b) of $f_2(y)$, and (c) of $f_3(y)$.

The $\cos 2\phi$ moment is significant to only 2σ, and the $\sin\phi$ moment is consistent with zero.

These moments extracted from the distributions provide a concise quantitative measure of the asymmetry. These can be calculated for various ranges of kinematics to search for a dependence. The models predicting asymmetry for these moments depend also on the hadron variables Z and P_t. Since X_F is equivalent to Z for almost all of the tracks in this analysis, only dependences on Z will be shown. In Figure 7.9, the $\cos\phi$ moments are plotted as functions of the kinematic variables Q^2, $\log_{10} Q^2$, W^2, $\log_{10} X_{Bj}$ and of the hadron variables Z and P_t. The statistics at high-Q^2 were small relative to low-Q^2, so it was more balanced to plot the moments as a function of $Log_{10}Q^2$, as in Figure 7.9(b). The $\cos 2\phi$ moments are plotted in Figure 7.10, and the $\sin\phi$ moments are plotted in Figure 7.11. The asymmetry due to the $\sin\phi$ moment is consistent with zero. The asymmetry due to the $\cos 2\phi$ moment shows no dependence on the kinematic variables; it is positive by 2σ for only the mid-range of Z. The asymmetry due to the $\cos\phi$ moment clearly rises with Z but shows little enhancement with P_t after ~ 0.5 GeV/c.

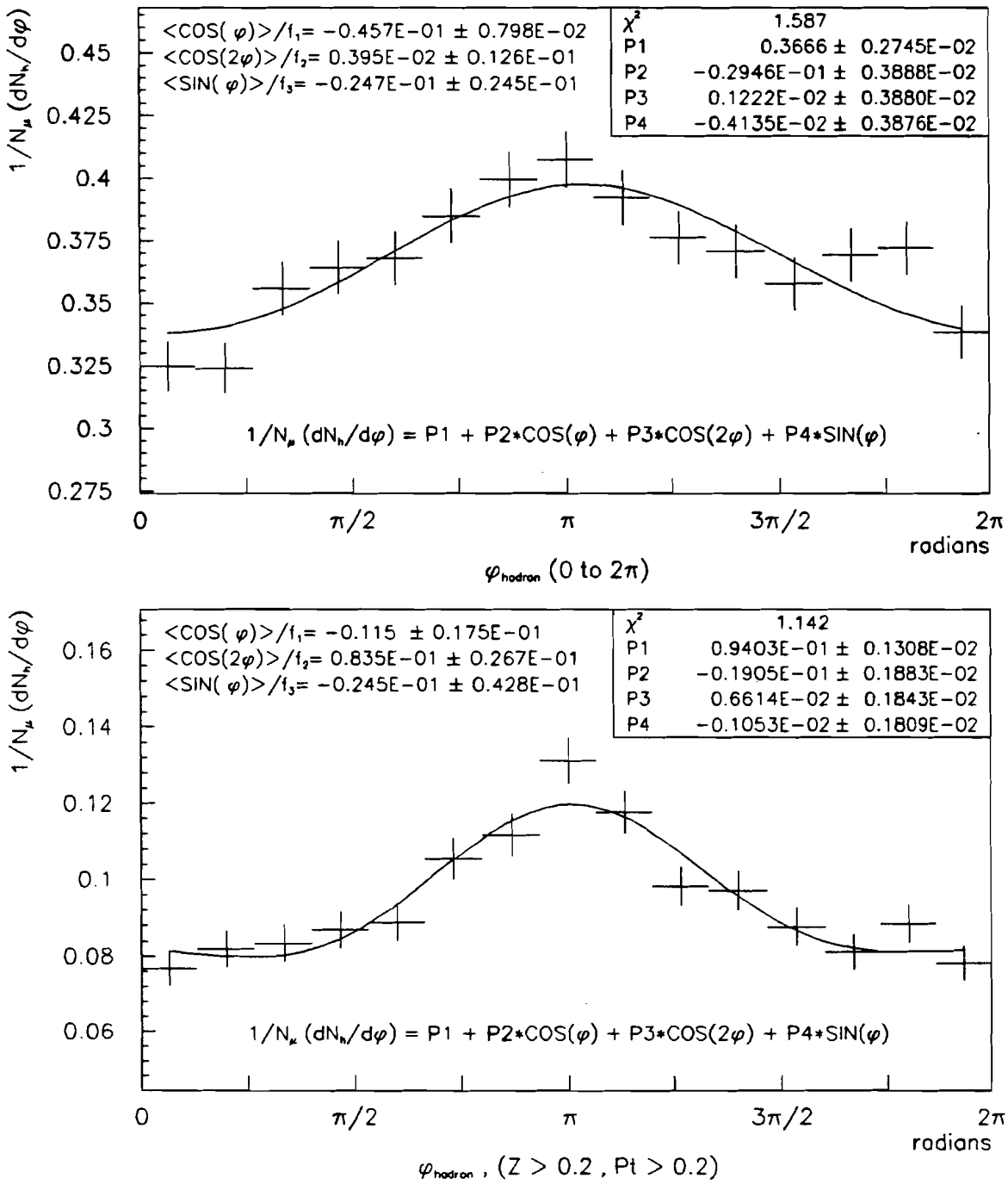

Figure 7.8: ϕ-distribution . Plot (a) shows the ϕ-distribution for all tracks. Plot (b) shows the ϕ-distribution for tracks which pass the two cuts: $P_t > 0.2$ GeV/c and $Z > 0.2$.

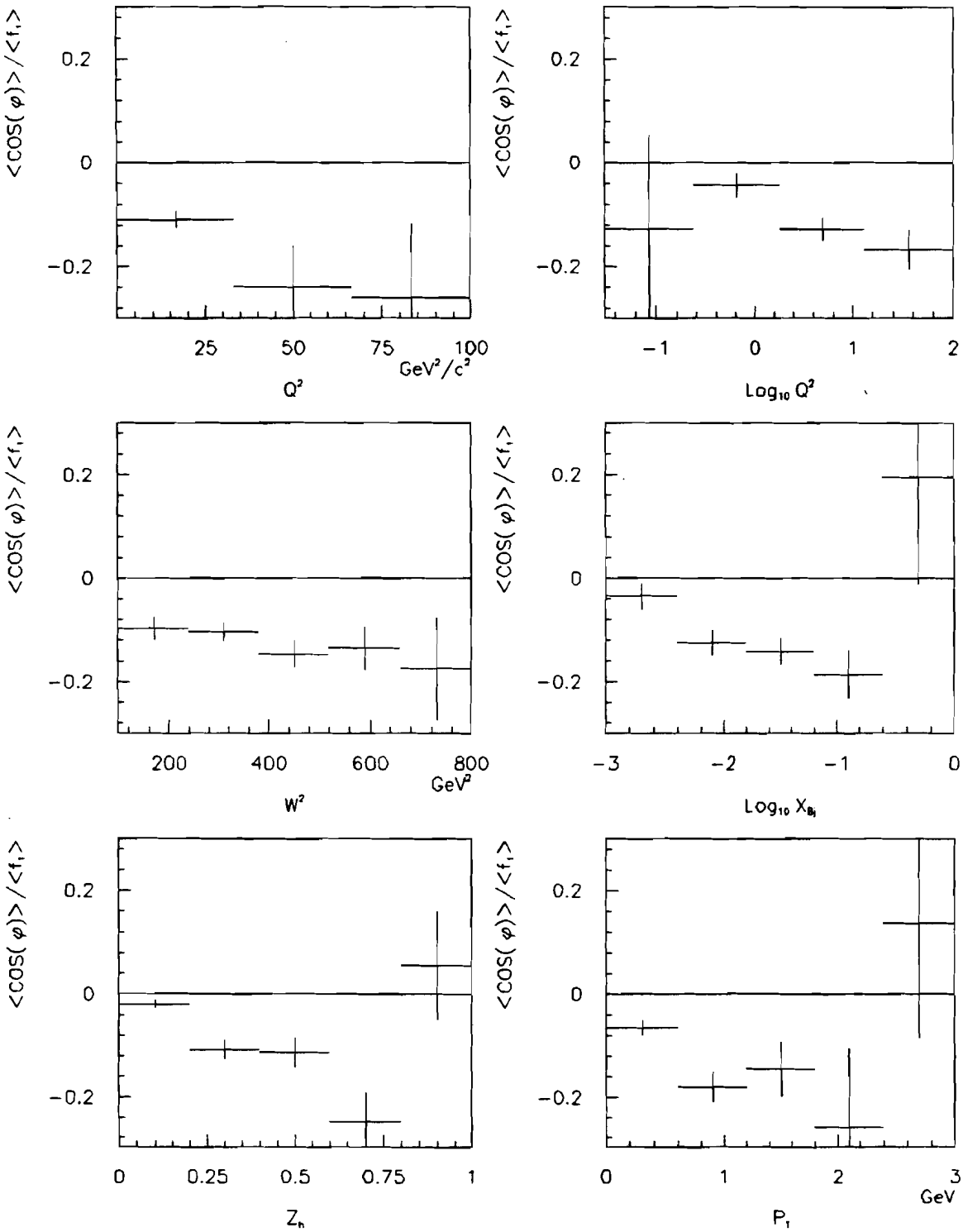

Figure 7.9: $\cos\phi$-moments, D_2.
Plots (a-d) show the $\cos\phi$-moments as functions of the kinematic variables $Q^2, \log_{10} Q^2, W^2, \log_{10} X_{Bj}$; these contributions to these distributions were limited to tracks with $Z > 0.2$ and $P_t > 0.2$ GeV/c. Plots (e) and (f) show the moments as functions of the hadron variables Z and P_t; plot (e) had only the P_t cut, and plot (f) had only the Z cut.

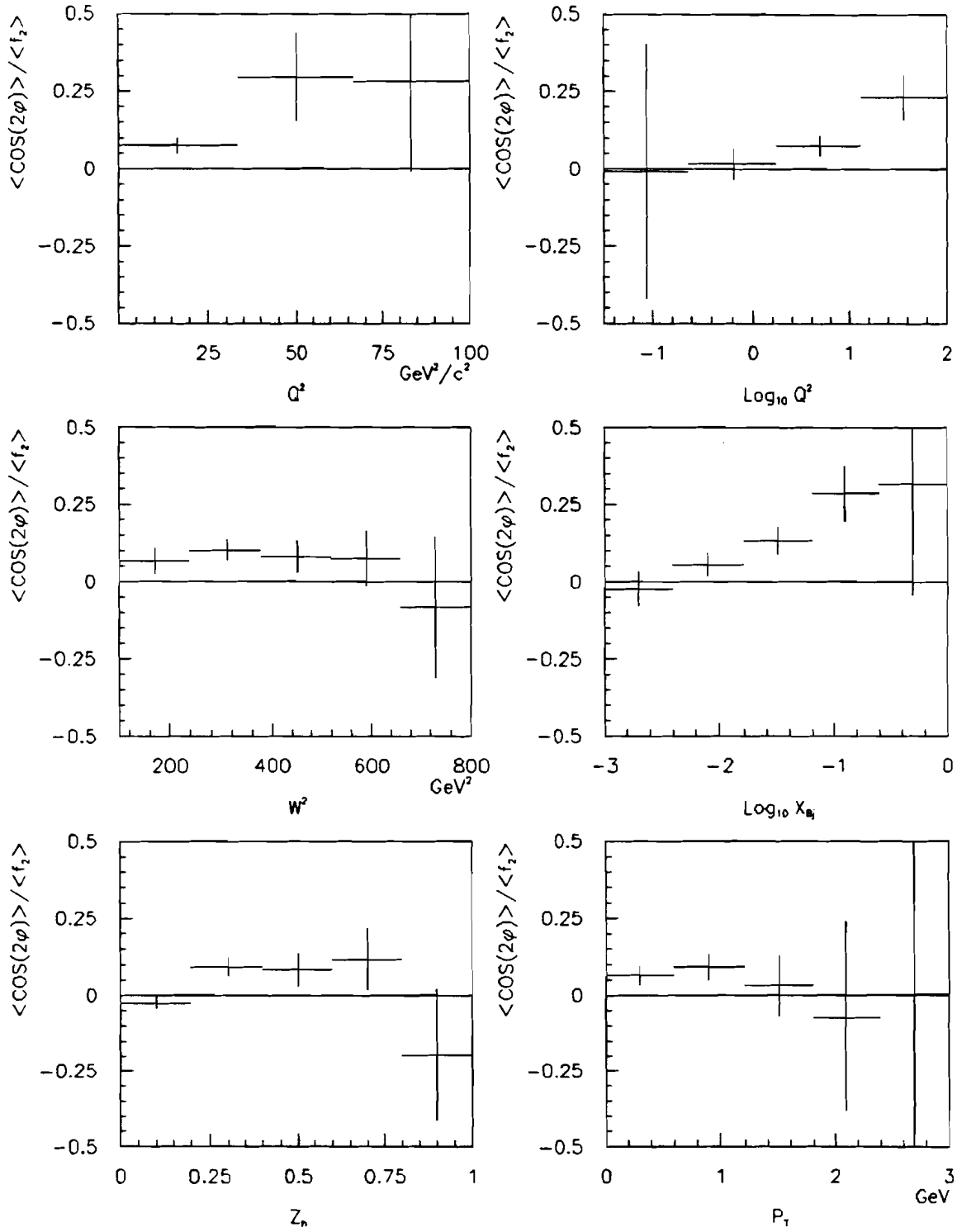

Figure 7.10: $\cos 2\phi$-moments, D_2.
Plots (a-d) show the $\cos 2\phi$-moments as functions of the kinematic variables $Q^2, \log_{10} Q^2, W^2, \log_{10} X_{Bj}$; these contributions to these distributions were limited to tracks with $Z > 0.2$ and $P_t > 0.2$ GeV/c. Plots (e) and (f) show the moments as functions of the hadron variables Z and P_t; plot (e) had only the P_t cut, and plot (f) had only the Z cut.

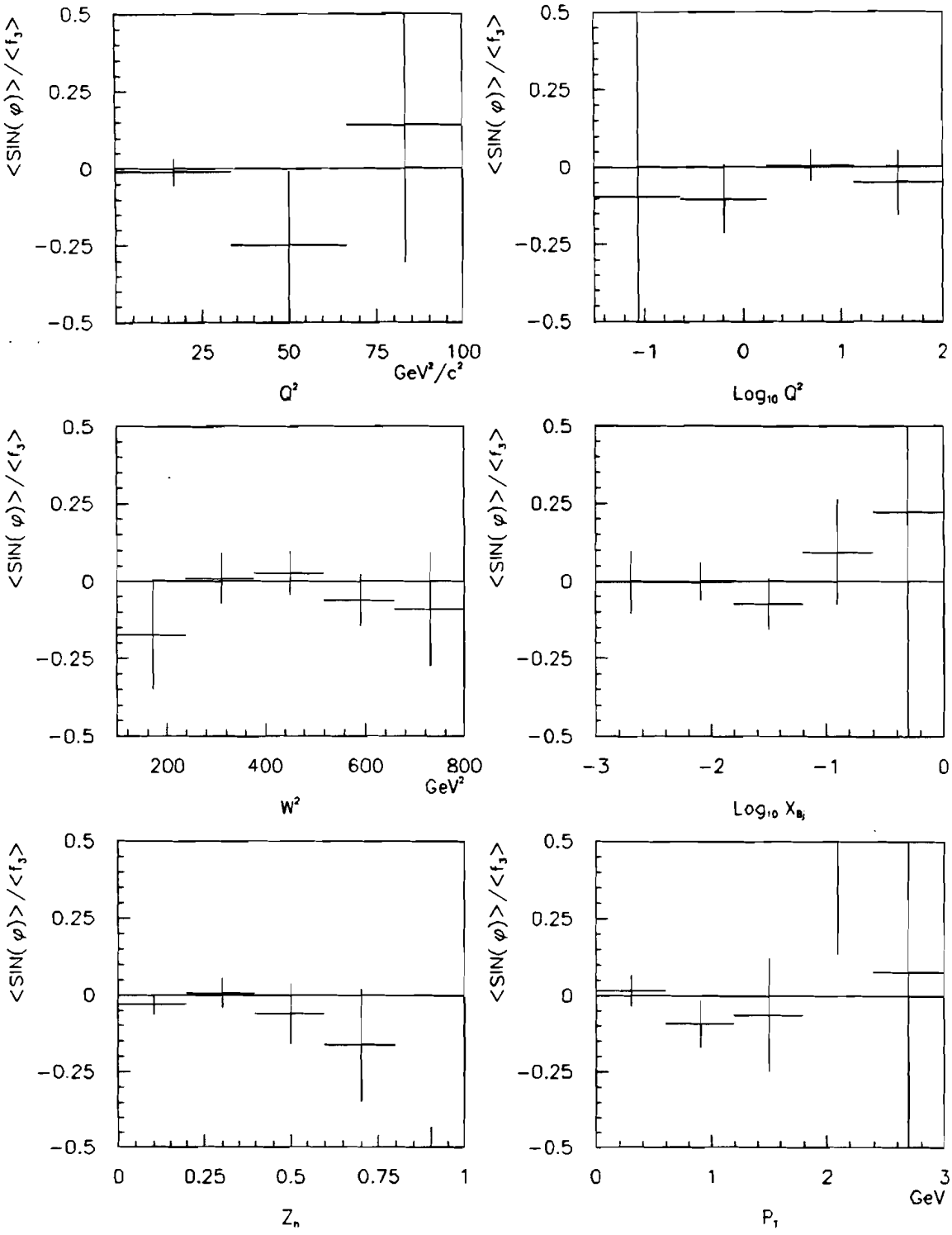

Figure 7.11: $\sin\phi$-moments, D_2.
Plots (a-d) show the $\sin\phi$-moments as functions of the kinematic variables $Q^2, \log_{10} Q^2, W^2, \log_{10} X_{Bj}$; these contributions to these distributions were limited to tracks with $Z > 0.2$ and $P_t > 0.2$ GeV/c. Plots (e) and (f) show the moments as functions of the hadron variables Z and P_t: plot (e) had only the P_t cut, and plot (f) had only the Z cut.

7.4.4 Xenon

If the asymmetry were due to an effect such as primordial k_t or gluon-bremsstrahlung radiation, then the modifications of these effects due to the neighboring nucleons in a nuclear target might alter the observed asymmetry. To search for any such effects, I show the moments of the ϕ-distribution for the Xenon sample overlaid on those for the Deuterium sample. The ϕ-distribution for the Xenon sample is shown in Figure 7.12. The $\cos\phi$ moments are plotted in Figure 7.13 as functions of the kinematic variables $Q^2, \log_{10} Q^2, W^2, \log_{10} X_{Bj}$ and of the hadron variables Z and P_t; the Xenon points are the diamonds, while the Deuterium points are the boxes. The moments from the Xenon sample exhibit no difference from those from the Deuterium sample. The $\cos 2\phi$ moments are plotted in Figure 7.14, and the $\sin\phi$ moments are plotted in Figure 7.15; again, the Xenon points are the diamonds, while the Deuterium points are the boxes. Neither of these moments from the Xenon sample exhibit any difference from those from the Deuterium sample.

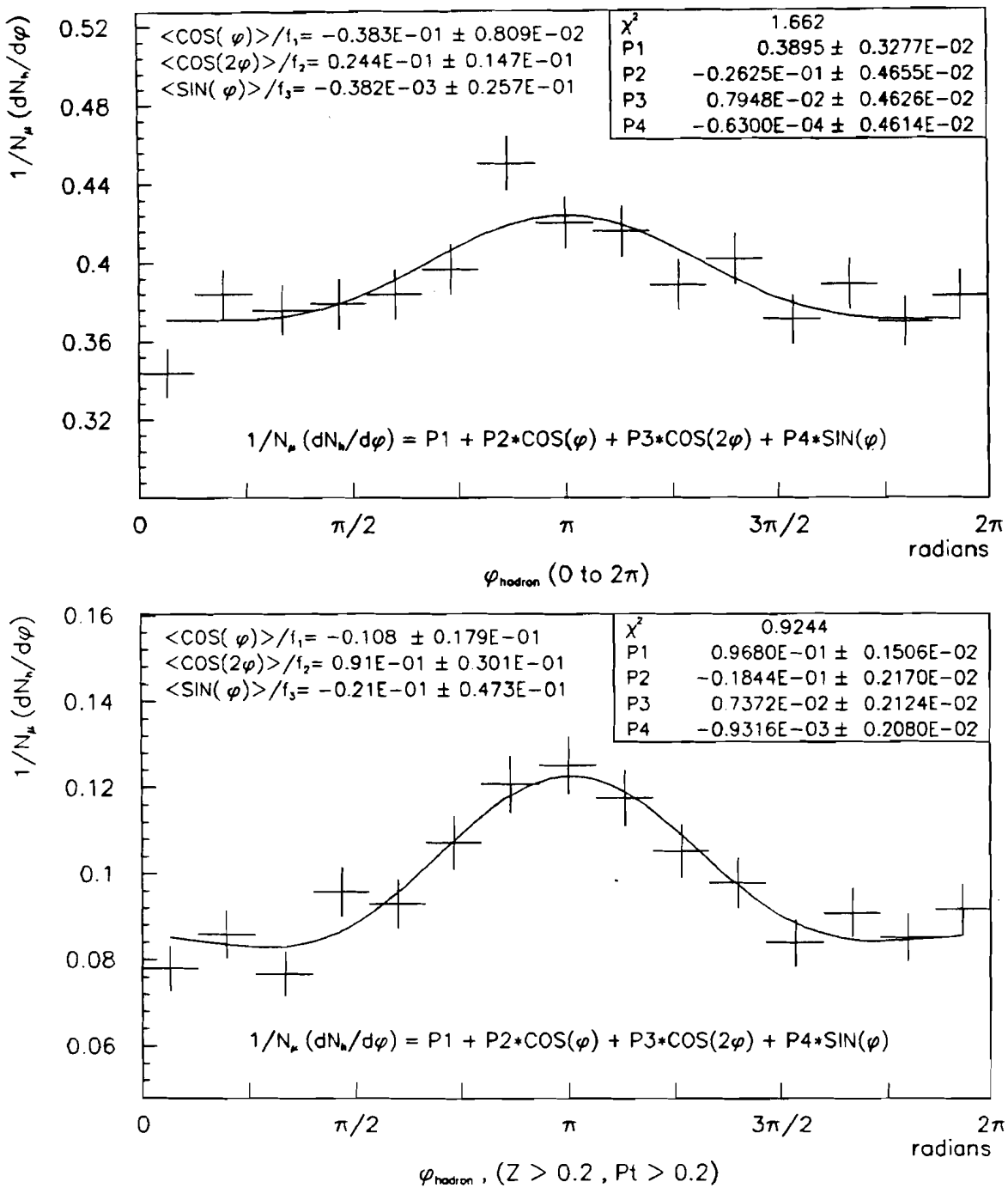

Figure 7.12: ϕ-distribution, Xenon. Plot (a) shows the ϕ-distribution for all tracks. Plot (b) shows the ϕ-distribution for tracks which pass the two cuts: $P_t > 0.2$ GeV/c and $Z > 0.2$.

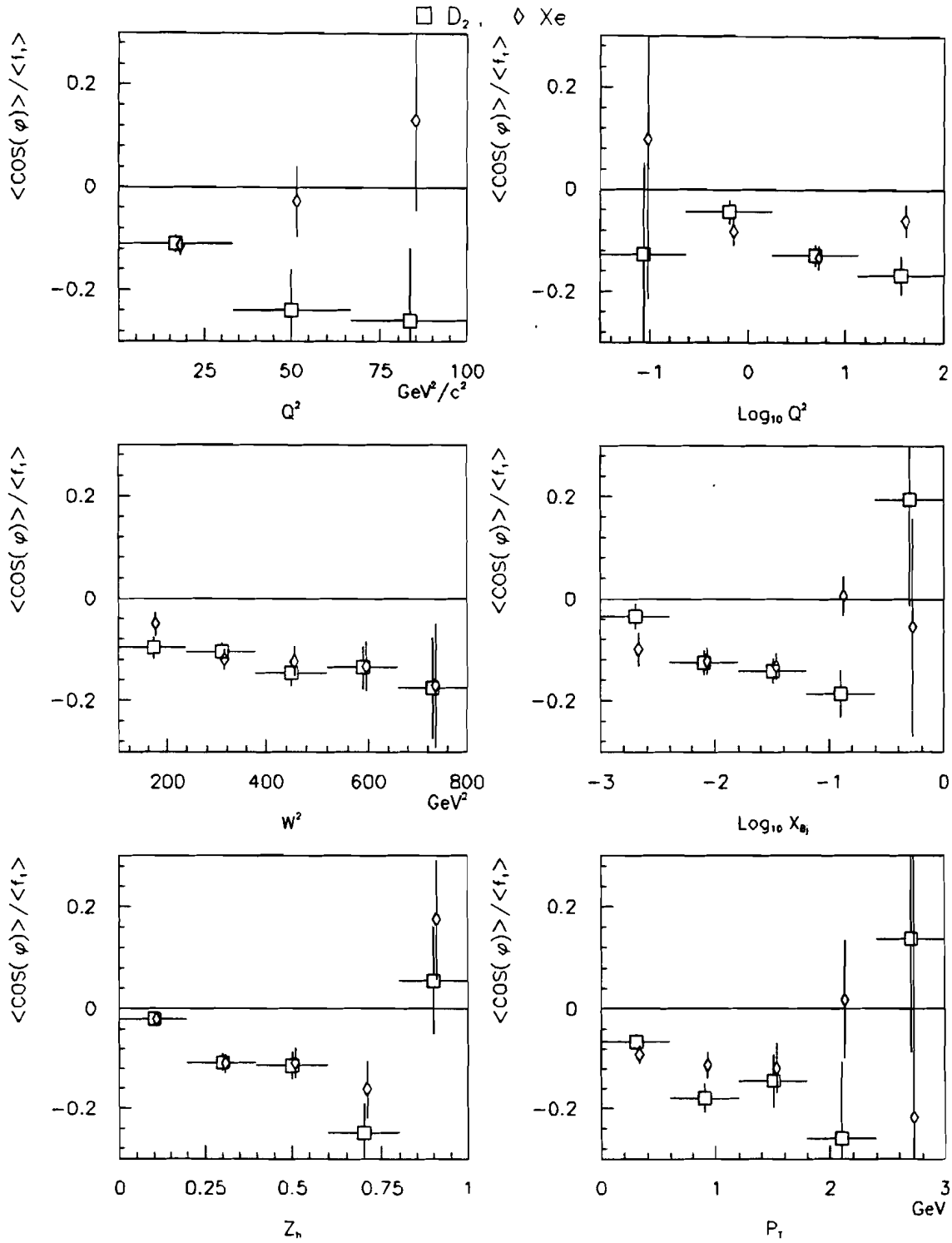

Figure 7.13: $\cos\phi$-moments, Xenon.
Plots (a-d) show the $\cos\phi$-moments as functions of the kinematic variables $Q^2, \log_{10} Q^2, W^2, \log_{10} X_{Bj}$; these contributions to these distributions were limited to tracks with $Z > 0.2$ and $P_t > 0.2$ GeV/c. Plots (e) and (f) show the moments as functions of the hadron variables Z and P_t; plot (e) had only the P_t cut, and plot (f) had only the Z cut.

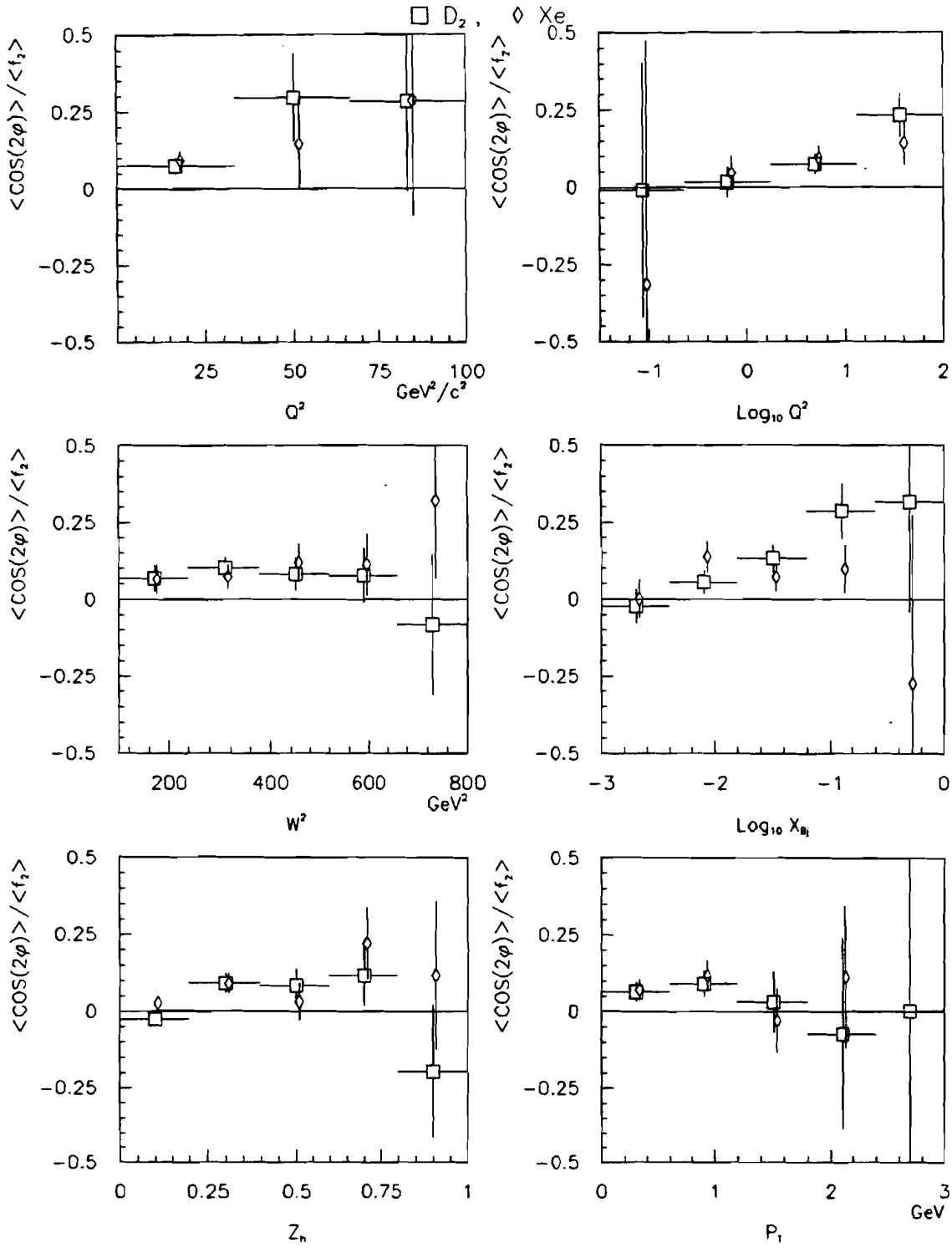

Figure 7.14: $\cos 2\phi$-moments, Xenon.
Plots (a-d) show the $\cos 2\phi$-moments as functions of the kinematic variables $Q^2, \log_{10} Q^2, W^2, \log_{10} X_{Bj}$; these contributions to these distributions were limited to tracks with $Z > 0.2$ and $P_t > 0.2$ GeV/c. Plots (e) and (f) show the moments as functions of the hadron variables Z and P_t; plot (e) had only the P_t cut, and plot (f) had only the Z cut.

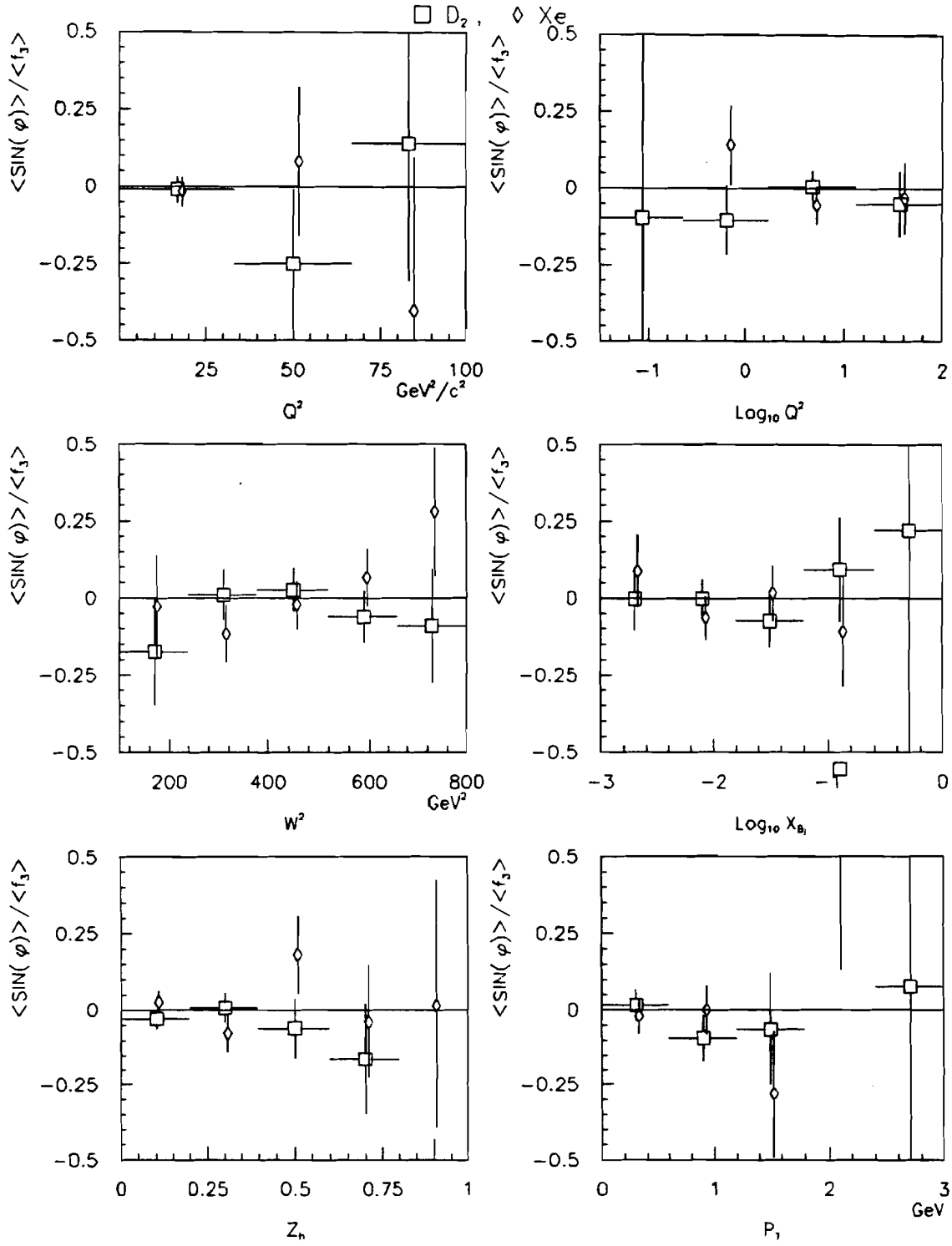

Figure 7.15: $\sin\phi$-moments, Xenon.
Plots (a-d) show the $\sin\phi$-moments as functions of the kinematic variables $Q^2, \log_{10} Q^2, W^2, \log_{10} X_{Bj}$; these contributions to these distributions were limited to tracks with $Z > 0.2$ and $P_t > 0.2$ GeV/c. Plots (e) and (f) show the moments as functions of the hadron variables Z and P_t; plot (e) had only the P_t cut, and plot (f) had only the Z cut.

7.4.5 Z-Ranking

The plots in Figures 7.9(e) and 7.13(e) indicate that the asymmetry associated with the $\cos\phi$ moment increases with Z. In a given fragmentation chain, the distributions of Z-values that each particle in the chain may receive cover a large range of Z; for example, the leading particle (the most energetic) can have Z-values from very small to almost 1. However, particles with high Z-values will usually be the leading particles. Therefore, from the observation that the $\cos\phi$ moment increases with Z, it is conceivable that the asymmetry is associated with the leading particles in the fragmentation chain. To examine this, I have used the Z-ranking machinery developed in the analysis of the Z-distributions of charged particles. For the power of increased statistics, I have merged the Deuterium and Xenon samples for these examinations: the justification for this is simply that the ϕ-distributions and the moments from the two samples were indistiguishable.

In Figure 7.16(a) I have plotted the ϕ-distribution of only the fastest particle in each event, in (b) the ϕ-distribution of only the second fastest particle, and in (c) the ϕ-distribution of only the third fastest particle. The $\cos\phi$-moment of the fastest particle was 7σ below zero, while that of the second fastest particle was only 2.8σ below zero; the $\cos\phi$-moment of the third fastest particle had changed sign but was only 1σ above zero. It appears that the asymmetry is carried predominantly by the leading particle. In Figure 7.17 I have plotted the ϕ-distribution of only the fastest particle for only those events with at least 3 charged tracks found. This has reduced the value of the $\cos\phi$-moment to 6σ below zero.

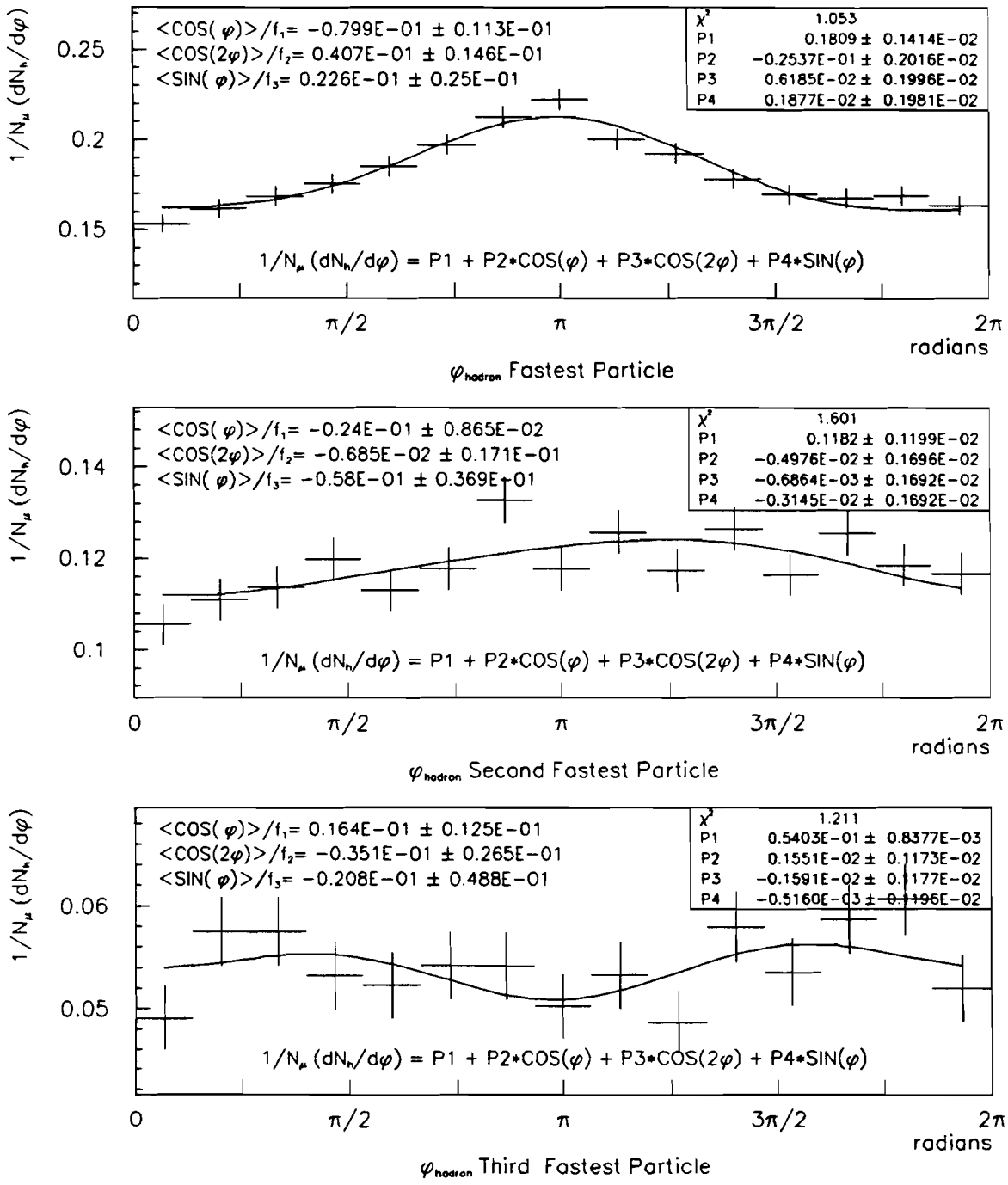

Figure 7.16: ϕ-distributions, Z-Ranked.
Plot (a) shows the ϕ-distribution for tracks of only the fastest particle in each event. Plot (b) shows the ϕ-distribution for tracks of only the second fastest particle in each event. Plot (c) shows the ϕ-distribution for tracks of only the third fastest particle in each event.

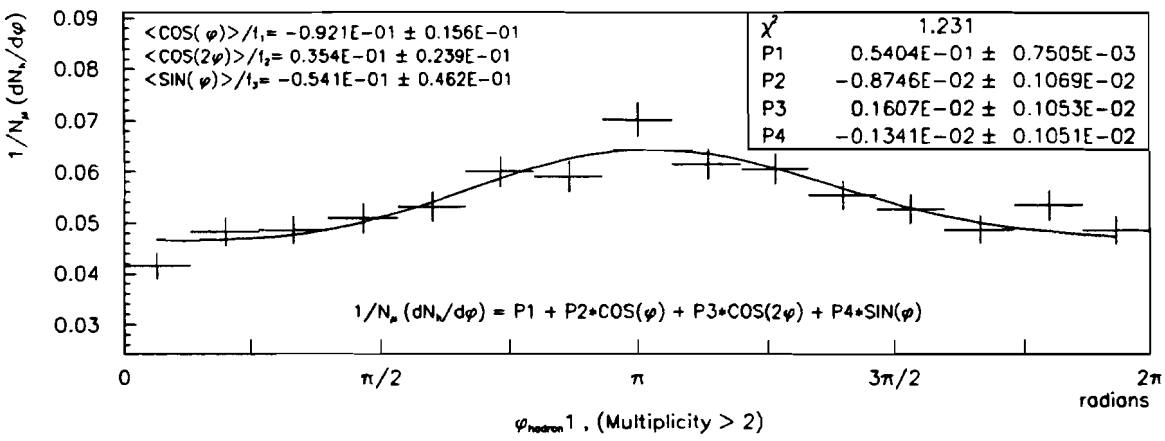

Figure 7.17: ϕ-distributions, Z_1, Multiplicity>2.
This plot shows the ϕ-distribution for tracks of only the fastest particle for events in which there were at least 3 charged tracks found.

The following deluge of plots will examine the dependence of the moments on kinematics, overlaying those for each Z-rank (1,2,3) in the fragmentation chain. The points for Z_2 and Z_3 have been shifted along the abscissa to allow viewing of the error-bars; the Z_1 points have horizontal error-bars, and these points are located at the actual abscissa values at which all values were calculated. These plots were generated from the merged Deuterium/Xenon sample. The contributions to these distributions were *not* limited to tracks with $Z > 0.2$ and $P_t > 0.2$ GeV/c. The $\cos\phi$ moments are plotted in Figure 7.18 as functions of the kinematic variables $Q^2, \log_{10} Q^2, W^{-2}, \log_{10} X_{Bj}$; these $\cos\phi$ moments as functions of the hadron variables Z and P_t are plotted in Figure 7.19. In these plots, the results for the fastest particles are displayed by the boxes, those for the second fastest by the circles, and those for the third fastest by the triangles. The moments of the fastest particle are consistently higher than those of the second and the third. In only the W^{-2} plot in Figure 7.18(c) does a moment for the second particle appear more than 2σ from zero, while the moments for the fastest particle appear to remain at $\sim 7\sigma$ below zero. The moments as a function of Z in Figure 7.19(a) indicate an asymmetry only for the fastest particle; the value of this asymmetry is almost flat as a function of Z. A similar dominance of the asymmetry in the fastest particle is seen in the dependence of the effect on the P_t of the particles; there is little change in the value of the asymmetry with increasing P_t for a given rank. The $\cos 2\phi$ moments are plotted in Figure 7.20, and the $\sin\phi$ moments are plotted in Figure 7.21; again, the results for the fastest particles are displayed by the boxes, those for the second fastest by the circles, and those for the third fastest by the triangles.

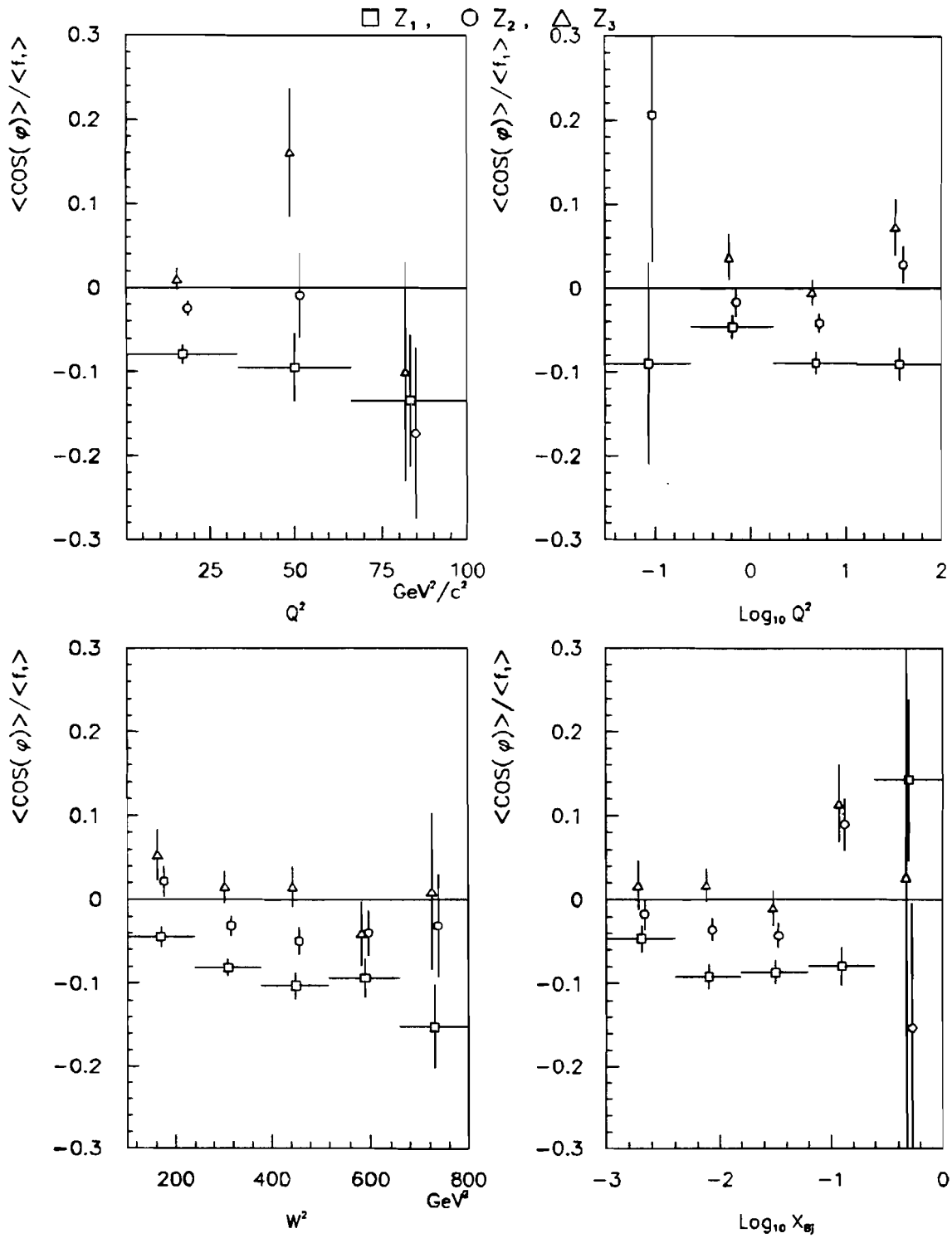

Figure 7:18: $\cos\phi$-moments, Z-Ranked.
Plots (a-d) show the $\cos\phi$-moments as functions of the kinematic variables $Q^2, \log_{10} Q^2, W^2, \log_{10} X_{Bj}$; these contributions to these distributions were *not* limited to tracks with $Z > 0.2$ and $P_t > 0.2$ GeV/c.

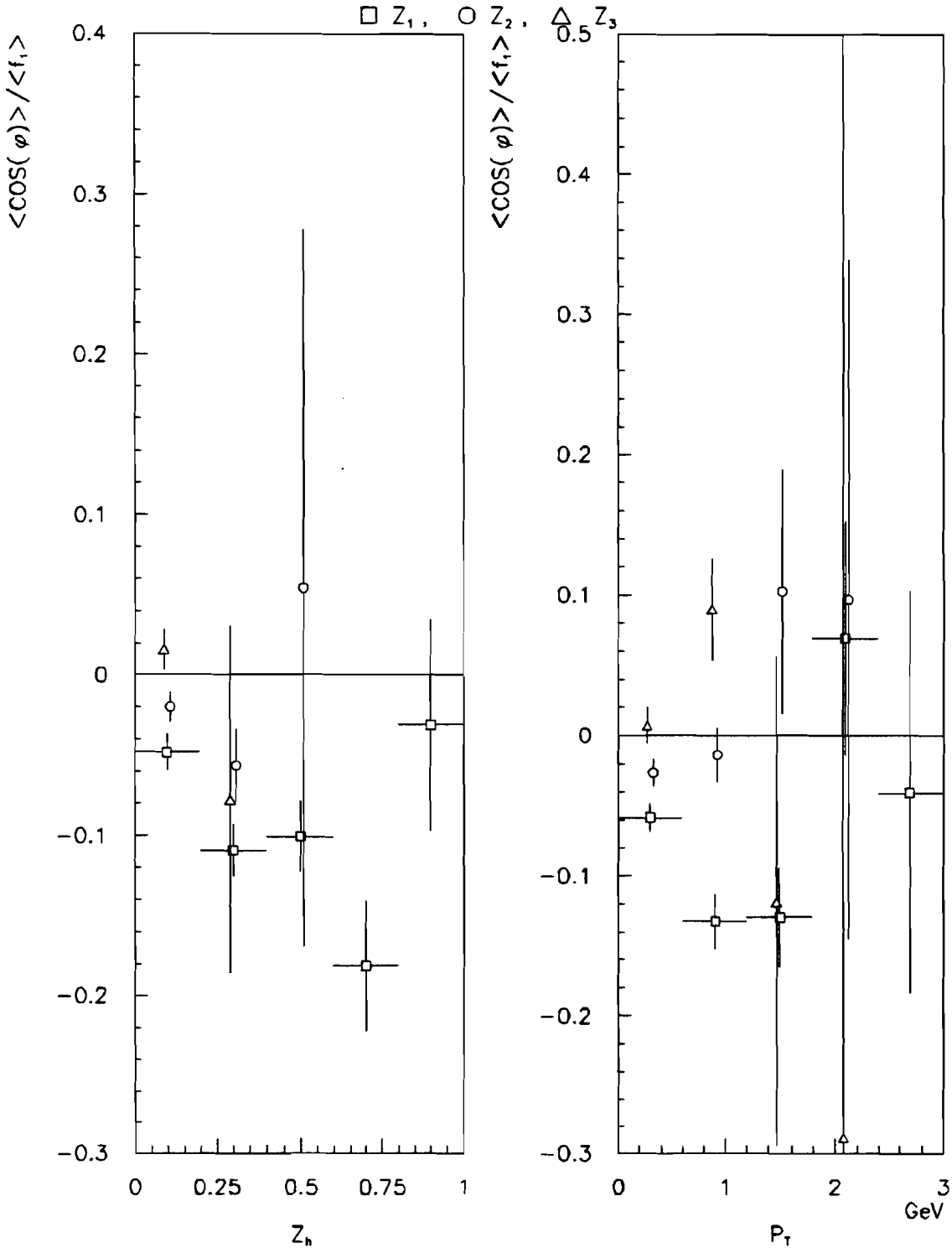

Figure 7.19: $\cos\phi$-moments, Z-Ranked versus Z and P_t.
Plots (a) and (b) show the $\cos\phi$-moments as functions of the hadron variables Z and P_t.

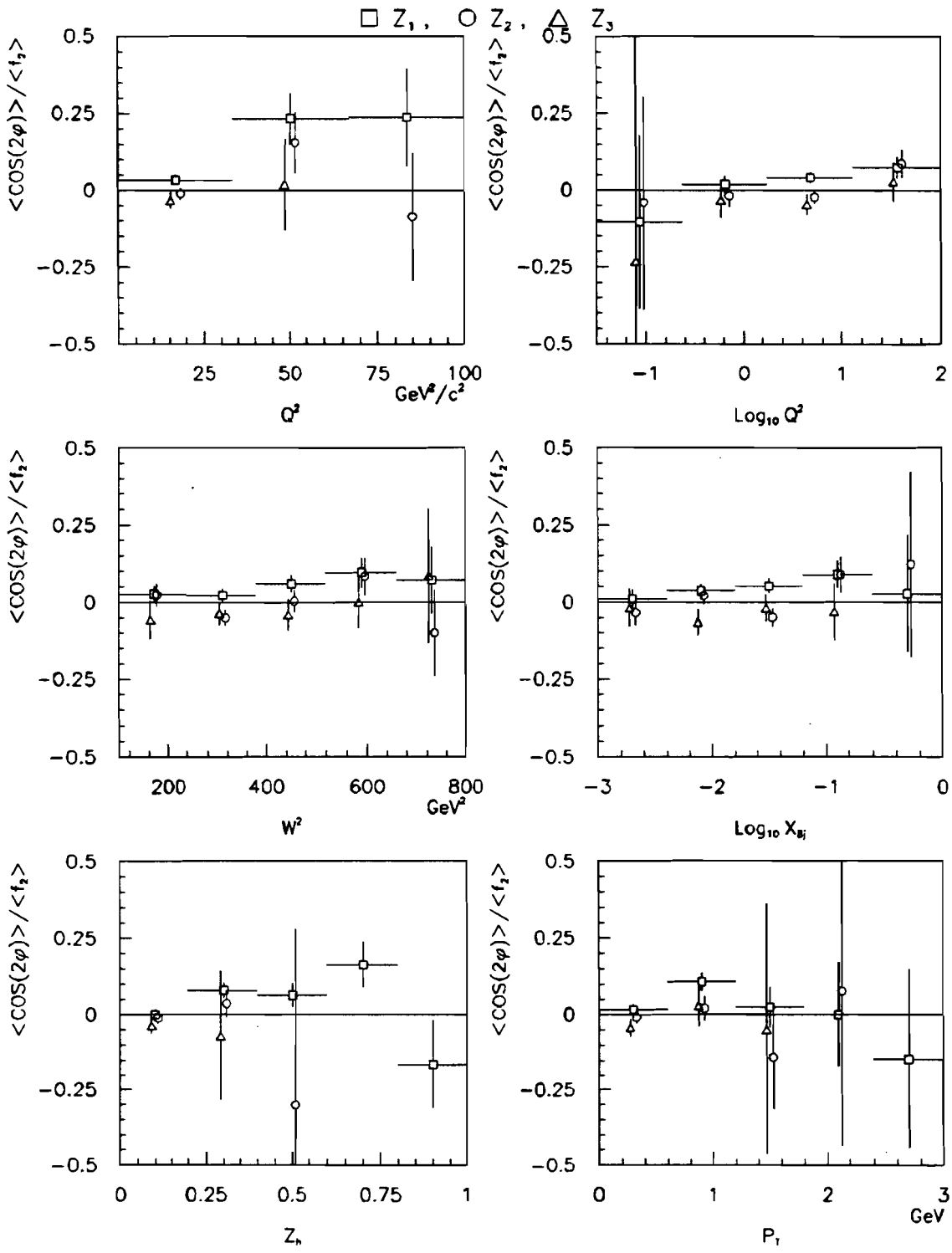

Figure 7.20: $\cos 2\phi$-moments, Z-Ranked.
Plots (a-d) show the $\cos 2\phi$-moments as functions of the kinematic variables $Q^2, \log_{10} Q^2, W^2, \log_{10} X_{Bj}$; these contributions to these distributions were *not* limited to tracks with $Z > 0.2$ and $P_t > 0.2$ GeV/c. Plots (e) and (f) show the moments as functions of the hadron variables Z and P_t.

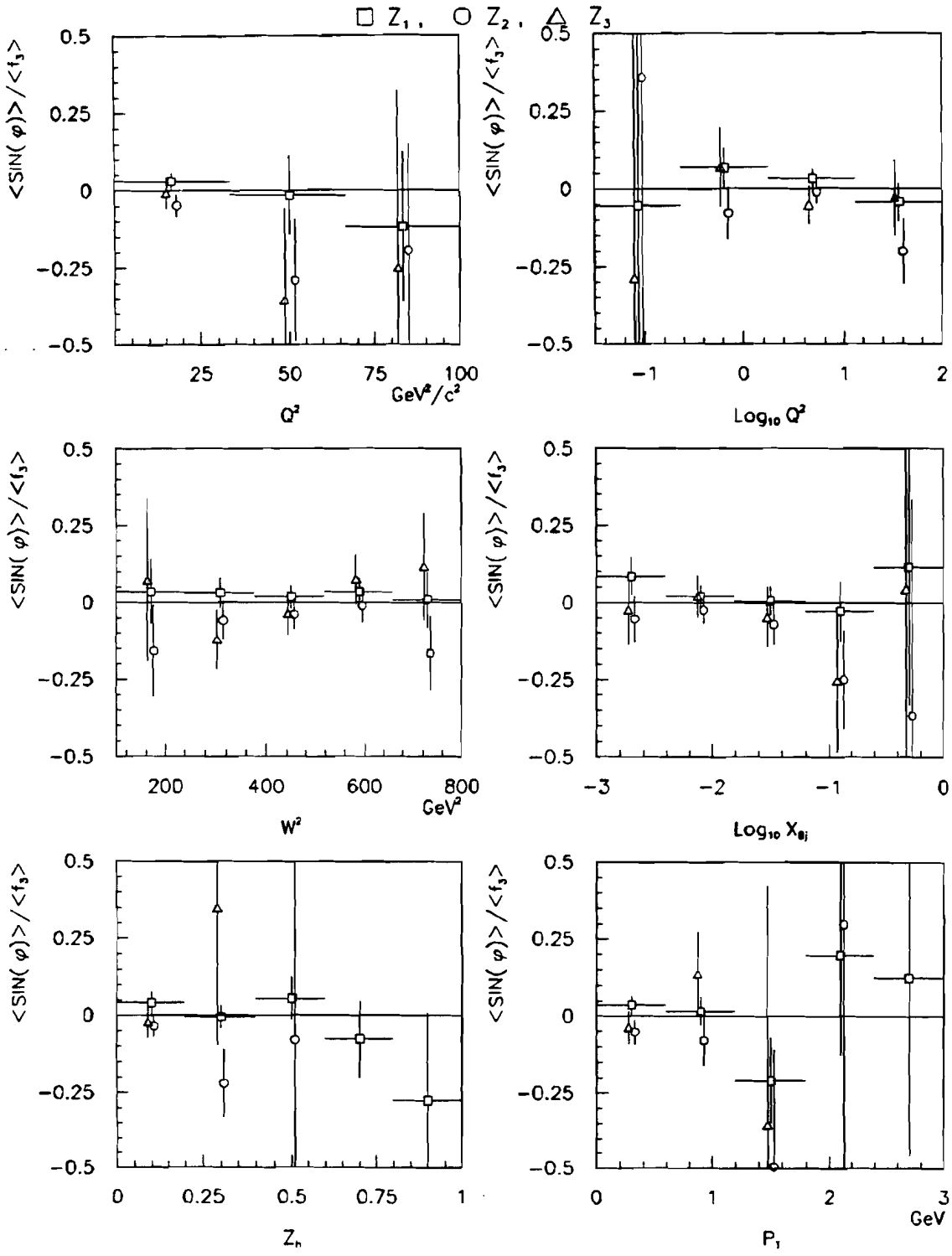

Figure 7.21: $\sin\phi$-moments, Z-Ranked.
Plots (a-d) show the $\sin\phi$-moments as functions of the kinematic variables $Q^2, \log_{10} Q^2, W^2, \log_{10} X_{Bj}$; these contributions to these distributions were *not* limited to tracks with $Z > 0.2$ and $P_t > 0.2$ GeV/c. Plots (e) and (f) show the moments as functions of the hadron variables Z and P_t.

The moments as a function of Z in Figure 7.19(a) indicate an asymmetry only for the fastest particle; the value of this asymmetry is almost flat as a function of Z. A similar dominance of the asymmetry in the fastest particle is seen in the dependence of the effect on the P_t of the particles; there is little change in the value of the asymmetry with increasing P_t for a given rank.

The relative flatness of the asymmetry for the fastest particles as a function of Z in Figure 7.19(a) suggests that the effect may be due to some phenomenon which is more dependent upon rank in the fragmentation chain than it is to the particles' Z-values. The cases where a leading particle was neutral and hence missed contaminated the fastest particle sample with next-to-fastest particles; this contamination would lessen the magnitude of the asymmetry if the effect were mainly Z-rank dependent. To investigate this hypothesis, I have examined the asymmetry from a sample of fastest particles which were definitely the fastest particles in their events. This was realized by requiring the Z of the fastest particle to be greater than the fraction of Z missed in the event: the $Z_1 > Z_{lost}$ cut defined in the previous chapter.

The $\cos\phi$ moments are plotted in Figure 7.22 as functions of the kinematic variables Q^2, $\log_{10} Q^2$, W^2, $\log_{10} X_{Bj}$; these $\cos\phi$ moments as functions of the hadron variables Z and P_t are plotted in Figure 7.23. In these plots, the results for the fastest particles which were definitely the fastest particles in their events — the unambiguously fastest particles — are displayed by the stars; the results for the full fastest-particle sample are reproduced from Figures 7.18 and Figure 7.19 and are displayed by the circles in these plots. The stars have been shifted along the abscissa to allow viewing of the error-bars; the points with horizontal error-bars are located at the actual abscissa values at which all values were calculated. The contributions to these distributions *were* limited to tracks with $Z > 0.2$ and $P_t > 0.2$ GeV/c.

The $\cos 2\phi$ moments are plotted in Figure 7.24, and the $\sin\phi$ moments are plotted in Figure 7.25; again, the results for the unambiguously fastest particles are displayed by the stars and those for the full fastest-particle sample by the circles.

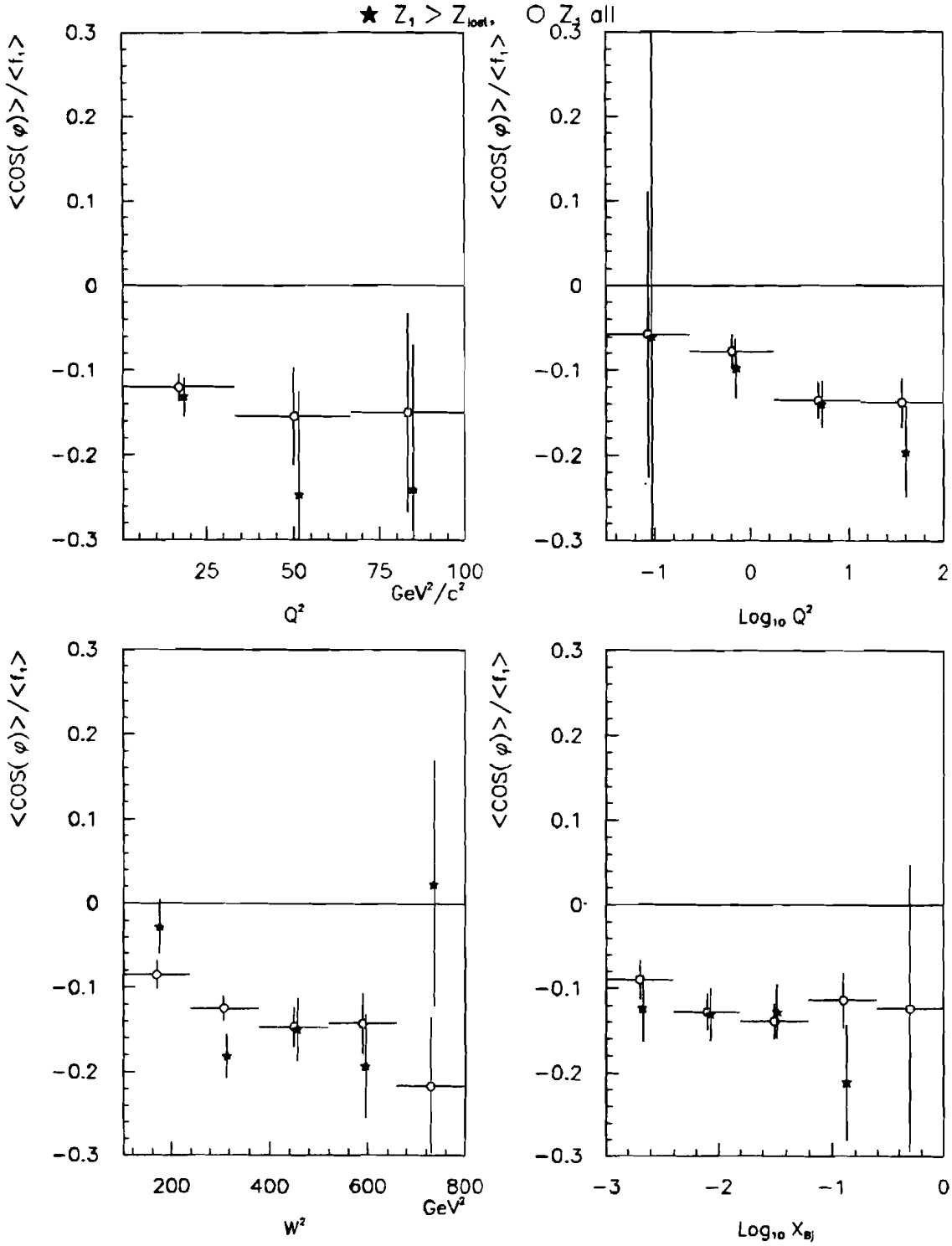

Figure 7.22: $\cos\phi$-moments for the unambiguously fastest particle.
These plots include only those charged particles ranked as the fastest and which satisfy the criterion $Z_1 > Z_{lost}$, which indicates that there was no missing neutral with greater Z in the events. Plots (a-d) show the $\cos\phi$-moments as functions of the kinematic variables $Q^2, \log_{10} Q^2, W^2, \log_{10} X_{Bj}$: these contributions to these distributions were limited to tracks with $Z > 0.2$ and $P_t > 0.2$ GeV/c.

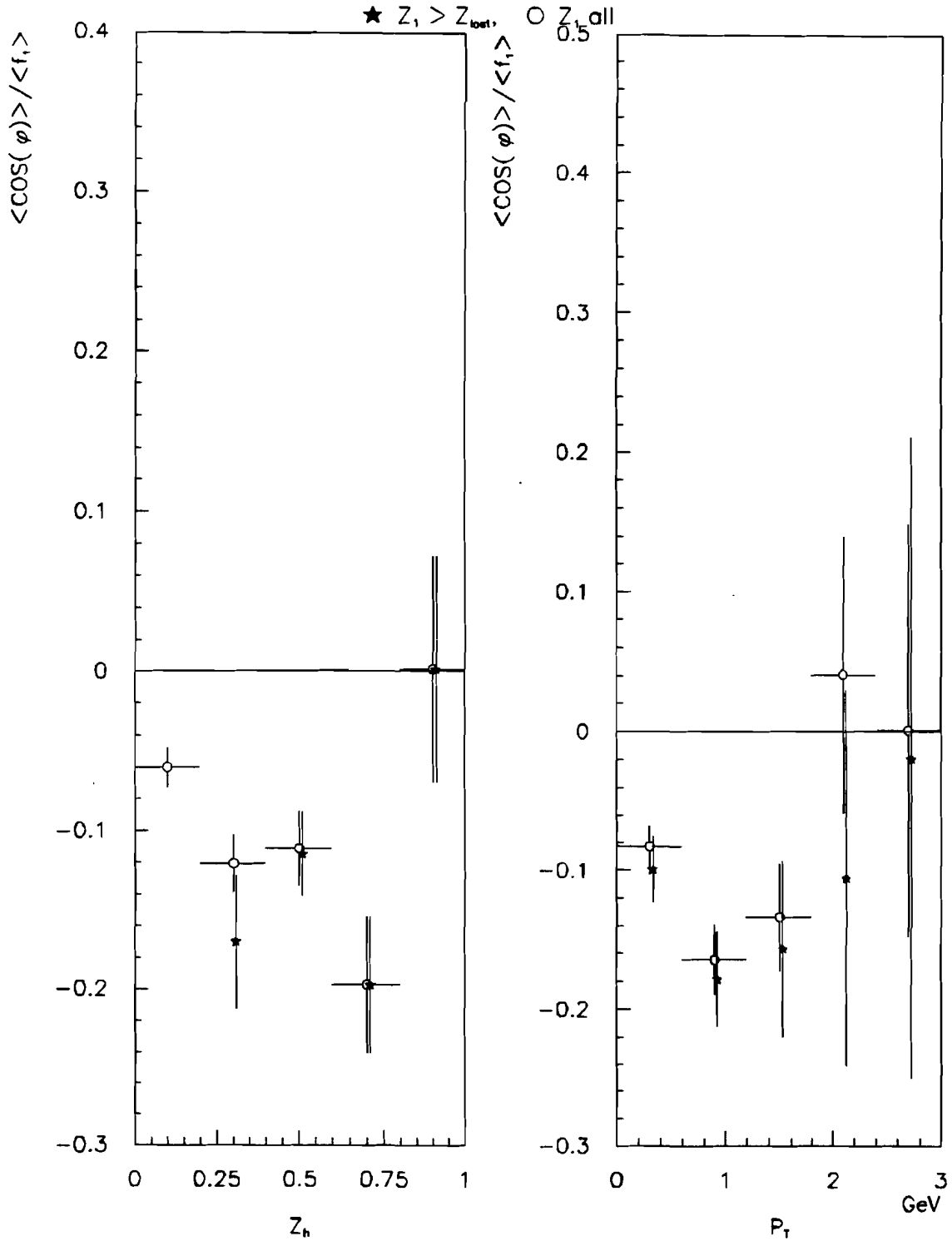

Figure 7.23: $\cos\phi$-moments for the unambiguously fastest particle versus Z and P_t. These plots include only those charged particles ranked as the fastest and which satisfy the criterion $Z_1 > Z_{lost}$, which indicates that there was no missing neutral with greater Z in the events. Plots (a) and (b) show the $\cos\phi$-moments as functions of the hadron variables Z and P_t, with the usual cuts.

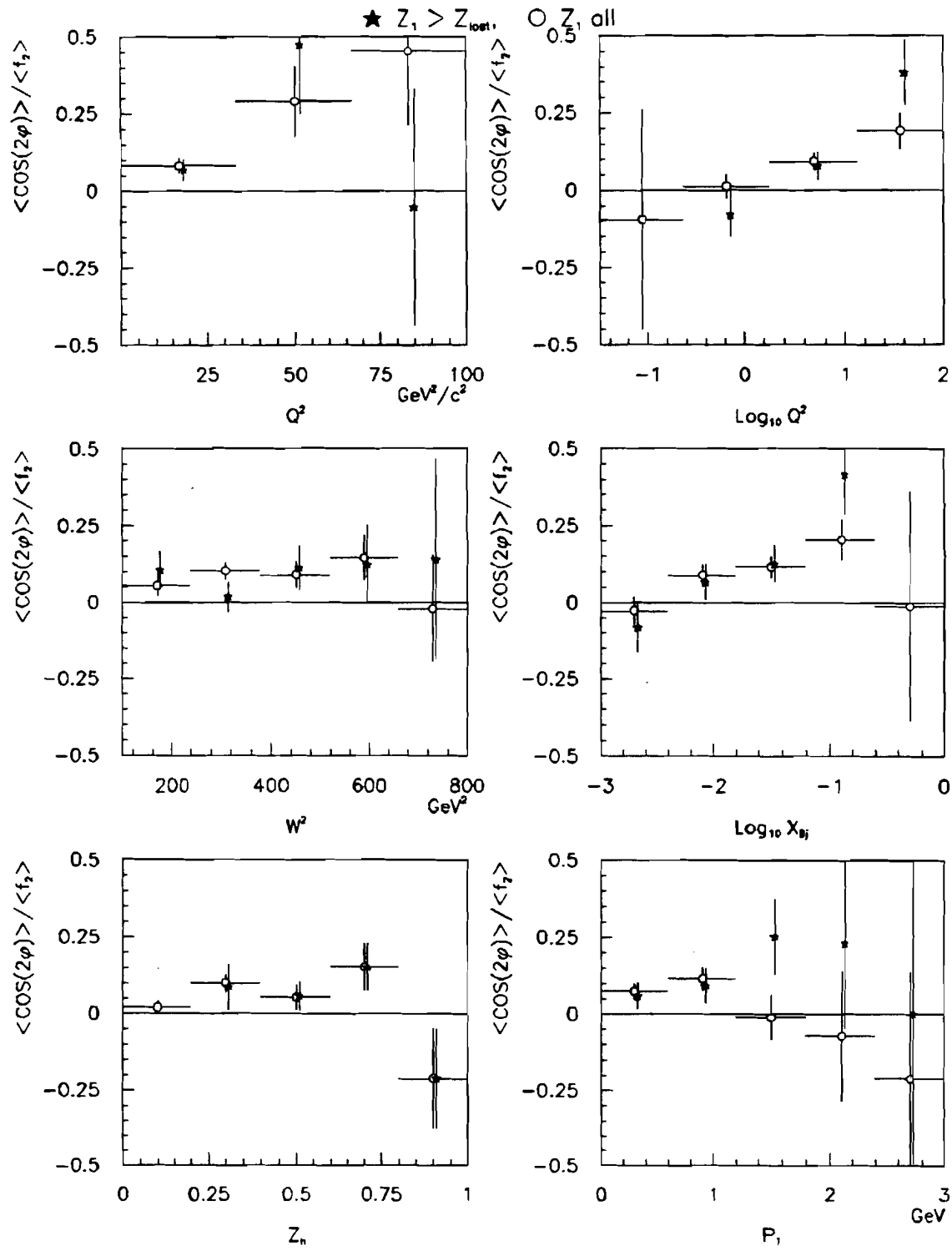

Figure 7.24: $\cos 2\phi$-moments for the unambiguously fastest particle.
Plots (a-d) show the $\cos 2\phi$-moments as functions of the kinematic variables $Q^2, \log_{10} Q^2, W^2, \log_{10} X_{Bj}$; these contributions to these distributions were limited to tracks with $Z > 0.2$ and $P_t > 0.2$ GeV/c. Plots (e) and (f) show the moments as functions of the hadron variables Z and P_t; plot (e) had only the P_t cut, and plot (f) had only the Z cut.

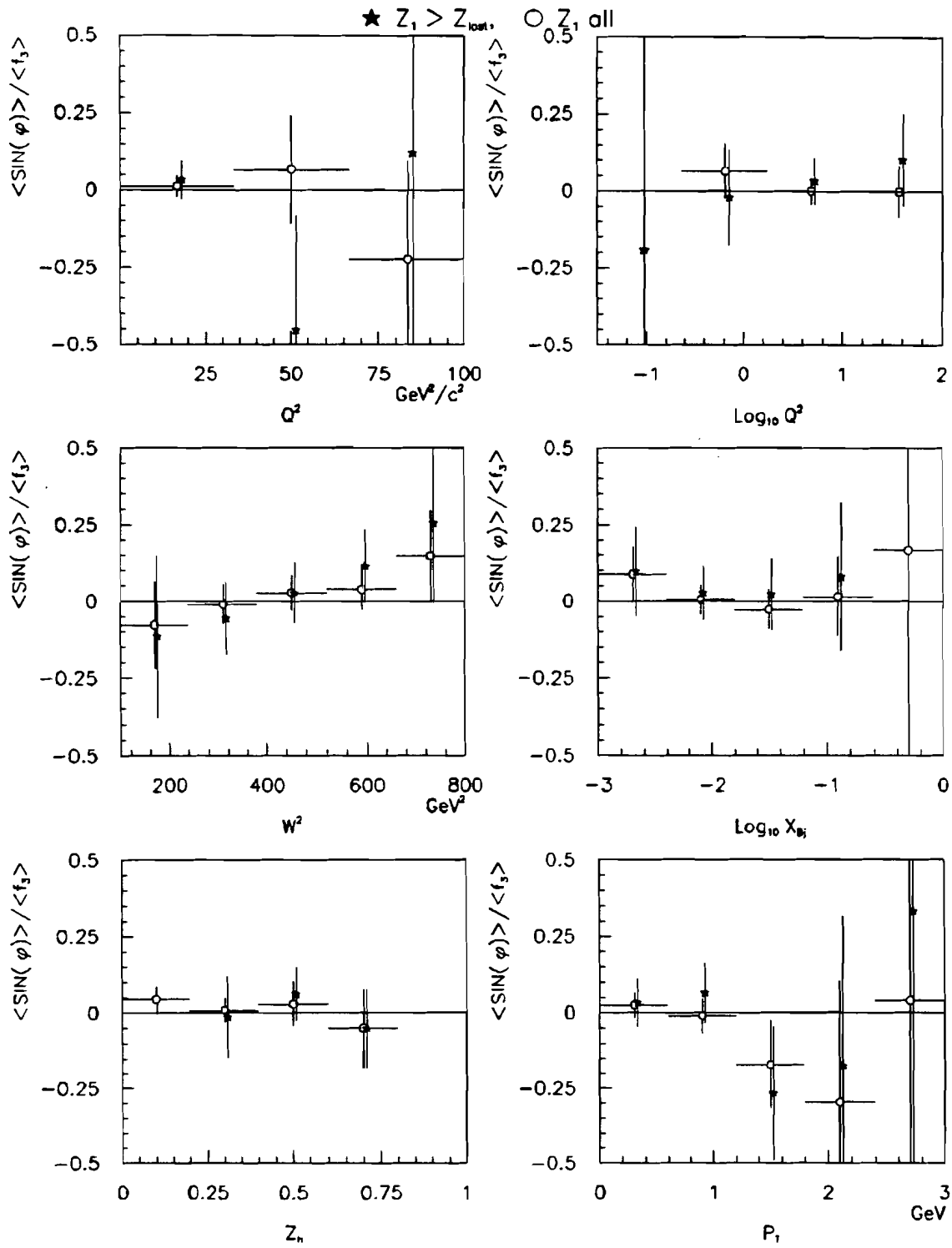

Figure 7.25: $\sin\phi$-moments for the unambiguously fastest particle.
Plots (a-d) show the $\sin\phi$-moments as functions of the kinematic variables $Q^2, \log_{10} Q^2, W^2, \log_{10} X_{Bj}$; these contributions to these distributions were limited to tracks with $Z > 0.2$ and $P_t > 0.2$ GeV/c. Plots (e) and (f) show the moments as functions of the hadron variables Z and P_t; plot (e) had only the P_t cut, and plot (f) had only the Z cut.

7.5 Conclusions

The azimuthal distribution of the produced hadrons exhibits an asymmetry; there is a 12% preference of the hadrons to be produced on the side of the virtual photon opposite that of the scattered muon. Predictions both of QCD and of primordial k_t suggest a dependence on the P_t and the Z of the hadrons, and both dependences are observed. Little dependence is observed on Q^2 or any other kinematic variable. However, the asymmetry of the ϕ-distribution seems to be carried primarily by the very leading particle; in this light, the dependence on Z is incidental to the fact that higher-Z particles tend to be the leading particle in an event.

Chapter 8

Summary

I have examined the Z-distributions of the final state hadrons and compared those from scatters off a Xenon target to those from scatters off a Deuterium target. I have examined the distributions in the kinematic region where the total cross section exhibits the effect of Shadowing; hadron studies have not been performed previously in this region. These Z-distributions of the final state hadrons have shown no dependence on the target, even in the kinematic regime of Shadowing, where the total cross section exhibits strong dependence. In addition, the distributions show no discernable dependence on the event kinematics. From these examinations of the Z-distributions it appears that there is little attenuation of the struck-quark system traversing nuclear matter.

In defining a variable which scales the energy of a given final state hadron to the energy available to that hadron, I have observed that the differential rate of production of a hadron as a function of this variable looks similar for all hadrons in the fragmentation chain. This suggests that the shape of the distribution is related to some fundamental property of fragmentation.

In searching for correlations between the hadrons produced in fragmentation, I have made several observations. Rescaling the scaled energy fractions, Z, removes a simple kinematic constraint from the correlations in terms of the high Z-values of the hadrons. The rescaled-Z values demonstrate a small, but positive, correlation for hadrons adjacent in rank in the fragmentation chain; the resolution of a 3σ effect is 15%. This correlation is roughly independent of event kinematics and of the scattering target material. The effects of acceptance on these measurements indicate a systematic uncertainty, which limits the strength of conclusions which may be drawn from the correlations.

The azimuthal distribution of the produced hadrons exhibits an asymmetry; there is a 12% preference of the hadrons to be produced on the side of the virtual photon opposite that of the scattered muon. This asymmetry does not depend upon Q^2 or X_{Bj}, but shows a (30% $\pm$ 10%) rise with W^2. The effect exhibits a strong dependence on the Z of the hadrons (100% increase from $Z = 0.1$ to $Z = 0.8$) but only a weak dependence on the P_t.

However, the asymmetry of the ϕ-distribution seems to be carried almost exclusively by the very leading particle; in this light, the dependence on Z is incidental to the fact that higher-Z particles tend to be *the* leading particle in an event. Predictions both of QCD and of primordial k_t suggest a dependence on the P_t and the Z of the hadrons, but neither of these descriptions would isolate the effect to the very leading particle. These two descriptions both involve a process which adds perpendicular momentum to the struck-quark system before it hadronizes; the fragmentation process is thought only to smear-out the effect. For the asymmetry from one of these processes to appear only in the very leading particle, this smearing must be large, or another unpredicted process must be at work. If the struck-quark system were to fragment in a linear chain, then an asymmetric addition of perpendicular momentum to the system should appear in all fragments of the chain, with fragmentation P_t smearing out the effect for the more descendent fragments. If the hadronization of the struck-quark system were to proceed in a more parallel manner, then it would be possible for the leading particle to receive perpendicular momentum independently of the other particles of the hadronization. Without detailed understanding of the P_t-smearing from the process of fragmentation, it would be difficult prove either hypothesis.

In this dissertation, I have examined final state hadrons. Distributions of the data correspond to those seen in previous experiments. However, distributions have been made in previously unexplored kinematic regions, and distributions of alternate variables have been examined. These results suggest avenues for further thought, and more analysis along these lines will be conducted.

Appendix A

The Fermilab E665 Collaboration

Argonne National Laboratory, Argonne IL USA
D. F. Geesaman, H. E. Jackson, S. Kaufman, R. Gilman, S. Tentindo-Respond

University of California, San Diego, La Jolla USA
R. D. Kennedy, H. G. E. Kobrak, A. Salvarani, R. W. Swanson

Institute for Nuclear Physics, Crakow, Poland
A. Eskreys, P. Malecki, K. Olkiewicz, B. Pawlik, P. Stopa

Fermi National Accelerator Laboratory, Batavia, IL USA
J. Hanlon, T. Kirk, H. Melanson, H. E. Montgomery, J. G. Morfin, S. A. Wolbers

University of Freiburg, Freiburg, W. Germany
M. Erdmann, J. Haas, W. Mohr, H. E. Stier, M. Wilhelm

Harvard University, Cambridge, MA USA
J. M. Conrad, D. G. Michael, R. B. Nickerson, F. M. Pipkin, M. Schmitt, R. Wilson

University of Illinois, Chicago, IL USA
M. R. Adams, T. Carroll, C. Halliwell, D. Jaffe, S. Magill, D. McLeod

University of Maryland, College Park, MD USA
S. Aid, S. Kunori, S. O'Day, E. J. Ramberg, A. Skuja, G. Snow, P. Steinberg

Massachusetts Institute of Technology, Cambridge, MA USA
P. L. Anthony, M. D. Baker, W. Busza, T. Lyons, L. Osborne, J. Ryan

Max-Planck-Institute, Munich, W. Germany
I. Derado, V. Eckardt, J. Gebauer, D. Hantke, G. Jancso, A. Manz, N. Schmitz, H. J. Seyerlein, S. Soldner-Rembold, P. Strube, H. J. Trost, M. Vidal, W. Wittek, G. Wolf

University of Washington, Seattle, WA USA
A. A. Bhatti, R. Davisson, W. Dougherty, D. M. Jansen, G. Liang, J. J. Lord, H. J. Lubatti, J. Wilkes, T. Zhao

University of Wuppertal, Wuppertal, W. Germany
H. M. Braun, U. Ecker, A. Roeser

Yale University, New Haven, CT USA
S. K. Dhawan, V. W. Hughes, V. Papavassiliou, K. P. Schuler, H. Venkataramania

Appendix B

Proportional Tube Physics

B.1 Introduction

In High-Energy Physics, many types of chambers are used to track the trajectories of charged particles, e.g. Proportional Tubes, Multi-Wire-Proportional-Chambers, and Drift Chambers. These chambers all rely on the fact that a charged particle passing through some material can knock electrons out from their orbits around the atoms of the material, thus ionizing the atoms. In the presence of an electric field, these ions and electrons will migrate toward their respective poles of the field: the positive ions will migrate toward the Cathode (the negative pole), and the electrons will migrate toward the Anode (the positive pole). Thus, the result of the passage of a charged particle through this material is the deposition of some electric charge on the electrodes of an applied electric field. In order to detect the initial ionization, the charge is magnified by the effect of *Gas Multiplication*. If the electric field is of sufficient strength, then the migrating electron can be accelerated to such an energy that it can ionize an atom itself; this increase in the number of electrons is a geometric progression, and it can result in a multiplication of the charge by a factor of 10^6. The mean-free-path of the electron — the distance between collisions with atoms — must be great enough to allow the electron to accelerate to the energy necessary for further ionization. The mean-free-path of an electron in gases at Standard Temperature and Pressure is adequate at accessible electric fields, so gases are usually used as the ionizable material.

The Primary Ionization is that ionization produced initially by the passage of the charged particle; the ionization produced by the Gas Multiplication is called Secondary Ionization. The geometric progression of ionization is called a *Townsend Avalanche* [44, p. 122]. The collection of all these anions and the motion of the ions yield the signal seen from these chambers. The term *Proportional* enters because the amount of charge collected is directly proportional to the energy of the particle that caused the primary ionization; the tube characteristics and the operating conditions determine the gain of the gas multiplication [44, p. 149].

B.2 Motions of Electrons and Ions in Gases

The mean-free-path of a particle is the average distance that the particle travels between collisions with the molecules of the gas and is inversely proportional to the density of the gas. For most common gases at Standard Temperature and Pressure, the mean-free-path is about $5 * 10^{-5}$ to $3 * 10^{-4}$ cm [44, p. 67]. Immediately after a collision, the motion of the electron is random; however, in an electric field during the time between collisions, the electron is accelerated toward the anode. This results in a net motion and an average velocity in the direction opposite to that of the electric field. This average velocity is called the *drift velocity* of the electron. The drift velocity, w, is dependent on the electric field (E), the Pressure of the gas (P), and the Mobility of the electron (μ), which is itself a function of the electric field, the gas pressure, and the type of gas:

$$w = \mu * (E/P).$$

For small values of (E/P), the mobility is approximately

$$\mu \sim 10^6(\text{cm/sec})(\text{volts/cm})^{-1}(\text{mmHg}).$$

For $(E/P) > 1$ to 10 $(\text{volts/cm})^{-1}(\text{mm Hg})$, the drift velocity saturates somewhere between 10^6 and 10^7 cm/sec.

For a cylindrical geometry, the electric field is given by the equation

$$E(r) = \frac{V}{r \ln(r_1/r_2)},$$

where V is the voltage between the two surfaces 1 and 2, of respective radii r_1 and r_2. Suppose the applied voltage V is 2500 volts. If surface 1 is a 50-micron diameter wire and surface 2 is a tube of diameter 2.54 cm, then the electric field near the outer wall will be 316 volts/cm, the ratio (E/P) will be 0.4, and the drift velocity will be $0.4 * 10^5$cm/sec. A distance half-way in will have an electric field of 632 volts/cm, an

(E/P) of 0.8, and a drift velocity of $5 * 10^6$cm/sec. Near the wire the electric field is much higher, $3.2 * 10^5$volts/cm, and the drift velocity will saturate near $5 * 10^6$cm/sec.

The ionization potential is the energy necessary to remove the first valence electron from the molecule. The electronegativity of a molecule of gas is the tendency to form a negative ion by attaching an electron. One might think that the best gas to use would be one with the lowest ionization potential; however, the electronegativity of the molecules of gas is also a very important factor. The Electron Affinity h is the probability per collision of forming a negative ion. In Table B.1 is a list of a few elements and their respective ionization potentials, Pauling's Electronegativities, and Electron Affinities.

ELEMENT	ION. POT. (volt)	E. NEG.	E. AFF.
Nitrogen	14.534	3.04	10^{-6}
Oxygen	13.618	3.44	10^{-4}
Fluorine	17.422	3.98	10^{-3}
Chlorine	12.967	3.16	10^{-3}
Neon	21.564	-	
Argon	15.759	-	10^{-6}
Hydrogen	13.598	2.20	10^{-6}
COMPOUNDS:			
Water			10^{-4}
CO			10^{-6}
Methane			10^{-6}
Ammonia			10^{-6}

Table B.1: Gas Properties. This table shows three properties of gases: Ionization Potential, Pauling's Electronegativity, and Electron Affinity. The values of Ionization Potential and Pauling's Electronegativity were taken from [56], and the Electron Affinity values taken from [44, p. 68].

In order to prevent the loss of electrons to the formation of negative ions, the probability of negative ion formation, summed over all collisions the electron makes on its way to the anode, must be held down. For an Electron Affinity of h, the number of collisions that an electron must make before it forms an ion is typically $(1/h)$; therefore, the number of collisions should be kept less than $(1/h)$. Thus, the better gases to choose would be those with small values of Electron Affinity, for example, $h = 10^{-6}$ for Argon, Nitrogen, CO, Methane, and Ammonia.

An additional consideration is necessary. When the positive ion reaches the cathode, it extracts an electron to fill its valence; this occurs because the ionization potential of the ion, which is also the amount of energy liberated on absorption of

an electron, is greater than the work function of the cathode, which is the amount of energy necessary to extract an electron. This energy difference results in an energy excess, which may result in the liberation of another electron or in the emission of a photon which can knock out a photoelectron. This is not good, because these extra electrons, from whatever source, will cause another avalanche; this avalanche will occur long after the first, since the drift time of the positive ions is very long. Therefore, a substance called a *quencher* is added to the gas. Alcohols and Hydrocarbons are frequently used as quenchers, because they are big, complicated molecules. If they have a lower ionization potential than the main gas, then they will yield one of their electrons to fill the valence of the main gas molecule and then migrate toward to cathode themselves. When they reach the wall and extract an electron, the extra energy may be absorbed in rotational energy or, more commonly, in the dissociation of the molecule. The consequence of this would be a finite lifetime of the stability of the chamber, since the quencher would be expended eventually; but these chambers are usually operated with a continual flow of gas mixture in order to replenish the quencher and to maintain a mixture for stable performance.

B.3 Resolving Times

After a particle has passed through a chamber and generated its signal, the chamber requires some time to recover from the conditions of *activation* to a normal *ready* state. During this time, the chamber cannot respond to another particle. This time is called the resolving time, because it is the minimum time between successive particles necessary in order to *resolve* the passage of both particles as two distinct signals. There are two specific resolving times: Dead Time and Recovery Time. Dead Time is the time after the passage of the first particle at which the second particle will generate a signal; Recovery Time is the time after which the second particle will generate the full amplitude of the signal.

The Resolving Times limit the rate, or intensity of particles passing through the chamber, at which the chamber can successfully operate. In Ionization chambers, where the energy of the passing particle may be measured by the amount of total charge collected, all the positive ions must be collected before the next particle can be accepted, and therefore the Resolving Time is quite large (milliseconds), and the counting rate must be less than 100 Hz. For Proportional chambers, the resolving time is on the order of microseconds, and the dead time is on the order of hundreds of nanoseconds. The resolving time is usually determined by the geometry of the chamber, in that the temporal extent of the avalanche is predominated by the difference in drift times of primary electrons from different parts of the track. For a 1-inch cell

with a central wire, this drift time difference can be 200 to 400 nanoseconds.

B.4 Pulse Shapes

The signals generated by these avalanches are pulses observed by some electronic equipment, such as an oscilloscope or a monostable latch. The characteristics of the observing equipment will determine the shape of the pulse observed, but the shape of the signal input to this equipment is determined by the electric field, which is a function of the geometry of the chamber and the voltage applied to the electrodes. I will first discuss the effects of the electric fields on the signals and then describe the shaping of the pulses by a particular configuration of electronics and an oscilloscope as the observing equipment. The simplest configuration is that of two parallel plates; I will discuss this first and then move on to a cylindrical tube around a concentric wire, which is relevant to the chambers used in the experiment of this dissertation.

B.4.1 Parallel Plate Geometry

If there are two conductive plates at locations $x = 0$ and $x = d$, with voltages V_1 and V_2, respectively, then for any position x between the two plates the voltage is given by

$$(V(x) - V_1) = (V_2 - V_1) * x/d.$$

If N ion pairs are formed at x at time $t = 0$, then the voltage as a function of time is given by

$$V(t) = \frac{Ne}{Cd}[(x - tw_-) - (x + tw_-)] \tag{B.1}$$

$$= -\frac{Ne}{Cd}(w_+ + w_-)t. \tag{B.2}$$

The drift velocity of the positive ions, w_+, is small compared to that of the electrons, w_-:

$$w_+ \sim 10^2\text{cm/sec}, \qquad w_- \sim 10^5\text{cm/sec}.$$

So, if one chooses an RC for the detector of $\sim$ 10 microseconds, then the motion of the positive ions can be ignored, and the signal is

$$V(t) = -\frac{Netw_-}{Cd}, \qquad \text{for } t < x/w_-. \tag{B.3}$$

After this time, it rises extremely slowly as the ions migrate toward the cathode:

$$V(t) = -\frac{Netw_+}{Cd}, \qquad \text{for } t < d/w_+, \tag{B.4}$$

until it reaches $-Ne/C$ at time $t = t_+$. If the slow rise is neglected, then the pulse height $-Nex/Cd$ depends only on the position between the plates. However, the initial slope of the voltage is the same for all positions: $dV/dt = -New_-/Cd$.

B.4.2 Cylindrical Geometry

Assume an infinite cylindrical tube of radius r_2 and a concentric wire of radius r_1. Let C represent the sum of all the capacitances: tube, probe, and counter. Then the voltage at any point between the radii is given by

$$V(r) - V_1 = (V_2 - V_1)\left[\frac{\ln(r/r_1)}{\ln(r_2/r_1)}\right]. \tag{B.5}$$

The Voltage as a function of time for N ion pairs produced at r_0 is given by

$$V(t) = -\frac{Ne}{C}\left[\frac{\ln(r_+/r_1)}{\ln(r_2/r_1)} - \frac{\ln(r_-/r_1)}{\ln(r_2/r_1)}\right], \tag{B.6}$$

$$= -\frac{Ne}{C}\left[\frac{\ln(r_+/r_-)}{\ln(r_2/r_1)}\right], \tag{B.7}$$

where $r_+ = r_0 + tw_+$ and $r_- = r_0 - tw_-$.

Again, if the slow rise is neglected, since $w_+ \ll w_-$, then, with all the positive ions starting at the wire ($r_+ = r_0$), the signal is

$$V(t) = -\frac{Ne}{C}\left[\frac{\ln(r_0/r_-)}{\ln(r_2/r_1)}\right]. \tag{B.8}$$

For large values of r_2/r_1, the pulse height sensitivity to the origin r_0 is small. The actual scenario is that the Gas Multiplication occurs only very close to the wire, so that all the electrons are quickly absorbed at the anode and all the positive ions start out just above the wire. The absorption of the electrons, surprisingly enough, accounts for only 3% of the net charge initially measured on the collector [65]. As the sheath of positive ions moves away from the wire, the induced charge on the anode decreases, and the net charge measured increases toward its maximum value (Ne).

It is possible to express the position of the positive ion sheath as a function of time and the various parameters. First, with μ_+ as the ion-mobility, the ion drift velocity is given by

$$w_+ = \mu_+ E/P = \frac{\mu_+ V}{p r_+ \ln(r_2/r_1)}. \tag{B.9}$$

Rearrangement and substitution of $w_+ = dr_+/dt$, followed by integration from 0 to t, yields the following expression:

$$\int_{r_1}^{r_+} r dr = \int_0^t dt \frac{\mu_+ V}{p \ln(r_2/r_1)}. \tag{B.10}$$

Then the expression for the position of the positive ion sheath is

$$r_+ = \left\{ \frac{2\mu_+ V t}{p \ln(r_2/r_1)} + r_1^2 \right\}^{1/2}. \tag{B.11}$$

With the setting of r_- to r_1 and the substitution of these expressions into Equation B.8, the voltage becomes

$$V(t) = \frac{-Ne}{C \ln(r_2/r_1)} \ln \left[\frac{\left(\frac{2\mu_+ V t}{p \ln(r_2/r_1)} + r_1^2 \right)^{1/2}}{r_1} \right], \tag{B.12}$$

$$V(t) = \frac{-Ne}{2C \ln(r_2/r_1)} \ln \left[\frac{2\mu_+ V t}{r_1^2 p \ln(r_2/r_1)} + 1 \right]. \tag{B.13}$$

These dynamics can be expressed as the charge deposited and induced upon the anode:

$$Q(t) = -Ne \frac{\ln(r_+/r_-)}{\ln(r_2/r_1)}. \tag{B.14}$$

The time dependence can be expressed explicitly by substitution of Equation B.11 into Equation B.14 for the positive ion sheath and a similar one for the electron cloud:

$$Q(t) = \frac{-Ne}{2 \ln(r_2/r_1)} \ln \frac{\left[r_0^2 + \frac{2\mu_+ V t}{p \ln(r_2/r_1)} \right]}{\left[r_0^2 - \frac{2\mu_- V t}{p \ln(r_2/r_1)} \right]}. \tag{B.15}$$

This equation is correct for the time before the electron cloud reaches the anode: $0 < t < t_{electron}$. The rate of deposition of charge is given by the derivative of Equation B.15:

$$\frac{dQ(t)}{dt} = \frac{-Ne}{\ln(r_2/r_1)} \frac{V}{p \ln(r_2/r_1)} \left\{ \frac{\mu_+}{\left[r_0^2 + \frac{2\mu_+ V t}{p \ln(r_2/r_1)} \right]} + \frac{\mu_-}{\left[r_0^2 - \frac{2\mu_- V t}{p \ln(r_2/r_1)} \right]} \right\}. \tag{B.16}$$

After the electrons reach the anode, r_- simply becomes the inner radius, r_1, so the equation for the charge *induced* on the anode due to the outwardly migrating positive ion sheath is given by

$$Q(t) = \frac{-Ne}{2\ln(r_2/r_1)} \ln \frac{\left[r_0^2 + \frac{2\mu_+ Vt}{p\ln(r_2/r_1)}\right]}{r_1^2}, \tag{B.17}$$

for $t_{electron} < t < t_{ion}$. The rate of induced charge is given by

$$\frac{dQ(t)}{dt} = \frac{-Ne}{\ln(r_2/r_1)} \frac{V}{p\ln(r_2/r_1)} \left\{ \frac{\mu_+}{\left[r_0^2 + \frac{2\mu_+ Vt}{p\ln(r_2/r_1)}\right]} \right\}. \tag{B.18}$$

Of course, when the ion sheath reaches the cathode, the rate of charge deposition and the total charge are given by

$$Q(t) = -Ne \tag{B.19}$$

$$\frac{dQ(t)}{dt} = 0, \qquad \text{for } t > t_{ion}. \tag{B.20}$$

B.4.3 A Proportional Tube Counter

In this section I will describe a particular arrangement of a proportional tube, electronic components, and an oscilloscope. This arrangement corresponded to an actual setup from which observations of pulses were made, and I will compare the pulses observed with those described by the following treatment.

In Figure B.1 the conservation of charge at V_{in} suggests

$$I_{HV} + I_{circuit} + I_{induced} = 0. \tag{B.21}$$

The induced current is just the rate of charge deposition, and the sign of this current is negative in this system, as the flow is of the electrons to the wire:

$$I_{induced} = \frac{dQ(t)}{dt}. \tag{B.22}$$

The circuit part of the system is a set of *legs* connected in parallel, where each leg is a resistor and a capacitor connected in series; the current in a single leg can be described as the rate of change of potential across the capacitor:

$$I_{leg} = -C_{leg} \frac{dV(t)}{dt}. \tag{B.23}$$

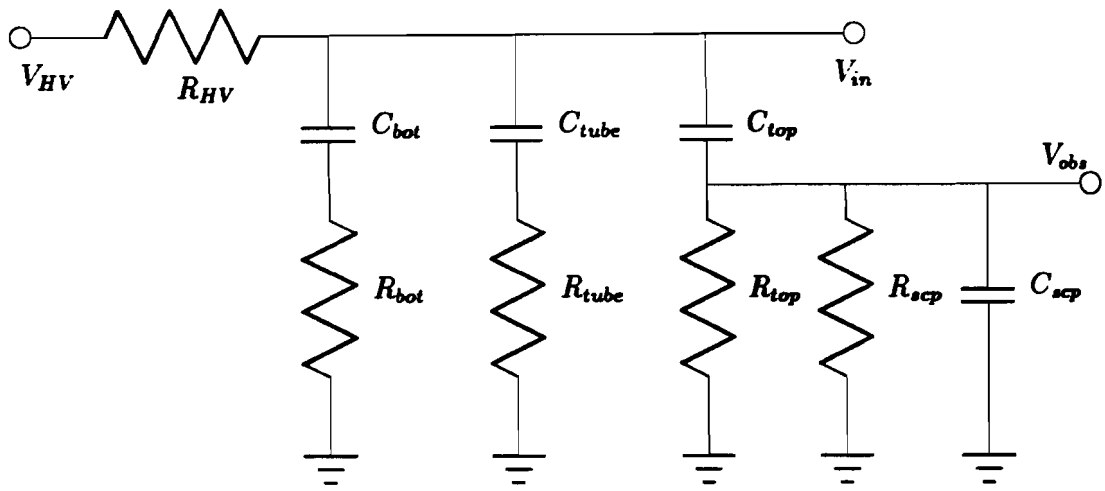

Figure B.1: Equivalent Circuit Diagram. This is the arrangement of the elements of the circuit. V_{HV} is the applied High Voltage, V_{in} is the voltage on the wire associated with the collected charge, and V_{obs} is the voltage observed on the oscilloscope.

The current $I_{circuit}$ is simply the sum of the currents in the legs:

$$I_{circuit} = -\frac{dV(t)}{dt}\sum_{leg} C_{leg}. \tag{B.24}$$

Then, the current through the blocking resistor from the High-Voltage source can be described by

$$-I_{HV} = \frac{dQ(t)}{dt} - \frac{dV(t)}{dt}\sum_{leg} C_{leg}. \tag{B.25}$$

The potential of the wire is given by the difference between the High-Voltage source V_{HV} and potential drop across the impedance R_{HV}:

$$V = V_{HV} - I_{HV}R_{HV}. \tag{B.26}$$

Upon substitution of Equation B.25 into Equation B.26, the expression for the time-dependent voltage of the wire becomes

$$V(t) = V_{HV} + R_{HV}\frac{dQ(t)}{dt} - R_{HV}\frac{dV(t)}{dt}\sum_{leg} C_{leg}. \tag{B.27}$$

This first-order differential equation can be rearranged to a more standard form:

$$\frac{dV(t)}{dt} + \frac{1}{R_{HV}\sum_{leg} C_{leg}}V(t) = \frac{V_{HV} + R_{HV}\frac{dQ(t)}{dt}}{R_{HV}\sum_{leg} C_{leg}}, \tag{B.28}$$

with the boundary condition $V(0) = V_{HV}$. It is possible to define the denominators of Equation B.28 as a *time constant*:

$$\tau_1 \equiv R_{HV} \sum_{leg} C_{leg}; \tag{B.29}$$

thus, Equation B.28 can be expressed as

$$\frac{dV(t)}{dt} + \frac{1}{\tau_1} V(t) = \frac{V_{HV}}{\tau_1} + \frac{R_{HV}}{\tau_1} \frac{dQ(t)}{dt}. \tag{B.30}$$

For a general first-order linear differential equation,

$$\frac{dy(t)}{dt} + a(t)y(t) = b(t), \tag{B.31}$$

it is possible to write a function,

$$\mu(t) = e^{\int a(s)ds} + c,, \tag{B.32}$$

such that the solution to Equation B.31 can be expressed as

$$y(t) = \frac{1}{\mu(t)} \int_{t_0}^{t} \mu(s)b(t)ds + \frac{\mu(t_0)}{\mu(t)} y(t_0). \tag{B.33}$$

The constant c is arbitrary and can be chosen to be zero.

Therefore, for Equation B.30 function can be defined as

$$\mu_1(t) = e^{\int \frac{ds}{\tau_1}} = e^{\frac{t}{\tau_1}} \tag{B.34}$$

so that the solution can be expressed as

$$V(t) = e^{-\frac{t}{\tau_1}} \int_{t_0}^{t} \left[\frac{V_{HV}}{\tau_1} + \frac{R_{HV}}{\tau_1} \frac{dQ(s)}{ds} \right] e^{\frac{s}{\tau_1}} ds + e^{-\frac{t-t_0}{\tau_1}} V(0). \tag{B.35}$$

The integration yields

$$\frac{1}{\tau_1} \int_{t_0}^{t} e^{\frac{s}{\tau_1}} ds = e^{\frac{t}{\tau_1}} - e^{\frac{t_0}{\tau_1}}, \tag{B.36}$$

and

$$V(t) = V_{HV} - V_{HV} e^{-\frac{t-t_0}{\tau_1}} + e^{-\frac{t-t_0}{\tau_1}} V(0) + \frac{R_{HV}}{\tau_1} e^{-\frac{t}{\tau_1}} \int_{t_0}^{t} \frac{dQ(s)}{ds} e^{\frac{s}{\tau_1}} ds. \tag{B.37}$$

The constraint of the boundary condition $V(0) = V_{HV}$ yields the solution to the differential equation:

$$V(t) = V_{HV} + \frac{R_{HV}}{\tau_1} e^{-\frac{t}{\tau_1}} \int_{t_0}^{t} \frac{dQ(s)}{ds} e^{\frac{s}{\tau_1}} ds. \tag{B.38}$$

The voltage measured on the oscilloscope is V_{obs}:

$$V_{obs}(t) = I_{eff}R_{eff}. \tag{B.39}$$

Conservation of charge at V_{obs} in Figure B.1 suggests

$$I_{total} = I_{eff} + I_{csc}, \tag{B.40}$$

and the total current is given by

$$I_{total} = C_{total}\frac{dV(t)}{dt}, \tag{B.41}$$

while the current through the scope is given by

$$I_{csc} = C_{csc}\frac{dV_{obs}(t)}{dt}. \tag{B.42}$$

The combination of the Equations B.42, B.41, B.40, and B.39 generates the differential equation for the observed voltage:

$$V_{obs}(t) = V_{obs}(0) + R_{eff}C_{total}\frac{dV(t)}{dt} - R_{eff}C_{csc}\frac{dV_{obs}(t)}{dt}; \tag{B.43}$$

the boundary condition on the observed voltage is that, before perturbation, the voltage is zero: $V_{obs}(0) = 0$. Again, a time constant may be defined:

$$\tau_2 \equiv R_{eff}C_{csc}, \tag{B.44}$$

and the first-order differential equation can be rearranged to a more standard form:

$$\frac{dV_{obs}(t)}{dt} + \frac{1}{\tau_2}V_{obs}(t) = \frac{C_{total}}{C_{csc}}\frac{dV(t)}{dt}. \tag{B.45}$$

A corresponding function can be defined:

$$\mu_2(t) = e^{\frac{t}{\tau_2}}, \tag{B.46}$$

which allows the expression of the solution for V_{obs}:

$$V_{obs}(t) = \int_{t_0}^{t} \frac{C_{total}}{C_{csc}}\frac{dV(w)}{dw}e^{\frac{w-t}{\tau_2}}dw. \tag{B.47}$$

Substitution of Equation B.38 into Equation B.30 yields the expression for $dV(t)/dt$:

$$\frac{dV(t)}{dt} = \frac{R_{HV}}{\tau_1}\frac{dQ(t)}{dt} - \frac{R_{HV}}{\tau_1^2}e^{-\frac{t}{\tau_1}}\int_{t_0}^{t}\frac{dQ(s)}{ds}e^{\frac{s}{\tau_1}}ds. \tag{B.48}$$

Substitution of Equation B.48 into Equation B.47: produces a large equation for V_{obs}:

$$V_{obs}(t) = \frac{C_{total}}{C_{csc}}\frac{R_{HV}}{\tau_1}\left\{\int_0^t \frac{dQ(w)}{dw} e^{\frac{w-t}{\tau_2}} dw - \frac{1}{\tau_1}\int_0^t \left[\int_0^w \frac{dQ(s)}{ds} e^{\frac{s-t}{\tau_1}} ds\right] e^{\frac{w-t}{\tau_2}} dw\right\}. \quad \text{(B.49)}$$

The second term in Equation B.49 can be integrated by parts with the use of the following two definitions:

$$du = \frac{1}{\tau_1} e^{\frac{w-t}{\tau_2}} dw, \qquad \text{and} \quad \textbf{(B.50)}$$

$$v = \left[\int_0^w \frac{dQ(s)}{ds} e^{\frac{s-t}{\tau_1}} ds\right]. \quad \textbf{(B.51)}$$

Then, the integral of Equation B.50 and the derivative of Equation B.51 are written as

$$u = \frac{\tau_2}{\tau_1} e^{\frac{w-t}{\tau_2}}, \qquad \text{and} \quad \text{(B.52)}$$

$$dv = \frac{dQ(w)}{dw} e^{\frac{w-t}{\tau_1}} dw. \quad \text{(B.53)}$$

This yields an expanded expression for Equation B.49:

$$V_{obs}(t) = \frac{C_{total}}{C_{csc}}\frac{R_{HV}}{\tau_1}\left\{\int_0^t \frac{dQ(w)}{dw} e^{\frac{w-t}{\tau_2}} dw - \frac{\tau_2}{\tau_1}\int_0^t \frac{dQ(s)}{ds} e^{\frac{s-t}{\tau_1}} ds + \frac{\tau_2}{\tau_1}\int_0^t \frac{dQ(w)}{dw} e^{\frac{w-t}{\tau_1}} e^{\frac{w-t}{\tau_2}} dw\right\}. \quad \text{(B.54)}$$

Equation B.54 can be rearranged in the following form:

$$V_{obs}(t) = \frac{C_{total}}{C_{csc}}\frac{R_{HV}}{\tau_1}\frac{\tau_2}{\tau_1}\int_0^t \frac{dQ(s)}{ds}\left\{\frac{\tau_1}{\tau_2} e^{\frac{s-t}{\tau_2}} - e^{\frac{s-t}{\tau_1}} + e^{\frac{s-t}{\tau_1}} e^{\frac{s-t}{\tau_2}}\right\} ds. \quad \text{(B.55)}$$

B.4.4 Application

The characteristics of the charge collection are described by Equations B.16 and B.18, and these can be substituted into Equation B.55 to describe the pulse shape observed on the oscilloscope. The values of the elements for the test operation of the PTM's in Fermilab Experiment-665 are listed in Table B.2. The predicted rate of change of charge on the wire is shown in Figure B.2, for a time scale longer than the arrival of the electrons at the wire. The steeply falling magnitude of the rate is due to the migration of the positive ion sheath away from the wire; when it moves a few radii away from the wire, the rate of induced charge levels off. The pulse shape observed

in the laboratory is shown in Figure B.4, while that predicted by this analysis is shown in Figure B.3. The agreement of the shapes is reasonably good; the absolute magnitude of the observed pulse is a bit smaller than that predicted, using a gas multiplication factor of 2×10^8, a gas-mobility for electrons of 10^6, a gas-mobility for ions of 1.04×10^3, and gas pressure of 760 torr.

ELEMENT	Value
R_{HV}	10 MΩ
R_{bot}	380 Ω
R_{tube}	0 Ω
R_{top}	680 Ω
R_{scp}	1 MΩ
C_{bot}	4.7 nF
C_{tube}	0.0033 nF
C_{top}	4.7 nF
C_{scp}	0.015 nF
V_{HV}	2700 volts

Table B.2: Circuit Element Values. This table lists the values of the circuit elements for the operation of the PTM proportional tubes during the test observations.

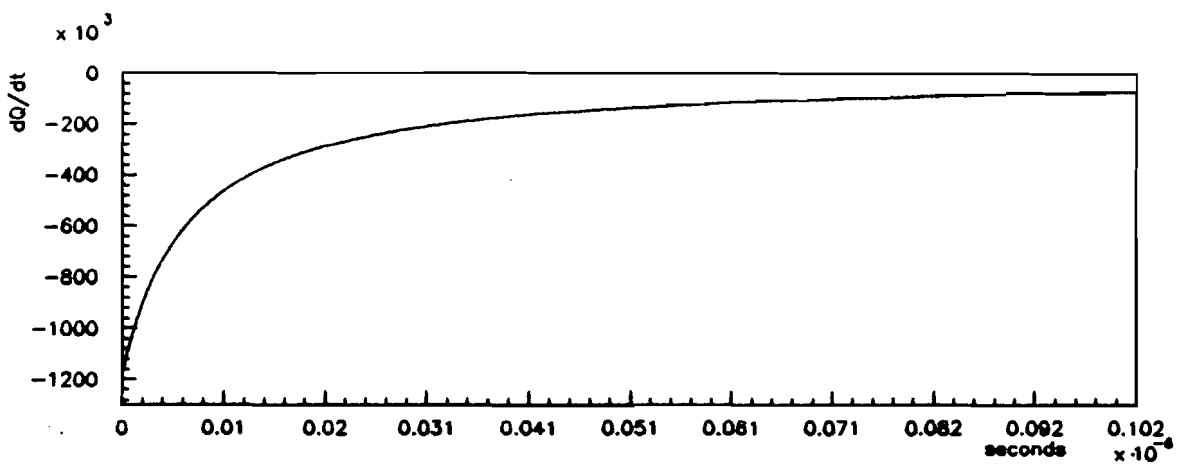

Figure B.2: Predicted Rate of Induced Charge. This is the rate of charge induced on the wire predicted by the analysis for the conditions listed in Table B.2.

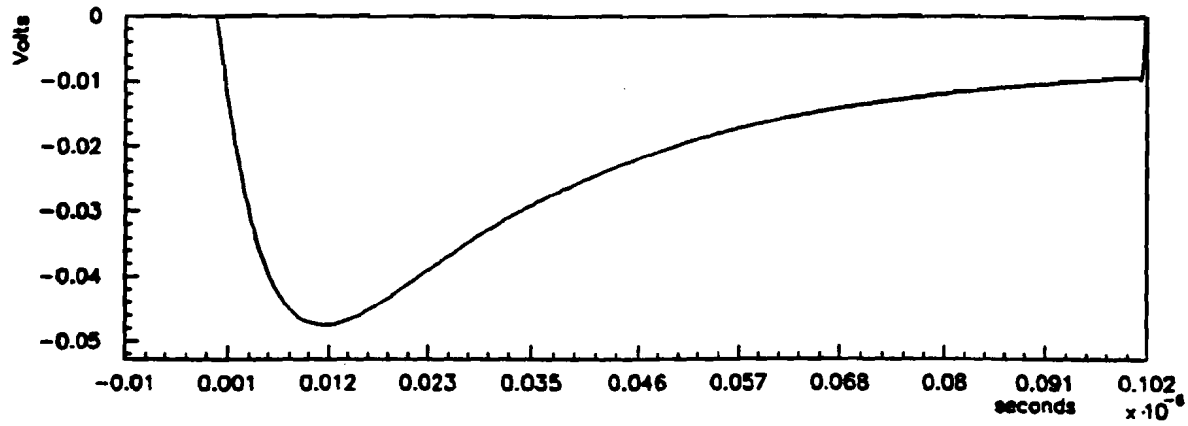

Figure B.3: Predicted PTM Pulse Shape. This is the pulse shape predicted by the analysis for the conditions listed in Table B.2.

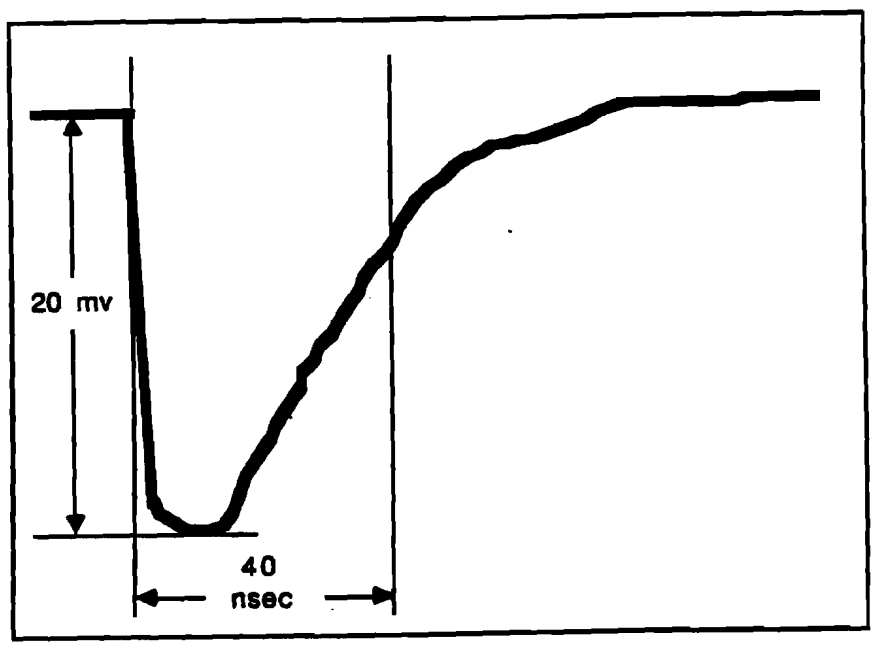

Figure B.4: Observed PTM Pulse Shape. This is the pulse shape observed on the oscilloscope under the conditions listed in Table B.2.

Appendix C

Delta-Rays

A delta-ray is a knock-on electron whose kinetic energy is much greater than its ionization potential. The scattering can then be treated as a free collision, and the Rutherford scattering formula can be used [9, p.251]:

$$d\sigma = \frac{2\pi e^4 z^2 Z^2}{16E^2 \sin^4 \frac{\theta}{2}} \sin\theta d\theta, \tag{C.1}$$

where E is the energy of the incident particle and θ is the scattering angle in the center of mass system. This angle can be related to the angle in the lab system: $\Theta = (\pi - \theta)/2$. Now, the energy of the ejected electron, T, is strictly related to the ejection angle:

$$T = 4E \sin^2 \frac{\theta}{2} = 4E \cos^2 \Theta. \tag{C.2}$$

Then, the cross section can be given by a function of the angle or of the kinetic energy:

$$d\sigma = \frac{\pi e^4 z^2 Z^2}{E} \frac{dT}{T^2} = \frac{\pi e^4 z^2 Z^2}{E^2} \frac{\sin\Theta d\Theta}{\cos^3\Theta}. \tag{C.3}$$

The maximum scattering angle is $\Theta = 90°$, with corresponding zero energy. So the angle of ejection peaks in the direction perpendicular to that of the incident particle; however, the energy of the ejected electron is lowest in this direction and highest along the path of the incident particle.

The probability of ejection of a delta-ray of energy between T_{min} and T_{max} is given by

$$\text{Probability} = \frac{\pi\alpha^2(4\pi\hbar c)^2}{E} x n_e \left[\frac{1}{T_{min}} - \frac{1}{T_{max}}\right], \tag{C.4}$$

where x is the path length of the delta-ray and n_e is the number density of electrons in the material.

From simple 2-body relativistic kinematics, the maximum energy that can be transferred is given by [48]:

$$T_{max} = 2\frac{(E + Mc^2 + mc^2)^2 mc^2}{M^2c^4 + m^2c^4 + 2mc^2(E + Mc^2)} - 2mc^2 \tag{C.5}$$

$$\approx \frac{2mc^2\beta^2}{1-\beta^2}, \tag{C.6}$$

and this will set one of the limits of integration.

The minimum ejection angle can be considered also in terms of the ionization potential, I. If I is written in terms of a frequency ν, $I = h\nu$, then the collision time t must be small compared to the period of these oscillations to be a free collision: $t \ll 1/\nu$. This time is approximately given by the impact parameter r: $t \approx r/v\gamma$, where v is the velocity. Then, the maximum impact parameter can be set to be $r_{max}/v\gamma = 1/\nu$, or $r_{max} = v\gamma/\nu$. The minimum scattering angle is given by [48, p.12] $\theta_{min} = \lambda/r_{max} = h\nu/pv\gamma$, where p is the momentum of the incident particle.

The effects of these ejected delta-rays will depend upon the distances which they travel in the detectors. The collisions that the electron makes will randomize its path long before it comes to a stop. This results in an effective range for a delta-ray; this is given by [57, p.6]:

$$\text{Range} = (0.71)T^{1.72}, \tag{C.7}$$

where E is in MeV and the Range is in (g/cm^2). For Argon the density at STP is $1.78 \cdot 10^{-3}$g/cm^3, so the range in gaseous Argon in centimeters is Range $= (399)T^{1.72}$. The minimum range of a delta-ray which will generate additional hits in a detector is roughly a couple of wire-spacings; if this is about a centimeter, then the minimum energy delta-ray will be

$$T_{min} = e^{[\ln(\frac{R_{min}}{399})/1.72]} = 30\text{keV}. \tag{C.8}$$

Thus, for a relativistic particle, the $1/T_{max}$ can be ignored; adding the appropriate dimensions yields the following expression for the probability:

$$\text{Probability} = \frac{\pi\alpha^2(4\pi\hbar c)^2}{E(\text{GeV})}\frac{(1.97 \cdot 10^{-14}\text{GeVcm})^2}{(\hbar c)^2} \times x(\text{cm})n_e(\text{cm}^{-3}) \tag{C.9}$$

$$\times[3 \cdot 10^4 - \frac{1}{((E/M)^2 - 1) \cdot 10^{-3}}](\text{GeV})^{-1} \tag{C.10}$$

$$\approx \frac{3.1 \cdot 10^{-25}(\text{GeVcm}^2)x(\text{cm})n_e(\text{cm}^{-3})}{E(\text{GeV})}. \tag{C.11}$$

Mylar ($C_5H_4O_2$) has 11 electrons per molecule and a density of 1.39 g/cm^3. The number density in mylar is given by the product

$$\begin{aligned} n_e &= \rho(\mathrm{g/cm^3})W(\mathrm{molecules/g})N_e(e^-/\mathrm{molecule}) && \text{(C.12)} \\ &= (1.39\mathrm{g/cm^3})(5.98\cdot 10^{21}\mathrm{molecules/g})(11e^-/\mathrm{molecule}) && \text{(C.13)} \\ &= 9.14\cdot 10^{22}e^-/\mathrm{g}). && \text{(C.14)} \end{aligned}$$

For a 10 GeV pion the maximum energy transferable to an electron is given by Equation C.6 to be T_{max} = 5.5 GeV. Thus, in a 0.1cm mylar window of a chamber the probability of ejection of a delta-ray of energy between T_{min} and T_{max} for a 10 GeV incident pion is given from Equation C.11:

$$\text{Probability} = 3\cdot 10^{-4}. \qquad \text{(C.15)}$$

Argon gas has 18 electrons per molecule and a density of $1.78\cdot 10^{-3}$ g/cm^3; the number density is given by the product

$$\begin{aligned} n_e &= \rho(\mathrm{g/cm^3})W(\mathrm{molecules/g})N_e(e^-/\mathrm{molecule}) && \text{(C.16)} \\ &= (1.78\cdot 10^{-3}\mathrm{g/cm^3})(1.49\cdot 10^{22}\mathrm{molecules/g})(18e^-/\mathrm{molecule}) && \text{(C.17)} \\ &= 4.79\cdot 10^{20}\mathrm{e^-/g}). && \text{(C.18)} \end{aligned}$$

For 10m of Argon gas, the probability would be

$$\text{Probability} = 1.5\cdot 10^{-2}. \qquad \text{(C.19)}$$

The distribution of this probability as a function of both the energy and the angle of emission of the delta-ray in the lab system is shown in Figure C.1.

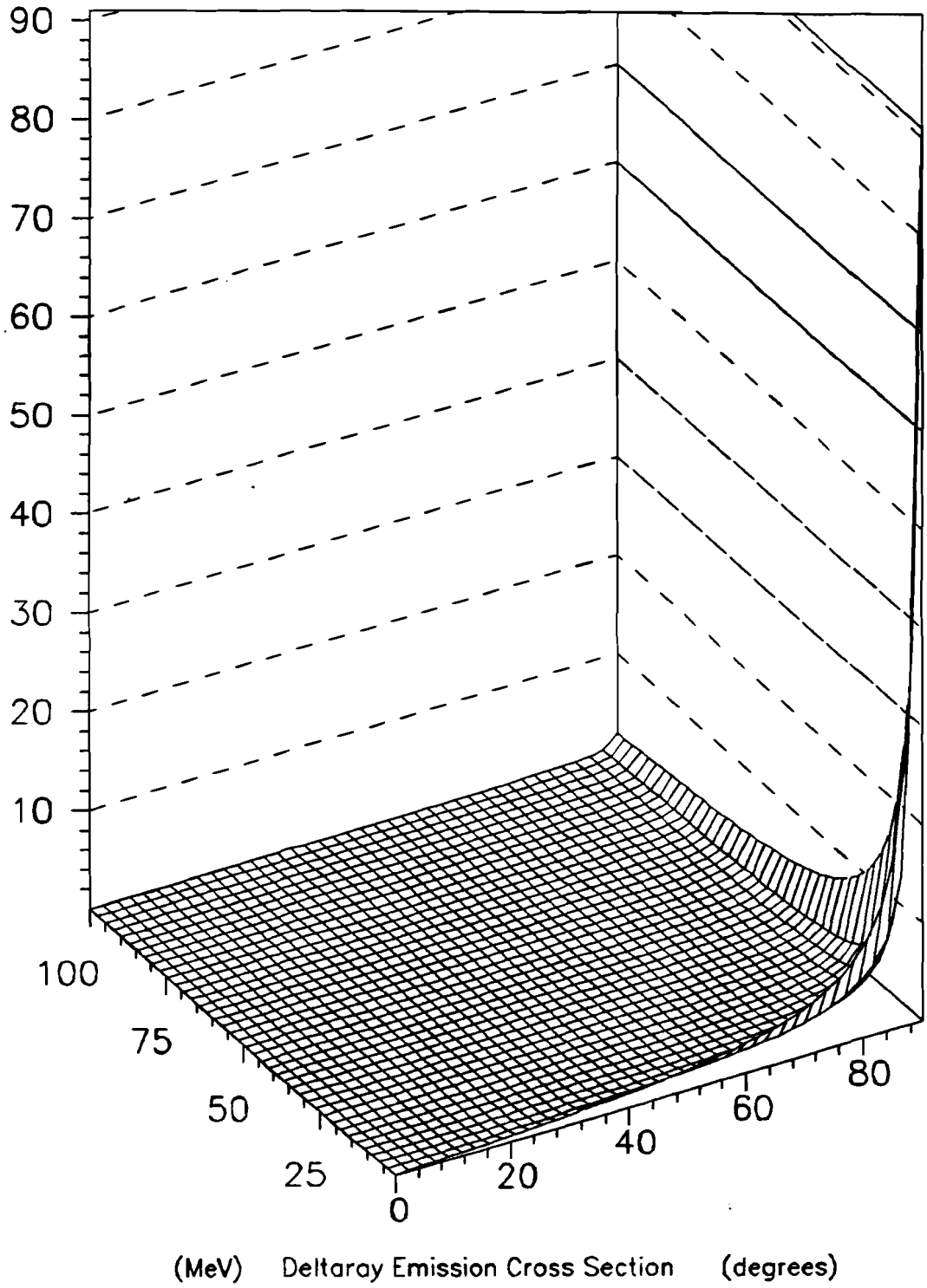

Figure C.1: Probability Distribution of Delta-Ray Emission. This plot shows the probability of emission of a delta-ray as as function of the energy (on the ordinate) and the angle of emission (on the abscissa) of the delta-ray, for a 10 GeV pion.

Appendix D

PTM Proportional Tubes

D.1 Construction of the Tubes

MIT was responsible for the installation of the Muon Proportional chambers. The proportional tubes were constructed of extruded aluminum in a staggered-double-cell formation of 15 square tubes per module (see Figure D.1a). An extruded manifold was secured in each end, and 15 machined Nylon bolts were epoxied into these manifolds. Each nylon bolt had a hollow brass pin secured through its axis, and the 2 mil (50μm) gold-plated tungsten wire was soldered inside these pins. A tension of 250 grams was affixed on each wire during this process. The tensions of all the wires were checked using a magnetic induction oscillation test, and all wires not meeting the ± 30 gram tolerance ($\sim 2\%$ of the wires) were replaced. In a Y-plane (vertical wires) there were thirty-eight 12' 3" modules; in a Z-plane (horizontal wires) there were nineteen 24' modules. We constructed 157 Y-modules and 80 Z-modules. For the two sets of wide-angle PTA chambers there were views (Z, Y, U, V); we constructed 98 modules: forty-two 6' 6" modules and eight modules each of 2', 3' 3", 4' 6", 5' 9", 7', 8' 3", and 9' 6" lengths.

The gas-tightness of the epoxy seals around the nylon bolts and the epoxy seam around the manifold were tested using a differential pressure system. Leaks were located with *Snoop* and repaired applying epoxy while the tubes were being pumped down; the reduced internal pressure drew the epoxy into the fault, forming a tighter repair. A quantitative measure of the gas-tightness was determined by measuring the loss rate to be less than 1% of the volume per day; the total volume was 380 cubic feet.

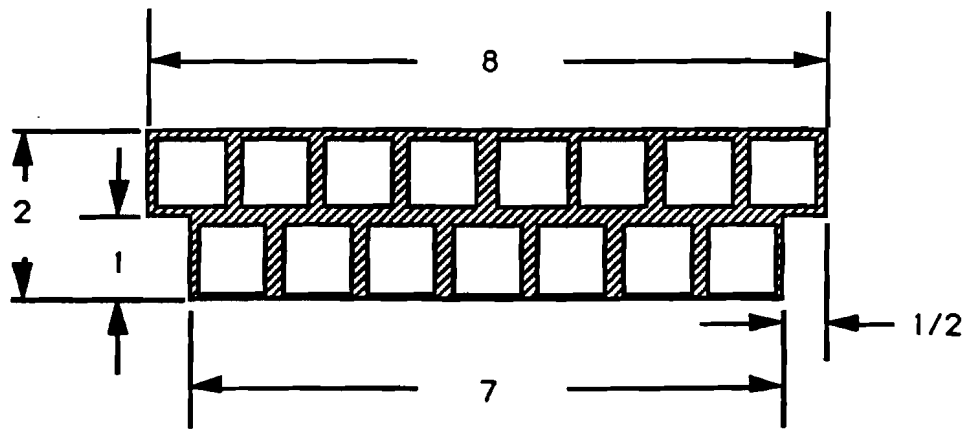

(a)

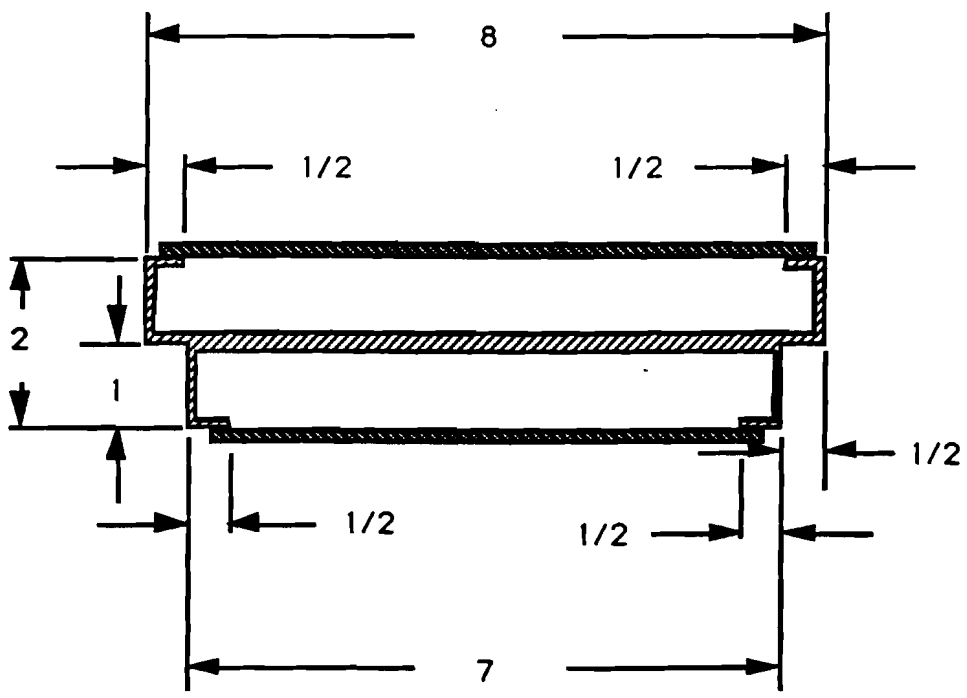

(b)

Figure D.1: PTM Cross section. In figure (a) is shown the cross sectional view of a PTM module; each cell was nominally a 1" square. In figure (b) is a cross sectional view of the milled-out region employed in the beam region of the PTM's; the intercell webbings were removed from both halves of the module for a distance 6" along the wires.

Next, every wire was tested in Limited-Streamer mode at 3 KVolts with a Cadmium^{115} source. We found 12 wires out of 5000 that would not yield clean signals, and these were replaced.

D.2 Construction of the Support Assembly

The next phase of operation was the design of the Support Assembly for the Muon Proportional Planes and the Scintillation Counters. A significant amount of time was spent maximizing the utility of the Assembly while minimizing the complexity of construction and limiting the massiveness of the structure. Three walls of shielding blocks were installed to "decouple" the four stations (X-components) of the detector assembly; the order of the stations was 1 through 4 along the beam, i.e. south to north (see Figure 3.1). Each station consisted of a plane of vertical wires for determining Y-position, a plane of horizontal wires for determining Z-position, and a plane of scintillator for giving a fast trigger. Each plane of wires covered an active area of 12 feet on the Z-axis by 23 feet 9inches on the Y-axis. The beam height was 8 feet above the floor. The shielding block walls were constructed to be 15 feet high by 24 feet east-west. The blocks were three feet thick in the X-direction and selected and stacked in such a manner that the cracks did not lineup on successive walls.

Each plane had to be rolled out of its station to the west, and the Support Assembly was designed to facilitate this method of access. The essence of the design was to have each plane supported by two commercial trolleys which rolled along a steel I-beam. These I-beams were fastened to the underside of a 8"×12" steel box-beam that ran north-to-south and was supported on legs that were secured to the tops of the shielding-block walls (see Figure D.2). I wanted to minimize the X-separation of our Y and Z-planes in each bay. The amount of the trolley overhang proved to be the delimiting factor; therefore, I staggered the heights of the Y and Z-I-beams in order to overlap this trolley overhang (see Figure D.3). This introduced some complexity into the design. The design of the fastening mechanisms for the I-beams included shims and slotted holes to allow for leveling and angular alignment. A further complication arose in the extensions of the I-beams to the west wall, on which the planes rolled out of their stations. Because the crane did not have a radio-control unit at that time, I had to design I-beam extensions that were removable.

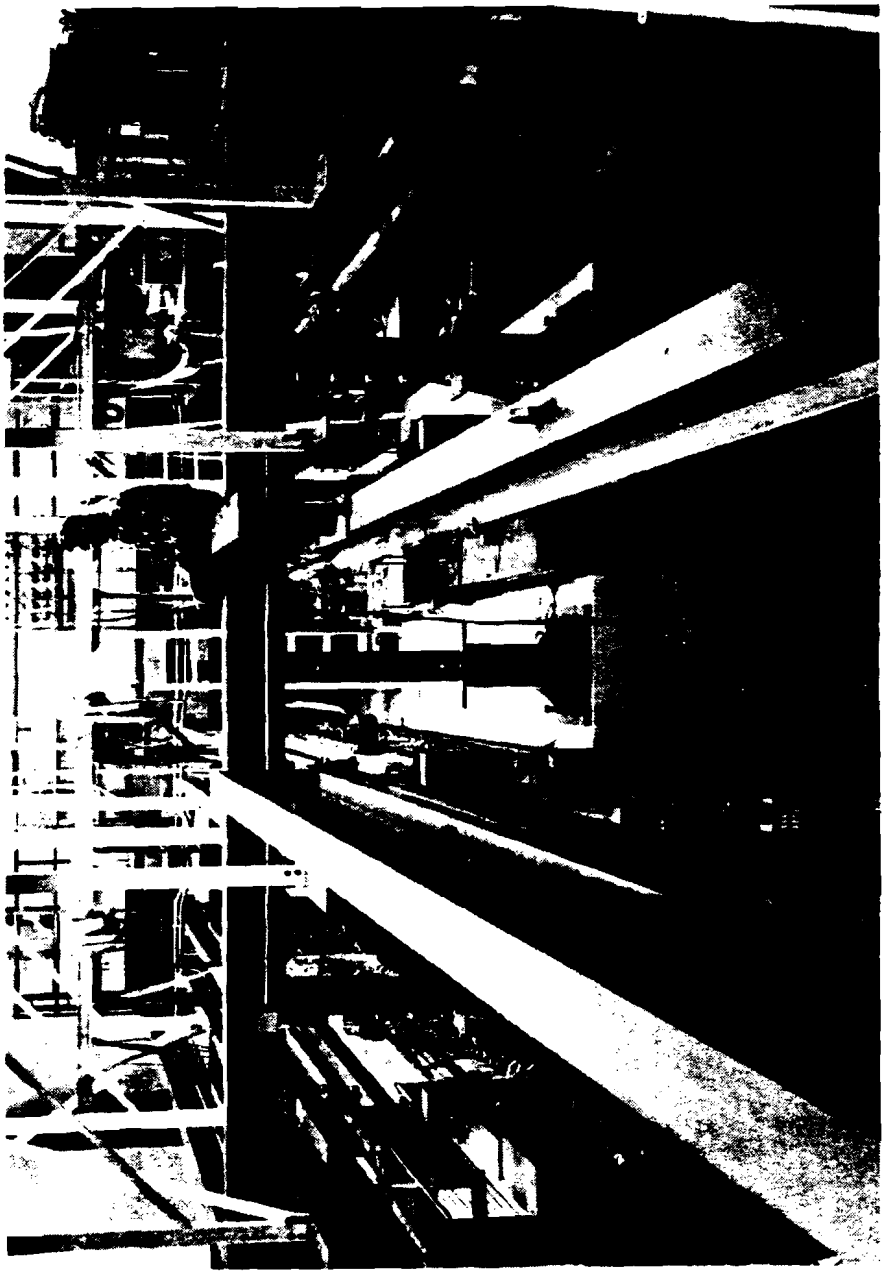

Figure D.2: Muon Support Assembly. The figure shows the Support Assembly for the Muon Spectrometer.

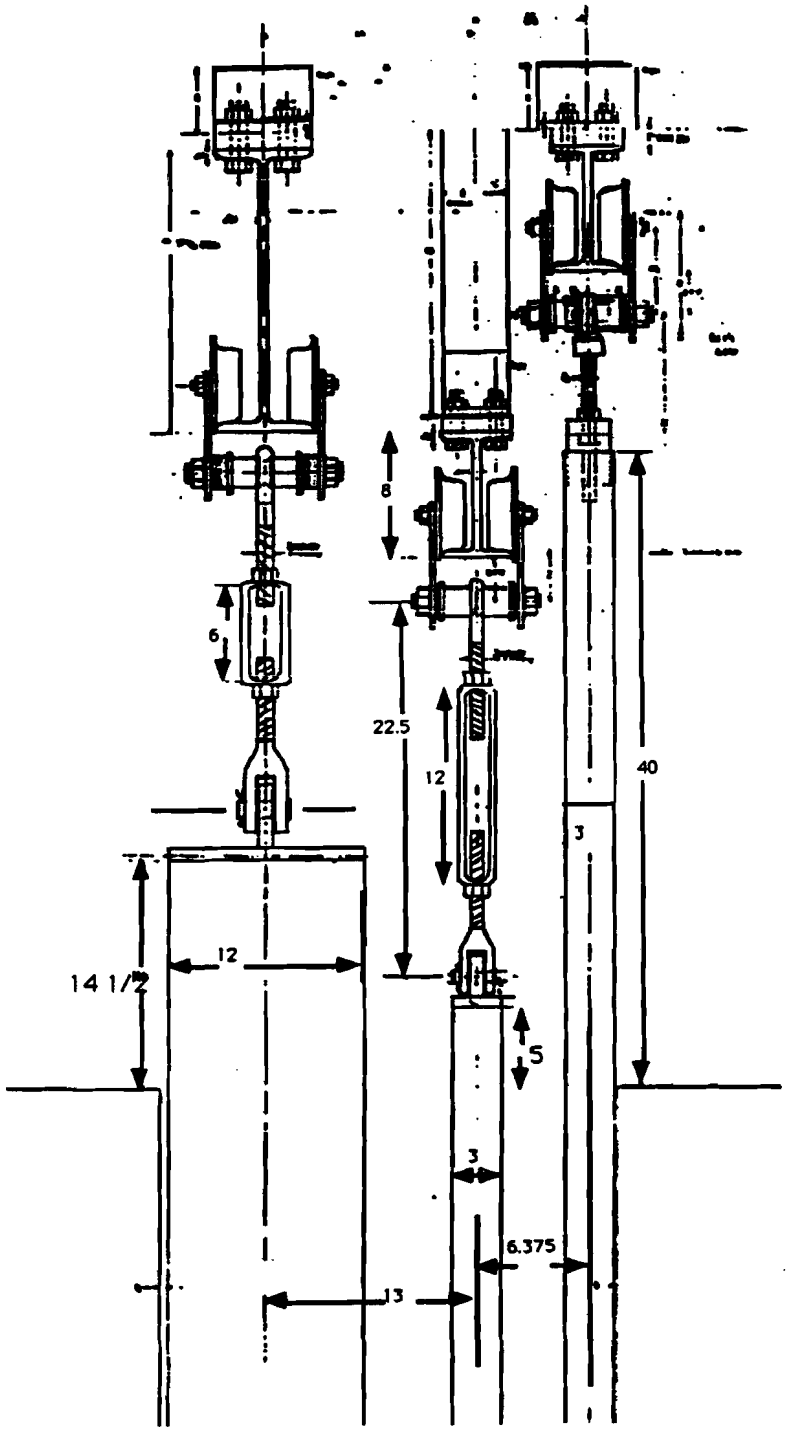

Figure D.3: Muon Support Assembly Overhang. This figure shows the overlapping of the supports for the I-beams for the Y and Z-planes.

D.3 Proportional Tube Frames

The proportional tube frames supported both the tubes and the electronics. The electronics were accessible from outside the shielding-block walls on both sides of the Z-planes (horizontal wires) and on the top side of the Y-planes (vertical wires) from on top of the shielding-block walls. The Y-planes had to be rolled out to access the injection electronics on the bottom side of the vertical tubes. The frames were constructed of aluminum box-beams and extruded aluminum pieces welded together. The extruded pieces had holes precision drilled into the sides for locating and fastening the proportional tube modules through a mating piece of 1"×2" aluminum angle which was epoxied to the module (see Figures D.4 and D.5).

The gas was injected at one end of each module and exhausted at the other, so gas flowed to each module within a plane in parallel with the other modules in that plane. The gas was bused onto and off a plane with 3/4-inch copper pipe, and each module tapped into these pipes via 1/4-inch poly-flo tubing.

As can be seen in Figures D.4 and D.5, the plans for the proportional tube frames, a 7"×7" hole had been planned in the beam region.

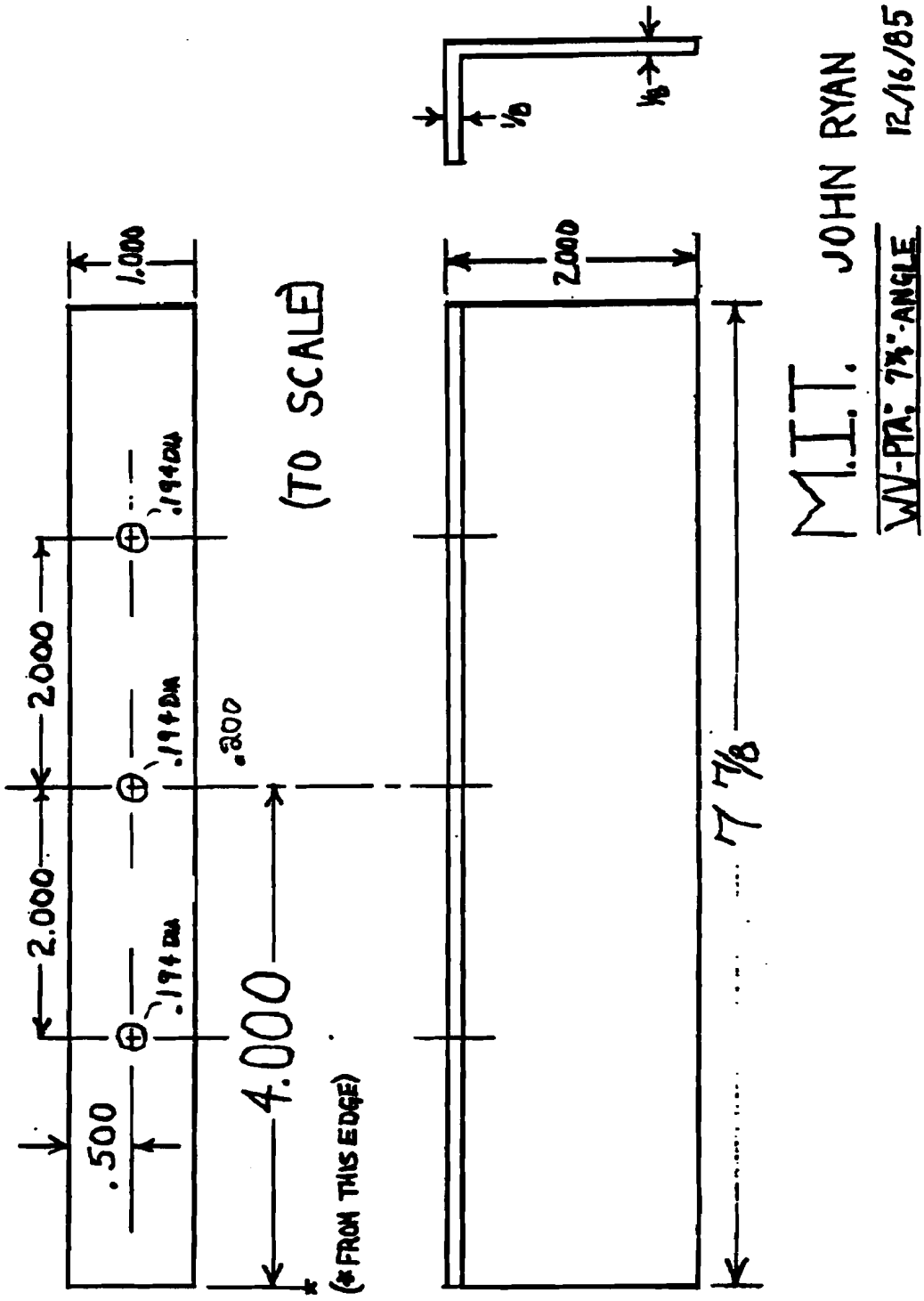

Figure D.4: Aluminum Angle Precision Fastening.

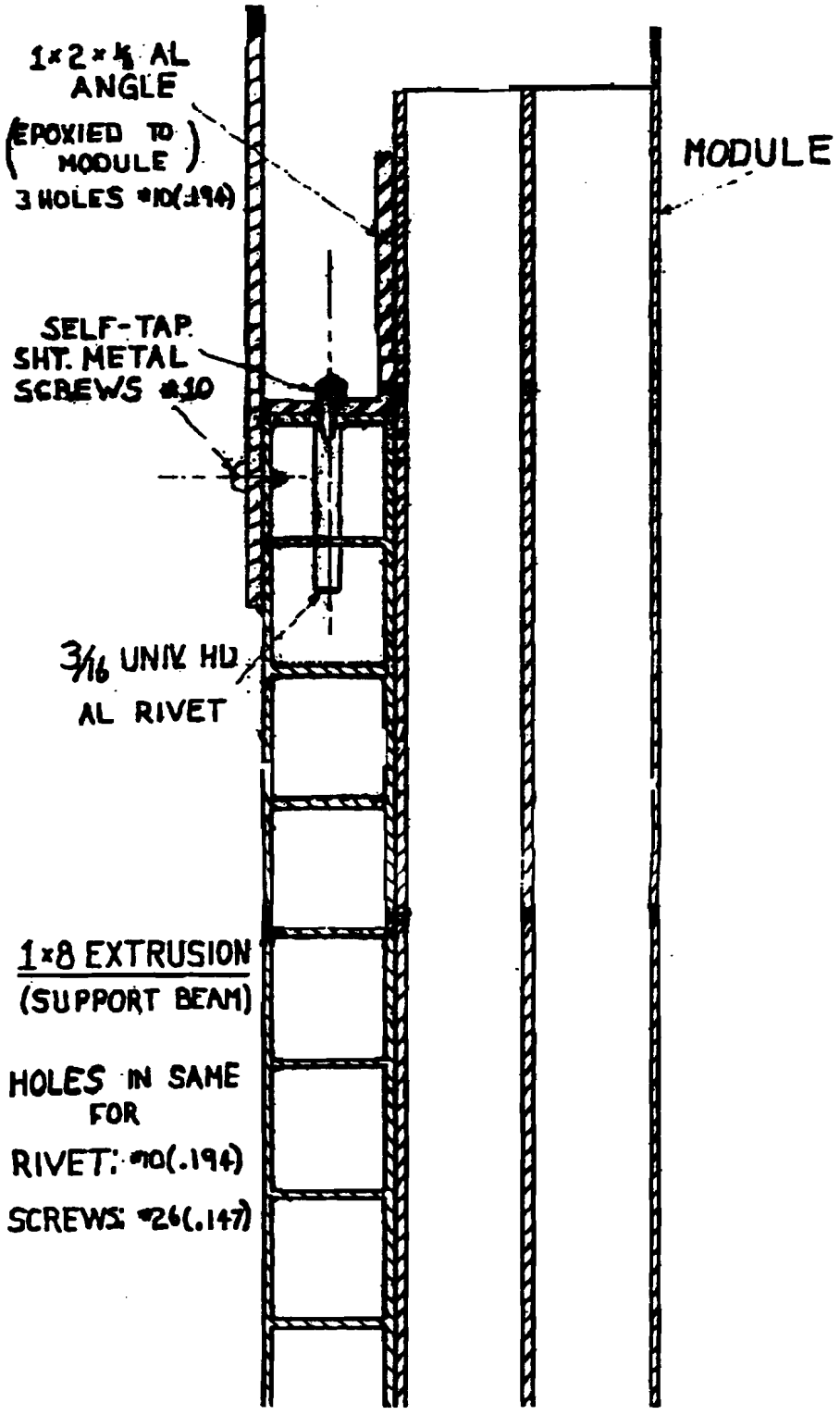

Figure D.5: Precision Fastening.

D.4 Beam-Hole Region

D.4.1 Motivation

The Intense flux of particles through the beam region of a chamber can produce dead-time problems due to space-charge buildup. The readout electronics frequently cannot handle the high rate of beam flux; intense flux can lead to radiation damage which results in loss in chamber efficiency. These reasons lead to the decision to modify the chamber in the beam region so that particles would not generate hits, thus "deadening" the region. There are many ways in which to deaden a region, and one had to be chosen according to the various aspects of chamber use and ease of construction.

Frequently, the wires are coated with some insulating sleeve, or the gas is restricted in the area. We wanted to retain some control over varying the size of the dead region, so we did not want to fix this size at construction time. Coating the wires is a permanent method of deadening, and to change the size of deadening along the wire would have required the restringing of the whole wire. However, Tom Lyons suggested that we could insulate the cathode walls of the chamber and, thereby, deaden the region.

The deadening worked according to the following description. The wires were the anodes, and the walls of the tubes were the cathodes. Electrons migrate toward the anode and the positive ions toward the cathode. When the ions reach a conductive cathode plane, they extract electrons to neutralize themselves. However, if the cathode plane is covered with an insulating material, then electrons will not be freely available, and the ions will not be able to recombine, and they will "cling" to this surface. Or, if the ion does extract an electron, the insulating material will be left with a "hole" which it will not be able to fill. These two processes will result in the buildup of a net positive charge on the insulating surface over the cathode. This will reduce the potential difference between this surface and the anode wire and, hence, the electric field in the tube, and this will reduce the gas multiplication effect. With this hypothesis in mind, we constructed a module to test the practicability of this deadening scheme.

The beam region of the chambers was to be roughly an 8-inch square. To deaden a region of this size in a test module, we machined a piece of extrusion to make a 3-foot module. Before stringing the wires, we machined a 6"×8" "window" through this module as seen in Figure D.1b: we machined off the outer walls from both sides (6"×8" on one side and 7"×8" on the other) and machined out the "webbing" walls

from between the adjacent cells. On this test module we milled out the mid-plane wall and machined screw holes for attaching 1/32"-aluminum strips to "shutter" this mid-plane window. These strips were 3/8"-wide by 7.5"-long, and we wrapped several of these strips with Kapton tape so that, when laid in place, they formed the pattern seen in Figure D.6. These strips were secured in place with nylon screws in order to limit the number of sharp edges which would distort the electric fields. Two 1/8"-aluminum plates were fitted with Kapton tape on their inner-surfaces and were screwed tightly against the outside of the module with stainless-steel screws; these plates were sealed gas-tight with RTV-silicone compound. The pattern of the deadened region was spray-painted on the outsides of these two plates in order to help locate the region during testing. Then the wires were strung, and the module was sealed with RTV.

The various configurations of the flux lines of the electric fields are depicted in Figures D.7a, b, and c. In Figure D.7a we see the configuration of a normal region of the module; in Figure D.7b we see the configuration due to the machining: the removal of the webbing and the placement of the outer plates. In this configuration there is no insulating material, and the electric fields should be roughly intact, except for the region between wires; there is no potential difference between wires, so this region is field-free. The efficiency of production of hits should be drastically reduced in this region between adjacent wires on a given side of the mid-plane. However, on the other side of the mid-plane, directly opposite to this inter-wire region is the intact region of a wire between the wires on the first side; thus, the overall efficiency of the module should not be reduced greatly due to the missing webbings. In Figure D.7c insulating material has been applied to the mid-plane and to one of the outer surfaces, which suggests the configuration of the electric fields as shown. One should note the possible "edge effects" of efficiency that might occur near the edges of the insulation and the conductor.

D.4.2 The Setup

The objectives of the tests were to observe "deadening" in the region of the insulating material relative to a normal region, to measure the reduction in efficiency in the regions with no insulation but with the webbing removed, and to measure the "edge effects" or the transition from the live regions into the deadened region.

I used a "telescope" of two scintillators to trigger the latching of the wire signals. This consisted of overlapping the two scintillators and placing them over a selected region of the test module and then using the inverse of their coincidence as a "VETO" to the latching of the scaler which registered the hits (the signals on the wires). Thus,

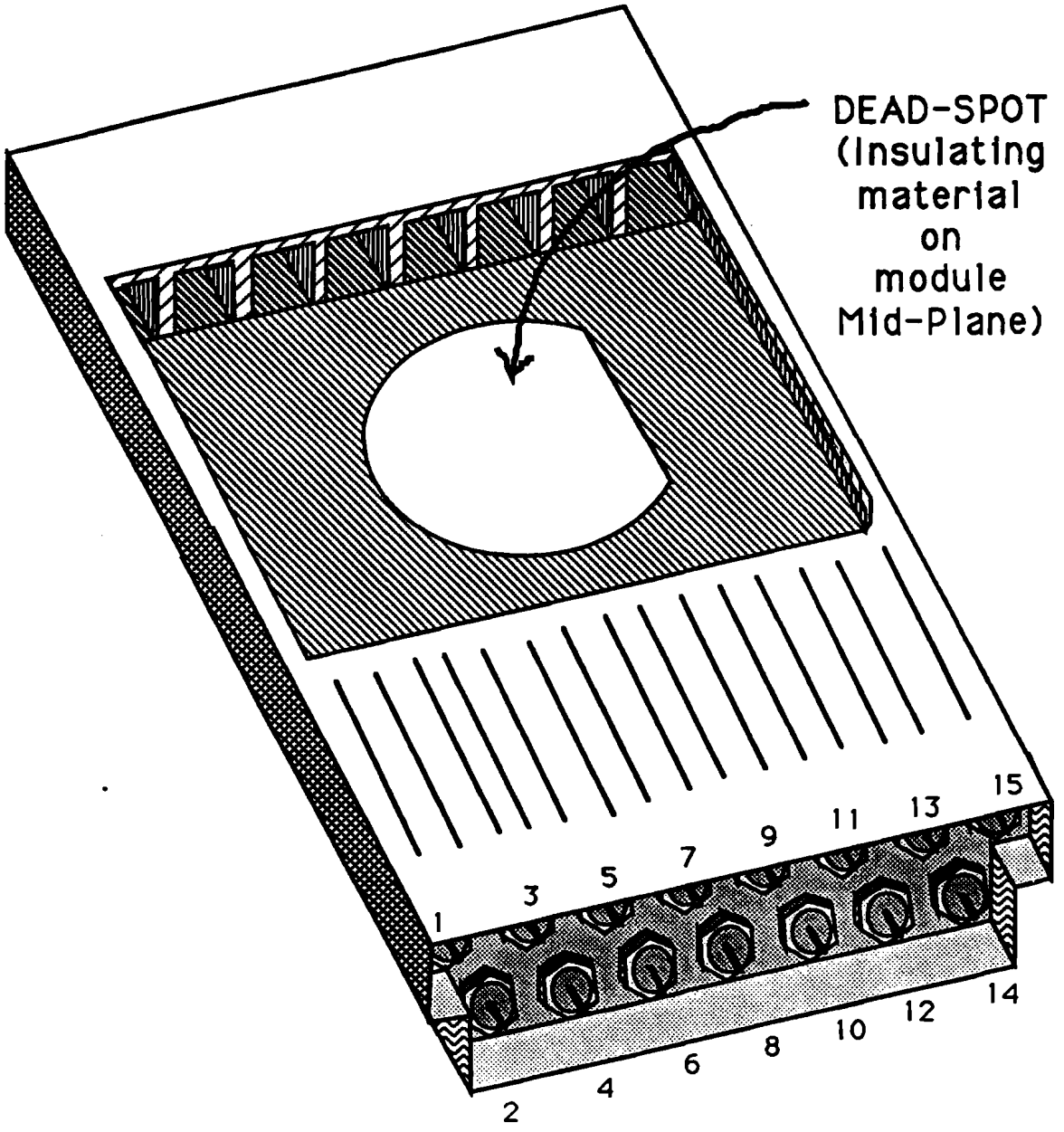

Figure D.6: PTM Test Module. This shows the milled-out window and the insulated region applied to the mid-plane. The wire numbers are indicated at the front edge.

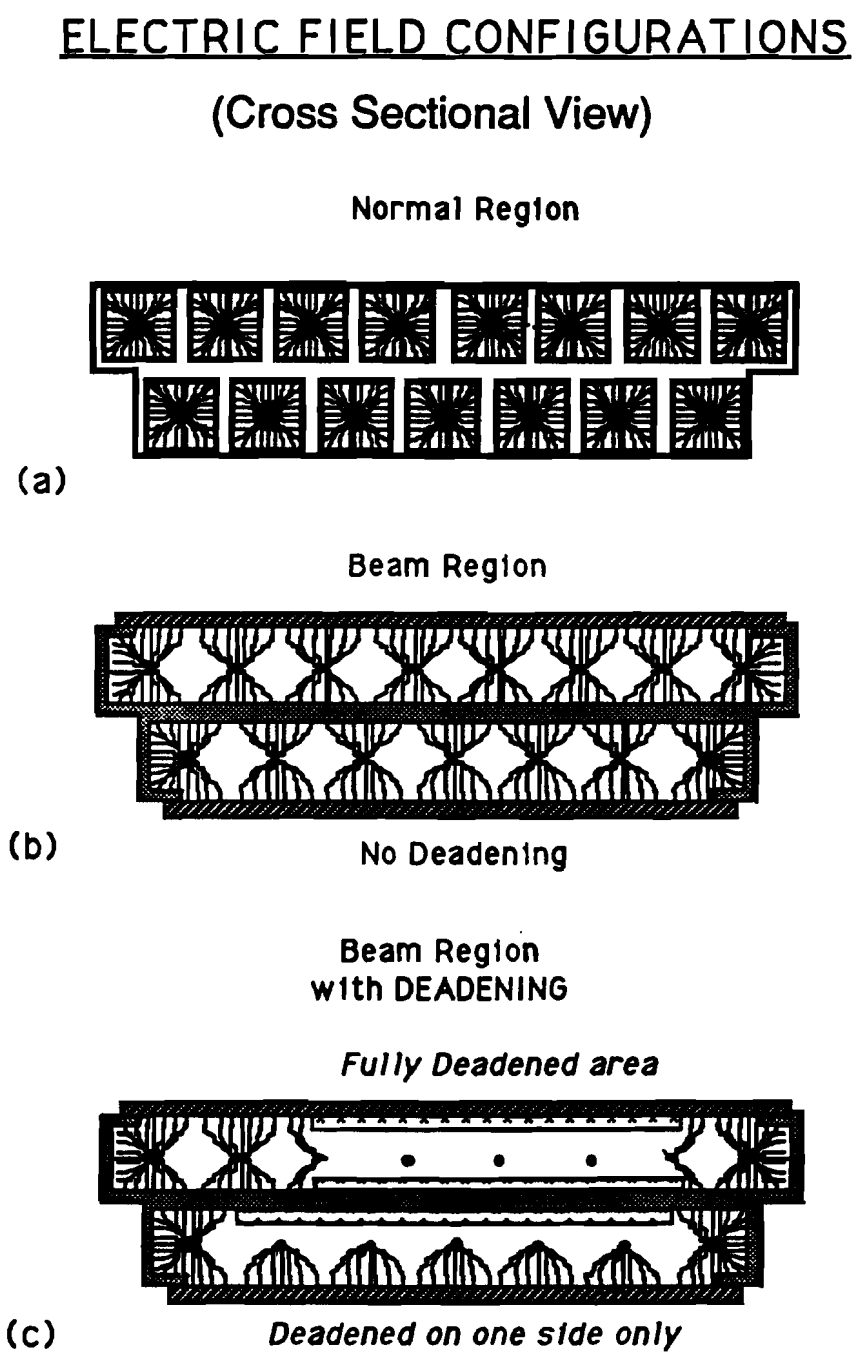

Figure D.7: Electric Field Configurations. This shows the configurations of the flux-lines of the electric fields generated in the normal cross section (a), in the milled-out region (b), and the insulated region (c).

in principle, a hit on a wire would be latched only if there were also hits in both of the scintillators at the same instant in time. The condition of simultaneity of the hits in the elements of the telescope greatly reduced the probability of false signals due to noise in the individual elements, and the separation of the elements restricted the acceptance of triggers to those particles whose trajectories passed through all the elements of the telescope. This arrangement was called the trigger "hodoscope".

I first normalize the setup by testing a region of the test module which was of normal cross section and, therefore, the definition of "fully live". Then, I marched the hodoscope into, across, and then out of the deadened region, taking incremental steps. Thus, I measured the relative efficiencies of the various regions of the test module.

The setup of the hardware was the following. The output from the wires were input to special amplifier/discriminator modules whose outputs were input to the LECROY 4434 SCALER, which was controlled by an IBM-PC, via a Transiac in the CAMAC crate. The two scintillators, S1 and S2, were constructed of scintillating material 6"-long, by 2"-wide, by 1/4"-thick, and light guides directed the light into the photomultipliers. These photomultipliers were supplied by outputs-1 and -2, respectively, of the Photo-tube High-Voltage Supply. The outputs from these photomultipliers were cabled into an LRS 621BL Quad-Discriminator: S1 into channel-2 and S2 into channel-4. The discriminated outputs had pulse heights of -1.5 volts and widths of 420 nsec, and these signals were connected to two of the inputs to a C304/N Dual 4-Fold AND module; the value of unused inputs defaulted to "TRUE". The NAND-output (the inverted coincidence of the input signals) was then connected to the VETO input of the LECROY SCALER. The VETO accepted a NIM input; it vetoed all scaler input when the NIM signal was "TRUE" (-0.8 volts) and accepted scaler input when the NIM signal was "FALSE" (ground). A Dual Channel BCD 1880A Scaler was used in the same NIM-Bin to calibrate the scintillators as a function of High-Voltage settings. The signal from S1 was input to channel-2, and the coincidence of S1 and S2, (S1 .AND. S2), was input to channel-1. The ratios of the rates of the coincidence to that of the single counter were consistently 0.35, over the High-Voltage range of 1700 to 1800 volts.

In addition, I tried adding a third scintillator, B1, which completely overlapped the other two scintillators. I measured the ratios of counting rates of channel-1 (B1 .AND. S1 .AND. S2) over channel-2 (B1 .AND. S1). For various High-Voltage settings, all near 2 Kvolts, the ratios were all close to 0.90. I concluded that the addition of scintillator B1 to the hodoscope did not greatly enhance noise reduction, so I did use it in any of the further tests.

I applied High-Voltage to the wires of the test module and used a probe to observe

the signals on an oscilloscope. At 4.7 Kvolts, wires-1 and -8 were "hot" (they displayed a great deal of secondary avalanching), so I 'burned them off' by raising the High-Voltage to 5.1 Kvolts for 48 minutes. Afterwards, the signals from all the wires looked good at 4.4 Kvolts. I next performed a "plateau curve" of the counting rate on a wire as a function of High-Voltage on the wire. The response of a proportional chamber was a function of the geometry of the chamber, the type of gas, the pressure of the gas, and the High-Voltage applied to the wires. For operation, only the High-Voltage was easily varied, and to limit systematic errors involved with variations in response due to variations in High-Voltage, I wanted to chose a value of High-Voltage in a range over which the response changed slowly as a function of the High-Voltage; this appeared as a "plateau" of the curve of counting rate as a function of High-Voltage. I was using a gas mixture of 50%-Argon and 50%-Isobutane, and this mixture had no large plateaus. I tried running at 3.3 Kvolts, but the signals on the wires were too small to register in the scalers. Therefore, at the suggestion of Tom Lyons, I increased the High-Voltage to 4.4 Kvolts and then saw counting.

D.4.3 Measurements

I ran first over the Normalization region, using the setup shown in Figure D.8; the S1 and S2 scintillators were fully overlapped (6"×2") and separated by 15". I used the inverse of (S1 .AND. S2) as the VETO to the scaler, with a gate width of 1000 nsec. Then, I marched the hodoscope across the deadened region, taking data at the locations denoted by the alphabetic letters shown in Figure D.9. For each run, the counting rates on the wires were normalized to the total number of hodoscope triggers (Anti-VETO signals).

It became apparent that the majority of the background signal was due to large air-showers. These showers could produce quite a large instantaneous density of charged particles in a localized region. So, in addition to the particle passing through the hodoscope, there was frequently a particle that simultaneously passed through a tube in a region not covered by the hodoscope. Since I was using the hodoscope as a trigger, I expected that all hits on wires were produced in the region covered by the hodoscope. These additional simultaneous hits on wires in live regions, then, appeared as hits in the region covered by the hodoscope, and this was a background signal for which I had to try to correct. To measure this background I used a setup with an additional "finger" counter, FM, which was a 1"×1" scintillator and photomultiplier, as shown in Figure D.10. S1 and S2 were completely overlapped but placed longitudinally along wire-8 (the central wire in the test module) in the normalization region of the test module, and FM was positioned directly above the tube of wire-8. The inverse of (FM .AND. S1 .AND. S2) was used as a VETO, so only particles passing through

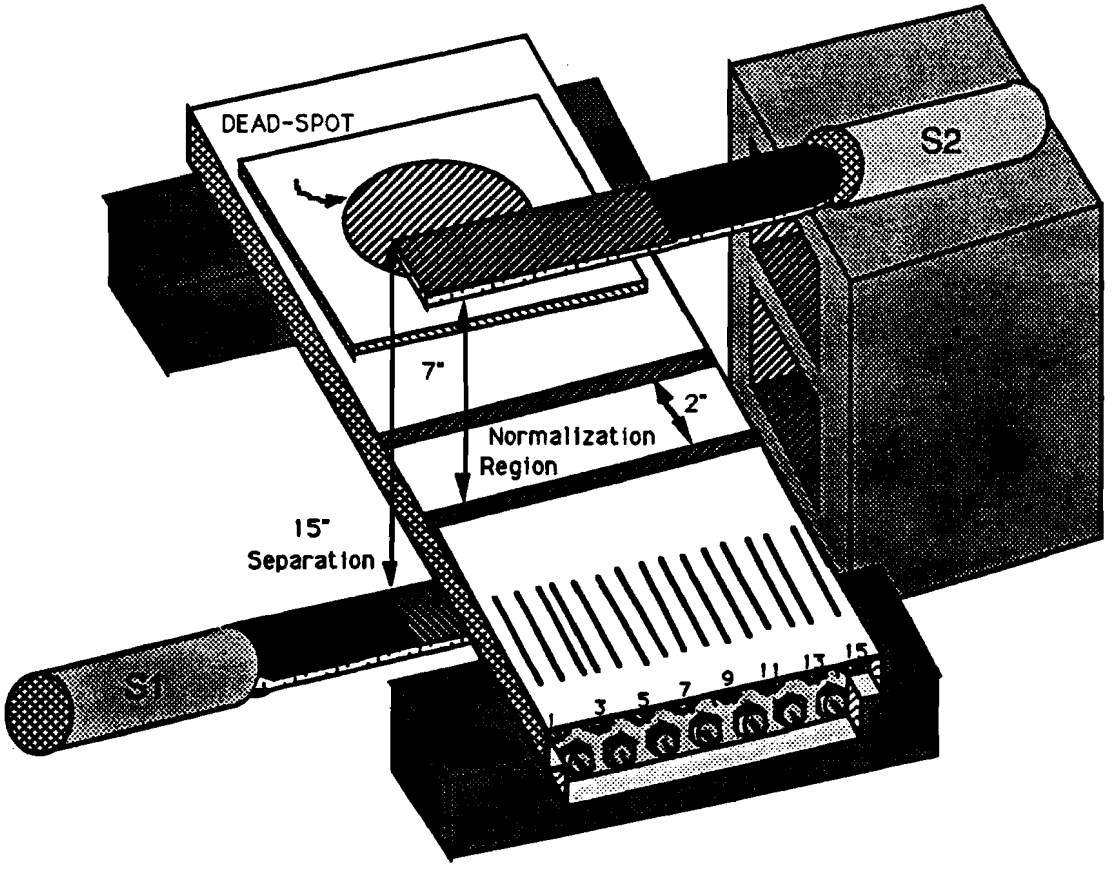

Figure D.8: Normalization Setup. This shows the arrangement of the active components for the measurements taken of the Normalization region.

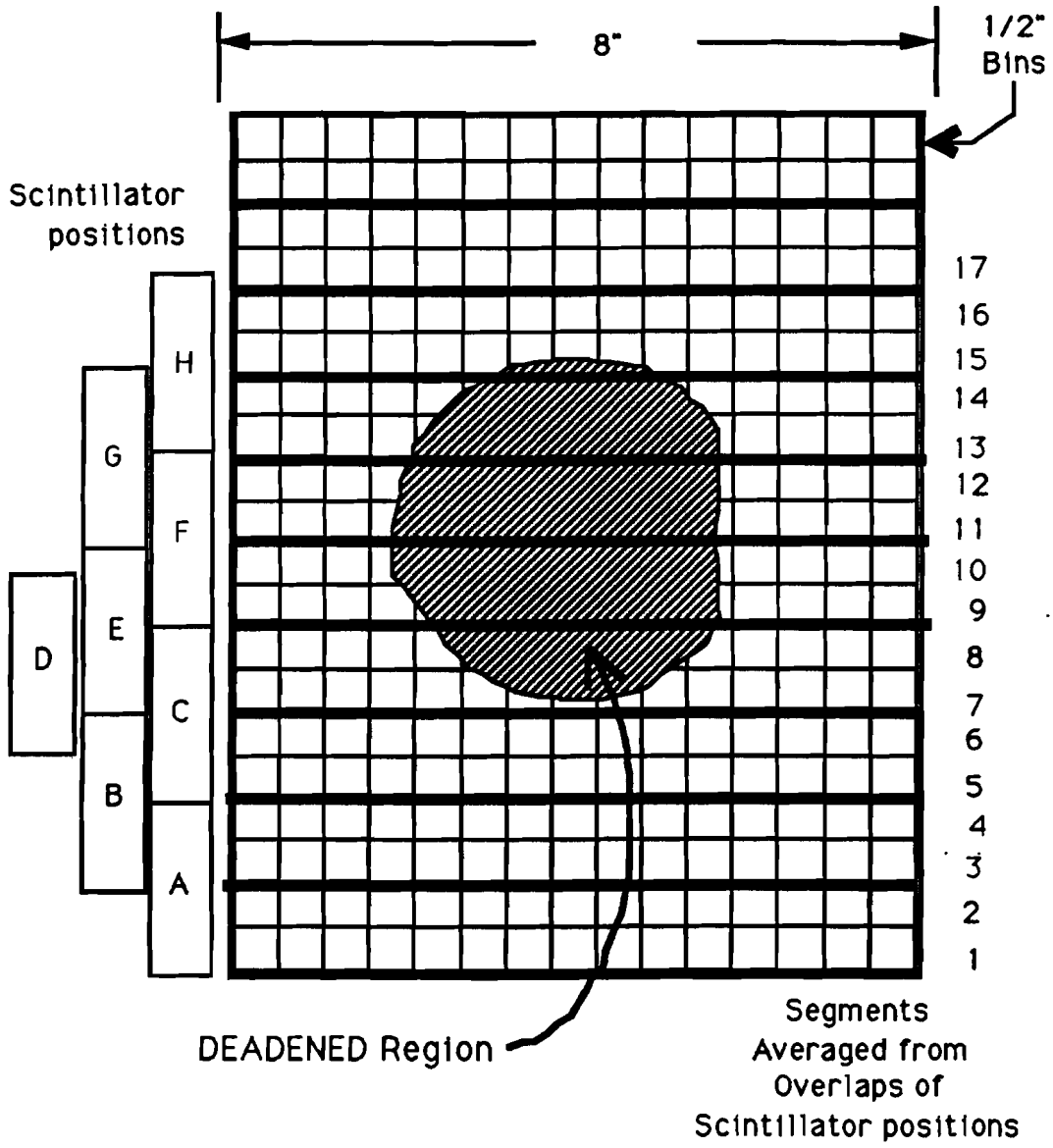

Figure D.9: Measurement Grid. This shows the arrangement of the successive measurements taken of the deadened region. The overlapping of the positions was used to generate a smoothed curve falloff of efficiency.

wire-8 should register. Of course, wire-8 overlapped wire-7 and wire-9, so these two wires should also register quite frequently. However, the counting rate observed in the wires far from wire-8 should describe the background rates due to showers and chamber resolving times.

Then, I used the same hodoscope configuration to take data in the center of the deadened region, except that S1 and S2 were rotated 90 degrees so as to be perpendicular to the wires, as shown in Figure D.11.

D.4.4 Analysis

First I looked at the Normalization data and the effects of the background signals. I used the measurements from the setup shown in Figure D.10. The counting rates per wire are graphed in Figure D.12; one can see the peak at wire-8, over which the hodoscope was placed, and the sharp drop off as the distance from wire-8 increased. From these far regions I calculated an average value for the background counting rate of 1.*10-3. Then, before plotting the measurement of the deadened region taken from the run shown in Figure D.11, I subtracted this average background counting rate from the measured counting rates for each wire. I divided these rates by the rates as measured in the **A**-region of the window; this **A**-region had the webbings removed but no deadening applied. The plot of these normalized dead spot measurements is shown in Figure D.13. The sharpness of the variations from a smooth curve was due to the subtraction of the background, a small number, from the counting rates, which were also small numbers. However, this plot suggests that the deadening reduced the counting rate below that of the background, which was one to two orders of magnitude. I could measure this reduction factor no better than the limit of the background.

Next I mapped out the window using the measurements made on the setup shown in Figure D.8. The counting rates for each wire were shown in Figures D.14a and b for each placement of the hodoscope; in Figure D.9, section-1 corresponds to the normalization region and sections-2 through -9 to the hodoscope positions **A** through **H**. In this plot is shown the result of the deadening in section-7 (the middle of the dead spot) as a reduction of counting rate by an order of magnitude; this counting rate, however, was close to the measured rate of background counting.

In order to see the mapping of the measurements more graphically, I superimposed the efficiency plot over the test module in order to compare to the applied deadening seen in Figure D.6. From the eight placements of the hodoscope, **A** through **H** in Figure D.9, I defined a finer-grained longitudinal segmentation for plotting and filled

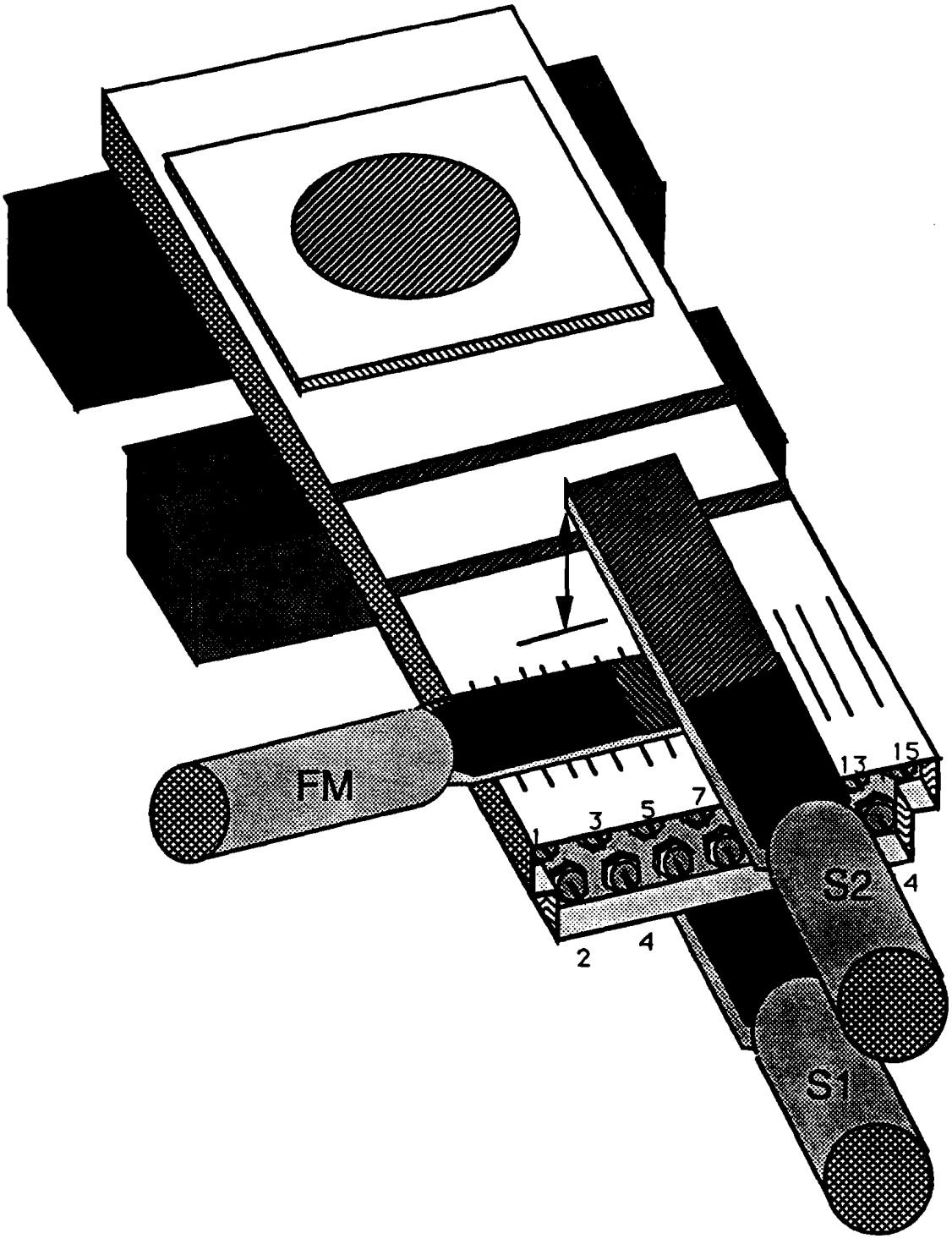

Figure D.10: Background Setup. This shows the arrangement of the active components for the measurements taken of the Background signal.

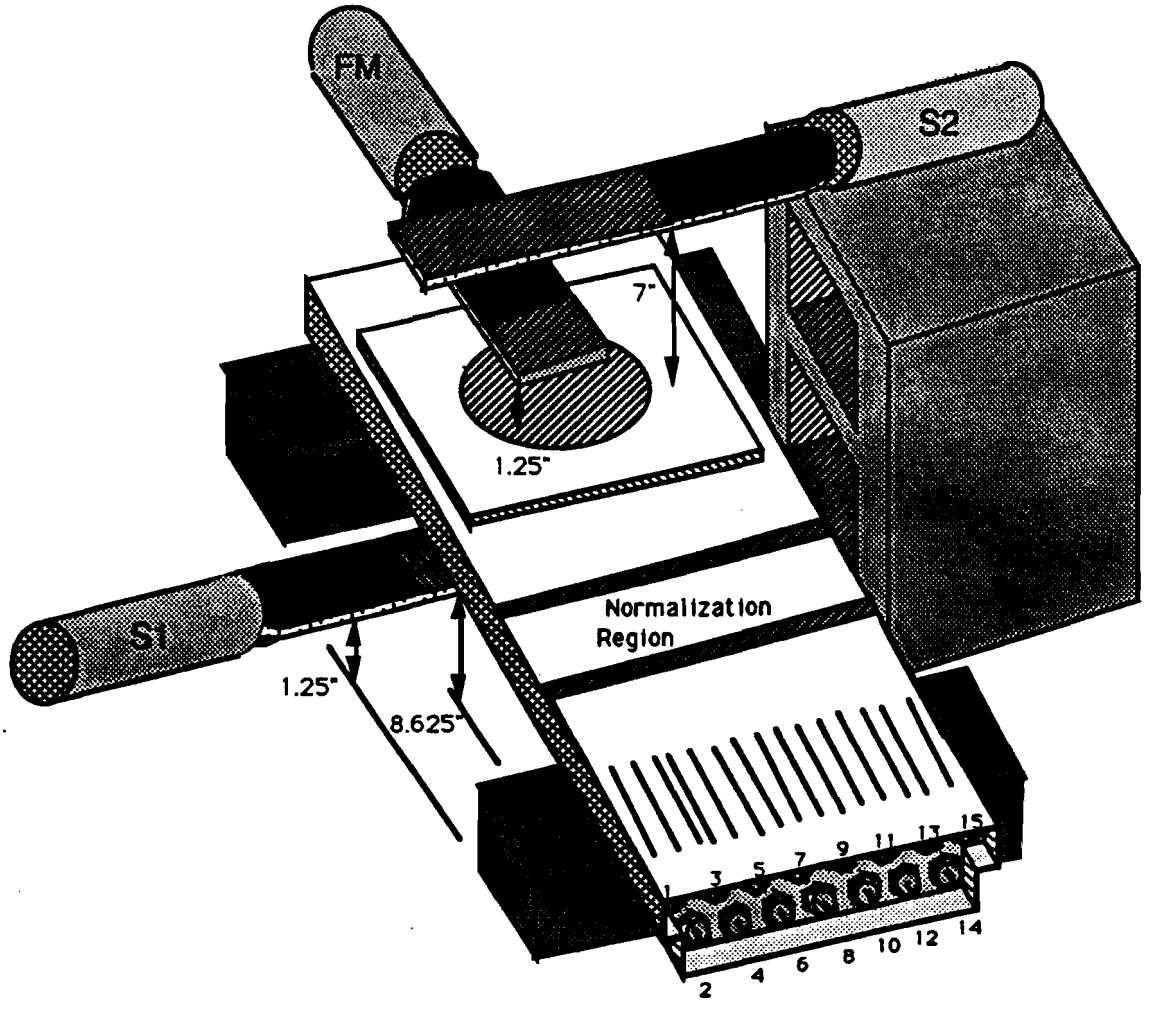

Figure D.11: Data Setup. This shows the arrangement of the active components for the measurements taken of the Deadened region.

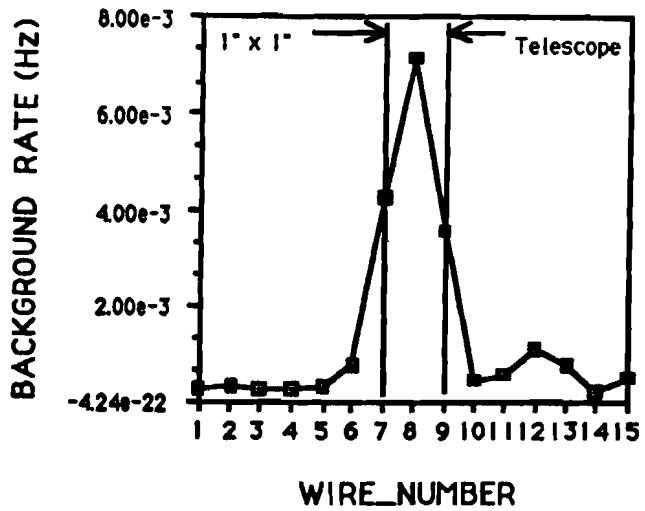

Figure D.12: Distribution in Normalization Region. This shows the distribution of the hits on the wires of the module that were coincident with hodoscope trigger. The hodoscopes were centered on wire-7, and the rate falls off away from this wire. The level of the background can be taken from regions far from wire-7.

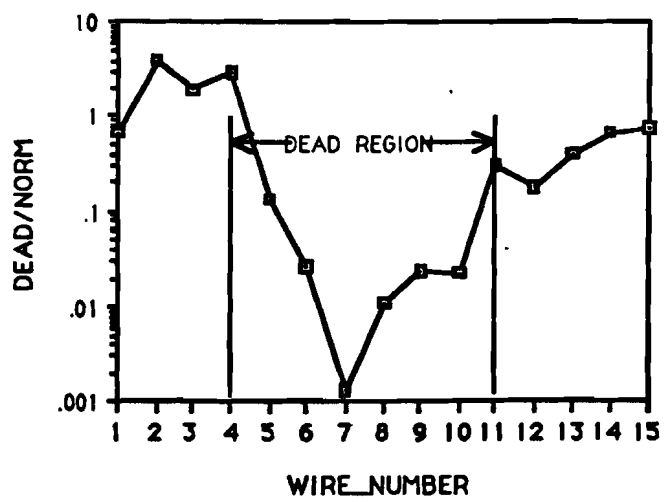

Figure D.13: Efficiency Across the Deadened Region. This shows the efficiency of the middle of the deadened region as a function of the wires of the module. This plot is the ratio of the rates taken in the deadened region over the rates taken in the normalization region; the estimate of the background was subtracted from each set of data before the ratio was taken. The two lines at wires 4 and 11 shown the edges of the deadening material.

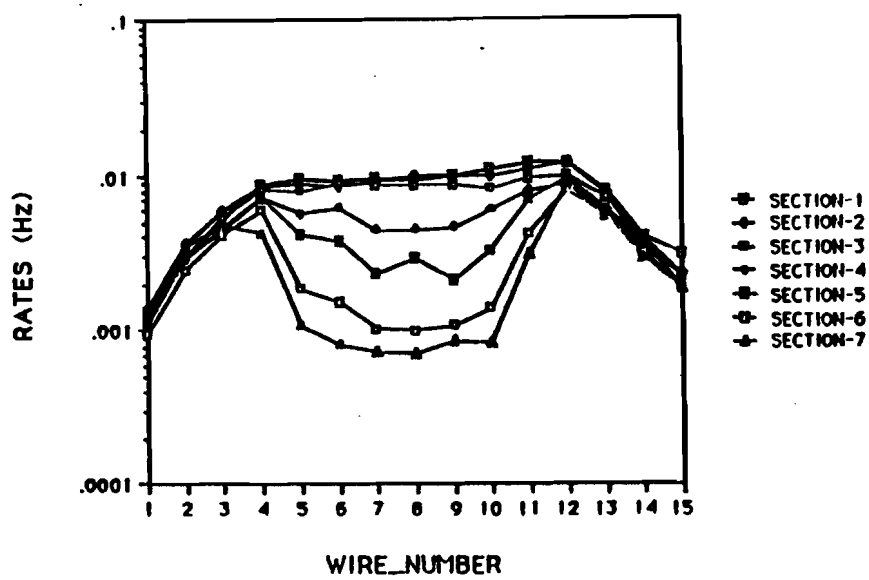

Figure D.14: Efficiency Across the Deadened Region. This shows the efficiency of the of the deadened region as a function of the wires of the module and as a function of the distance along the wires. This plot is the ratio of the rates taken in the deadened region over the rates taken in the normalization region; the estimate of the background was subtracted from each set of data before the ratio was taken.

this binning with values calculated from the measurements. For each bin I performed a weighted average of the measurements taken from the hodoscope locations which overlapped that bin, which helped smooth the curve; these are listed in Table D.1. I then calculated the averages for each wire for each longitudinal bin. I then normalized these rates with those measured in hodoscope position A, or Bin number-3, in order to divide out the hodoscope's positional acceptance biases and to see only the effect of the deadening. This plot is seen in Figure D.15.

D.4.5 Conclusions

I concluded from these tests that the deadening scheme produced the desired effect. It reduced the efficiency of the chamber for generating hits in the region by at least a factor of 10; this factor was a lower limit deduced from limitations of our measurements due to background signal. The effectiveness of this deadening scheme is examined in Section D.7.4, where the efficiency of the beam region of the PTM's is shown.

Bin	Weights of Segments
1	A
2	A
3	$[A + (A + B)]/3$
4	$[A + B]/2$
5	$[(A + B) + (B + C)]/4$
6	$[2(B + C) + D]/5$
7	$[C + 2(D + E) + F]/6$
8	$[C + D + E]/3$
9	$[C + 2(D + E) + F]/6$
10	$[D + 2(E + F)]/5$
11	$[(E + F) + (F + G)]/4$
12	$[F + G]/2$
13	$[(F + G) + (G + H)]/4$
14	$[G + H]/2$
15	$[G + 2H]/3$
16	H
17	H

Table D.1: Sample Smoothing. This table contains the algorithm used to smooth the measurements made on the deadened region. The letters correspond to the positions of the hodoscopes, as shown in Figure D.9.

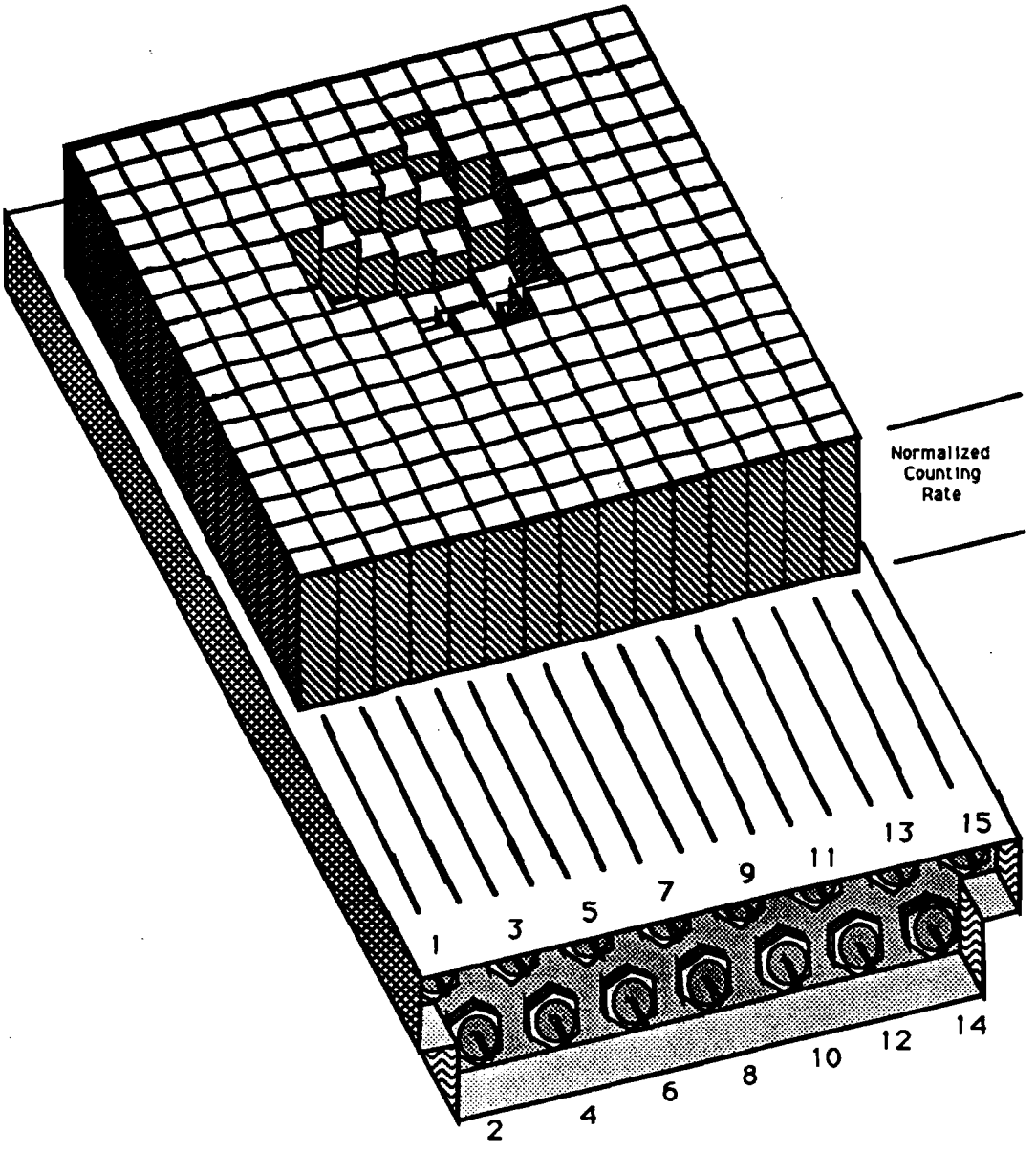

Figure D.15: Efficiency of Module. This shows the efficiency of the deadened region superimposed on the module. The position of the inefficient region can be seen in the middle of the plot.

D.5 Airflow Cooling of Electronics

Each electronic card was reported to produce about 13 watts of heat that needed to be dissipated. Since I was using box-beams to construct the frames, it seemed natural to employ these in a forced-air cooling system. The amount of heat that Δn moles of gas can absorb in a change of temperature of ΔT can be written

$$\Delta Q = C_{V(\mathrm{molar})} \Delta T \Delta n. \tag{D.1}$$

If ΔT is held fixed, then to absorb ΔQ heat in Δt time requires replacement of Δn moles of gas in Δt time:

$$\frac{dQ}{dt} = C_{V(\mathrm{molar})} \Delta T \frac{dn}{dt}; \tag{D.2}$$

dQ/dt is the power dissipated. Then, the desired airflow can be expressed as

$$\frac{dn}{dt} = \frac{P}{C_{V(\mathrm{molar})} \Delta T}; \tag{D.3}$$

The heat capacity of air is $C_P = 0.2401$ cal/(gm K); the volumetric heat capacity is related by the equation $C_V = C_P/\gamma$. The value of γ is 1.4, and the Molar weight of air is 28.964 gm/mole [64, p. F12]. Thus, the volumetric molar heat capacity for air is

$$C_{V(\mathrm{molar})} = 20.79 \frac{\mathrm{j}}{\mathrm{moleK}}. \tag{D.4}$$

I took the assumption that a temperature difference between the card and the ambient of 10° C would be reasonable; then the airflow per card would be

$$\frac{dn}{dt} = 0.0626 \frac{\mathrm{moles}}{\mathrm{sec}}; \tag{D.5}$$

this is normally described in terms of the volumetric airflow, where CFM stands for *Cubic Feet per Minute*:

$$v \equiv \frac{dv}{dt} = 2.971 \text{ CFM}. \tag{D.6}$$

I wanted to drill a hole opposite each card and use squirrel-cage fans to force air into the box and out the holes, across the cards, and then out the front RF cover, delivering sufficient airflow to each card. The Z-planes had one fan on each side (east and west), mounted on the middle of the box-beam. The Y-planes had two fans on each side (top and bottom), mounted a quarter-of-the-frame-width in from each edge. I chose a fan (W.W. Grainger Stk. No. 4C447) that was specified to delivered 135 CFM at a static pressure of 1/2-inch of water (0.03psi).

Of course, this did not work as planned since the motors of the fans could not produce the power necessary to force the desired volume of air across the pressure head developed inside the box-beam. I subsequently looked at the calculations more thoroughly and discussed the problem with Bob Swanson of UCSD; then, I performed some tests to determine the necessary combination of power and impedance to provide the desired flow of air across the electronics.

Bernoulli's Equation can describe the relationship of the pressure differential across a hole and the velocity of the "fluid" out of the hole:

$$\triangle P_{\text{hole}} = \frac{1}{2}\rho v_{\text{hole}}^2, \tag{D.7}$$

where $\triangle P_{\text{hole}}$ is the pressure differential, ρ is the density of the "fluid", and v_{hole} is the velocity of the fluid out of the hole. According to Bob Swanson, the velocity of the flow is not constant across the area of the hole, due to the friction near the edges; however, the flow rate, v, can be expressed as a constant velocity out of an effective area, which turns out to be approximately half of the actual area of the hole:

$$v_{\text{hole}} = A_{\text{eff}} v_{\text{hole}} \sim \frac{1}{2} A_{\text{hole}} v_{\text{hole}}; \tag{D.8}$$

$$v_{\text{hole}}(\text{CFM}) = 16.4\ A_{\text{hole}}(\text{in}^2)\sqrt{\triangle P(\text{psi})}. \tag{D.9}$$

Substituting Equation D.8 into Equation D.7 yields an expression for the pressure differential as a function of the volumetric flow rate:

$$\triangle P_{\text{hole}} = \frac{1}{2}\rho \left[2\frac{v_{\text{hole}}}{A_{\text{hole}}}\right]^2. \tag{D.10}$$

From Equation D.10 the necessary size of the outlet holes could be chosen:

$$A_{\text{hole}} = v_{\text{hole}}\sqrt{\frac{2\rho}{\triangle P_{\text{hole}}}}. \tag{D.11}$$

Most fans can only maintain a pressure head of a few inches of water above ambient pressure; so setting $\triangle P_{\text{hole}} = 1"$ water yields a hole size of area $A_{\text{hole}} = 1.04\text{cm}^2$. This is a radius of 0.23 inches, so I decided to drill 1/2"-diameter holes.

The pressure differential which the fan can sustain is determined by the power output of the fan; if Q is the power, then this can be expressed as

$$Q_{\text{fan}} = k \triangle P_{\text{fan}} v_{\text{fan}}. \tag{D.12}$$

The pressure differential of the fan, $\triangle P_{\text{fan}}$, is the force of the fan over the area of the fan's output. Now, the fan can be described as a propeller; there are several parameters involved with this description. The *Lift Coefficient* is defined as

$$\mathcal{L} = C_{L0}\left(\alpha_0 - \frac{\nu}{\omega}\right), \tag{D.13}$$

where ν is the forward velocity of the blade and ω is the rotational speed of the fan. C_{L0} is defined as the *Slope of the Lift Coefficient*, and α_0 is defined as the *Angle of Attack of the Blade* with respect to zero Lift conditions. With the definition of S as the *Surface Area of the Blades*, the force of the propeller can be written as the following expression [61]:

$$F = \frac{1}{2}\rho(\nu^2 + \omega^2)SC_{L0}\left(\alpha_0 - \frac{\nu}{\omega}\right). \tag{D.14}$$

The speed of the fan is generally much greater than the forward velocity, and the Slope of the Lift Coefficient, C_{L0}, is roughly 2π; with these approximations and the definition of A_F as the input area of the fan, the pressure differential across the fan can be written as

$$\triangle P_{\text{fan}} = \frac{1}{2}\rho\omega^2\frac{2\pi S}{A_F}\left(\alpha_0 - \frac{\nu}{\omega}\right). \tag{D.15}$$

The velocity of the flow can be described by the volumetric flow: $v = A_F\nu$; thus, the pressure differential across the fan can be written as

$$\triangle P_{\text{fan}} = \left[\rho\omega^2\frac{\pi S}{A_F}\alpha_0\right] - \left[\rho\pi S\frac{\omega v}{A_F^2}\right] \tag{D.16}$$

$$= \triangle P_0 - \left[\rho\pi S\frac{\omega v}{A_F^2}\right]. \tag{D.17}$$

Conservation of particles indicates that the volumetric flow into box-beam from the fan and the flow out due to the holes must cancel exactly: $v = -N_{\text{holes}}v_{\text{hole}}$. Finally, the pressure differential across the fan can be written as

$$\triangle P_{\text{fan}} = \triangle P_0 + \rho\pi S\frac{\omega}{A_F^2}N_{\text{holes}}v_{\text{hole}}. \tag{D.18}$$

This pressure differential must equal that across the holes near the fan:

$$\triangle P_0 + \rho\pi S\frac{\omega}{A_F^2}N_{\text{holes}}v_{\text{hole}} = 2\rho\frac{v_{\text{hole}}^2}{A_{\text{hole}}^2}. \tag{D.19}$$

This can be solved for v_{hole}, a quadratic equation:

$$v_{\text{hole}}^2 - \left[\frac{1}{2}\pi S\omega N_{\text{holes}}\frac{A_{\text{hole}}^2}{A_F^2}\right]v_{\text{hole}} - \frac{\triangle P_0 A_{\text{hole}}^2}{2\rho} = 0. \tag{D.20}$$

The solution to this equation can be written as

$$v_{\text{hole}} = \frac{1}{4}\pi S\omega N_{\text{holes}}\frac{A_{\text{hole}}^2}{A_F^2}\left(1 \pm \left[1 + \frac{16 \triangle P_0}{(\pi S\omega N_{\text{holes}})^2}\frac{A_F^4}{A_{\text{hole}}^4}\right]^{\frac{1}{2}}\right). \tag{D.21}$$

Actually, for choosing an appropriate fan, the relevant parameters are the desired volumetric flow and the size of the outlet holes. This should determine the pressure head which will build up inside the box-beam, and this will dictate how much power will be necessary to move the required amount of airflow:

$$Q_{\text{fan}} = k \triangle P_{\text{fan}} v \tag{D.22}$$

$$= -k2\rho\frac{v_{\text{hole}}^2}{A_{\text{hole}}^2}N_{\text{holes}}v_{\text{hole}}. \tag{D.23}$$

The new fans were W.W. Grainger Stk. No. 4C006B, and were specified to delivered 118 CFM at a static pressure of 1/2-inch of water (0.03psi) and 42 CFM at 0.8" water. The curve of volumetric flow versus static pressure for this fan from the specifications is seen in Figure D.16; also plotted on this graph is the pressure head developed inside the box-beam as a function of the total area of exhaust from the box-beam. The point of intersection is the operation point of the system.

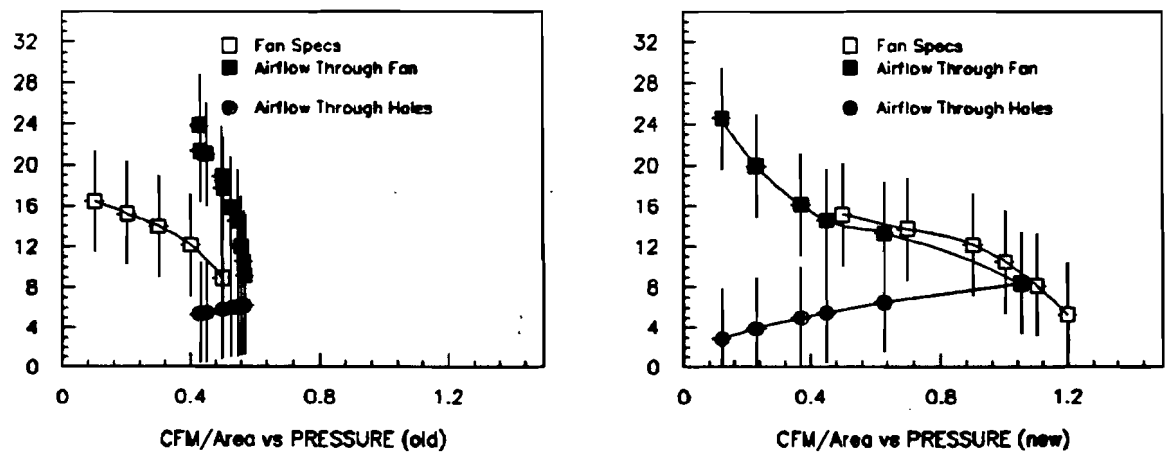

Figure D.16: Volumetric Flow versus Static Pressure.

I tested the operation of the fan as a function of the impedance imposed by the box-beam, varying the total cross sectional area available for exhaust. I mounted

one fan on a Y-plane and left open the other fan hole; by taping over portions of this hole, I varied the area available for exhaust. Then, I measured the differential pressure at each of the outlet holes along the box-beam, moving from the mounted fan toward the open fan-hole. In this manner, I measured the pressure gradient along the inside of the box-beam. With both fans mounted and running, the static pressure across each outlet hole was 1.05" water; with the cross sectional area of each hole at 0.196 in^2, the volumetric airflow per hole was, from Equation D.10, 0.81 CFM.

D.6 PTA Chambers

The PTA's consisted of a set of proportional tube planes, incorporating views in Y (Vertical), Z (Horizontal), U (-45°), and V (+45°). Each plane was constructed of the same extruded aluminum as the PTM's, a double-void, staggered-cell array. The Y and Z planes consisted of ten of these modules, and the diagonal chambers consisted of fourteen modules. One set of chambers was positioned on each side of the beamline: PTAEast and PTAWest.

In the summer of 1986, I used the E665 Monte Carlo to study the number of particles lost through the hole in the acceptance: the dead space between the PCN and the PTA's. Most of the particles do not stray far from the beamline, so the closer to the beamline the active area of the PTA's started the better the acceptance.

In February, 1987, I designed the frames for the PTA's, using predominantly 3"×3" aluminum box-beams. The design was meant to minimize the loss of active area near the beamline; a minimum amount of dead space was required to apply high-voltage to the tubes. Aluminum rectangular tubing, 1"×2", was precision drilled to accommodate the mounting of the proportional tube modules exactly as was done with the PTM's. Again, the mounting angles were epoxied to the modules, and the modules were installed into the frames. Then, as each plane was completed, it was hung in the PTA Support Structure, which I had designed in the summer of 1986 and which had been built by Fermilab support; this was shown in Figure D.17. The Support Structure was constructed of steel Ship-and-Car Channel and of Double-Channel Unistrut, which acted as the Tracks for the Trolleys on which the PTA planes hung. Each Trolley was rated for 600 pounds, and a full PTA plane weighed about 500 pounds. As each plane was completed, a Trolley was attached to the plane by a turnbuckle which allowed for leveling and adjustment of height. Then, the plane was rolled into its track of its Support Structure.

The PTA's were part of the Wide-Angle Particle Detection system and, conse-

quently, were mounted between the two magnets of the experiment. This area was extremely crowded with equipment, and therefore the PTA chambers had to be constructed as a package outside of their proper location and inserted after completion. This required a temporary facility in which to hang each plane as it was completed. I designed the PTA Temporary Support Structure shown in Figure D.18, and Tom Prosapio's men assembled it in the Northeast section of the New Muon Lab's pit. This Structure was known as ***Stonehenge-II.***

The gas was flowed in series through the modules of a given plane; short links of 1/8" poly-flo tubing were connected between modules. The Input and Exhaust lines were extended along the frames to a location that would be easily accessible once the PTA's were ***in situ.*** A valve was connected to each end to allow isolation of individual planes.

The High-Voltage was bused along one side of the tubes on a Copper-Clad fiberglass board; one end of a 10 MegaOhm (1/8 Watt) Resistor was soldered to this bus, and soldered to the other end of the resistor was an alligator-clip which connected to a wire of a tube. In this way, High-Voltage was applied to each wire. We decided not to bother with "Egg-crates" on the PTA's, and installed Coupler-Cards using M.I.T.'s method (see Section E.2.2. Then the Readout Cards were installed onto the PTA planes; Motherboards and cables were installed, and the Memory Address Boards were connected.

D.7 PTM Efficiencies

D.7.1 Sigmas

The resolution of the PTM's was governed by the width of the cells. The resolution of a 'hit' on a detector is dependent upon the number of wires which register and upon the resolution of a given wire. In the PTM's we have wires inside individual tubes, so the resolution of a hit on a single wire is the resolution of a single tube. The resolution of two tubes side-by-side would be simply twice the resolution of a single tube. However, in the PTM's adjacent tubes are staggered, and the resolution is not simply the resolution of a single tube multiplied by the number of tubes involved.

The resolution of a hit is described by the variance of the hit. For a cell of active width K centered at $x = 0$, the variance is defined as the integral over this width of

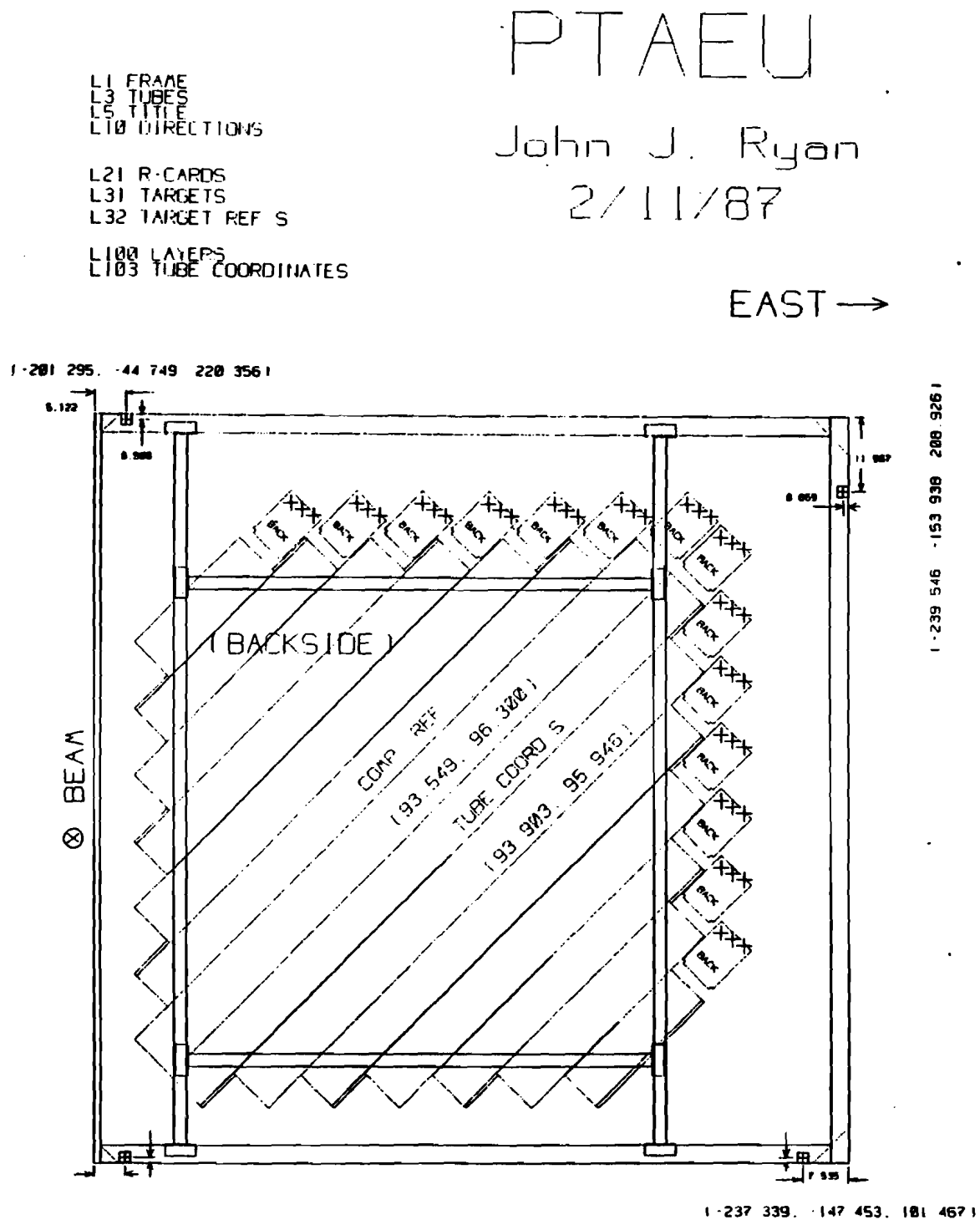

Figure D.17: PTA Support Assembly.

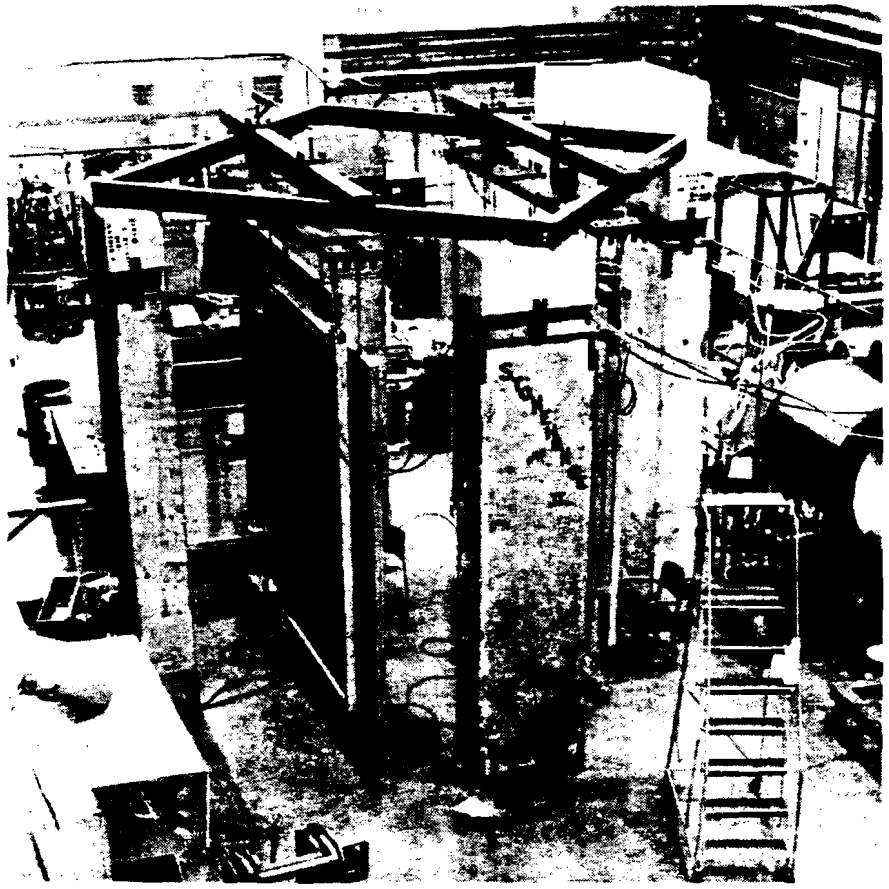

Figure D.18: Stonehenge-II Support Assembly.

the square of the difference of the position from X_0, normalized to the width:

$$\begin{aligned}\sigma^2 &\equiv \frac{\int_{-K/2}^{K/2} x^2\,dx}{\int_{-K/2}^{K/2} dx} \\ &= \frac{(2/3)(K/2)^3}{K} \\ &= \frac{K^2}{12}.\end{aligned}$$

For a single cell, K is just the cell width; for a cluster of cells, K is the width of the cluster. For the PTM's the width of a cluster is described by the Cluster-Size C and the tube width a as

$$\begin{aligned}K &= \frac{Ca}{2} + \frac{a}{2} \\ &= \frac{(C+1)}{2}a.\end{aligned}$$

This indicates that the variance for a PTM hit of Cluster-Size C can be described by the cluster size and the resolution of a single tube, σ_0^2:

$$\sigma^2 = \left[\frac{(C+1)}{2}\right]^2 \sigma_0^2.$$

Because of the staggered cell arrangement, the wire-spacing of the PTM's, W, is not equal to the cell width but half-of-the-cell-width; therefore, the resolution of a single tube can be written as

$$\sigma_0^2 = \frac{[2W]^2}{12}.$$

D.7.2 Single Cell Efficiencies

The efficiency measured for a PTM plane was the efficiency that *at least one* of the two cells in the *Staggered Cell Array* fired when a particle passed through; I will call the measured value ε_{double}. This value did not correspond directly to the efficiency of each individual cell in the Staggered Cell Array but was a function of the individual cell efficiency and the geometry of the walls of the array. It was also possible that all of the region of the individual cells was not used efficiently, and this would lead to an effective wall thickness that was larger than the physical wall thickness. The absolute width of a cell, c, is defined as the distance between a wire and its immediate neighbor

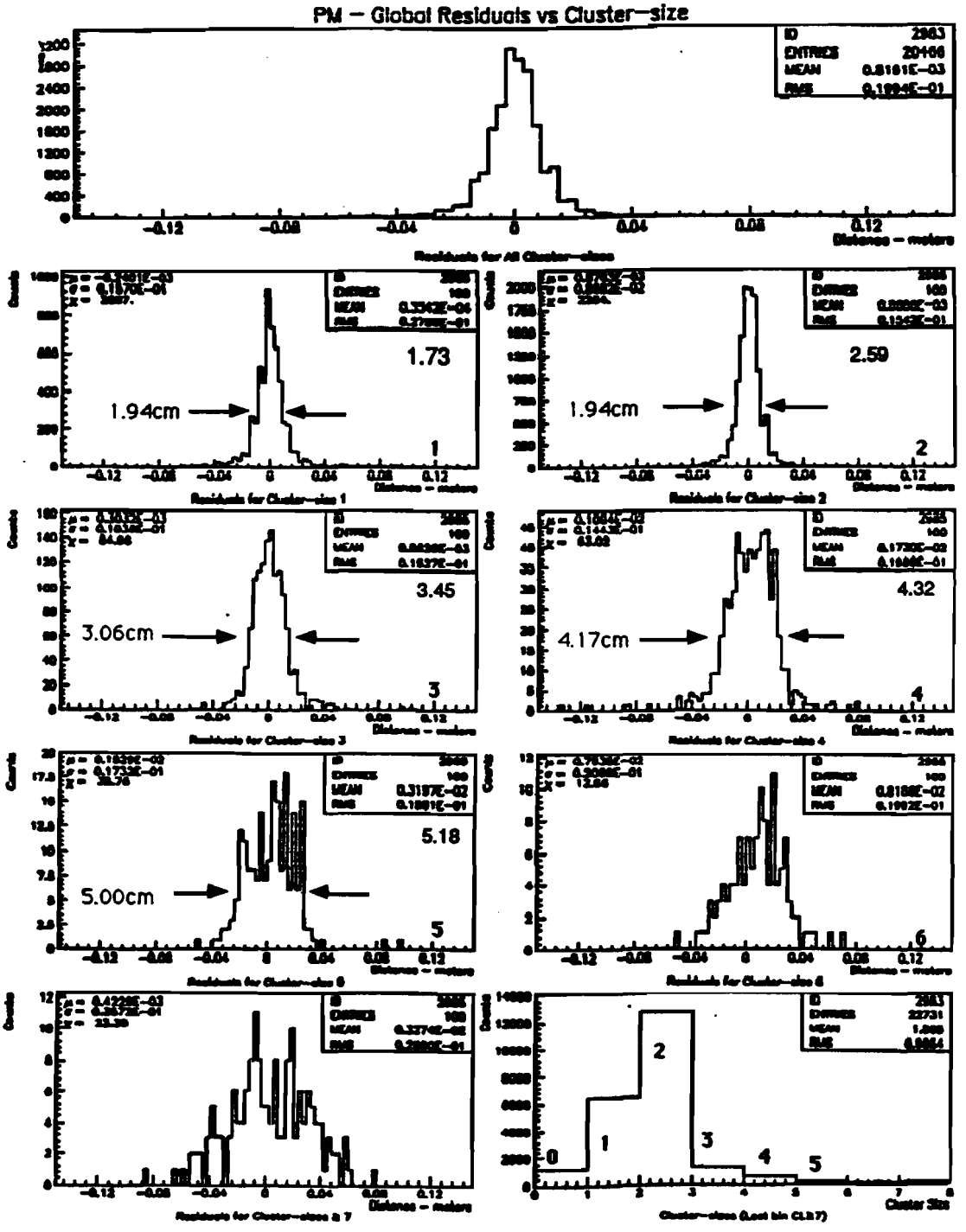

Figure D.19: PTM Sigmas

in the *same* half of the plane (see Figure 1), and the effective wall thickness will be w. If only the front half of the Staggered Cell Array is used, then the measured value of efficiency will be the efficiency of the cells but reduced by the inefficiency of the walls:

$$\epsilon_{single} = \frac{c-w}{c}\epsilon_{cell}. \tag{D.24}$$

The efficiency for a double plane will be greater since the inactive region of the wall in one layer will be covered by the active region of the other layer; this double-layer efficiency is given by the equation

$$\epsilon_{double} = \frac{2w}{c}\epsilon_{cell} + \frac{c-2w}{c}[1-(1-\epsilon_{cell})^2] \tag{D.25}$$

$$= \epsilon_{cell}2(1-\frac{w}{c}) - \epsilon_{cell}^2(1-\frac{2w}{c}).. \tag{D.26}$$

These two equations may be solved explicitly for ϵ_{cell} and w:

$$w = c\left(1-\frac{\epsilon_{single}}{\epsilon_{cell}}\right) \tag{D.27}$$

$$\epsilon_{cell} = \epsilon_{single}\left(1 \pm \sqrt{1-\frac{2}{\epsilon_{single}}+\frac{\epsilon_{double}}{\epsilon_{single}^2}}\right). \tag{D.28}$$

The root with the positive sign must be chosen as the physical root, since the efficiency of a cell must be larger than the measured value of the single-layer efficiency. Then, the solutions for the efficiency per cell and the effective wall thickness are the following two equations:

$$\epsilon_{cell} = \epsilon_{single}\left(1 + \sqrt{1-\frac{2}{\epsilon_{single}}+\frac{\epsilon_{double}}{\epsilon_{single}^2}}\right) \tag{D.29}$$

$$w = c - c\left[1+\sqrt{1-\frac{2}{\epsilon_{single}}+\frac{\epsilon_{double}}{\epsilon_{single}^2}}\right]^{-1}. \tag{D.30}$$

Now, the measured values for plane PTM2Y are

$$\epsilon_{double} = 0.95$$
$$\epsilon_{single} = 0.74.$$

Substituting these numbers into the Equations D.29 and D.30 yields values for the cell efficiency and the effective walls thickness:

$$\begin{aligned} \epsilon_{cell} &= 0.87 \\ w &= 0.386\text{cm}. \end{aligned}$$

D.7.3 Rate Dependence

In an effort to estimate the rate dependence of the efficiency of the PTM's operation, I have performed some crude studies. In the 1987-88 data taking period, the low-momentum tail of the muon beam was bent out of the deadened regions of the PTM's. Because of this, the tubes directly outside of the deadened region received a great deal more flux than a normal region of the detector. In my studies of the PTM efficiencies, I observed a reduction of efficiency in this region. The crude studies of rate dependence were to plot the efficiency of this region as a function of the flux received in this region.

I used the PTM Y-planes in the study because the low-momentum tail of the beam was distributed across the wires, with intensity decreasing as the wire position gets more negative (more east). Thus, each successive wire in this direction received less flux, and hence the efficiency versus position could be related to flux versus position. I plotted efficiency versus flux for the last three Y-planes of the PTM's: PTM2Y, PTM3Y, PTM4Y. I restricted these plots to use only the region just east of the deadened region, which was the high-flux region. On the three-zone plots, the first plot was the efficiency of that plane as a function of the Y-position for $-30\text{cm} < Y < +30\text{cm}$, and the second was the flux as a function of the Y-position for $-30\text{cm} < Y < +30\text{cm}$; the third plot was the efficiency versus flux for the region $-30\text{cm} < Y < -10\text{cm}$.

Then, I put a straight line on the decrease in efficiency, using a ruler and my eye; I did not do a fit or consider errors on the points. Nevertheless, I conclude that the three planes exhibit the same general rate dependence. As can be seen from the plots, this dependence was roughly a decrease of 4% with an increase in flux by a factor of 4. In the region just east of the deadened region, the efficiency was about 90%, so if the rate increased by a factor of 4, the efficiency in this high flux region would drop to about 86%. The efficiency of the normal active regions of the planes should not be affected by an increase in beam intensity.

D.7.4 Beam Region Efficiencies

The following plot shows the efficiencies for the PTM's in the deadened region. This region was divided into slices, and each successive histogram shows the efficiency across the dead region further into the middle, and then out again. Clearly, the efficiency of the deadened region was at most 5%.

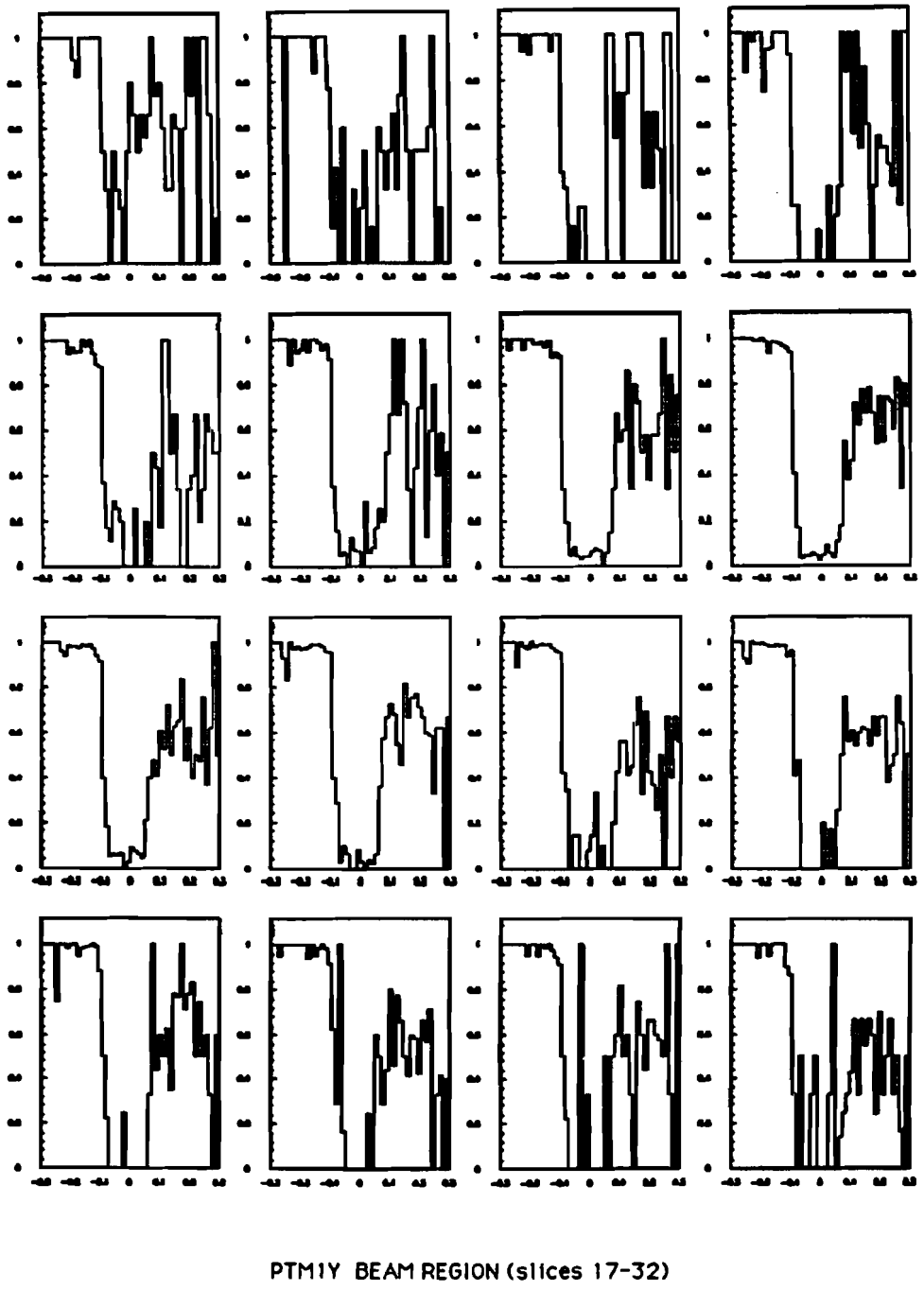

Figure D.20: PTM Beam Region Efficiencies.

Appendix E

Electronics for the PTM Proportional Tubes

E.1 Introduction

The PTM's were proportional tubes constructed from aluminum extruded in an array of 15 cells, staggered such that there were 7 cells on one face and 8 cells on the other. The cells were approximately 1" squares. In the middle of each cell was pulled a 2-mil gold-plated tungsten wire, which acted as the anode. This wire was kept at Positive High-Voltage, and the aluminum modules were kept at ground.

The signals from the PTM proportional tubes had to be amplified and then read into the Data-Acquisition stream. We were employing the tubes to register positional information only, and we were not using any pulse-height information; therefore, the signal from a wire was digitized as a "hit". In a given event, the information in a plane consisted of a collection of "hits" on wires; this information was loaded into Shift-Registers and shifted off the plane and into a Wire Chamber Scanner. This Scanner resided in a CAMAC crate, and the information was transferred to a host computer via CAMAC operations.

There were various pieces in this Readout Chain for the PTM's: the Coupler-Card, the Readout Card, the Motherboard, the Memory Address Board, the Megavertor, the PTM Fanout, and the Scanner. Each piece will be discussed in detail.

E.2 Coupling Electronics

E.2.1 Coupler-Card

The first piece in the PTM Readout Chain was the Coupler-Card. As its name suggests, the Coupler-Card acts as an interface between the proportional tube and the Readout Card. It was grounded to the tubes, and it hosts the Blocking Capacitors, 4700 pF, and a 100 kilo-Ohm resistor connected to ground. Connected to the capacitors were gold-plated female connectors with internal Be-Cu spring-clips, and these connectors slid onto the brass pins of the proportional tubes. On the other side of the Blocking Capacitor, the signal follows a trace to an Edge Connector ELCO # 00-6007-036-940-012 8325 R; the Readout Card slid into this connector.

The components of the electronics installed onto the ends of the modules were supplied by UCSD. The active card on the read-out end of the tubes, called the Read-out card, consisted of an amplifier stage, a discriminator stage, and a latch stage for serial readout. The passive interface (coupler)-card on the read-out end consisted of blocking capacitors and 100 kilohm resistors to ground. Connected to the capacitors were gold-plated female connectors with internal Be-Cu spring-clips, and these connectors slid onto the brass pins of modules. On the injection end, the active card was the Signal-Injection card, and the passive coupler-card had blocking capacitors and 380 ohm resistors-to-ground in order to terminate the wires' reflected signals.

E.2.2 Egg-crates

The Egg-crate was milled from the same aluminum extruded stock out of which the modules were made. After milling, the Egg-crate was electroplated with copper. The Egg-crate was designed by Hans Kobrak in an attempt to solve a problem with channel-cross-talk. In August 1984 Louis Osborne and I tested for cross-talk with and without the Egg-crate and observed no difference. We drilled a hole in the middle of a 12-foot extrusion in order to pulse the wire in the middle. We pulsed a wire and read out the signal at the end. The pulse height was 75 millivolts. We then probed the neighboring wires for any cross-talk signals; no signals were observable over the background noise of 0.3 millivolts. Therefore, any cross-talk must be down by a factor of 1/250.

We then conducted tests on the grounding systems which were proposed to be

attached to the ends of the extrusions. The San Diego Nanometric readout card was attached to this grounding system and then to the wires. We pulsed a 300 millivolt signal into the middle of the test wire and looked at the output of the adjacent amplifiers. On the test wire, an 8 millivolt pulse yielded a 500 millivolt signal at the output of the amplifier; this indicated a gain of 62.5. If the amplifiers were linear, this would give a value of about 19 volts on the input pulse of 300 millivolts.

We tested three grounding systems:

1. a prototype ground consisting of two 3"×7" copper-clad G10 cards,
2. the full "Egg-crate" with Be-Cu fingers soldered on, and
3. the MIT-modified "Egg-crate".

The MIT-modified "Egg-crate" consisted of several modifications to the original versions; the fins were shortened so that they would no longer interfere with the nylon bolt heads, and 4 copper tabs were added in order to fasten the Egg-crate securely to the module.

The results of the tests were tabulated in Table E.1. The conclusion of these tests was that there was no cross-talk evidenced from the pins or from the amplifiers on the Readout card. However, the coupler-cards were already designed to use the Egg-crate as a base and as a ground connection to the module. Therefore, we suggested the use of the MIT-modified "Egg-crate" since the cross-talk to signal ratio was best and because the tabs provided a solid, reliable method of grounding and attaching the "Egg-crate" to the extrusions. M.I.T. subsequently installed "Egg-crates" on all of the modules in the Muon Spectrometer.

After starting to install Readout cards on all the modules, we discovered that we had to repair many of the coupling cards because of poor soldering of the components. We decided that we would not reinstall the Egg-crates but use a new scheme of attaching the coupling cards to the modules. We soldered four 18-gauge wires to the ground strip of the coupling card and crimped a ring-tongue connector to the other end of each wire. We then bolted these four wires to the four mounting holes in each end of the proportional tube modules. Without the "Egg-crates", it was easily possible to attach the Readout wires to their respective pins. It was also evident that mounting the "Egg-crates" induced stress on the gas seals of the modules. By eliminating the "Egg-crates", we also eliminated this problem. By 1989, the source of the cross-talk problem had been pin-pointed by Mark Baker to the scheme of voltage division used on the injection coupler cards which had been used in the original tests [7].

Type of Ground	*Output Signal in mVolts for Wire-#*						*Cross-Talk to Signal Ratio*
	-2	-1	0	1	2	Max of Others	
Copper-Clad G10 prototype	80	200	18750	400	40	20	1/47
Full Egg-crate with Be-Cu Spring-clips	80	200	15000	180	50	20	1/75
MIT-modified Egg-crate Bolted on	60	160	18750	160	40	10	1/117

Table E.1: Egg-crate Cross-Talk Measurements. The test wire is labeled as '0' in the table, and two wires on either side of this wire were probed.

E.3 Nanometric N-272-E Readout Card

The next piece was the heart of the Readout Chain: the Nanometric System's N-272-E sixteen channel readout card. The design of this card was a joint effort of Tom Nunamaker of Nanomatric Systems and of Bob Swanson and Hans Kobrak of the University of California at San Diego. The topology of the card is shown in Figure E.1. The bottom edge of the card, connector P1, slipped into the Amphenol connector of the coupler-card and, thus, received the signals from the tubes. The first stage of the card was the amplification stage; the schematic for this stage is shown in Figure E.2. The signal from a tube was amplified, using the NE592D chip, and then sent into the discriminator NE521D; as seen in Figure E.2, an external threshold voltage was applied to control the discrimination of the amplified signal. There was a Test-Point immediately after the discriminator, from which it was possible to examine the signals after amplification and discrimination. The MC10102 NOR-Gate was used as a ONE-SHOT, as shown in Figure E.2, and the discriminated signal triggers this ONE-SHOT. The "One-Shot-Clear-Line" (OSCL) was used to reset the ONE-SHOT.

This Final Signal was then mapped to three locations on the upper portion of the card: the "Fast-Trigger Mode" Output, the "Fast-OR" Output, and the On-Board RAM's for read-out via the Shift Register.

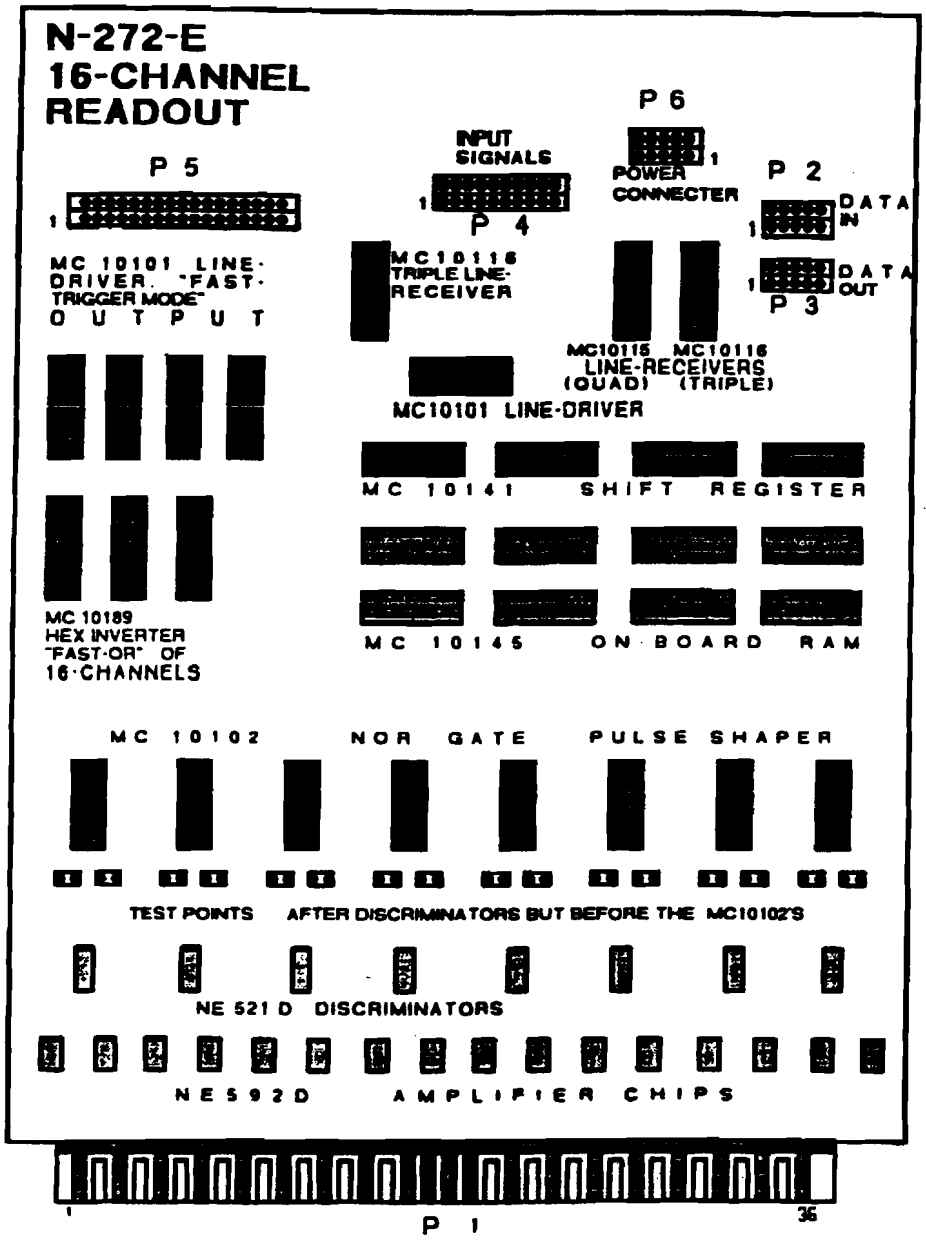

Figure E.1: PTM Read-out Card.

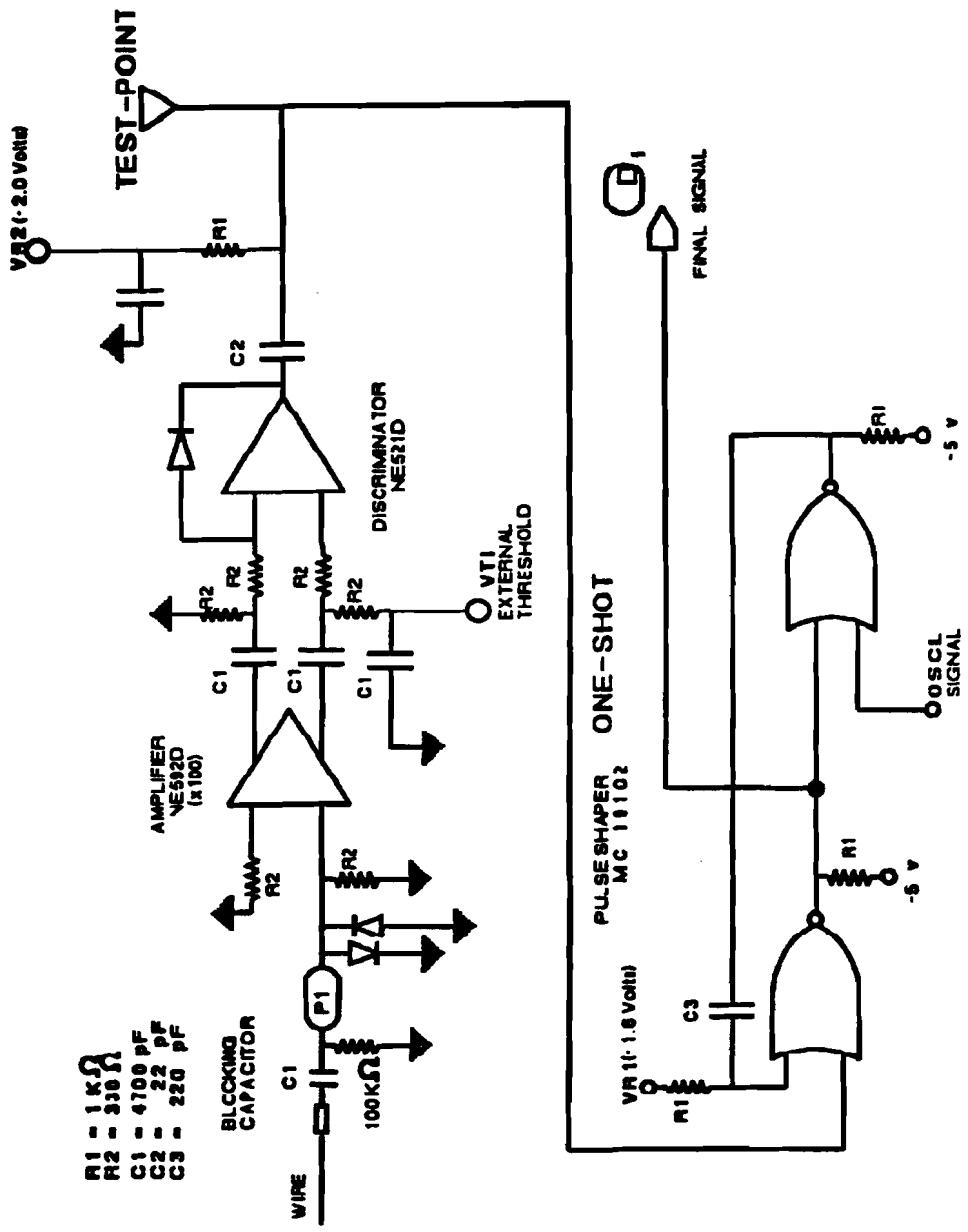

Figure E.2: Amplifier Stage of the PTM Read-out Card.

E.3.1 Fast-Trigger Section

The signals fed into the "Fast-Trigger" section from the 16 channels were input into the MC10101 Line-Driver chips; the ECL output from these chips was routed to the 17-pair connector P5 on the top left of the card, mapping channel-1 to pins (1,2) through channel-16 to pins (31,32). The MC10101 NOR-Gate has a common input at pin-12, which controls the output of each gate. The signal for this pin, the Fast Trigger Strobe (FTS), was brought onto the card through the pin-pair (19,20) of connector P4. As shown in Figure E.3, if this pair was left open, pin-12 of the MC10101's remains High, and there was no ECL output from the MC10101's. However, if there was a voltage greater than (-0.9v) applied to pin-20 and a voltage less than (-1.75v) applied to pin-19 of connector P4, then pin-12 of the MC10101's would go Low, and there would be ECL output at pin-pairs (1,2) through (31,32) of connector P5.

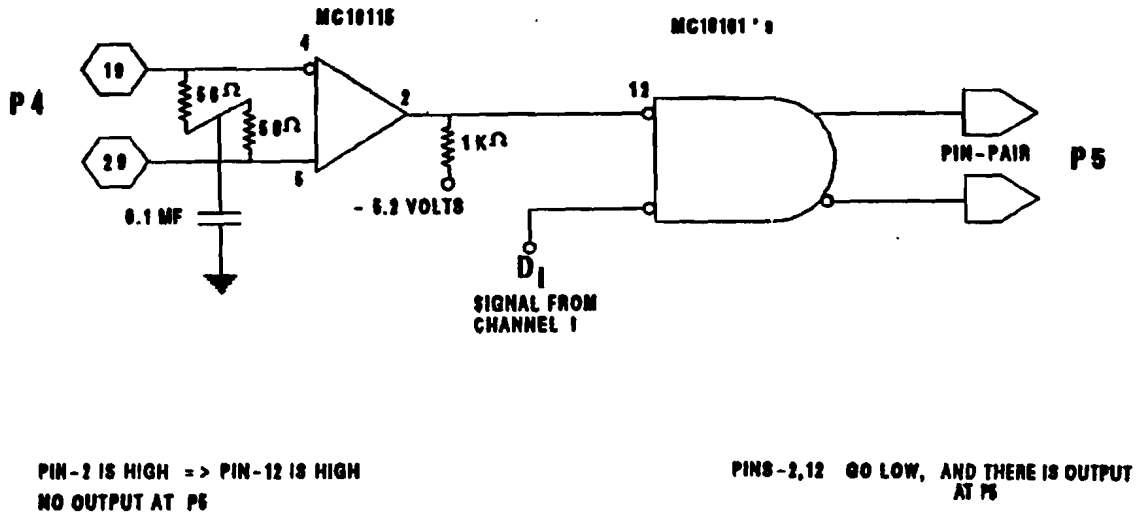

Figure E.3: Fast-Trigger Stage of the PTM Read-out Card.

E.3.2 Fast-OR Section

In the "Fast-OR" section, the signals from the 16-channels were fed into the inputs of the MC10189's, which inverted the signals, since pin-9, the common input, was held Low at -5.2 volts. The output from these chips. pins-2, 3, 4, 13, 14, 15, were tied together and sent to the input pin-13 of the MC10101 which was located "horizontally", just above the Shift Registers (actually, pins-2 and 15 of the middle MC10189 chip of the group of three were not ganged with the rest as these two sections were

it to the -5.2 volts. The ECL output of this section, pins-9 and 15, were connected to the pin-pair (33,34), respectively, of connector P5: this was the "Fast-OR" output.

E.3.3 On-Board Memory Section

The last section that received signals from the 16-channels was the On-Board Memory. This memory was comprised of four pairs of MCM10145 RAM chips. The signals were input to these pairs in parallel, and the selection of which chip received the information was determined by the state of the "Chip Select" signal on pin-3: one member of the pair got the conjugate signal of the other member's signal; this signal was applied to the board as an ECL input to the pin-pair (1,2) of connector P4.

As shown in Figure E.4, each MCM10145 had four "Address" inputs, four Data inputs, a $\overline{\text{Chip Select}}$ input, a $\overline{\text{Write Enable}}$ input, and four Data outputs. The four Address inputs made each chip a 16 (addresses) $\times$ 4 (data channels) memory cell array. The chip was disabled when the $\overline{\text{Chip Select}}$ input was High. When the $\overline{\text{Chip Select}}$ was Low, the chip was active. When the $\overline{\text{Write Enable}}$ input was Low, the chip was in the write state, and the outputs were all held Low; when it was High, the chip was in the read state, and the outputs would show their stored bits.

The Shift Register chip, MC10141, had four Data inputs, a Shift-in, a Shift-out, a Shift Clock input (SC), a Shift/Load Level (SLL) input, and an input to select Shift-Right or Shift-Left (pin-10). Pin-10 was held Low, so the Register was in the Shift-Right Mode; when the SLL signal was Low, the chip was in the mode for parallel entry of the four Data signals. When the SLL signal went High, the operating mode switched to "Shift-Right" mode. Then, Q0 was shifted to the Shift-Out (pin-14), Q1 $\rightarrow$ Q0, Q2 $\rightarrow$ Q1, Q3 $\rightarrow$ Q2, and Q3 would take the value of the Shift-In. Therefore, each Read-out card was scanned out in sequence from channel-1 to channel-16. The output of the "right-most" Shift Register was input to pin-4 of the "horizontal" MC10101 Line-Driver, and the output was sent to the pin-pair (9,10) of connector P3; the Data bit shifted onto the card "from the left" was received on the pin-pair (9,10) of connector P2 and fed into pin-5 of the "left-most" Shift Register.

E.3.4 Connectors

The various inputs to the connectors were depicted in Figure E.5.

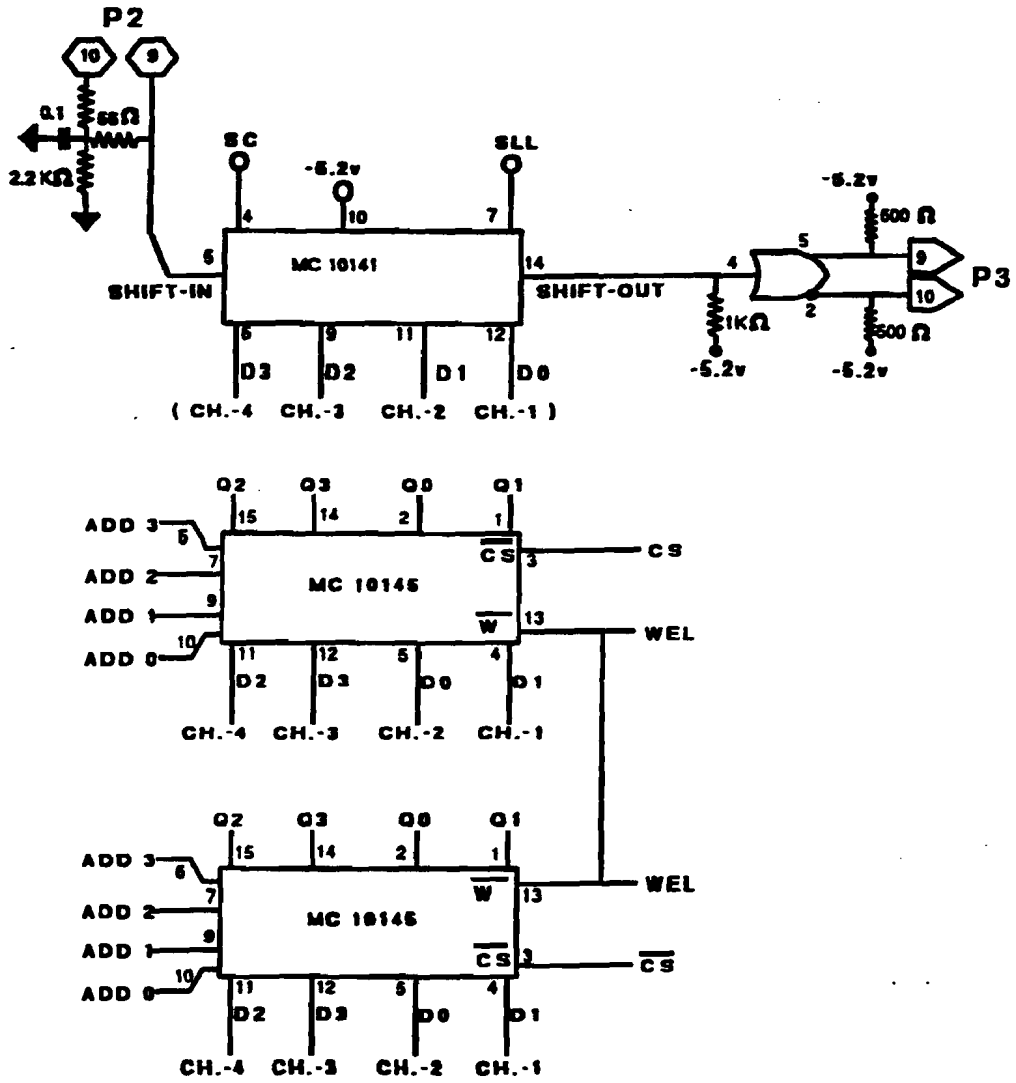

Figure E.4: RAM and Shift Stage of the PTM Read-out Card.

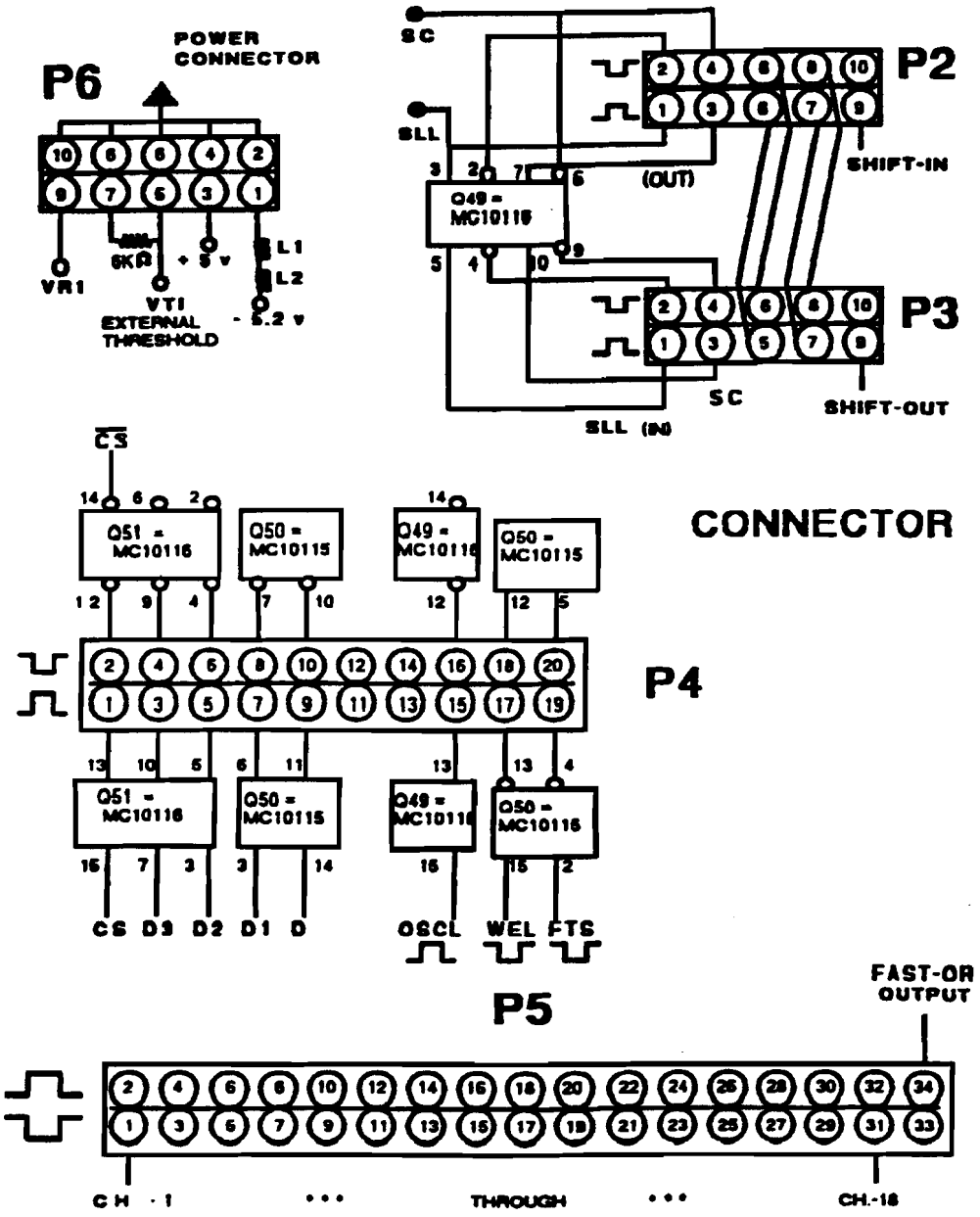

Figure E.5: Connectors of the PTM Read-out Card.

E.3.5 Setbit Cards

We made several modifications to the last Readout Card in the Readout Chain of each plane. We disconnected the parallel-input (pin-6) of the last (rightmost) Shift-Register from its corresponding channel of RAM and clamped it LOW. The Logic-True state of a "hit" was a LOW level, so this forced the last channel on each plane to be "hit"; not finding this channel "hit" in a read-out event was an indication that the Readout Chain had failed. To guarantee that there were no "hits" found after the last channel, we clamped the Shift-In pin-5 of the last Shift-Register in a HIGH state with a diode to ground, removing the termination resistor network of P2 in the process.

E.4 Motherboards

The Motherboards were designed to be a clearing house for all the Readout Cards' Input/Output information. We modified the function of the Motherboards because it proved to be unnecessary to route all of the Readout Cards' Input/Output through the Motherboard.

The Fast-Trigger signals were meant to transfer through a pair of 17-pair headers on the Motherboards, which generated a pair-flip to each of the signals. However, since the cables were passed instead to the Bulkhead Feedthrough, we provided the pair-flip at the Bulkhead and connected the 17-pair Fast-Trigger cables directly from the P5 Header on the Readout Card to the Bulkhead Feedthrough. Historically, the first two planes, PTMY1 and PTMZ1, had these cables connected through the pair-flipping headers on the Motherboards, and their Bulkhead Feedthroughs had no pair-flip.

The Serial-out signal cables from P2 on one Readout Card to P3 on the next Card were meant to transfer through the Motherboards; this was obviously a superfluous connection, so we eliminated it from the Motherboard and connected the Serial-out cables directly from Readout Card to Readout Card.

The P6 header of the Readout Card connected to a pair of headers on the Motherboard, one of which merely acted as a convenient place to measure the voltages carried by the P6-cable. All of the "even" wires were held at ground, and only two of the "odd" wires provided voltage levels as input to the Readout Cards; these two voltages were bused along thick traces on the Motherboard: the Applied-Threshold voltage and the One-Shot Width Adjustment voltage. To avoid voltage drop along

the lines, the threshold level was bused as a large value and then voltage divided by a factor of 100 at input to the Readout Card; we eventually set the Applied-Threshold voltage at 16 volts, which produced a Threshold Voltage of 160 mvolts on the Readout Card. The One-Shot Width Adjustment voltage provided a variable current source for the time-out circuit on the Readout Card.

The main function of the Motherboards was to provide a fanout for the signals carried on the cables connecting to the P4 headers of the Readout Cards. Each Motherboard had a 10-pair header through which it accepted input from the Memory Address board. This input was received by a pair of MECL-10115 receiver chips and fanned-out to five MECL-10101 driver chips. For the active signals, timing was important; therefore, the timing of each leg of the fanout was matched using a 40" length of ribbon cable from the output of the differential-ECL driver to the Motherboard P4 header. Pair-8 of this cable hosted the DC-level of the One-Shot Clear Line, which we set permanently to the Logic-Low state (no clear). Pair-10 hosted the DC-level for the Fast-Trigger Strobe, which we set permanently to the Logic-High state to hold the gate Open. Pair-9 carried the Write-Enable pulse, which latched the Data into the RAM's on the Readout Card. The other pairs carried the Logic bits which addressed the cells of the RAM's.

The Motherboard had a few design flaws and some serious manufacturing mistakes. The active signals operated at 53 MHz; for such high frequency signals it is usually recommended to maintain a ground plane around and underneath the traces of these signals. The pads for the headers and the chips were drawn too small for the size of the hole that had to be drilled in the boards. The most serious problem with the Motherboards, however, was that they were not manufactured with plated-through holes and not pre-tinned. In order to save money, Hans Kobrak of the University of California at San Diego decided to have the Motherboards etched at the Fermilab Printed Circuit lab, which did not support facilities to plate holes or pre-tin boards. This proved to be stupendously false economy, as we spent more than three Man-Months of work correcting cold-solder joints and solder bridges on these boards. I consider it inexcusable for a board of such little function to require so much intensive debugging.

E.5 Memory-Address Board

The real brains of the Readout Chain was the Memory Address board, which was designed by Jim Stronsky at the Electronics Shop of UCSD. This board controlled the latching of the data on the Readout Cards and also the shifting of the data through

the Shift-Registers. There was one of these boards for each PTM plane; I mounted it piggyback-back onto one of the Motherboards, and it drew its power from the Motherboard. All communication with the Readout Cards and the Motherboards was propagated through the Memory Address board. The Memory Address board produced the Address bits and the Write-Enable pulses which latched the data at the Readout Cards, and it controlled the Shifting of the Shift-Registers and received the shifted-in data and transmitted it off of the plane to the "external world".

The Memory Address board communicated with the "external world" through a 20-pair connector, K1. It accepted five logic levels which corresponded to the bits of a "Delay Word", which was the 2's-complement of the number of cells down in the memory stack to look for "hit" information on read-out; an input strobe clocked these bits into flip-flops and returned the logic states through differential drivers, MECL-11016, to the header K1 for external monitoring. A Clock signal was input on the K1 header; this clock, 53 MHz, drove the latching of the data into the RAM's of the Readout Cards. Also input was a Frequency Control "switch", a logical level which chose whether to run at full frequency or at half of this frequency.

E.5.1 Input Bit Latch

The five Delay bits, DEL0 through DEL4, entered K1 on pairs 6 through 10, respectively; the Frequency Control bit entered on pair-5, and the Delay-bit Strobe entered on pair-18. These signals were received by the MECL-10115 receiver chips U3 and U4; the DEL0-DEL4 outputs of these chips were input to the "Hex 'D' Master-Slave Flip-Flop" MECL-10176 on pins 5, 6, 10, 11, and 12, respectively, and the Strobe pulse latched these states at pin-9. The Frequency Control bit was latched into one half of the "Dual 'D' Master-Slave Flip-Flop" MECL-10131, U7, on pin-7 by the Strobe pulse on pin-6. The output pins 2, 3, 13, 15, and 14 of the MECL-10176 carried the logic states of the Delay bits DEL0, DEL1, DEL2, DEL3, and DEL4, respectively; the Frequency Control bit and DEL0, DEL1, and DEL2 were buffered through the differential-ECL driver MECL- 10101, U5, to the K1 header on pairs-11 through 14, respectively. DEL3 and DEL4 were buffered through U19, the differential driver MECL-10116, to pairs-15 and 16.

E.5.2 Clock

The 53 MHz clock signal arrived on K1 pair-4 and was buffered through U3, MECL-10115, after which it was branched to two places. In one place the 53 MHz was

used to toggle a Flip-Flop, the other half of U7 (MECL-10131), and thereby generate 53/2 MHz; the other place used an OR-Gate of U9, a "Quad 2-Input OR-Gate" MECL-10103, as a delay. Whether the Memory Address board used the straight 53 MHz or the 27 MHz was determined by the state of the Frequency Control bit; the Frequency Control Q-output of U7, pin-2, was AND-ed with the 27 MHz in U8, a "Quad 2-Input AND-Gate" MECL-10104, and the $\overline{Q}$ -output was AND-ed with the straight 53 MHz, also in U8. The results of these ANDs were OR-ed together in U9 to form the Clock Signal used on the Memory Address board.

E.5.3 Address Bits

The Clock Signal was used to clock the "Universal Hexadecimal Counter" MECL-10136, U10; the output pins-14, 15, 2, and 3 furnished the Memory Address bits DA0, DA1, DA2, and DA3, which were in least-to-most significant binary order. The Carry-Out of U10, pin-4, went LOW on the overflow count and was used as input to the "Dual J-K Master-Slave Flip-Flop" U17 on the both the $\overline{J}$ and $\overline{K}$ pins-10 and 11; the Clock Signal on pin-9 while $\overline{J}$ and $\overline{K}$ were LOW toggled the output of the Flip-Flop. This output, pin-15, formed the fifth (the most significant) Memory Address bit, DA4; this bit was used on the Readout Card as the Chip Select bit (CS).

E.5.4 Write Enable Pulse

The Memory Address board was in the Write state when the Level-II-Gate Signal was in the LOW state; this signal was input on pair-17 (pins-33,34) of K1 and buffered through U19, a "Triple Line Receiver" MECL-10116, (pins-5,4). Pin-3 was the Q-output, Level-II-Gate, and pin-2 was the $\overline{Q}$ -output, $\overline{\text{Level} - \text{II} - \text{Gate}}$. This Level-II-Gate Signal was applied to the $\overline{J}$ and $\overline{K}$ inputs of both halves of U18, J-K Flip-Flop MECL-10135, and the positive edge of the Clock Signal strobed both halves on pin-9. The Write-Enable pulse was the Q-output on pin-15; when the Clock Signal strobed U18 while the inputs were LOW, pin-15 went HIGH. The Q-output of the other half, pin-2, was connected through an Integrator, a resistor of 270 Ohms, to the Reset input to both halves, pins-13 and 4. The integrator provided a delay of 9 nsec before the Reset "cuts off" the pin-15 HIGH output; thus, the Write-Enable signal was a pulse of Half-Max Width of 9 nanoseconds.

E.5.5 Adder and Multiplexer

The Memory Address bits, DA0 — DA4, were applied to the direct inputs of three "Quad 2-Input Multiplexers" MECL-10158 (U12, U14, and U15), and to the "A-Inputs" of a series of three "Dual 2-Bit Adders" MECL-10180 (U11, U13, and U16); the Delay Bits, DEL0 — DEL4, were applied to the "B-Inputs" of the Adders. The Adder Carry-Outs were tied to successive chip Carry-Ins so that the 'sum' was not merely a bit-wise AND but an actual sum of the two 5-bit words; this was why the Delay Word was the 2's-Complement of the desired number of the memory offset. The Adder outputs were applied to the Alternate inputs of the Multiplexers U12, U14, and U15. The $\overline{\text{Level} - \text{II} - \text{Gate}}$, which was HIGH during the Write state, was applied to the Select Input, pin-9; this passed the unaltered Memory Address bits through the Multiplexers. During the Read state, the $\overline{\text{Level} - \text{II} - \text{Gate}}$ was LOW, and the output 'Sum' from the Adders was passed through the Multiplexer. The Write-Enable pulse was also passed through the Multiplexer; however, to allow for setup time at the Readout Cards' RAM's, the Write-Enable pulse was delayed, with respect to the Memory Address bits, by about 9 nsec in a 60" length of Twist-&-Flat cable before entering the Multiplexer.

E.5.6 Fast-Trigger-Strobe and One-Shot-Clear-Line

The Fast-Trigger-Strobe and the One-Shot-Clear-Line were both actually DC-Logic levels; they were clamped in the HIGH state by tying a diode to ground, and these levels were bused to each of the eight output sectors.

E.5.7 Output Sectors

There were eight output sectors on a Memory Address board, each consisting of two MECL-10101 differential drivers with pull-down SIP's and a single 10-pair header. The driver chips were U20 to U35. The pin-assignments of the header were identical to those of the P4 header of the Readout Card, and a 10-pair Twist-&-Flat cable connected this header to the Input header of a Motherboard. The output consisted of the five Memory Address bits, the Write-Enable pulse, and the Fast-Trigger-Strobe and One-Shot-Clear-Line Logic levels.

Since it was important to latch simultaneously data that occurred simultaneously, the lengths of all the 10-pair Twist-&-Flat cables from all the Memory Address boards

to all the Motherboards were made the same: 11 "sections" (lengths between Flats, 22") = 242 inches, which was about 20 feet. I measured the propagation time from the Memory Address board output to the P4 output header of the Motherboard to be 37.88 nsec.

E.5.8 READ State Operations

In order to read out the information of an event, the Memory Address board had to be toggled into the Read state; this was performed by sending the Level-II-Gate signal into a HIGH state. The Memory Address board then suspended writing and prepared the Readout Cards for Shifting out data into the WCS-200 Scanner. The Level-II-Gate signal was connected to the mode-select pin-9 of the Address Counter U10; so, when the Level-II-Gate signal was HIGH, the Address Counter suspended counting, and the Flip-Flop U18 produced no more Write-Enable pulses. The LOW state of the $\overline{\text{Level} - \text{II} - \text{Gate}}$ signal caused the Multiplexers to pass the Adders' sum to their output; the bits of this Sum made up the Address Word that corresponded to the cell in the Readout Cards' RAM in which data was latched when the particle that triggered the event was passing through the PTM's.

The Memory Address board also prepared the Readout Cards for the Shifting operation. The $\overline{\text{Level} - \text{II} - \text{Gate}}$ signal was propagated through several RC-Integrators and OR-Gate Buffers, which were used to delay the transition of the state and to generate a fixed length pulse to latch the data into the Shift-Registers on the Readout Cards. During the Write state, the $\overline{\text{Level} - \text{II} - \text{Gate}}$ signal was HIGH, and this produced a LOW state on the Serial-Output header K2-(1,2), which was the Load state of the Shift/Load-Level signal on the Readout Cards; during the Read state, the $\overline{\text{Level} - \text{II} - \text{Gate}}$ signal went LOW, and the Shift/Load-Level signal eventually followed this transition into the Shift state (HIGH on K2-pin-1), in which it would remain until the Level-II-Gate again closed. The Negative-going Edge of the Level-II-Gate Transition generated the latch pulse for the Shift-Registers before the Shift/Load-Level made its transition into the Shift state.

The Level-II-Gate first propagated through the Integrator composed of R8 (150 Ohms) and C5 (100 pF) with a delay to half-max of around 13 nsec. It was at this point that the $\overline{\text{Level} - \text{II} - \text{Gate}}$ signal was branched off to the Multiplexers; the delay was to allow the last Write-Enable pulse to make it through the Multiplexers before they toggled into the Sum-Pass Read mode. The shape of the $\overline{\text{Level} - \text{II} - \text{Gate}}$ signal at this point was the characteristic "exponential slope", which was not good for tight timing; therefore, it was reshaped by passing it through the AND-gate U8 (MECL-10104) with both inputs tied together. The inverted output, pin-9, was sent

directly into the input pin-10 of another AND-gate section of U8; the noninverted output, pin-15, passed through another Integrator, composed of R9 (220 Ohms) and C6 (510 pF), which delayed the Half-Max of this signal by 78 nsec. This integrated signal was routed to both the input pin-11 of the same AND-gate of U8 into which the inverted signal passed and to the input pin-7 of an OR-gate section of U2. The Write state input levels of the AND-gate were LOW on pin-10 and HIGH on pin-11; the transition from LOW to HIGH on pin-10 occurred in several nanoseconds while the transition from HIGH to LOW on pin-11 took nearly 80 nsec. Therefore, the output pin-14 of the AND-gate went HIGH for 59 nsec; this signal was then the Shift-Clock pulse. It was buffered through the differential driver U2 (MECL-10101) and output from the Memory Address board on pair-2 (pins-3,4) of the header K2. The positive edge of this pulse latched the data from the RAM into the Shift-Registers on the Readout Cards; the Shift/Load-Level had to remain in the Load state (LOW) for several nanoseconds after the latching of the Shift-Registers. The Shift/Load-Level signal was produced from the signal passed into the pin-7 input to the U2 (MECL-10101) OR-gate; the pin-6 output of this OR-gate was delayed with respect to the Shift-Clock pulse by sending it through another Integrator, composed of R1 (220 Ohms) and C1 (510 pF), with a delay to Half-Max of 41 nsec. This signal was reshaped by another U2 OR-gate and then buffered through another U2 OR-gate, used as a driver, and output on pair-1 (pins-1,2) of header K2 as the Shift/Load-Level signal. The resulting delay between the positive edge of the Shift-Clock pulse and the transition of the Shift/Load-Level signal was 108 nsec.

The positive edge of the Shift-Clock pulse had to arrive at the Shift-Registers after allowing for the propagation delay of the RAMs' outputs and for sufficient setup time for the data arriving at the Shift-Registers' inputs; this required that the signals traveling on the K2 cable had to arrive at the Readout Cards sufficiently long after the arrival of the Address bits, which traveled on the K3 cables and propagated through the Motherboards. I measured the relative timing of the signals and determined that a cable of 130 nsec (78 ft.) would be satisfactory. Relative to the arrival of the Level-II-Gate signal on the Memory Address board, the final arrival times of signals at the Readout cards were the following: the arrival time of the DA0 bit was 325 nsec, the arrival time of the positive edge of the Shift-Clock pulse was 387 nsec, and the arrival time of the Shift/Load-Level transition was 498 nsec.

The Memory Address board received the Clock-Out signal on pair-1 (pins-1,2) of header K2, which it buffered through U1 (MECL-10116) and ORs with the Shift-Clock line into U2, sending the Clock-Out signal to the Readout Cards on pair-2 of the K2 cable. At the P3 header of the first Readout Card of a plane, pair-4 (wires-7,8) was jumpered to pair-2 (wires-3, 4), which generated the Clock-Back signal; the Clock-Back signal was buffered through U1, MECL-10116, and returned to the Scanner on pair-2 of K1. The data were received by the Memory Address board on

pair-5 (pins-9,10) of K2, buffered through U1, and sent to the Scanner on pair-3 of K1.

E.6 PTM-Fanout

Each plane had a resident Memory Address board, which required several external signals: a 53 MHz clock, a Strobe to latch the Delay bits, and a Level-II-Gate. The 53 MHz clock signal was taken from the 53 MHz Accelerator clock, which was available to all experiments; the Strobe was generated most easily in a CAMAC call; and the Level-II-Gate signal was taken from the Experimental Level-II Trigger of the event. I decided to fanout these signals in a CAMAC module, because we wanted to generate the Strobe signal automatically at the beginning of every Experimental Run Block.

The CAMAC command "Execute" (F25) was chosen to generate the Strobe pulse, and I followed CAMAC standards in generating X and Q responses. A successful F25 triggered a One-Shot of width 200 nsec, which was fanned out as the Strobe pulse, and a One-Shot of width 0.5 seconds, which was used to light a front-panel LED, signaling a successful strobe. We also allowed the Strobe pulse to be triggered by a front-panel push-button.

Both the 53 MHz clock and the Level-II-Gate signals were NIM-standard signals, input to the Fanout on 50-Ohm RG-58 cable. These signals were terminated into 50-Ohms, and the NIM Logic levels were converted to ECL levels via a 2N5770 transistor; the transistor output was input to a MECL-10101 OR- gate, and the pair-flipped ECL-output was fanned out to five MECL-10116 transceivers. Each MECL-10116 used its three sections to drive the three signals: 53 MHz, Strobe, and Level-II-Gate. The five outputs of the Fanout were 5-pair headers, hosting the 53 MHz signal on pair-1 (pins-1, 2), the Strobe signal on pair-3 (pins-5,6), and the Level-II-Gate signal on pair-5 (pins-9,10).

E.7 WCS-200 Scanner

The WCS-200 Scanner generated a 10 MHz clock signal, called the Clock-Out signal, which it used to shift-in the data from the Shift-Registers; the returned clock signal was called the Clock-Back signal. The third signal which the Scanner used was the Data signal returned from the plane along with the Clock-Back signal. The Scanner used a front-panel Amphenol female Connector #57-40140 as its Input/Output port,

to which the cable connected through an Amphenol male Connector #57-30140. The Clock-Out signal was output on pin-4; the Clock-Back signal was received on pin-3; and the Data signal was received on pin-7.

The WCS-200 Scan Cycle was started by a Logic-True NIM pulse input to a front-panel LEMO socket; I found that the pulse had to be 50 nsec wide to trigger the Scan Cycle reliably. The Scan Cycle started with a 10 microsecond initialization period in which it cleared its internal 64-word buffer; after this was complete, the Scanner started producing the 10 MHz Clock-Out signal. The Scanner counted the positive edges of the Clock-Back pulses which it received and terminated the Scan Cycle when this count reached the hard-wired Scan-Limit. We hard-wired all of the PTM Scanners' Scan-Limits to be 1024- counts. We measured the total time of the Scan Cycles to be close to the expected 110 microseconds.

The Scanner performed clustering on successive "hits", with a maximum cluster size of 7; additional "hits" would start a new cluster. These clusters formed the Data Words of the Scanner output: the 13 most-significant bits contained the Clock Count of the "last-hit" of the cluster, and the 3 least-significant bits described the size of the cluster. The first word read out via CAMAC was the Delimiter Word: bits 1 to 6 reported the number of Data Words that follow, bits 7 to 15 formed a hard-wired Identification number of the Scanner, and bit 16 indicated the overflow status of the Scan.

E.8 Megavertors

The WCS-200 Scanners input and output signals of Positive-TTL logic. The Memory Address boards and all of the On-Plane logic was ECL. It was vaguely discussed that a SEC-612 Output Register, a CAMAC module, could be used to generate the necessary delay bits. An interface, it became apparent, was necessary to convert logic levels and to match signals and pin-assignments to the appropriate equipment. I described what we needed to the Electronics shop of the Fermilab Physics Department, and they designed and constructed the appropriate interface, which became known as a "Megavertor" ("Mega — Convertor").

The Megavertor was a single-width NIM-Module which housed conversion for two planes: section-A (the top half) and section-B (the bottom half). Mounted on the back of the module were the 20-pair headers for both sections, which were connected to the 20-pair headers on the Memory Address boards of the corresponding planes; these signals, both input and output, were all differential-ECL. The rest of the connections

were made on the front of the module. The signals from the PTM Fanout were received on a 5-pair header in the middle of the panel and were fanned out internally to both sections. Each section had another 5-pair header, which accommodated the Positive-TTL signals that were Input/Output to the Scanner; the Clock-Out signal was input on pin-1, the Clock-Back signal was output on pin-7, the Data signal was output on pin-9, and the even pins were all grounded. Each section also had a 10-pair header, which had Negative-TTL logic level Input/Readback of the Delay bits and the Frequency Control bit; this was provided to facilitate possible future use of an Output Register to set the necessary bits. Finally, each section sported an eight-segment DIP-switch, which was used to set manually the Delay bits and the Frequency Control bit. The signals from the 10-pair header and from the DIP-switch were actually OR-ed together, but the positions of switches-7 and 8 selected either the DIP-switch or the 10-pair header as input.

CURRICULUM VITAE

NAME: John James Ryan
116 N. Van Buren St.
Batavia, IL 60510
(708) 840-2087 (work)
(708) 406-1812 (home)
BITNET address = RYAN@FNAL

EDUCATION: Doctor of Philosophy in Physics,
Massachusetts Institute of Technology,
Cambridge, MA, 1990

Artium Baccalaurei cum Laude, Princeton University,
Princeton, NJ, 1983

PUBLICATIONS: M. R. Adams et al., A Spectrometer for Muon Scattering at the Tevatron,
Nucl. Instrum. Methods, A291:533, 1990

J. J. Ryan, F. Acceta, and R. H. Austin,
A Cryogenic Photon Mass Experiment,
Physical Review D, 32:802, 1985

CONFERENCE PRESENTATION: J. J. Ryan,
Nuclear Dependence in
Deep Inelastic Muon-Nucleon Scattering at 490 GeV/c,
PANIC XII - M.I.T., 25–29 June, 1990

Bibliography

[1] Adams et al. A spectrometer for muon scattering at the Tevatron. *Nuclear Instruments and Methods*, A291:533–551, 1990.

[2] S. Aid. *Deep Inelastic Muon Scattering at 480 GeV*. PhD thesis, University of Maryland, 1991.

[3] Silhacen Aïd. How to cluster the wire chambers in the E665 spectrometer? E665 Internal Report SW108, Fermilab, Batavia, IL, 31 October 1989.

[4] Silhacen Aid et al. LUND parameters in E665 MC1. E665 Internal Report SW142, Fermilab, Batavia, IL, December 1990.

[5] Perry Lee Anthony. The utility match pam (UMPAM). E665 Internal Report SW082, Fermilab, Batavia, IL, 12 April 1989.

[6] J. Bailey, D. R. Botterill, D. W. Braben, D. Clarke, H. E. Montgomery, P. R. Norton, G. Matone, A. Del Guerra, A. Giazotto, M. A. Giorgi, and A. Stefanini. Inclusive neutron spectra in electroproduction above the resonance region. *Nuclear Physics B*, 106:385+, 1976.

[7] Mark D. Baker, 1989. Private conversation.

[8] S. M. Berman and R. J. Oakes. Angular correlations in production processes. *Physical Review*, 135(4B):B1034–B1040, 24 August 1964.

[9] H. A. Bethe and J. Ashkin. Passage of radiations through matter. In E. Segrè, editor, *Experimental Nuclear Physics*, number 1, part II. John Wiley, New York, NY, 1959.

[10] Anwar Bhatti, Stephen Wolbers, and Wolfgan Wittek. E665 vertex processor user's guide, version 2.0. E665 Internal Report SW072, Fermilab, Batavia, IL, March 1989.

[11] A. Bialas and E. Bialas. Determination of quark-nucleon inclusive cross section from leptoproduction of hadrons in nuclear targets. *Physical Review D*, 21(3):675–684, 1980.

[12] J. D. Bjorken. Electroproduction at very small values of the scaling variable. Technical Report PUB-86/16, Fermilab, Batavia, IL, 1986.

[13] A. E. Brenner et al. Experimental study of single-particle inclusive hadron scattering and associated multiplicities. *Physical Review D*, 26(7):1497–1533, 1982.

[14] Wit Busza. Review of experimental data on hadron-nucleus collisions at high energies. *Acta Physica Polonica*, B(8):333+, 1977.

[15] Robert N. Cahn. Azimuthal dependence in leptoproduction: A simple parton model calculation. *Physics Letters*, 78B(2,3):269–273, 25 September 1978.

[16] Frank E. Close, Jianwei Qiu, and R. G. Roberts. QCD parton recombination and applications to nuclear structure functions. *Physical Review D*, 40(9):2820–2831, November 1989.

[17] The European Muon Collaboration, M. Arneodo, et al. Measurement of hadronic distributions in deep inelastic muon proton scattering. *Zeitschrift für Physik C*, 34:277–282, 1987.

[18] The European Muon Collaboration, J.J. Aubert, et al. Scaled energy distributions of single hadrons observed in muon proton scattering. Technical Report CERN-EP/80-130, CERN, Geneva, Switzerland, 23 July 1980.

[19] The European Muon Collaboration, J.J. Aubert, et al. Measurement of hadronic distributions in deep inelastic muon proton scattering. *Physics Letters*, 130B(1,2):118–122, 13 October 1983.

[20] G. V. Davidenko and N. N. Nikolaev. Hadron final states in deep-inelastic leptoproduction on nuclei. *Nuclear Physics*, B(135):333–353, 1978.

[21] M. De Palma et al. A system of large multiwire proportional chambers for a high intensity experiment. *Nuclear Instruments and Methods*, 217:135–139, 1983.

[22] M. Derrick et al. *Physical Review D*, 24:1071+, 1981.

[23] J. Engler, W. Flauger, B. Gibbard, F. Mönnig, K. Runge, and H. Schopper. A total absorption spectrometer for energy measurements of high-energy particles. *Nuclear Instruments and Methods*, 106:189–200, 1973.

[24] Fermilab-IHEP-ITEP-Michigan University Collaboration. *International Symposium on Lepton and Photon Interactions at High Energies*, 1981.

[25] R.D. Field and R.P. Feynman. Quark elastic scattering as a source of high-transverse-momentum mesons. *Physical Review D*, 15(9):2590, 1977.

[26] Howard Georgi and H. David Politzer. Clean tests of quantum chromodynamics in μp scattering. *Physical Review Letters*, 40(1):3–6, 2 January 1978.

[27] S. Gupta and A. H. Mueller. *Physical Review D*, 20:118, 1979.

[28] Ian Hacking. Leibniz and descartes: Proof and eternal truths. In Ted Honderich, editor, *Philosophy Through Its Past*, number LIX (1973) in Dawes Hicks Lecture on Philosophy to the British Academy, New York, 1984. Proceedings of the British Academy, Peguin Books.

[29] Iarocci. Plastic streamer tubes and their applications in high-energy physics. *Nuclear Instruments and Methods*, 217:30, 1984.

[30] David Jaffe and Richard Nickerson, 1988. Private conversation.

[31] Robert Kennedy. SPM efficiency studies. E665 Internal Report ST0118, Fermilab, Batavia, IL, December 1988.

[32] A. König and P. Kroll. A realistic calculation of the azimuthal asymmetry in semi-inclusive deep inelastic scattering. *Zeitschrift für Physik C*, 16:89–92, 1982.

[33] G. Köpp, R. Maciejko, and P. M. Zerwas. Angular asymmetries in hadron distributions of neutrino-nucleon reactions in quantum chromodynamics. *Nuclear Physics*, B144:123–140, 1978.

[34] Dr. Timothy Leary. "The religious experience: Its production and interpretation", in *The Psychedelic Reader*, ed. Gunther M. Weil (New Hyde Park, N.Y.: University Books), pp. 191-213, . In David E. Smith M.D., M.S., editor, *Journal of Psychedelic Drugs*, number I — Issue 2 in "Psychedelic Drugs and Religion", pages 191–213, San Francisco, CA, 1967. Haight-Ashbury Medical Clinic.

[35] D. H. Lyth. Exclusive electroproduction processes. In A. Donnachie and G. Shaw, editors, *Electromagnetic Interactions of Hadrons*, number 1, chapter 3. Plenum Press, New York, NY, 1978.

[36] Stephan Rayleigh Magill. *Xe/D2 Cross Section Ratio from Muon Scattering at 490 GeV/c*. PhD thesis, University of Illinois at Chicago, Chicago, IL, July 1990.

[37] A. Malensek and J.G. Morfin. The tevatron muon beam: A high intensity beam with well defined polarization. Technical Report TM1193 2966.00, Fermilab, Batavia, IL, July 1983.

[38] A. Méndez, A. Raychaudhuri, and V. J. Stenger. QCD effects in semi-inclusive neutrino processes. *Nuclear Physics*, B148:499–512, 1979.

[39] Douglas Grant Michael. *A Study of Transverse Momentum and Jets Using Forward Hadrons and Photons in Deep Inelastic Muon Scattering at 490 GeV/c.* PhD thesis, Harvard University, Cambridge, MA, April 1990.

[40] G. Miller, E. D. Bloom, G. Buschhorn, D. H. Coward, H. Destaebler, J. Drees, J. I. Friedman, G. C. Hartmann, C. L. Jordan, H. W. Kendall, L. W. Mo, R. E. Taylor, and R. Verdier. Inelastic electron-proton scattering at large momentum tranfers and the inelastic structure functions of the proton. ***Physical Review D***, 5(3):528–544, 1 February 1972.

[41] Philip M. Morse and Herman Feshbach. ***Integral Equations***, volume I, chapter 8. McGraw-Hill, New York, 1953.

[42] A. H. Mueller. *Physical Review D*, 18:3705, 1978.

[43] Donald H. Perkins. *Introduction to High Energy Physics.* Addison-Wesley, Don Mills, Ontario, 1982.

[44] William J. Price. *Nuclear Radiation Detection.* Magraw-Hill, New York, 1958.

[45] Arnd Röser. Method of the PCV pattern recognition and first preliminary results. E665 Internal Report SW0079, Fermilab, Batavia, IL, 15 October 1988.

[46] Arnd Röser. A Monte Carlo study of the PCV pattern recognition method. E665 Internal Report SW0085, Fermilab, Batavia, IL, 15 April 1989.

[47] Arnd Röser. Summary of the PCV efficiency calculation. E665 Internal Report SW0099, Fermilab, Batavia, IL, 10 August 1989.

[48] B. Rossi. *High Energy Particles.* Prentice Hall, Englewood Cliffs, NJ, 1952.

[49] John James Ryan. Pattern recognition efficiencies, RUN 87. E665 Internal Report SW141, Fermilab, Batavia, IL, November 1989.

[50] John James Ryan. PC pattern recognition studies. E665 Internal Report SW103, Fermilab, Batavia, IL, August 1989.

[51] John James Ryan. PTM chamber efficiencies, RUN 87. E665 Internal Report AN079, Fermilab, Batavia, IL, March 1990.

[52] John James Ryan. SMS chamber efficiencies, RUN 87. E665 Internal Report AN080, Fermilab, Batavia, IL, June 1990.

[53] John James Ryan, Michael Schmitt, and Anwar Bhatti. Chamber efficiencies, RUN 87. E665 Internal Report AN081, Fermilab, Batavia, IL, December 1990.

[54] Alex Salvarani. Track fitting description document. E665 Internal Report SW040, Fermilab, Batavia, IL, August 1986.

[55] Alexandro Salvarani. *Forward Hadron Production in Muon-Nucleus Scattering.* PhD thesis, University of California at San Diego, San Diego, CA, 1991.

[56] Table of periodic properties of the elements. Technical report, Sargent-Welch Scientific Company, Skokie, Il, 1980.

[57] Sauli. Principles of operation of multiwire proportional and drift chambers. Lectures given in the Academic Training Programme of CERN CERN 77-09, CERN, Geneva, Switzerland, May 1977.

[58] Michael Schmitt. *Neutral Vector Meson Production in Deep Inelastic Muon Scattering.* PhD thesis, Harvard University, Cambridge, MA, 1991.

[59] T. Sjostran. The LUND monte carlo for jet fragmentation (LUND 4.3). Technical Report LU TP 82-3, March 1982.

[60] Peter F. Strawson. *The Bounds of Sense: An Essay on Kant's Critique of Pure Reason.* Methuen, London, 1966.

[61] Swanson, 1987. Private communication.

[62] C. Tao et al. *Physical Review Letters*, 44:1726+, 1980.

[63] W. Kittel (Nijmegen U.). Partons in soft hadro-production. *Acta Physica Polonica*, B12(12):1093–1113, 1981.

[64] Robert C. Weast, editor. CRC Press, Boca Raton, FA, 67 edition, 1987.

[65] D. H. Wilkinson. *Ionization Chambers and Counters.* Cambridge University Press, London, 1950.

[66] Chiri Yamaguchi, Takakazu Shintomi, and Masayoshi Masuda. Accuracy of the photon-difference method in the giant dipole resonance region. *Nuclear Instruments and Methods*, 106:471–476, 1973.